Computer Simulation and Interpretation of the Transport Coefficients of the Lennard-Jones Model Fluid

DISSERTATION

A Thesis Accepted
by the Department of Mechanical Engineering
of the University of the Federal Armed Forces Hamburg
in Partial Fulfillment of the Requirements
for the Degree of Doktor-Ingenieur
by

Dipl.-Ing. Karsten Meier

of Rehren

Hamburg, June 2002

Acknowledgments

Hamburg, June 2002

Karsten Meier

Contents

Nomenclature

Latin Letters

Symbol	Unit	Quantity
$\boldsymbol{A}$	m^2	surface normal vector
A		arbitrary phase variable
$A(\boldsymbol{r},t)$		arbitrary local macroscopic quantity
$a(r)$		pair function corresponding to phase variable A
$\boldsymbol{a}_\mathrm{i}$	$\mathrm{m\,s}^{-2}$	acceleration vector of particle i
a_i		contribution of particle i to A
B		arbitrary phase variable
B	m^3	second thermal virial coefficient
B_D	$\mathrm{m}^2\,\mathrm{s}^{-1}$	second self-diffusion virial coefficient
B_{η_b}	$\mathrm{Pa\,s\,m}^3$	second bulk viscosity virial coefficient
B_{η_cc}	$\mathrm{Pa\,s\,m}^3$	configurational-configurational contribution to the second viscosity virial coefficient
B_{η_tc}	$\mathrm{Pa\,s\,m}^3$	translational-configurational contribution to the second viscosity virial coefficient
b	-	number of blocks
C	m^6	third thermal virial coefficient
C_0		normalization constant
$C_\mathrm{AA}(t)$		autocorrelation function of phase variable A
$C_\mathrm{AB}(t)$		cross-correlation function of phase variables A and B
$C_\mathrm{AB}^\mathrm{eq}(t)$		time-correlation function of phase variables A and B in an equilibrium ensemble
C^D	$\mathrm{kg}^2\,\mathrm{m}^{-6}$	tagged particle density autocorrelation function
C_N		normalization constant
C_p	$\mathrm{J\,K}^{-1}$	isobaric heat capacity
$C^\mathrm{p,l}$	$\mathrm{kg}^2\,\mathrm{m}^{-4}\,\mathrm{s}^{-2}$	longitudinal momentum density autocorrelation function
$C^\mathrm{p,t}$	$\mathrm{kg}^2\,\mathrm{m}^{-4}\,\mathrm{s}^{-2}$	transverse momentum density autocorrelation function
C_V	$\mathrm{J\,K}^{-1}$	isochoric heat capacity
c_p	$\mathrm{J\,K}^{-1}$	isobaric heat capacity per particle
$c_\mathrm{p,0}$	$\mathrm{J\,K}^{-1}$	ideal gas isobaric heat capacity per particle

$c_{\mathrm{p,m}}$	$\mathrm{J\,kg^{-1}\,K^{-1}}$	mass specific isobaric heat capacity
c_{V}	$\mathrm{J\,K^{-1}}$	isochoric heat capacity per particle
$c_{\mathrm{V,m}}$	$\mathrm{J\,kg^{-1}\,K^{-1}}$	mass specific isochoric heat capacity
D	$\mathrm{m^2\,s^{-1}}$	self-diffusion coefficient
E	J	energy, internal energy, energy eigenvalue
E_{i}	J	energy of particle i
e	J	internal energy per particle
e_{m}	$\mathrm{J\,kg^{-1}}$	mass specific internal energy
e_{i}	J	contribution of particle i to the internal energy
$\boldsymbol{F}$	N	force
$\boldsymbol{F}_{\mathrm{i}}$	N	force on particle i
$\boldsymbol{F}_{\mathrm{ij}}$	N	force on particle i due to particle j
f	$\mathrm{s^{-1}}$	frequency
$\boldsymbol{G}$	$\mathrm{kg\,m}$	constant of motion related to the initial position of the centre of mass of the system
G	Pa	shear modulus
$G_{\mathrm{tc,max}}$	Pa	normalization factor of the translational-configurational shear stress correlation function
$g(r)$	-	radial pair distribution function
H	J	classical Hamiltonian
$\mathcal{H}$	J	Hamiltonian
h_{i}	J	contribution of particle i to the enthalpy
h_{m}	$\mathrm{J\,kg^{-1}}$	mass specific enthalpy
$\boldsymbol{J}^{\mathrm{i}}$		thermodynamic flux vector
$\boldsymbol{J}^{\mathrm{D}}$	$\mathrm{kg\,m^{-2}\,s^{-1}}$	tagged particle flux vector
$\boldsymbol{J}^{\mathrm{e}}$	$\mathrm{W\,m^{-2}}$	energy flux vector
$\boldsymbol{J}^{\mathrm{p}}$	$\mathrm{kg\,m^{-2}\,s^{-1}}$	momentum density vector
$\boldsymbol{J}^{\mathrm{p,l}}$	$\mathrm{kg\,m^{-2}\,s^{-1}}$	longitudinal momentum density vector
$\boldsymbol{J}^{\mathrm{p,t}}$	$\mathrm{kg\,m^{-2}\,s^{-1}}$	transverse momentum density vector
$\boldsymbol{J}^{\mathrm{q}}$	$\mathrm{W\,m^{-2}}$	heat flux vector
$\boldsymbol{J}^{\mathrm{s}}$	$\mathrm{W\,K^{-1}\,m^{-2}}$	entropy flux vector
K	J	kinetic energy
K	Pa	bulk modulus
$\boldsymbol{k}$	$\mathrm{m^{-1}}$	wave vector
$\boldsymbol{L}_{\mathrm{ij}}$		phenomenological coefficient tensor
L_{ij}		phenomenological coefficient

L	m	box length
$\boldsymbol{M}$	$\mathrm{kg\,m\,s^{-1}}$	total momentum vector of the system
$M_{\mathrm{i}}^{\mathrm{j}}$	kg	abbreviation in the Jacobi coordinate representation
m	kg	mass, particle mass
m	-	slope of the linear part of the long time tail in double logrithmic representation
m_{i}	kg	mass of particle i
N	-	number of particles
N^{D}	-	number of tagged particles
N^{i}		time-correlation function of thermodynamic flux $\boldsymbol{J}^{\mathrm{i}}$
$N_{\mathrm{cc}}^{\mathrm{i}}$		time-correlation function of configurational flux $\boldsymbol{J}_{\mathrm{c}}^{\mathrm{i}}$
$N_{\mathrm{tc}}^{\mathrm{i}}$		time-correlation function of translational flux $\boldsymbol{J}_{\mathrm{t}}^{\mathrm{i}}$ and configurational flux $\boldsymbol{J}_{\mathrm{c}}^{\mathrm{i}}$
$N_{\mathrm{tt}}^{\mathrm{i}}$		time-correlation function of translational flux $\boldsymbol{J}_{\mathrm{t}}^{\mathrm{i}}$
n_{b}	-	number of time steps in a block
n_{PE}	-	number of processing elements
n_{step}	-	number of time steps in a simulation
n_{to}	-	number of time origins
$\boldsymbol{P}$	Pa	pressure tensor
P	Pa	average pressure
$\boldsymbol{P}_{\mathrm{i}}$	$\mathrm{kg\,m\,s^{-1}}$	Jacobi momentum vector
$\boldsymbol{p}$	$\mathrm{kg\,m\,s^{-1}}$	momentum vector
$\boldsymbol{p}_{\mathrm{i}}$	$\mathrm{kg\,m\,s^{-1}}$	momentum vector of particle i
p	Pa	pressure
p_{c}	Pa	configurational pressure
$\boldsymbol{R}^{\mathrm{e}}$	$\mathrm{J\,m^{-2}}$	vector related to the centre of energy
$\boldsymbol{R}_{\mathrm{i}}$	m	Jacobi coordinate vector
$\boldsymbol{R}_{\mathrm{i}}'$	-	scaled Jacobi coordinate vector
$\boldsymbol{R}^{\mathrm{p}}$	$\mathrm{kg\,m^{-1}\,s^{-1}}$	tensor related to the centre of momentum
$\boldsymbol{r}$	m	position vector
$\boldsymbol{r}_{0}$	m	reference position vector
$\boldsymbol{r}_{\mathrm{i}}$	m	position vector of particle i
$\boldsymbol{r}_{\mathrm{ij}}$	m	distance vector between particle i and j
r	m	distance
r_{cut}	m	cutoff radius
r_{ij}	m	distance between particle i and j

S	$\mathrm{J\,K^{-1}}$	entropy
S	-	speed-up
S_{A}	-	statistical inefficiency in phase variable A
s_{m}	$\mathrm{J\,kg^{-1}K^{-1}}$	mass specific entropy
s		Laplace parameter
T	K	thermodynamic temperature
T_{p}	s	time period
t	s	time
t_0	s	time origin
t'	s	integration variable
t''	s	integration variable
$t(1)$	s	real time for a sequential run on a single PE
$t(n_{\mathrm{PE}})$	s	real time for a run on n_{PE} PE's
U	J	potential energy
u	J	potential energy per particle
$u(r)$	J	intermolecular pair potential function
u_{i}	J	contribution of particle i to the potential energy
$\boldsymbol{v}$	$\mathrm{m\,s^{-1}}$	velocity vector
$\boldsymbol{v}_{\mathrm{i}}$	$\mathrm{m\,s^{-1}}$	velocity vector of particle i
V	$\mathrm{m^3}$	volume
w_0	$\mathrm{m\,s^{-1}}$	zero frequency speed of sound
$\boldsymbol{X}^{\mathrm{i}}$		thermodynamic force
Z		arbitrary thermodynamic state variable
Z_{i}		fictitious instantaneous value of the arbitrary thermo-dynamic state variable Z

Greek Letters

Symbol	Unit	Quantity
α	m^{-1}	sound absorption coefficient
β_a	m^3	second acoustic virial coefficient
β_S	Pa^{-1}	isentropic compressibility
β_T	Pa^{-1}	isothermal compressibility
γ_a	m^6	third acoustic virial coefficient
γ_V	$\mathrm{Pa\,K}^{-1}$	isothermal pressure coefficient
Δt	s	time step size
δA		fluctuation of phase variable A
δp	Pa	pressure fluctuation
δV	m^3	infinitesimal volume element
$\boldsymbol{\varepsilon}$	-	strain tensor
ε	J	Lennard-Jones potential well depths
$\dot{\boldsymbol{\varepsilon}}$	s^{-1}	strain rate tensor
η	$\mathrm{Pa\,s}$	viscosity
η_b	$\mathrm{Pa\,s}$	bulk viscosity
η_l	$\mathrm{Pa\,s}$	longitudinal viscosity
μ_JT	$\mathrm{K\,m}^3\,\mathrm{J}^{-1}$	Joule-Thompson coefficient
μ_α	kg	reduced mass
λ	$\mathrm{W\,m}^{-1}\,\mathrm{K}^{-1}$	thermal conductivity
Ω	-	phase space volume
$\Omega^{(\mathrm{i,j})*}$	-	reduced collision integral
$\Omega_\mathrm{m,n}$	$\mathrm{J}^{-\mathrm{n}}\,\mathrm{m}^{-3\mathrm{m}}$	phase space function
ω	s^{-1}	angular frequency
ω	-	phase space density
Ψ	-	wave function
$\boldsymbol{\Pi}$	Pa	viscous pressure tensor
Θ	$\mathrm{W\,(s\,m\,K)}^{-1}$	thermal modulus
$\Theta_\mathrm{tc,max}$	$\mathrm{W\,(s\,m\,K)}^{-1}$	normalization factor of the translational-configurational heat flux correlation function
ρ	m^{-3}	particle density
ρ_l	m^{-3}	saturated liquid density
ρ_v	m^{-3}	saturated vapour density
ρ_m	$\mathrm{kg\,m}^{-3}$	mass density

$\rho_\mathrm{m}^\mathrm{D}$	$\mathrm{kg\,m^{-3}}$	partial mass density of tagged particles
σ	$\mathrm{W\,K^{-1}\,m^{-3}}$	entropy source strength
σ	m	Lennard-Jones potential parameter
$\boldsymbol{\tau}$	Pa	stress tensor
τ	s	integration variable
τ_D	s	self-diffusion relaxation time
τ_η	s	shear relaxation time
τ_{η_b}	s	bulk relaxation time
τ_λ	s	thermal relaxation time

Indices and Abbreviations

Symbol	Quantity
*	reduced quantity
0	zero frequency
0	zero density
1b	one-body
2b	two-body
3b	three-body
4b	four-body
∞	infinite frequency
a	acoustic
auto	autocorrelation contribution
b	bulk
b	block
c	configurational
c	critical point
cc	configurational-configurational
cr	critical enhancement
cross	cross-correlation contribution
D	tagged particle
e	energy
el	electronic
eq	equilibrium
FEOS	fundamental equation of state
i	index

I	outer loop iteration
j	index
k	index
LRC	long range correction
l	longitudinal
MD	molecular dynamics
m	index
n	index
p	momentum
q	heat
PE	processing element
r	rotational
res	residual
s	entropy
t	translational
t	transverse
tc	translational-configurational
tt	translational-translational
tr	triple point
vib	vibrational
x	Cartesian coordinate
y	Cartesian coordinate
z	Cartesian coordinate
α	Cartesian coordinate index
α	Jacobi coordinate index
β	Cartesian coordinate index

Fundamental Physical Constants

Quantity	Symbol	Numerical value [154]
Avogadro constant	N_{A}	$6.02214199 \cdot 10^{23}$ mol^{-1}
Boltzmann constant	k	$1.3806503 \cdot 10^{-23}$ J K^{-1}
Planck constant	h	$6.62606876 \cdot 10^{-34}$ J s
molar gas constant	R	8.314472 J mol^{-1} K^{-1}

Mathematical Symbols and Operations

Symbol	Operation
i	imaginary unit
$\mathrm{Re}(A)$	real part of A
A^*	complex conjugate of A
$\langle A \rangle$	average of A
$\langle A \rangle_\mathrm{b}$	block average of A
$\sigma(A)$	standard deviation of A
$\sigma(\langle A \rangle)$	standard deviation of $\langle A \rangle$
$\sigma(\langle A \rangle_\mathrm{gauss})$	standard deviation of $\langle A \rangle$ on the assumption of Gaussian statistics
$\sigma^2(A)$	variance of A
$\sigma^2(\langle A \rangle_\mathrm{b})$	variance of block averages $\langle A \rangle_\mathrm{b}$
$\sigma^2(\langle A \rangle_\mathrm{gauss})$	variance of $\langle A \rangle$ on the assumption of Gaussian statistics
$\mathrm{cov}(A, B)$	covariance of A and B
$\mathcal{O}(N)$	of the order of N
$\delta(\boldsymbol{r} - \boldsymbol{r}_\mathrm{i})$	Kirkwood δ-function
$\delta(t)$	Dirac δ-function
$\Theta(t)$	unit step function

Vector and tensor notation

$\boldsymbol{a} \cdot \boldsymbol{b}$	scalar product of vector $\boldsymbol{a}$ and vector $\boldsymbol{b}$
$\boldsymbol{a} \times \boldsymbol{b}$	vector product of vector $\boldsymbol{a}$ and vector $\boldsymbol{b}$
$\boldsymbol{a}\,\boldsymbol{b}$	tensor product of vector $\boldsymbol{a}$ and vector $\boldsymbol{b}$
$\boldsymbol{a} \cdot \boldsymbol{B}$	scalar product of vector $\boldsymbol{a}$ and second-rank tensor $\boldsymbol{B}$
$\boldsymbol{A}\boldsymbol{B}$	tensor product of second-rank tensor $\boldsymbol{A}$ and second-rank tensor $\boldsymbol{B}$
$\boldsymbol{A} : \boldsymbol{B}$	scalar product of second-rank tensor $\boldsymbol{A}$ and second-rank tensor $\boldsymbol{B}$
$\mathrm{tr}(\boldsymbol{A})$	trace of tensor $\boldsymbol{A}$
$\widehat{\boldsymbol{A}}$	traceless part of tensor $\boldsymbol{A}$
$\boldsymbol{A}^T$	transpose of tensor $\boldsymbol{A}$

$\boldsymbol{I}$

unit tensor, $I_{\alpha\beta} = \begin{cases} 1 & \text{if } \alpha = \beta \\ 0 & \text{otherwise} \end{cases}$

∇

Nabla operator

$\nabla_{\boldsymbol{r}_{ij}} a$

gradient of scalar a with respect to $\boldsymbol{r}_{ij}$

Fourier and Laplace transforms

$$F(i\omega) = \mathcal{F}\{f(t)\} = \int_{-\infty}^{\infty} e^{-i\omega t} f(t)\, \mathrm{d}t \qquad \text{Fourier transform}$$

$$F(s) = \mathcal{L}\{f(t)\} = \int_{0}^{\infty} e^{-st} f(t)\, \mathrm{d}t \qquad \text{Laplace transform}$$

$$C(i\omega) = \mathcal{L}_{\omega}\{C(t)\} = \int_{0}^{\infty} e^{-i\omega t} C(t)\, \mathrm{d}t \qquad \text{Fourier-Laplace transform}$$

$$F(i\boldsymbol{k}) = \int f(\boldsymbol{r}) \exp\{i\boldsymbol{k} \cdot \boldsymbol{r}\}\, \mathrm{d}\boldsymbol{r} \qquad \text{spatial Fourier transform}$$

$$f(\boldsymbol{r}) = \frac{1}{(2\pi)^3} \int F(i\boldsymbol{k}) \exp\{-i\boldsymbol{k} \cdot \boldsymbol{r}\}\, \mathrm{d}\boldsymbol{k} \qquad \text{inverse spatial Fourier transform}$$

1 Introduction

Hydrodynamic transport processes in fluids play fundamental roles in many diverse areas of science, engineering and every day life. The knowledge of the transport coefficients in the fluid region of the phase diagram and elementary understanding of the transport mechanisms on the molecular scale are essential requirements for modelling hydrodynamic transport processes. This work aims at the computation of the transport coefficients of the Lennard-Jones model fluid in the fluid region of the phase diagram by equilibrium molecular dynamics simulations using time-correlation function theory.

In 1931, the later Nobel Prize laureate Lars Onsager[1] introduced the *regression hypothesis* in his famous derivation of the reciprocal relations between the phenomenological transport coefficients [168, 169]. This hypothesis states that microscopic fluctuations of thermodynamic fluxes decay on the average according to the macroscopic transport relations that relate the fluxes to their corresponding thermodynamic forces. Since it is not possible to distinguish if a fluctuation in a system is a microscopic equilibrium fluctuation or if the system experiences the last stages of the decay of a transport process to equilibrium, the regression hypothesis can be utilized to determine transport coefficients from measurements of the average temporal decay of the fluctuations in a system at thermodynamic equilibrium. This approach is realized in light scattering experiments, where transport coefficients are extracted from the spectral distribution of light scattered by a fluid [117, 159]. Transport coefficient data measured in such experiments are known to agree with data obtained in experiments where conventional hydrodynamic measurement principles are employed, see for example [27]. Moreover, the regression hypothesis is the basis for time-correlation function theory [222]. In this statistical theory of transport processes, transport coefficients are expressed as integrals of time-correlation functions of their corresponding thermodynamic fluxes. Such relations are employed in equilibrium molecular dynamics simulations to determine transport coefficients.

---

[1] Lars Onsager (1903-1976) was awarded the Nobel Prize in Chemistry in 1968 for the discovery of the reciprocal relations between the phenomenological transport coefficients that are fundamental for the thermodynamics of irreversible processes (L. Onsager: "The motion of ions: principles and concepts", Nobel Lecture 1968, in: *Nobel Lectures Chemistry 1961-1970*, pp. 272-288, Elsevier, Amsterdam, 1972).

Time-correlation function theory was developed in the period between 1950 and 1965. The expressions for the hydrodynamic transport coefficients viscosity, thermal conductivity, bulk viscosity and the mutual diffusion coefficient in mixtures were derived by Green [58, 59, 60] in 1954. Independently, Kubo et al. [111, 112] extracted the same expressions directly from Onsager's work on the reciprocal relations in 1957. Later, other authors devised alternative methods for the derivation of the Green-Kubo integral formulas, which are summarized in a review article by Zwanzig [222]. In 1960, Helfand [77] derived alternative expressions for the hydrodynamic transport coefficients which are completely equivalent to the Green-Kubo integral formulas. These expressions, the so-called Einstein relations, relate the transport coefficients to the long time limit of the slope of generalized mean-squared displacement functions.

Both, Green-Kubo integral formulas and Einstein relations are valid at any density and temperature, whereas kinetic theory has only been successfully applied at low density gaseous states. Among others, McLennan and Swenson [139] proved that in the zero density limit time-correlation function theory yields the same results for the transport coefficients of monatomic fluids as the Chapman-Enskog solution to the Boltzmann equation [88]. These proofs employed the Boltzmann equation or some generalized kinetic equation to evaluate the Green-Kubo formulas. A calculation of the zero density viscosity and thermal conductivity based entirely on time-correlation function theory was first carried out by Alavi and Snider [3] in 1998. In subsequent articles, Alavi and Snider [4, 199] derived expressions for the second viscosity and thermal conductivity virial coefficients for purely repulsive intermolecular potentials from time-correlation function theory and showed that their results agree with those obtained by Curtiss et al. [89, 90, 91, 198] from a generalized Boltzmann equation by means of kinetic theory. Except for the zero density transport coefficients and the second transport virial coefficients, accurate solutions to the Green-Kubo integral formulas have not yet been obtained due to the complexity of the transport mechanisms on the molecular scale.

Transport coefficients at arbitrary fluid states can, at present, only be *computed* by means of molecular dynamics simulations. In molecular dynamics simulations, the phase space trajectory of a many particle system is generated by numerical solution of the microscopic equations of motion on a computer [10, 65, 182]. At every simulated time step, the instantaneous thermodynamic fluxes are calculated and stored on a hard disk. In a subsequent analysis step, time-correlation functions and generalized mean-squared displacement functions can be computed without approximations. Molecular dynamics simulations enable investigations in state regions

where experiments are difficult to perform, for example in the metastable region or compressed liquid region near the freezing line. Properties that are difficult to measure in experiments such as the self-diffusion coefficient or bulk viscosity can be examined in molecular dynamics simulations. Beside the macroscopic transport coefficients, time-correlation functions themselves are interesting subjects to study as they provide insights into transport mechanisms on the molecular scale. The discovery of long time tails in the velocity autocorrelation function by Alder and Wainright [6, 8] might serve as an example for a result obtained by molecular dynamics simulations that would have been difficult to find in any other way. Limitations are imposed on the molecular dynamics simulation method only by the available computational resources that dictate the range of parameters that can be employed, for instance the number of particles or length of the simulated time period.

Another computational approach to transport coefficients is provided by nonequilibrium molecular dynamics simulations. Many different nonequilibrium simulation techniques are described in literature, see for example [10, 12, 49, 97, 160, 161, 182]. Although being usually considered as more efficient from a computational point of view than the application of time-correlation function theory in equilibrium simulations, they provide conceptual problems, which make the rigorous analysis and interpretation of the results difficult. For example, the artificial removal of heat from a system with thermostatting algorithms [120], extrapolation of simulation results to thermodynamic equilibrium [210] or introduction of periodic effects by the often employed Lees-Edwards boundary conditions [174] are still under discussion. Moreover, only one transport coefficient can be computed by a nonequilibrium simulation run, whereas equilibrium molecular dynamics is inherently a multi-property method. In principle, all thermodynamic state variables and transport coefficients can be computed at the same state point by a single simulation run so that consistent data sets can be generated over wide ranges of thermodynamic states.

For the determination of transport coefficients of a real fluid by equilibrium molecular dynamics simulations, first, an accurate intermolecular potential function is required, and, second, the choice of the simulation parameters must ensure that the results correspond to macroscopic transport coefficients. Accurate intermolecular potential functions are only available for some simple real fluids, for example the noble gases helium [99] and argon [16], the diatomic gases nitrogen [15] and carbon monoxide [176], and carbon dioxide [22]. Computations of transport coefficients of real fluids were in most cases restricted to the zero density values by kinetic theory methods [16, 23, 74, 75, 76, 99] and achieved agreement with experimental data

within a few percent for the viscosity, while larger deviations were observed for the thermal conductivity and bulk viscosity. Hurly and Moldover [99] fitted an empirical function to *ab initio* data for the interaction energies of helium atoms and calculated the zero density transport coefficients. Their results agreed with the best experimental data within the combined uncertainties, while their uncertainties were smaller than those of the experimental data. Huber et al. [39, 98] carried out elaborate equilibrium molecular dynamics simulations with *ab initio* potentials to determine the self-diffusion coefficient, viscosity and thermal conductivity of neon, argon and carbon dioxide at liquid and supercritical states. Their simulation data for the viscosity and thermal conductivity had uncertainties between 5 and 10 % and agreed with experimental viscosities and thermal conductivities within two times these uncertainties. Although the uncertainties of the self-diffusion data were smaller, higher systematic deviations between simulation and experimental data than for the viscosity and thermal conductivity were observed.

Since molecular dynamics simulations of transport coefficients for real fluids require large computational resources, simple idealized intermolecular potential models, such as the hard sphere, square well or Lennard-Jones potential, are often employed to predict transport coefficients of real fluids or to study transport mechanisms on the molecular scale. In applications of statistical thermodynamics, they serve as simple models for fluids consisting of spherical molecules or, for instance in the united atom approach, as a building block for structural groups in complex molecules such as long-chain alkanes, polymers or even proteins. Furthermore, precise simulation data for transport coefficients of theses model fluids serve as references for testing new theories or simulation techniques. For these reasons, some simple idealized intermolecular potential functions have the character of reference models in statistical thermodynamics.

This work focuses on the transport coefficients of the Lennard-Jones model fluid. Thermodynamic state variables of this model were studied by several authors, for example [102, 109, 122], and with the recent fundamental equations of state of Kolafa and Nezbeda [110] and Mecke et al. [142], they can accurately be calculated over a wide range of fluid states. Simulation studies of transport coefficients are scarce and often only few state points are considered. In related works, comprehensive simulation studies on transport coefficients of model fluids were carried out by Alder et al. [7], Erpenbeck and Hoover [43], Ratanapisit [183] for the hard sphere and by Michels and Trappeniers [147, 148, 149, 150, 151, 152] for the square well model fluid. Only few publications report simulation data for the transport coefficients

of models for non-polar molecular fluids, see for example [92, 93, 94, 125, 163], or the Stockmayer model for polar fluids [115]. The transport coefficients of the Lennard-Jones model fluid were previously examined by Michels and Trappeniers [145, 146, 153], Heyes [79, 84], Hammonds and Heyes [66] and Rowley and Painter [185]. The works of Michels and Trappeniers and Rowley and Painter concentrate on the self-diffusion coefficient and viscosity, while Heyes [84] and Hammonds and Heyes [66] additionally report thermal conductivities. Little is known about the bulk viscosity. In these studies, the uncertainties of simulation data were in part up to two orders of magnitude larger than those commonly achieved in experiments for real fluids. In this work, it is attempted to determine the transport coefficients at near-experimental uncertainties by means of equilibrium molecular dynamics simulations.

This work is organized as follows: The second chapter describes fundamentals of statistical thermodynamics and time-correlation function theory. In chapter three, the practical realization of a simulation and analysis of results is described. Chapters four, five and six analyze the self-diffusion coefficient, the viscosity and bulk viscosity, respectively, in detail. The thesis concludes with an interpretation of the transport coefficients in the relaxation time concept introduced by Zwanzig and Mountain in their work on the high-frequency elastic moduli of fluids [158, 223]. Conclusions are presented in chapter eight.

2 Fundamentals

This chapter describes fundamentals of statistical thermodynamics and provides the relations that are required to compute macroscopic thermodynamic state variables and transport coefficients in equilibrium molecular dynamics simulations.

2.1 Macroscopic Equilibrium States, Microscopic States and Ensembles

According to Hanley [67], the macroscopic thermodynamic equilibrium state of a single phase system for a prescribed set of macroscopic state variables, for instance the number of particles N, volume V and energy E, is completely described by the following properties: All macroscopic intensive state variables are constant at all times and take the same values at all positions in the system. There are no gradients in any state variable and no fluxes in the system. According to the second law, the entropy of the system takes a maximum at equilibrium and there is no entropy production in the system. The complete thermodynamic information about the system is contained in the fundamental equation of state. For isolated systems that are sampled in molecular dynamics simulations, the fundamental equation of state is given by the entropy formulation $S = S(N, V, E)$. Any other thermodynamic state variable of the system can be calculated from the fundamental equation of state by thermodynamic relations [29].

On the molecular scale, all properties of the system which are not constrained by the thermodynamic environment fluctuate. Macroscopic system properties, for example thermodynamic state variables, that are measured in experiments are time averages of fluctuating microscopic system properties. Instantaneous microscopic system properties are termed *phase variables*. The time average of an arbitrary phase variable A is defined by

$$A = \langle A(t) \rangle = \lim_{T_\mathrm{p} \to \infty} \frac{1}{T_\mathrm{p}} \int_0^{T_\mathrm{p}} A(t) \, \mathrm{d}t \quad , \tag{2.1}$$

where T_p denotes a time period. The instantaneous difference between a phase variable and its time average

$$\delta A(t) = A(t) - \langle A(t) \rangle \tag{2.2}$$

is termed *fluctuation*. Instantaneous values of phase variables and their time averages are denoted by the same symbols if their meaning is evident from the context. In doubtful cases, the time dependence of instantaneous phase variables is explicitly shown or angular brackets are used to indicate average values. Figure 2.1 illustrates the definition of the time average and fluctuation of an arbitrary phase variable.
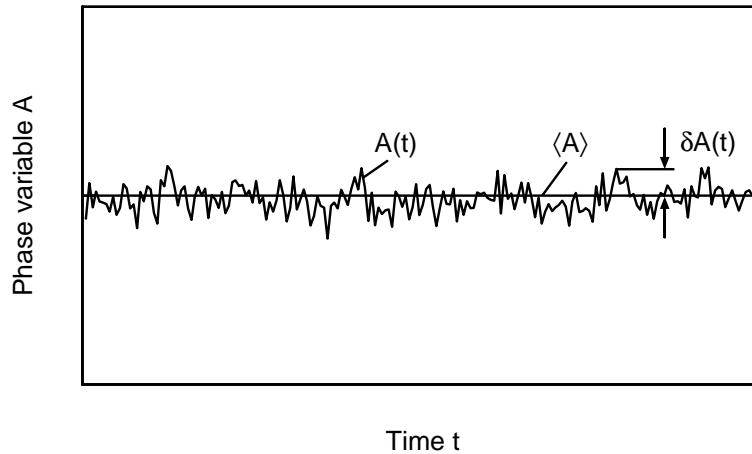
Figure 2.1. Temporal evolution of an arbitrary phase variable A, its time average and fluctuations.

The microscopic time-evolution of a system at the most detailed level is described by the time-dependent Schrödinger equation of quantum mechanics,

$$\frac{ih}{2\pi}\frac{\partial \Psi}{\partial t} = \mathcal{H}\Psi \quad , \tag{2.3}$$

where $\mathcal{H}$ is the Hamiltonian of the system and Ψ denotes the wave function of the system. In principle, the solution to this equation, the time-dependent wave function $\Psi(t)$, is the most complete description of the macroscopic system. However, solving the Schrödinger equation for a system composed of $\mathcal{O}(10^{23})$ molecules is in general impossible. Instead, a statistical approach is realized by ensemble theory. An ensemble is a virtual collection of an infinite number of systems that are all copies of the macroscopic system. Macroscopically, the systems in the ensemble are identical, but their microscopic states are different. Time averages of phase variables of the original system are replaced by weighted ensemble averages over all systems of the ensemble and the partition function replaces the macroscopic fundamental equation of state. The partition function is a weighted sum of all possible microscopic energy states of the system. For any macroscopic thermodynamic environment, a

corresponding ensemble can be invented. In molecular dynamics simulations at *constant energy*, a subset of the so-called microcanonical ensemble, the molecular dynamics ensemble, is sampled (see Section 2.3). For the purposes of this section, it is sufficient to restrict the discussion to the microcanonical ensemble that represents isolated macroscopic systems.

The macroscopic entropy of an isolated system at constant energy and the microcanonical partition function are related by Boltzmann's postulate,

$$S = k \ln \Omega \quad , \tag{2.4}$$

in which S is the macroscopic entropy, k the Boltzmann constant and Ω the microcanonical partition function. In the microcanonical ensemble, all systems occur with the same probability and are therefore assigned equal weights. The microcanonical partition function is the number of all microscopic energy states of the system that are compatible with the prescribed macroscopic energy.

Instead of the solution of the time-dependent Schrödinger equation, the calculation of the microscopic energy states requires the solution of the time-independent Schrödinger equation of the system

$$\mathcal{H}\Psi = E\Psi \quad , \tag{2.5}$$

where E denotes an energy eigenvalue. The solution is much simplified when the Hamiltonian is partitioned into contributions due to different excitation modes and every mode is treated separately. For many substances, this separation is a reasonable approximation. The Hamiltonian of the system is then written as a *sum* of contributions due to the individual modes

$$\mathcal{H} = \mathcal{H}_{\mathrm{t}} + \mathcal{H}_{\mathrm{r}} + \mathcal{H}_{\mathrm{vib}} + \mathcal{H}_{\mathrm{el}} + \mathcal{H}_{\mathrm{c}} \quad . \tag{2.6}$$

$\mathcal{H}_{\mathrm{t}}$, $\mathcal{H}_{\mathrm{r}}$, $\mathcal{H}_{\mathrm{vib}}$ and $\mathcal{H}_{\mathrm{el}}$ stand for the modes of molecular translation and rotation, intramolecular vibrations and electronic excitation, respectively. These contributions involve only excitations of single molecules[1], whereas the last contribution $\mathcal{H}_{\mathrm{c}}$ describes the forces between different molecules. Since only spherical molecules are treated in this work, $\mathcal{H}_{\mathrm{r}}$ and $\mathcal{H}_{\mathrm{vib}}$ are zero. $\mathcal{H}_{\mathrm{el}}$ yields significant contributions only at very high temperatures and may be neglected so that only $\mathcal{H}_{\mathrm{t}}$ and $\mathcal{H}_{\mathrm{c}}$ remain. Both contributions may be treated by classical mechanics when the temperatures

---

[1] The terms *molecule* and *particle* are used interchangeably throughout this work.

are not too low and the molecules are not too light. This simplification is used throughout this work.

In classical mechanics, the microscopic state of a system composed of N spherical molecules is specified at any instance by the N Cartesian position vectors $\{\boldsymbol{r}_N\}$ and the N velocity vectors of the molecules $\{\boldsymbol{v}_N\}$ which together form the phase of the system. The N coordinate vectors specify the *configuration* of the system. The $6N$ variables span a vector in a $6N$-dimensional space, the *phase space* of the system. The total energy of the system is given by the Hamiltonian

$$E = H(\{\boldsymbol{r}_N\}, \{\boldsymbol{v}_N\}) = K(\{\boldsymbol{v}_N\}) + U(\{\boldsymbol{r}_N\}) = \frac{1}{2}\sum_{i=1}^{N} m\boldsymbol{v}_i^2 + U(\{\boldsymbol{r}_N\}) \quad , \quad (2.7)$$

where the first term in the last identity is the kinetic energy K of the system and the second term is the potential energy U. K depends only on the velocities and U only on the positions of the molecules. The functional form of the potential energy depends on the specific model for the intermolecular forces.

2.2   Simple Models for Intermolecular Forces

This section introduces basic concepts that are commonly used to model intermolecular forces. Comprehensive treatments of the field of intermolecular forces are given in the books of Hirschfelder et al. [88] and Maitland et al. [133].

The forces between molecules result from electromagnetic interactions of the their constituent charged elementary particles, the electrons in the shells of the atoms and the protons in the atomic nuclei. In general, they depend on the distance between the molecules and are repulsive at short and attractive at large distances. When two molecules come together close enough so that their electronic clouds overlap, some electrons are forbidden to occupy the overlap region by the Pauli exclusion principle and so the electron density is reduced in this region. This effect reduces the shielding of the positively charged nuclei so that they repel each other. The attractive long range forces are in general due to three different mechanisms: electrostatic interactions between permanent dipoles, induced interactions and dispersion interactions. Polar molecules possess permanent dipole moments due to their electrostatic charge distribution. When a polar molecules interacts with a non-polar molecule, it distorts the charge distribution of the previously uncharged molecule inducing a dipole moment in it. The induced dipole interacts with the permanent dipole moment of the polar molecule resulting in a force between the two molecules. Dispersion forces

arise from fluctuations in the electronic clouds surrounding a molecule. Due to the continuous motion of the electronic charges, every molecule possesses an instantaneous electric dipole moment at any instant. This instantaneous dipole induces an instantaneous dipole in another molecule causing the two molecules to interact with each other.

The forces between two molecules fluctuate on a time scale of the order of the rapid motion of the electronic charge distributions. Since the motion of molecules is by some orders of magnitude slower than the motion of the electronic charges, the motion of molecules may be regarded as only due to the translational motion of the nuclei. This simplification is termed Born-Oppenheimer approximation. On the time scale of the motion of the molecules, the instantaneous intermolecular forces are time averages of the rapidly fluctuating forces between the electronic clouds.

Intermolecular interactions are quantitatively described in terms of intermolecular potential functions. The intermolecular potential function is introduced by the following thought experiment for a system of two spherical symmetric molecules i and j [133]. When the molecules are separated by an infinite distance, the total energy of the simple system is the sum of the energies of the two molecules

$$E(r_{ij} \to \infty) = E_i + E_j \quad . \tag{2.8}$$

At finite distances, the intermolecular interaction energy contributes to the total energy of the system, so that

$$E(r_{ij}) = E_i + E_j + u(r_{ij}) \quad . \tag{2.9}$$

When the interacting molecules are spherically symmetric, the interaction energy $u(r)$ depends only on the distance r between them. $u(r)$ is termed the intermolecular pair potential energy function. It becomes zero when the molecules are infinitely separated. In classical mechanics, the force $\boldsymbol{F}_{ij}$ acting upon molecule i due to molecule j is given by

$$\boldsymbol{F}_{ij} = -\nabla_{\boldsymbol{r}_{ij}} u(r_{ij}) = -\frac{\partial u(r_{ij})}{\partial \boldsymbol{r}_{ij}} \quad . \tag{2.10}$$

The force is positive when it is repulsive and negative when it is attractive.

In a system of more than two interacting molecules, the potential energy is in general not equal to the sum of all pair contributions. Non-additive effects arising from constellations of more than two molecules may contribute significantly to the total potential energy of the system [133]. However, since the evaluation of

non-additive contributions in molecular dynamics simulations requires large computational resources, usually only pairwise interactions between two particles are taken into account. The total potential energy of a system containing N molecules is hence given by

$$U(\{\boldsymbol{r}_{ij}\}) = \frac{1}{2} \sum_{\substack{i=1}}^{N} \sum_{\substack{j=1 \\ j \neq i}}^{N} u(\boldsymbol{r}_{ij}) \quad , \tag{2.11}$$

and the total force $\boldsymbol{F}_i$ acting upon molecule i due to all other molecules is

$$\boldsymbol{F}_i = \sum_{\substack{j=1 \\ j \neq i}}^{N} \boldsymbol{F}_{ij}(r_{ij}) = - \sum_{\substack{j=1 \\ j \neq i}}^{N} \frac{\partial u(r_{ij})}{\partial \boldsymbol{r}_{ij}} \quad . \tag{2.12}$$

For the reasons given in the introduction, simple effective intermolecular potential models are applied in molecular dynamics simulations. Precise agreement of the simulation results with macroscopic properties of real fluids over wide state regions cannot be achieved with such simple models. However, many physical effects are captured quantitatively and can be investigated on the molecular scale and macroscopic properties of real fluids can be predicted with technical accuracy.
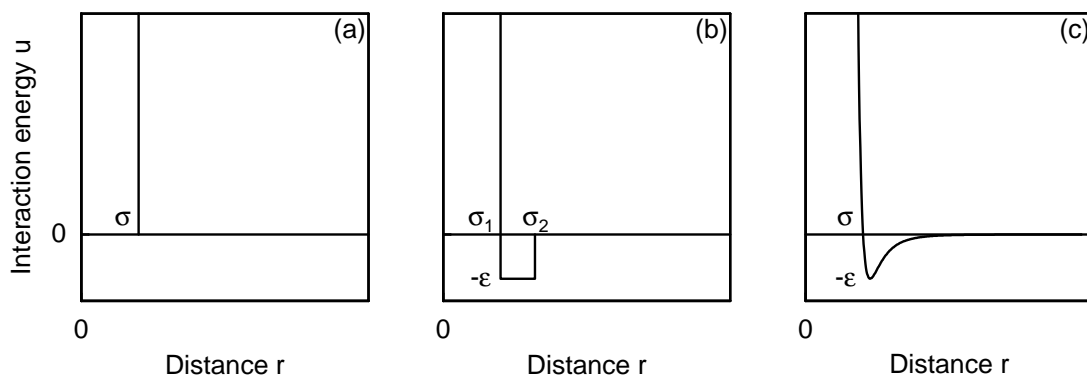
Figure 2.2. Simple intermolecular potential functions for non-polar model fluids: a) hard sphere potential, b) square well potential and c) Lennard-Jones potential.

Examples for simple intermolecular potential functions are shown in Figure 2.2. All three models, the hard sphere, square well and Lennard-Jones potential [103], are used in many applications of statistical thermodynamics or to predict macroscopic properties of real fluids [121, 186, 187, 196, 200, 217]. Due to the absence

of attractive forces, the hard sphere model does not exhibit a vapour-liquid phase transition. Nevertheless, it is often used in macroscopic models for thermophysical properties, especially at high pressures, since its thermodynamic and transport properties are well known. Both the square well and Lennard-Jones model fluid show many characteristics of real fluids, for instance a vapour-liquid phase transition, a critical and triple point or liquid-solid equilibria. Whereas the hard sphere and square well potential are discontinuous, the Lennard-Jones potential is one of the simplest continuous potential models and therefore closer to a potential for real molecules than the other two. Its functional form is given by

$$u(r) = 4\varepsilon \left[\left(\frac{\sigma}{r} \right)^{12} - \left(\frac{\sigma}{r} \right)^{6} \right] \quad . \tag{2.13}$$

It shows the characteristics of a realistic potential for spherical molecules: a steep repulsive part at short separations, a minimum at intermediate and a more slowly decaying attractive tail at large distances. The r^{-6}-tail of the Lennard-Jones potential agrees qualitatively with the leading term of the theoretical result for the dispersion energy between two non-polar spherical molecules [133]. Thus, the Lennard-Jones potential is a simple, but realistic model for interactions between non-polar spherical molecules.

The potential parameter σ is interpreted as a particle diameter and ε is the depths of the potential minimum. Since the Lennard-Jones potential can be written in the form

$$u(r) = \epsilon f(r/\sigma) \quad , \tag{2.14}$$

a corresponding states principle applies for the macroscopic thermodynamic state variables and transport coefficients of the potential model. Thus, the model properties can be represented in a reduced form and scaled by an appropriate choice of σ, ε and the particle mass m to represent properties of a real fluid. A summary of the reduced quantities used in this work is given in Appendix A.

2.3   Molecular Expressions for Thermodynamic State Variables

For their computation in molecular dynamics simulations, thermodynamic state variables must be related to ensemble averages of phase variables. As the simulations of this work were carried out at constant energy, the fundamental equation of state

$S = S(N, V, E)$ is the starting point for the derivation of molecular expression for the thermodynamic state variables. Classical mechanics imposes restrictions on the phase space that is accessible to the system. In addition to the total energy, the total momentum vector of the system [114]

$$\boldsymbol{M} = \sum_{i=1}^{N} \boldsymbol{p}_{\text{i}} \tag{2.15}$$

and the quantity

$$\boldsymbol{G} = \sum_{i=1}^{N} \boldsymbol{p}_{\text{i}} t - \sum_{i=1}^{N} m \boldsymbol{r}_{\text{i}} \tag{2.16}$$

are kept constant [184]. The value of $\boldsymbol{G}$ is determined by the initial position of the centre of mass of the system. In simulations with periodic boundary conditions, not the quantity $\boldsymbol{G}$ of the original system, but the quantity $\boldsymbol{G}$ of all infinitely repeated systems is a constant of the equations of motion. Thus, not the microcanonical NVE-ensemble, but a subset of it, the molecular dynamics $NVE\boldsymbol{MG}$-ensemble, is sampled. The total momentum vector of the system is set to zero $\boldsymbol{M} = \boldsymbol{0}$ so that the system as a whole is at rest during the simulation. These restrictions must be taken into account when deriving molecular expressions for thermodynamic state variables.

The correct molecular expressions for thermodynamic state variables in the microcanonical NVE-ensemble were first derived in 1985 by Pearson et al. [171]. In their derivation, Pearson et al. introduced a Laplace-transform technique to evaluate the phase space integrals over the momenta. Cağin and Ray extended this technique to the $NVE\boldsymbol{M}$-ensemble [28] and reported expressions for thermodynamic state variables for this ensemble. While these treatments were restricted to systems of spherical molecules, Lustig [126, 127, 128, 129] introduced a systematic representation for the expressions of derivatives of arbitrary order of the fundamental equation of state for systems of nonlinear molecules. Recently, Ray and Zhang [184] realized that $\boldsymbol{G}$ is an additional constant of the equations of motion and derived the correct expression for the temperature, isochoric heat capacity and pressure in the $NVE\boldsymbol{MG}$-ensemble.

Beside the temperature and pressure that are required for the calculation of the transport coefficients, further thermodynamic state variables can be evaluated with little additional computational effort. Therefore, first and second order derivatives of the fundamental equation of state were included in the present study.

The molecular expressions for the thermodynamic state variables are derived for the $NVE\boldsymbol{M}\boldsymbol{G}$-ensemble using the formalism developed by Lustig [126, 127, 128, 129] and the Laplace-transform technique of Pearson et al. [171]. As the derivation is quite involved, only a short account of it is given in the remainder of this section. A detailed derivation of the expressions for all thermodynamic state variables considered in this work is provided in Appendix C.

An isolated system in classical statistical thermodynamics is characterized by the phase space volume Ω and the phase space density ω. The phase space volume is given by

$$\Omega(N, V, E, \boldsymbol{M}, \boldsymbol{G}) = \frac{1}{C_{\mathrm{N}}} \iint \Theta(E - \frac{\boldsymbol{M}^2}{2Nm} - H)\, \delta\left(\boldsymbol{M} - \sum_{i=1}^{N} \boldsymbol{p}_{\mathrm{i}}\right) \cdot$$
$$\cdot \delta\left(\boldsymbol{G} - t\sum_{i=1}^{N} \boldsymbol{p}_{\mathrm{i}} + \sum_{i=1}^{N} m\boldsymbol{r}_{\mathrm{i}}\right) \mathrm{d}\boldsymbol{r}_{\mathrm{N}}\mathrm{d}\boldsymbol{p}_{\mathrm{N}} \qquad (2.17)$$

and the phase space density by

$$\omega(N, V, E, \boldsymbol{M}, \boldsymbol{G}) = \frac{\partial\Omega}{\partial E} = \frac{1}{C_{\mathrm{N}}} \iint \delta(E - \frac{\boldsymbol{M}^2}{2Nm} - H)\, \delta\left(\boldsymbol{M} - \sum_{i=1}^{N} \boldsymbol{p}_{\mathrm{i}}\right) \cdot$$
$$\cdot \delta\left(\boldsymbol{G} - t\sum_{i=1}^{N} \boldsymbol{p}_{\mathrm{i}} + \sum_{i=1}^{N} m\boldsymbol{r}_{\mathrm{i}}\right) \mathrm{d}\boldsymbol{r}_{\mathrm{N}}\mathrm{d}\boldsymbol{p}_{\mathrm{N}} \quad . \quad (2.18)$$

In these equations, C_{N} is a normalization constant, which cancels out when deriving explicit expressions for the thermodynamic state variables and, thus, it does not need to be specified for the purposes of this section. Nm is the total mass of the system. Θ denotes the unit step function and δ the Dirac δ-function. The phase space volume includes all points of phase space where the total energy of the system is lower or equal to the prescribed macroscopic energy. On the other hand, the phase space density is obtained by integration over points for which the total energy is equal to the macroscopic energy.

Becker [18] and Münster [162] pointed out that both the phase space volume and phase space density may be used in the entropy postulate (2.4) to replace the quantum mechanical partition function in the classical case. Both entropy definitions lead to different expressions for thermodynamic state variables, but the results become numerically equivalent since

$$\lim_{N\to\infty} \frac{\ln\Omega}{N} = \lim_{N\to\infty} \frac{\ln\omega}{N} \qquad (2.19)$$

holds for large systems [18]. Arguments for and against both entropy definitions were presented by Münster [162] and Becker [18]. However, it could not be proved by pure physical argumentation which entropy definition is correct. Lustig examined both definitions with molecular dynamics [126, 127] and Monte Carlo simulation data [130] for several thermodynamic state variables of the Lennard-Jones model fluid. These investigations did not allow to decide conclusively between the two entropy definitions. However, Lustig showed that the data for the thermodynamic state variables from both definitions extrapolate to the same values in the limit of infinite system size as predicted by theory. In this work, the entropy is related to the phase space volume,

$$S(N, V, E, \boldsymbol{M}, \boldsymbol{G}) = k \ln \Omega(N, V, E, \boldsymbol{M}, \boldsymbol{G}) \quad , \tag{2.20}$$

because this definition is mostly used in literature. As the simulations of this work were carried out with relatively large systems, the choice of the entropy definition should have little influence on the results for the thermodynamic state variables.

Lustig [126, 129] introduced the abbreviation

$$\Omega_{\mathrm{mn}} = \frac{1}{\omega} \frac{\partial^{m+n} \Omega}{\partial E^m \partial V^n} \tag{2.21}$$

to represent the derivatives of the phase space volume with respect to the independent variables E and V and termed the Ω_{mn} *phase space functions*. Expressions for the thermodynamic state variables in terms of the phase space functions are presented in the upper part of Table 2.1. The phase space functions must be related to ensemble averages that can be calculated in molecular dynamics simulations. Such relations are established by the Laplace-transform technique of Pearson et al. [171] as described in detail in Appendix C. The resulting expressions for all phase space functions Ω_{mn} needed in this work are summarized in Table 2.1. Expressions for the instantaneous volume derivatives of the configurational internal energy appearing in the expressions for the pressure and the pressure derivatives were reported by Lustig [126, 129] and are given in Table 2.1 without derivation.

Table 2.1. Molecular expressions for thermodynamic state variables in the molecular dynamics $NVE\boldsymbol{MG}$ ensemble with $\boldsymbol{M} = \boldsymbol{0}$.

thermodynamic state variables:

$$T = \left(\frac{\partial E}{\partial S}\right)_{\mathrm{V}} = \frac{\Omega_{00}}{k}$$

$$p = T\left(\frac{\partial S}{\partial V}\right)_{\mathrm{E}} = \Omega_{01}$$

$$C_{\mathrm{V}} = \left[\left(\frac{\partial^2 S}{\partial E^2}\right)_{\mathrm{V}}\right]^{-1} = k(1 - \Omega_{00}\Omega_{20})^{-1}$$

$$\gamma_{\mathrm{V}} = \left(\frac{\partial p}{\partial T}\right)_{\mathrm{V}} = k\frac{\Omega_{11} - \Omega_{01}\Omega_{20}}{1 - \Omega_{00}\Omega_{20}}$$

$$\beta_{\mathrm{S}}^{-1} = -V\left(\frac{\partial p}{\partial V}\right)_{\mathrm{S}} = V\left[\Omega_{01}(2\,\Omega_{11} - \Omega_{01}\Omega_{20}) - \Omega_{02}\right]$$

$$w_0 = \left[-\frac{V}{\rho_{\mathrm{m}}}\left(\frac{\partial p}{\partial V}\right)_{\mathrm{S}}\right]^{1/2} = \left[\frac{V}{\rho_{\mathrm{m}}}[\Omega_{01}(2\,\Omega_{11} - \Omega_{01}\Omega_{20}) - \Omega_{02}]\right]^{1/2}$$

phase space functions $\Omega_{\mathrm{mn}} = \dfrac{1}{\omega}\dfrac{\partial^{m+n}\Omega}{\partial E^m \partial V^n}$:

$$\Omega_{00} = kT = \frac{2}{3N-3}\langle K\rangle$$

$$\Omega_{01} = \frac{N-1}{V}kT - \left\langle\frac{\partial U}{\partial V}\right\rangle$$

$$\Omega_{11} = \frac{N-1}{V} + \left[1 - \frac{3N-3}{2}\right]\left\langle K^{-1}\left(\frac{\partial U}{\partial V}\right)\right\rangle$$

$$\Omega_{20} = -\left[1 - \frac{3N-3}{2}\right]\langle K^{-1}\rangle$$

$$\Omega_{02} = \frac{2}{3V}\frac{N-2}{V}\langle K\rangle - \left[1 - \frac{3N-3}{2}\right]\left\langle K^{-1}\left(\frac{\partial U}{\partial V}\right)^2\right\rangle - \left\langle\frac{\partial^2 U}{\partial V^2}\right\rangle - 2\frac{N-1}{V}\left\langle\frac{\partial U}{\partial V}\right\rangle$$

volume derivatives of the instantaneous potential energy:

$$\frac{\partial U}{\partial V} = \frac{1}{3V}\sum_{i=1}^{N-1}\sum_{j=i+1}^{N}r_{\mathrm{ij}}\frac{\partial u(r_{\mathrm{ij}})}{\partial r_{\mathrm{ij}}}$$

$$\frac{\partial^2 U}{\partial V^2} = \frac{1}{9V^2}\sum_{i=1}^{N-1}\sum_{j=i+1}^{N}\left[r_{\mathrm{ij}}\frac{\partial u(r_{\mathrm{ij}})}{\partial r_{\mathrm{ij}}} + r_{\mathrm{ij}}^2\frac{\partial^2 u(r_{\mathrm{ij}})}{\partial r_{\mathrm{ij}}^2}\right]$$

2.4 Macroscopic Hydrodynamics

So far only systems that are in thermodynamic equilibrium have been considered in Sections 2.1 to 2.3. The remainder of this chapter deals with the description of nonequilibrium systems and time-correlation function theory. Figure 2.3 provides a guideline to the following sections. The next three Sections 2.4.1 to 2.4.3 treat nonequilibrium systems from the macroscopic viewpoint. After introducing the basic terminology in Section 2.4.1, the hydrodynamic conservation equations for mass, momentum and energy and the entropy balance are described in Section 2.4.2. The transport coefficients are defined in Section 2.4.3 by the linear phenomenological

EQUILIBRIUM   **NONEQUILIBRIUM**

sec. 2.1   sec. 2.4.1

fundamental equation of state: $S = S(N,V,E)$ sec. 2.1

hydrodynamic balance equations sec. 2.4.2 + phenomenological equations sec. 2.4.3

$S = k \ln \Omega$ **regression hypothesis**   macroscopic / microscopic

ensembles, fluctuations sec. 2.1

time-correlation functions sec. 2.5.1

molecular expressions for thermodynamic state variables sec. 2.3 and app. C

Green-Kubo formulas sec. 2.5.3

molecular expressions for thermodynamic fluxes sec. 2.5.2

generalized Einstein relations sec. 2.5.4

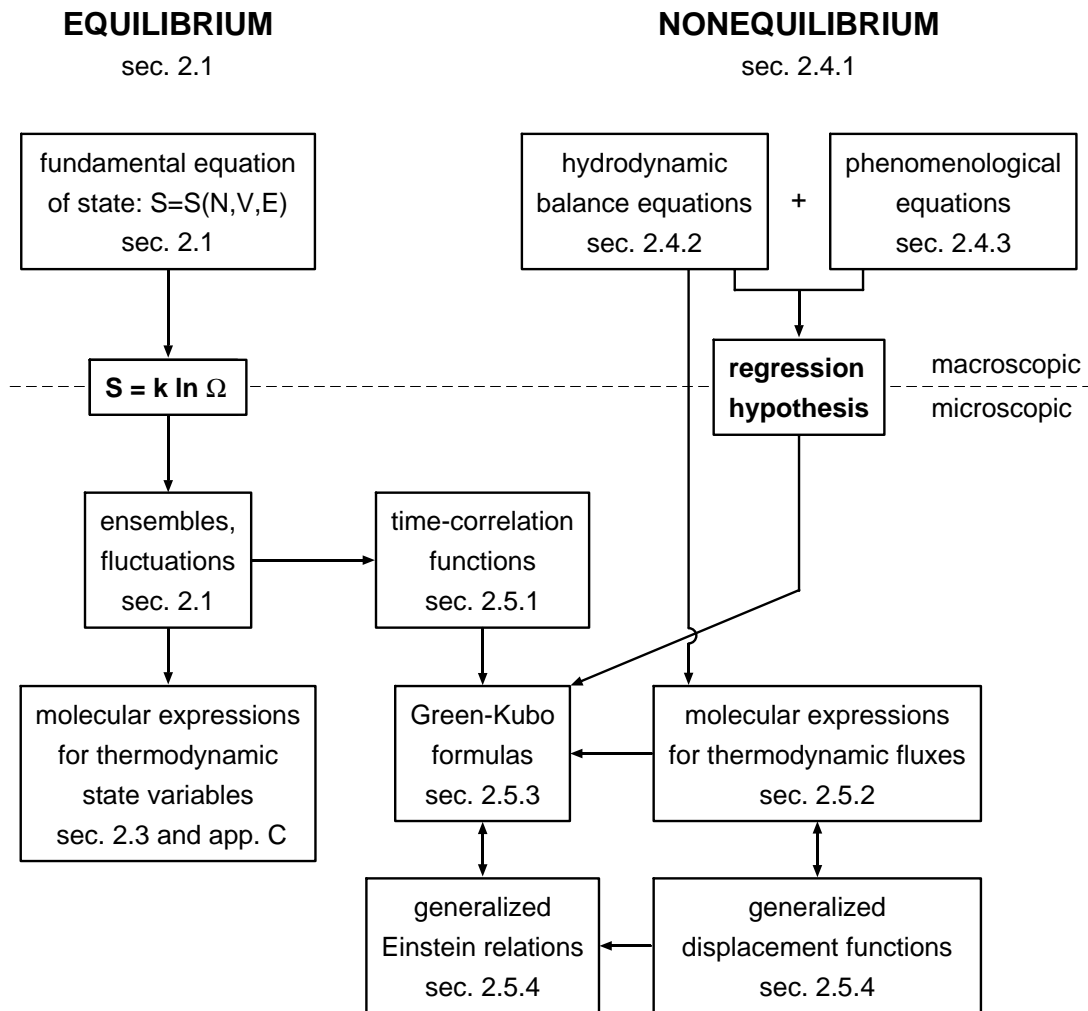generalized displacement functions sec. 2.5.4

Figure 2.3. Guideline to Chapter 2.

equations.

The Green-Kubo integral formulas and Einstein relations for the transport co-
efficients are derived within time-correlation function theory in Sections 2.5.1 to
2.5.4. Section 2.5.1 provides the definition of time-correlation functions and impor-
tant properties of time-correlation functions which are needed later on. Molecular
expressions for the thermodynamic fluxes are found in Section 2.5.2 by deriving mi-
croscopic analogs of the the macroscopic hydrodynamic balance equations. Based
on the regression hypothesis, the Green-Kubo integral formulas are derived in Sec-
tion 2.5.3. In Section 2.5.4 an Einstein relation is derived for an arbitrary phase
variable. It is shown that the Einstein relation is mathematically equivalent to the
corresponding Green-Kubo formula for the phase variable. Generalized displace-
ment functions for the hydrodynamic transport coefficients are then obtained in a
simple way from the molecular expressions for the thermodynamic fluxes.

2.4.1   Nonequilibrium States and Transport Processes

The definition of nonequilibrium states is closely linked to the definition of equi-
librium states: A system which is not in an equilibrium state is said to be in a
nonequilibrium state [67]. The thermodynamic equilibrium state is unique, but
there are infinitely many nonequilibrium states. In nonequilibrium states, at least
one of the state variables is not constant in the system, but depends on the posi-
tion. Nonequilibrium states are caused by imposing boundary conditions on or by
applying external fields to the system. If the disturbance is removed, an *irreversible
process* occurs in the system and the system advances through a series of nonequi-
librium states until equilibrium is reached. Such a process is termed a *transport
process* since some quantity is transported through the system, as the system tries
to make all state variables independent on position. If a gradient of a state variable
in the system is constrained by a continuous application of an external disturbance,
the system is maintained in a nonequilibrium steady state. Transport processes are
always irreversible and are associated with the production of entropy. *Transport
coefficients* are linked to the time dependent decay of a nonequilibrium state to
thermodynamic equilibrium.

There are two different types of transport processes. Hydrodynamic transport, for
example the conduction of heat or the transport of momentum in a fluid, is caused
by imposing boundary conditions on the system. On the other hand, electrical
or magnetic transport phenomena, such as electrical currents in conductors, are

caused by the application of external fields to the system. External fields change the Hamiltonian of the system, whereas hydrodynamic transport processes leave the Hamiltonian unchanged. The hydrodynamic transport coefficients viscosity, bulk viscosity, thermal conductivity and the self-diffusion coefficient describe transport processes of the first type.

Macroscopic nonequilibrium states are described by the hydrodynamic conservation equations for mass, momentum and energy and the entropy balance. A closed set of equations for the hydrodynamic field variables requires constitutive relations which relate the thermodynamic fluxes to their corresponding thermodynamic forces, the hydrodynamic field gradients. The constitutive relations define the transport coefficients.

In the remainder of this chapter, the conventional hydrodynamic description of transport processes and the description by nonequilibrium thermodynamics are used in parallel. In nonequilibrium thermodynamics, transport processes are treated systematically within a common frame. Constitutive relations are replaced by phenomenological equations and the hydrodynamic transport coefficients are replaced by the phenomenological coefficients. This description has the advantage that results derived for one transport process can easily be transferred to another. However, the discussion of the simulation results in the following chapters is then carried out by focussing on the conventional hydrodynamic description because it is used almost exclusively in practice.

2.4.2 Hydrodynamic Balance Equations

The hydrodynamic balance equations and the entropy balance are repeated in this section without derivation. Derivations are for example given in the books of Evans [49], de Groot and Mazur [61], Hanley [67] and McQuarrie [141]. The equations are written in terms of densities of the quantities mass Nm, momentum $\boldsymbol{p}$, energy E and entropy S. These densities are defined by

$$\rho_{\mathrm{m}} = \frac{Nm}{V} \quad , \quad \rho_{\mathrm{m}}\boldsymbol{v} = \frac{\boldsymbol{p}}{V} \quad , \quad \rho_{\mathrm{m}}e_{\mathrm{m}} = \frac{E}{V} \quad \text{and} \quad \rho_{\mathrm{m}}s_{\mathrm{m}} = \frac{S}{V} \quad , \tag{2.22}$$

where ρ_{m} denotes the mass density, e_{m} the mass specific internal energy and s_{m} the mass specific entropy. While mass, momentum and energy are conserved, entropy is not a conserved quantity. Without external fields the hydrodynamic conservation equations for mass, momentum and energy for a pure fluid read [49, 61, 141]:

$$\frac{\partial \rho_{\mathrm{m}}(\boldsymbol{r},t)}{\partial t} = -\nabla \cdot [\underbrace{\rho_{\mathrm{m}}(\boldsymbol{r},t)\boldsymbol{v}(\boldsymbol{r},t)}_{\text{convection}}] \tag{2.23}$$

$$\frac{\partial \rho_{\mathrm{m}}(\boldsymbol{r},t)\boldsymbol{v}(\boldsymbol{r},t)}{\partial t} = -\nabla \cdot [\underbrace{\rho_{\mathrm{m}}(\boldsymbol{r},t)\boldsymbol{v}(\boldsymbol{r},t)\boldsymbol{v}(\boldsymbol{r},t)}_{\text{convection}} + \underbrace{\boldsymbol{P}(\boldsymbol{r},t)}_{\text{surface forces}}] \tag{2.24}$$

$$\frac{\partial \rho_{\mathrm{m}}(\boldsymbol{r},t)e_{\mathrm{m}}(\boldsymbol{r},t)}{\partial t} = -\nabla \cdot [\underbrace{\rho_{\mathrm{m}}(\boldsymbol{r},t)e_{\mathrm{m}}(\boldsymbol{r},t)\boldsymbol{v}(\boldsymbol{r},t)}_{\text{convection}} + \underbrace{\boldsymbol{J}^{\mathrm{q}}(\boldsymbol{r},t)}_{\text{heat conduction}}$$

$$+ \underbrace{\boldsymbol{P}(\boldsymbol{r},t) \cdot \boldsymbol{v}(\boldsymbol{r},t)}_{\substack{\text{mechanical work} \\ \text{and dissipation}}}] \tag{2.25}$$

The conservation equations are valid instantaneously and locally at every position $\boldsymbol{r}$ and any time t in a macroscopic nonequilibrium system. They have to be supplemented by initial and boundary conditions to completely specify a nonequilibrium state. In macroscopic hydrodynamics, the position vector $\boldsymbol{r}$ has a special meaning. It denotes the position of an infinitesimal small volume element δV which is located at $\boldsymbol{r}$. The volume element is large on the molecular length scale, but infinitely small compared with the dimensions of the macroscopic nonequilibrium system. Similarly, the time t describes an infinitesimal small time interval that is long on the molecular time scale, but infinitely small compared with the time period the macroscopic nonequilibrium system needs to reach equilibrium. From the macroscopic view point, the fluid is a continuum. Thus, the state variables and the local velocity are continuous functions of the spatial coordinates and time. Within a small volume element, the thermodynamic state variables are assumed to be constant. The volume element is said to be in *local equilibrium*, so macroscopic thermodynamic relations can be applied to the volume element.

Mass is transported only by convective flow into the volume element, whereas the momentum density can additionally be changed by surface forces acting upon the volume element. The density of energy in the volume element can be changed by convective flow of energy, conduction of heat, dissipation and mechanical compression or expansion work performed on the volume element.

The quantities $\boldsymbol{P}$ and $\boldsymbol{J}^{\mathrm{q}}$ are the pressure tensor and heat flux vector. The pressure tensor is defined by the relation

$$\mathrm{d}\boldsymbol{F} = -\mathrm{d}\boldsymbol{A} \cdot \boldsymbol{P} \quad , \tag{2.26}$$

where $\mathrm{d}\boldsymbol{F}$ is the force acting upon the infinitesimal surface element $\mathrm{d}A$ with the

outward directed surface normal $\mathrm{d}\boldsymbol{A}$. The pressure tensor

$$\boldsymbol{P} = \begin{pmatrix} P_{\mathrm{xx}} & P_{\mathrm{xy}} & P_{\mathrm{xz}} \\ P_{\mathrm{yx}} & P_{\mathrm{yy}} & P_{\mathrm{yz}} \\ P_{\mathrm{xz}} & P_{\mathrm{yz}} & P_{\mathrm{zz}} \end{pmatrix} \tag{2.27}$$

is a second-rank tensor and represents the action of surface forces on the volume element. The first index of a tensor element denotes the direction of the normal vector of the surface upon which the tensor element acts, while the second index shows the direction of the tensor element. There two types of surface forces: shear forces are parallel to the surface and normal forces are normal to the surface. The diagonal elements of the pressure tensor represent the normal forces and the off-diagonal elements represent the shear forces. For fluids consisting of spherical molecules the pressure tensor is symmetric so that $P_{\alpha\beta} = P_{\beta\alpha}$ [49]. The average pressure is the arithmetic mean of the diagonal elements of the pressure tensor:

$$P = \frac{1}{3}(P_{\mathrm{xx}} + P_{\mathrm{yy}} + P_{\mathrm{zz}}) \quad . \tag{2.28}$$

In general, the average pressure is not equal to the thermodynamic pressure given by the thermal equation of state $p = p(\rho_{\mathrm{m}}, T)$. When the fluid is in equilibrium, the off-diagonal elements of the pressure tensor vanish and the diagonal elements become the hydrostatic pressure. In this case, the average pressure is the thermodynamic pressure. Thus, the pressure tensor can be split into a hydrostatic and a viscous contribution [49, 61, 67]:

$$\boldsymbol{P} = p\,\boldsymbol{I} + \boldsymbol{\Pi} \quad . \tag{2.29}$$

The symbol $\boldsymbol{I}$ denotes the unit tensor and the viscous pressure tensor $\boldsymbol{\Pi}$ represents the nonequilibrium part of the pressure tensor. Often, the stress tensor

$$\boldsymbol{\tau} = -\boldsymbol{P} = \begin{pmatrix} \tau_{\mathrm{xx}} & \tau_{\mathrm{xy}} & \tau_{\mathrm{xz}} \\ \tau_{\mathrm{yx}} & \tau_{\mathrm{yy}} & \tau_{\mathrm{yz}} \\ \tau_{\mathrm{xz}} & \tau_{\mathrm{yz}} & \tau_{\mathrm{zz}} \end{pmatrix} \tag{2.30}$$

rather than the pressure tensor is used. The off-diagonal elements $\tau_{\alpha\beta}$ are the shear stresses and the diagonal elements $\tau_{\alpha\alpha}$ are the normal stresses.

If only small perturbations from equilibrium or fluctuations at thermodynamic equilibrium are examined, the momentum balance, Eq. (2.24), can be linearized by neglecting the gradient of the thermodynamic equilibrium pressure and terms which are quadratic in the velocities. The linearized momentum balance takes the form

$$\frac{\partial \rho_{\mathrm{m}}(\boldsymbol{r}, t)\boldsymbol{v}(\boldsymbol{r}, t)}{\partial t} = -\nabla \cdot \boldsymbol{\Pi} \quad . \tag{2.31}$$

The energy conservation equation can be rewritten by introducing an energy flux vector $\boldsymbol{J}^{\mathrm{e}}$ [203]:

$$
\begin{aligned}
\frac{\partial(\rho_{\mathrm{m}}e_{\mathrm{m}})}{\partial t} &= -\nabla \cdot [\rho_{\mathrm{m}}e_{\mathrm{m}}\boldsymbol{v} + \boldsymbol{J}^{\mathrm{q}} + \boldsymbol{P}\cdot\boldsymbol{v}] \\
&= -\nabla \cdot [(e_{\mathrm{m}} + p/\rho_{\mathrm{m}})\,\rho_{\mathrm{m}}\boldsymbol{v} + \boldsymbol{J}^{\mathrm{q}} + \boldsymbol{\Pi}\cdot\boldsymbol{v}] \\
&= -\nabla \cdot [\rho_{\mathrm{m}}h_{\mathrm{m}}\boldsymbol{v} + \boldsymbol{J}^{\mathrm{q}} + \boldsymbol{\Pi}\cdot\boldsymbol{v}] \\
&= -\nabla \cdot \boldsymbol{J}^{\mathrm{e}} \quad .
\end{aligned}
\tag{2.32}
$$

The energy flux vector

$$
\boldsymbol{J}^{\mathrm{e}} = \boldsymbol{J}^{\mathrm{q}} + \rho_{\mathrm{m}}e_{\mathrm{m}}\boldsymbol{v} + \boldsymbol{P}\cdot\boldsymbol{v} = \boldsymbol{J}^{\mathrm{q}} + \rho_{\mathrm{m}}h_{\mathrm{m}}\boldsymbol{v} + \boldsymbol{\Pi}\cdot\boldsymbol{v}
\tag{2.33}
$$

summarizes the contributions from the four transport mechanisms for energy. The term $\boldsymbol{\Pi}\cdot\boldsymbol{v}$ accounts for the dissipation of energy due to viscous heating.

Entropy is not conserved because transport processes are irreversible and thus associated with the production of entropy. The entropy balance reads [49, 61, 67]

$$
\frac{\partial\rho_{\mathrm{m}}(\boldsymbol{r},t)s_{\mathrm{m}}(\boldsymbol{r},t)}{\partial t} = \underbrace{\sigma(\boldsymbol{r},t)}_{\text{production}} -\nabla\cdot[\underbrace{\rho_{\mathrm{m}}(\boldsymbol{r},t)s_{\mathrm{m}}(\boldsymbol{r},t)\boldsymbol{v}(\boldsymbol{r},t)}_{\text{convection}} + \underbrace{\boldsymbol{J}^{\mathrm{s}}(\boldsymbol{r},t)}_{\text{entropy flux}}] \quad , \tag{2.34}
$$

where σ is the local entropy source strength and $\boldsymbol{J}^{\mathrm{s}}$ the entropy flux vector which describes the entropy flux into the volume element. In pure fluids, entropy is only transported into the volume element with a heat flux and the entropy flux vector becomes

$$
\boldsymbol{J}^{\mathrm{s}}(\boldsymbol{r},t) = \frac{\boldsymbol{J}^{\mathrm{q}}(\boldsymbol{r},t)}{T(\boldsymbol{r},t)} \quad .
\tag{2.35}
$$

The entropy source strength is given by

$$
\sigma(\boldsymbol{r},t) = -\frac{1}{[T(\boldsymbol{r},t)]^2}\boldsymbol{J}^{\mathrm{q}}(\boldsymbol{r},t)\cdot\nabla T(\boldsymbol{r},t) - \frac{1}{T(\boldsymbol{r},t)}\boldsymbol{\Pi}(\boldsymbol{r},t):\dot{\boldsymbol{\varepsilon}}(\boldsymbol{r},t) \quad ,
\tag{2.36}
$$

where $\dot{\boldsymbol{\varepsilon}}$ is the strain rate tensor, which will be treated in detail in the next section. The operator " $:$ " denotes a scalar product of two second-rank tensors. The entropy source strength has the general form

$$
\sigma = \sum_i \boldsymbol{J}^{\mathrm{i}}\cdot\boldsymbol{X}^{\mathrm{i}} \quad ,
\tag{2.37}
$$

in which the $\boldsymbol{J}^{\mathrm{i}}$ stand for the thermodynamic fluxes and the $\boldsymbol{X}^{\mathrm{i}}$ represent their corresponding thermodynamic forces.

Another transport phenomenon of common interest in pure fluids is self-diffusion[2]. Self-diffusion is the diffusion of tagged particles in a fluid, while all particles are of the same species and have the same mass. Self-diffusion differs from the other hydrodynamic transport phenomena because it describes the average motion of single molecules in the fluid. Therefore, macroscopic hydrodynamics is strictly not applicable. However, formally self-diffusion can be treated by the macroscopic hydrodynamic description of transport processes [24, 69].

The partial mass density of tagged particles is defined by

$$\rho_{\mathrm{m}}^{\mathrm{D}} = \frac{N^{\mathrm{D}} m}{V} \quad , \tag{2.38}$$

where N^{D} stands for the number of tagged particles. If the motion of single molecules is to be described, as for example in the derivation of the Green-Kubo formula for the self-diffusion coefficient, N^{D} is set to one. The partial mass density of tagged particles satisfies the continuity equation

$$\frac{\partial \rho_{\mathrm{m}}^{\mathrm{D}}(\boldsymbol{r}, t)}{\partial t} = -\nabla \cdot [\rho_{\mathrm{m}}^{\mathrm{D}}(\boldsymbol{r}, t) \boldsymbol{v}(\boldsymbol{r}, t) + \boldsymbol{J}^{\mathrm{D}}(\boldsymbol{r}, t)] \quad . \tag{2.39}$$

The vector $\boldsymbol{J}^{\mathrm{D}}$ is the tagged particle flux in the centre of mass frame of an infinitesimal volume element moving with the velocity $\boldsymbol{v}$ at the position $\boldsymbol{r}$. The continuity equation for the partial mass density has the same form as the continuity equation for the mass density, Eq. (2.23), with the additional term accounting for the diffusion of tagged particles into the volume element.

2.4.3   Phenomenological Transport Equations

In order to form a closed set of equations for the velocity, pressure and temperature field, the conservation equations must be supplemented by phenomenological relations which relate the thermodynamic fluxes $\boldsymbol{J}^{\mathrm{i}}$ to their corresponding thermodynamic forces $\boldsymbol{X}^{\mathrm{i}}$. Since the phenomenological equations ought to describe the material behaviour, they provide the definition for the transport coefficients. They can be thought of as arising from a Taylor series expansion of the fluxes in terms of

---

[2]   Pioneering work in the field of self-diffusion was carried out by Albert Einstein, who first derived an expression for the self-diffusion coefficient of a Brownian particle suspended in a liquid [37, 38].

the forces at the thermodynamic equilibrium state [49, 61, 67]:

$$
\boldsymbol{J}^{\mathrm{i}}(\{\boldsymbol{X}^{\mathrm{j}}\}) \;=\; \boldsymbol{J}^{\mathrm{i}}(\{\boldsymbol{X}^{\mathrm{j}}\} = \boldsymbol{0}) + \sum_j \left.\frac{\partial \boldsymbol{J}^{\mathrm{i}}}{\partial \boldsymbol{X}^{\mathrm{j}}}\right|_{\boldsymbol{X}^{\mathrm{j}}=\boldsymbol{0}} \cdot \boldsymbol{X}^{\mathrm{j}} +
$$
$$
\sum_j \sum_k \frac{1}{2} \left.\frac{\partial^2 \boldsymbol{J}^{\mathrm{i}}}{\partial \boldsymbol{X}^{\mathrm{j}}\partial \boldsymbol{X}^{\mathrm{k}}}\right|_{\boldsymbol{X}^{\mathrm{j,k}}=\boldsymbol{0}} : \boldsymbol{X}^{\mathrm{j}}\boldsymbol{X}^{\mathrm{k}} + \mathcal{O}(\boldsymbol{X}^3) \quad . \quad (2.40)
$$

The fluxes $\boldsymbol{J}^{\mathrm{i}}(\{\boldsymbol{X}^{\mathrm{j}}\} = \boldsymbol{0})$ vanish since there are no fluxes in macroscopic equilibrium systems. In linear irreversible thermodynamics, terms of second and higher order are neglected and the fluxes are represented by the general linear phenomenological equation

$$
\boldsymbol{J}^{\mathrm{i}}(\{\boldsymbol{X}^{\mathrm{j}}\}) \stackrel{!}{=} \sum_j \left.\frac{\partial \boldsymbol{J}^{\mathrm{i}}}{\partial \boldsymbol{X}^{\mathrm{j}}}\right|_{\boldsymbol{X}^{\mathrm{j}}=\boldsymbol{0}} \cdot \boldsymbol{X}^{\mathrm{j}} =: \sum_j \boldsymbol{L}_{\mathrm{ij}} \cdot \boldsymbol{X}^{\mathrm{j}} \quad , \tag{2.41}
$$

where the $\boldsymbol{L}_{\mathrm{ij}}$ are the linear *phenomenological* coefficients. In general, the $\boldsymbol{L}_{\mathrm{ij}}$ are second-rank tensors. Eq. (2.41) can be viewed as a formal definition of the phenomenological coefficients $\boldsymbol{L}_{\mathrm{ij}}$: They are defined as the derivative of the thermodynamic flux with respect to the thermodynamic force in the limit of thermodynamic equilibrium. Therefore, they are functions of thermodynamic state variables only. The linear phenomenological relation applies for many transport phenomena close to equilibrium.

According to Curie's theorem, there are no cross couplings between fluxes and forces of different tensorial rank in isotropic fluids [61] and the phenomenological coefficients are scalar quantities. In pure fluids, heat is only transported by a temperature gradient and the phenomenological equation for the heat flux vector has the form

$$
\boldsymbol{J}^{\mathrm{q}} = -L_{\mathrm{qq}} \frac{\nabla T}{T^2} \quad . \tag{2.42}
$$

The phenomenological coefficient L_{qq} differs from the thermal conductivity defined by Fourier's approach for the heat flux vector

$$
\boldsymbol{J}^{\mathrm{q}} \stackrel{!}{=} -\lambda \nabla T \quad . \tag{2.43}
$$

They are related by

$$
\lambda = \frac{L_{\mathrm{qq}}}{T^2} \quad . \tag{2.44}
$$

This provides the definition of the macroscopic thermal conductivity λ.
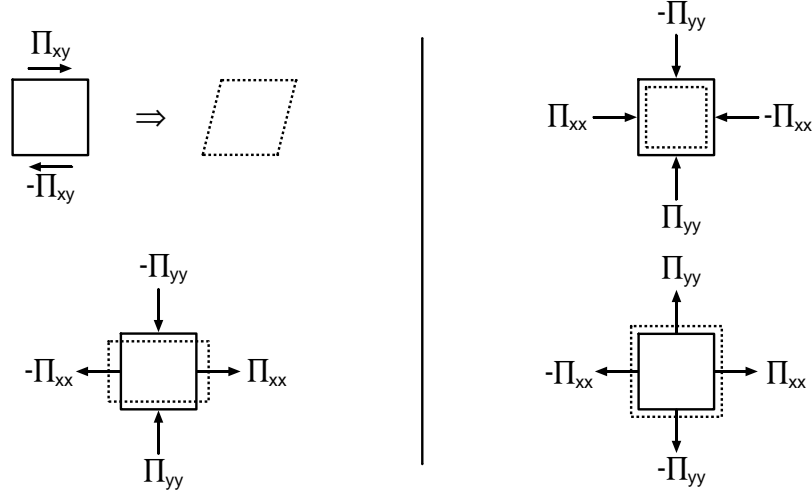
Figure 2.4. Deformation of a small fluid element by diagonal and off-diagonal elements of the viscous pressure tensor.

When the viscous pressure tensor acts upon the surfaces of a fluid element with a prescribed mass, it is deformed. The deformation rate depends on the relative motion of the mass points of the fluid element and thus on the velocity field. Therefore, the viscous pressure tensor also depends on the velocity field. This connection between the viscous pressure tensor and the velocity field is described by a phenomenological relation. Possible deformations of a fluid element by elements of the viscous pressure tensor are shown in Figure 2.4. Diagonal elements of the viscous pressure tensor change the volume of the fluid element, whereas off-diagonal elements change its shape. If the diagonal elements are different, they additionally change the shape of the fluid element. The deformation rate of a fluid element is characterized by the symmetric strain rate tensor

$$\dot{\boldsymbol{\varepsilon}} = \frac{1}{2}\left(\nabla\boldsymbol{v} + (\nabla\boldsymbol{v})^T\right) \quad . \tag{2.45}$$

When the strain rate tensor is split into two contributions,

$$\dot{\boldsymbol{\varepsilon}} = \left[\frac{1}{2}\left(\nabla\boldsymbol{v} + (\nabla\boldsymbol{v})^T\right) - \frac{1}{3}\operatorname{tr}(\nabla\boldsymbol{v})\boldsymbol{I}\right] + \frac{1}{3}\operatorname{tr}(\nabla\boldsymbol{v})\boldsymbol{I} = \widehat{\dot{\boldsymbol{\varepsilon}}} + \frac{1}{3}\operatorname{tr}(\dot{\boldsymbol{\varepsilon}})\boldsymbol{I} \quad , \tag{2.46}$$

the first term $\widehat{\dot{\boldsymbol{\varepsilon}}}$, the traceless part of the strain rate tensor, describes the change of shape of the fluid element at constant volume because the sum of its diagonal elements vanishes. The second term, which is related to the trace of the strain rate

tensor, describes the change of the volume of the fluid element at constant shape. The symbol $\boldsymbol{I}$ denotes the unit tensor.

The phenomenological equation relating the pressure tensor to the strain rate tensor for Newtonian fluids reads

$$\boldsymbol{\Pi} = \widehat{\boldsymbol{\Pi}} + \frac{1}{3}\operatorname{tr}(\boldsymbol{\Pi})\boldsymbol{I} \stackrel{!}{=} -\frac{L_{\widehat{\Pi}\widehat{\Pi}}}{T}\widehat{\dot{\boldsymbol{\varepsilon}}} - \frac{L_{\Pi\Pi}^{\mathrm{tr}}}{T}\operatorname{tr}(\dot{\boldsymbol{\varepsilon}})\boldsymbol{I} \quad, \tag{2.47}$$

where $L_{\widehat{\Pi}\widehat{\Pi}}$ and $L_{\Pi\Pi}^{\mathrm{tr}}$ are two phenomenological coefficients. The conventional hydrodynamics analog of this equation in terms of the stress tensor is

$$\boldsymbol{\tau} = \widehat{\boldsymbol{\tau}} + \frac{1}{3}\operatorname{tr}(\boldsymbol{\tau})\boldsymbol{I} \stackrel{!}{=} 2\eta\widehat{\dot{\boldsymbol{\varepsilon}}} + \eta_{\mathrm{b}}\operatorname{tr}(\dot{\boldsymbol{\varepsilon}})\boldsymbol{I} \quad. \tag{2.48}$$

Hence, the phenomenological coefficients $L_{\widehat{\Pi}\widehat{\Pi}}$ and $L_{\Pi\Pi}^{\mathrm{tr}}$ are related to the transport coefficients viscosity and bulk viscosity by

$$\eta = \frac{L_{\widehat{\Pi}\widehat{\Pi}}}{2T} \tag{2.49}$$

and

$$\eta_{\mathrm{b}} = \frac{L_{\Pi\Pi}^{\mathrm{tr}}}{T} \quad. \tag{2.50}$$

These equations define the viscosity η and bulk viscosity η_{b}. The viscosity describes viscous effects that are associated with the change of shape of a small fluid element at constant volume, while the bulk viscosity describes viscous effects that are associated with changes of the volume of a fluid element leaving the shape of the fluid element unchanged. In literature, bulk viscosity is sometimes termed volume viscosity or dilatation viscosity [57]. Another representation for the phenomenological equation for bulk viscosity is found when it is written using the average pressure, Eq. (2.28):

$$P - p = -\eta_{\mathrm{b}}(\nabla \cdot \boldsymbol{v}) \quad. \tag{2.51}$$

In analogy to the viscosity, bulk viscosity and thermal conductivity, the self-diffusion coefficient is defined by the linear phenomenological equation, Fick's approach,

$$\boldsymbol{J}^{\mathrm{D}} = -D\nabla\rho_{\mathrm{m}}^{\mathrm{D}} \quad, \tag{2.52}$$

which relates the tagged particle flux vector to the gradient of the partial mass density of tagged particles.

When discussing self-diffusion coefficients, it is often more convenient to consider the product self-diffusion coefficient times density $D\rho$ than the self-diffusion coefficient itself. The self-diffusion coefficient tends to infinity in the zero density limit, where the mobility of the molecules is not restricted by surrounding molecules. Since this singularity is of order one, it can be removed by multiplying the self-diffusion coefficient with density. In the zero density limit, the product $D\rho$ remains finite and takes the values known from the Chapman-Enskog solution to the Boltzmann equation (see Appendix B).

When the phenomenological equations for the three hydrodynamic phenomenological coefficients are inserted into the entropy source strength, Eq. (2.37), it becomes

$$\sigma = \sum_i \sum_j \boldsymbol{X}^{\mathrm{i}} \cdot \boldsymbol{L}_{\mathrm{ij}} \cdot \boldsymbol{X}^{\mathrm{j}} \tag{2.53}$$

in the general case and

$$\sigma = L_{\mathrm{qq}} \left[\nabla \left(\frac{1}{T} \right) \right]^2 + L_{\widehat{\Pi}\widehat{\Pi}} \frac{\widehat{\dot{\varepsilon}}}{T} : \frac{\widehat{\dot{\varepsilon}}}{T} + L_{\Pi\Pi}^{\mathrm{tr}} \left[\frac{\mathrm{tr}(\dot{\varepsilon})}{T} \right]^2 \tag{2.54}$$

if hydrodynamic transport phenomena are to be described. For establishing the last equation, the tensor identity

$$\boldsymbol{\Pi} : \dot{\varepsilon} = \widehat{\boldsymbol{\Pi}} : \widehat{\dot{\varepsilon}} + \frac{1}{3} \mathrm{tr}(\boldsymbol{\Pi}) \, \mathrm{tr}(\dot{\varepsilon}) \tag{2.55}$$

has been used. From this representation of the entropy source strength, the thermodynamic forces can be identified as $\boldsymbol{X}^{\mathrm{q}} = \nabla(1/T)$, $\boldsymbol{X}^{\widehat{\Pi}} = \widehat{\dot{\varepsilon}}/T$ and $X^{\Pi^{\mathrm{tr}}} = \mathrm{tr}(\dot{\varepsilon})/T$. If the phenomenological coefficients are replaced by the transport coefficients, Eq. (2.54) takes the form

$$\sigma = \frac{\lambda}{T^2} (\nabla T)^2 + \frac{2\eta}{T} \widehat{\dot{\varepsilon}} : \widehat{\dot{\varepsilon}} + \frac{\eta_{\mathrm{b}}}{T} [\mathrm{tr}(\dot{\varepsilon})]^2 \quad . \tag{2.56}$$

Since the entropy source strength is always positive when an irreversible process occurs in a system, all transport coefficients are positive quantities.

2.5 Time-Correlation Function Theory

In time-correlation function theory, macroscopic transport coefficients are represented by the well-known Green-Kubo integral formulas or their corresponding Einstein relations. Although the derivation of these expressions is quite lengthy, it is

instructive to follow it in detail. For their correct application in molecular dynamics simulations, it is important to understand the assumptions that are introduced through the course of the derivation and, consequently, the limitations of these expressions.

2.5.1 Definition and Properties of Time-Correlation Functions

Instantaneous interdependencies between two complex phase variables A and B are measured by the covariance [193]

$$\text{cov}(A, B) = \langle (A - \langle A \rangle)^*(B - \langle B \rangle) \rangle \quad , \tag{2.57}$$

where '*' denotes the complex conjugate. Large values of the covariance represent a strong interdependency between A and B. Interdependencies between two time-dependent phase variables A and B at different times t_0 and $t_0 + t$ are described by time-correlation functions, which can be viewed as an extension of the covariance to time-dependent phenomena. The product $\langle A^*(t_0)B(t_0 + t) \rangle$ replaces the covariance to characterize the correlation between $A^*(t_0)$ and $B(t_0 + t)$. Since the choice of the time interval t is free, $\langle A^*(t_0)B(t_0 + t) \rangle$ is a function of t. Precisely, the time-correlation function $C_{\text{AB}}(t)$ is defined as

$$C_{\text{AB}}(t) = \langle A^*(t_0)B(t_0 + t) \rangle = \lim_{T_{\text{p}} \to \infty} \int_0^{T_{\text{p}}} A^*(t_0)B(t_0 + t)\mathrm{d}t_0 \quad . \tag{2.58}$$

The angular brackets either denote an average over an ensemble of phase space trajectory sections that are characterized by their time origins t_0 or a time average as defined by the integral through the second equality. In equilibrium ensembles, time-correlation functions are invariant to shifts of the time origin t_0,

$$C_{\text{AB}}^{\text{eq}}(t) = \langle A^*(t_0)B(t_0 + t) \rangle = \langle A^*(t_0 + t_1)B(t_0 + t_1 + t) \rangle \quad , \tag{2.59}$$

so that they are functions of the time interval t only. In the remainder of this work, only time-correlation functions in equilibrium ensembles are considered. Therefore, the index 'eq' is omitted and time origins are denoted by $t_0 = 0$ to simplify notation. A time-correlation function of two different phase variables $C_{\text{AB}}(t)$ is termed cross-correlation function, while a time-correlation function of a phase variable with itself $C_{\text{AA}}(t)$ is termed autocorrelation function. The definition, Eq. (2.58), ensures that autocorrelation functions are always real.

Time-correlation functions are bounded as they obey a Schwartz inequality [69]:

$$-(\langle A^*(0)A(0)\rangle\langle B^*(0)B(0)\rangle)^{1/2} \leq \mathrm{Re}(\langle A^*(0)B(t)\rangle) \leq$$
$$(\langle A^*(0)A(0)\rangle\langle B^*(0)B(0)\rangle)^{1/2} \quad . \qquad (2.60)$$

Normalized time-correlation functions

$$\widetilde{C}_{\mathrm{AB}}(t) = \frac{\langle A^*(0)B(t)\rangle}{(\langle A^*(0)A(0)\rangle\langle B^*(0)B(0)\rangle)^{1/2}} \qquad (2.61)$$

are obtained by dividing the correlation function by its maximum possible value imposed by the Schwartz inequality, Eq. (2.60). Time-correlation functions have the initial values

$$C_{\mathrm{AB}}(0) = \langle A^*(0)B(0)\rangle \qquad (2.62)$$

and, provided that A and B do not contain periodic components, they reach

$$\lim_{t\to\infty} C_{\mathrm{AB}}(t) = \langle A^*(0)\rangle\langle B(0)\rangle \qquad (2.63)$$

in the long-time limit since A and B become uncorrelated when the time interval between them becomes infinite. As transport coefficients are related to integrals of time-correlation functions that extend to infinity, the correlated phase variables must be freed from their constant parts to ensure that the integrals converge:

$$\begin{aligned} C_{\mathrm{AB}}(t) &= \langle A^*(0)B(t)\rangle - \langle A^*(0)\rangle\langle B(0)\rangle \\ &= \langle (A(t) - \langle A\rangle)^*(B(t) - \langle B\rangle)\rangle \quad . \end{aligned} \qquad (2.64)$$

This function is a generalization of the covariance to time dependent phenomena and is therefore termed covariance function in the theory of stationary stochastic processes [193]. In this work, the term time-correlation function is used for both time-correlation and covariance functions in accordance with the terminology used in the simulation literature.

In the remainder of this section, further properties of time-correlation functions are collected. By setting $t_1 = -t$ in Eq. (2.59) it follows that

$$C_{\mathrm{AB}}(t) = \langle A^*(0)B(t)\rangle = \langle A^*(-t)B(0)\rangle \quad . \qquad (2.65)$$

The derivative with respect to the origin t_0 vanishes

$$\frac{\mathrm{d}C_{\mathrm{AB}}(t)}{\mathrm{d}t_0} = \langle A^*(t_0)\dot{B}(t_0 + t) + \dot{A}^*(t_0)B(t_0 + t)\rangle = 0 \qquad (2.66)$$

so that

$$\langle A^*(t_0)\dot{B}(t_0 + t)\rangle = -\langle \dot{A}^*(t_0)B(t_0 + t)\rangle \quad . \tag{2.67}$$

The first and second derivatives with respect to time t are given by

$$\frac{\mathrm{d}C_{\mathrm{AB}}(t)}{\mathrm{d}t} = \langle A^*(t_0)\dot{B}(t_0 + t)\rangle \tag{2.68}$$

and

$$\frac{\mathrm{d}^2 C_{\mathrm{AB}}(t)}{\mathrm{d}t^2} = \langle A^*(t_0)\ddot{B}(t_0 + t)\rangle = -\langle \dot{A}^*(t_0)\dot{B}(t_0 + t)\rangle \quad . \tag{2.69}$$

For autocorrelation functions of real phase variables, Eqs. (2.60), (2.65) and (2.67) become

$$-\langle A(0)A(0)\rangle \le C_{\mathrm{AA}}(t) \le \langle A(0)A(0)\rangle \quad , \tag{2.70}$$

$$\langle A(0)A(t)\rangle = \langle A(-t)A(0)\rangle \tag{2.71}$$

and

$$\langle A(0)\dot{A}(0)\rangle = 0 \quad . \tag{2.72}$$

Eq. (2.71) shows that autocorrelation functions are even functions of time.

Contrary to the formal definition of normalized correlation functions, Eq. (2.61), in this work normalized cross-correlation functions of real phase variables are formed by dividing the correlation function by its maximum value:

$$\widetilde{C}_{\mathrm{AB}}(t) = \frac{\langle A(0)B(t)\rangle}{\max(\langle A(0)B(t)\rangle)} \quad . \tag{2.73}$$

This definition turns out to be more reasonable when discussing the transport coefficients in the relaxation time concept in Chapter 7.

2.5.2 Molecular Expressions for Thermodynamic Fluxes

For the evaluation of transport coefficients in molecular dynamics simulations, microscopic analogs for the thermodynamic fluxes are required that express the fluxes in terms of the instantaneous coordinates and velocities of the molecules. These expressions for the thermodynamic fluxes were first derived by Irving and Kirkwood [100]. In their derivation, formal Taylor expansions of delta functions are required

at individual steps of the derivation. Although this provides no conceptual problem, it is more convenient to introduce spatial Fourier transformed quantities and derive the expressions in reciprocal space, i.e. $\boldsymbol{k}$-space. The corresponding expressions in real space, i.e. $\boldsymbol{r}$-space, are found by applying the inverse spatial Fourier transform on the results in reciprocal space. This alternative and simpler derivation was for example used by Evans and Morriss [49]. Furthermore, the procedure of Irving and Kirkwood yields microscopic expressions in terms of ensemble averages, whereas the Fourier transform technique gives instantaneous microscopic expressions for the thermodynamic fluxes. For these reasons, the Fourier transform technique as outlined by Evans and Morriss is followed here.

The connection between the macroscopic and the microscopic viewpoint is provided by a macroscopic δ-function $\delta(\boldsymbol{r} - \boldsymbol{r}_\mathrm{i})$ that is used to represent densities of macroscopic quantities by the coordinates of the particles [49, 100]. As it was introduced by Irving and Kirkwood, it is termed Kirkwood δ-function to distinguish it from the Dirac point δ-function. This δ-function is zero if particle i is outside an infinitesimal macroscopic volume element δV which is located at the macroscopic position $\boldsymbol{r}$. It is a constant if particle i is inside δV. The value of the constant is determined by the normalization condition

$$\int\limits_{\delta V} \delta(\boldsymbol{r})\, \mathrm{d}\boldsymbol{r} = \frac{1}{\delta V} \quad . \tag{2.74}$$

Here, the macroscopic infinitesimal volume element δV represents the microscopic system. Later on, the infinitesimal volume element δV will become the volume V of the microscopic system.

With the macroscopic δ-function, an arbitrary local macroscopic quantity is defined as [49, 69, 100]

$$A(\boldsymbol{r}, t) = \sum_{i=1}^{N} a_\mathrm{i}(t)\, \delta(\boldsymbol{r} - \boldsymbol{r}_\mathrm{i}(t)) \quad . \tag{2.75}$$

It has the spatial Fourier transform

$$A(\boldsymbol{k}, t) = \sum_{i=1}^{N} \frac{a_\mathrm{i}(t)}{\delta V}\, e^{i\boldsymbol{k}\cdot\boldsymbol{r}_\mathrm{i}(t)} \quad . \tag{2.76}$$

The quantity a_i determines the contribution of particle i to the value of A and the δV arises from the spatial Fourier transform of the δ-function.

In this representation of macroscopic quantities, the instantaneous mass density becomes

$$\rho_{\mathrm{m}}(\boldsymbol{r}, t) = \sum_{i=1}^{N} m\,\delta(\boldsymbol{r} - \boldsymbol{r}_{\mathrm{i}}(t)) \tag{2.77}$$

and its spatial Fourier transform is given by

$$\rho_{\mathrm{m}}(\boldsymbol{k}, t) = \sum_{i=1}^{N} \frac{m}{\delta V}\, e^{i\boldsymbol{k}\cdot\boldsymbol{r}_{\mathrm{i}}(t)} \quad . \tag{2.78}$$

The time dependence of $\rho_{\mathrm{m}}(\boldsymbol{r}, t)$ at a fixed position $\boldsymbol{r}$ is implicitly contained in the expression through the time dependence of the particle positions $\boldsymbol{r}_i(t)$. The rate of change of the mass density is obtained by taking the derivative of Eq. (2.78) with respect to time at a fixed position $\boldsymbol{r}$

$$\frac{\partial \rho_{\mathrm{m}}(\boldsymbol{k}, t)}{\partial t} = i\boldsymbol{k} \cdot \sum_{i=1}^{N} \frac{m\boldsymbol{v}_{\mathrm{i}}}{\delta V}\, e^{i\boldsymbol{k}\cdot\boldsymbol{r}_{\mathrm{i}}} \quad , \tag{2.79}$$

where $\boldsymbol{v}_{\mathrm{i}} = \mathrm{d}\boldsymbol{r}_{\mathrm{i}}/\mathrm{d}t$ and $(\partial/\partial t)_{\mathbf{r}} = (\partial/\partial t)_{\mathbf{k}}$ has been used. By applying the inverse spatial Fourier transform on Eq. (2.79),

$$\frac{\partial \rho_{\mathrm{m}}(\boldsymbol{r}, t)}{\partial t} = -\nabla \cdot \left(\sum_{i=1}^{N} m\boldsymbol{v}_{\mathrm{i}}\,\delta(\boldsymbol{r} - \boldsymbol{r}_{\mathrm{i}}) \right) \quad , \tag{2.80}$$

an instantaneous microscopic equation for the mass continuity equation, Eq. (2.23), is recovered. When the right hand side of Eq. (2.80) is compared with the right hand side of Eq. (2.23) and the left hand side of Eq. (2.24), the molecular expression for the momentum density is identified as

$$\rho_{\mathrm{m}}(\boldsymbol{r}, t)\boldsymbol{v}(\boldsymbol{r}, t) = \sum_{i=1}^{N} m\boldsymbol{v}_{\mathrm{i}}\,\delta(\boldsymbol{r} - \boldsymbol{r}_{\mathrm{i}}) \tag{2.81}$$

in real space or by

$$\rho_{\mathrm{m}}(\boldsymbol{k}, t)\boldsymbol{v}(\boldsymbol{k}, t) = \sum_{i=1}^{N} \frac{m\boldsymbol{v}_{\mathrm{i}}}{\delta V}\, e^{i\boldsymbol{k}\cdot\boldsymbol{r}_{\mathrm{i}}} \tag{2.82}$$

in reciprocal space. To derive a microscopic expression for the pressure tensor, the rate of change of the momentum density must be calculated. The rate of change in reciprocal space is

$$\frac{\partial[\rho_{\mathrm{m}}(\boldsymbol{k}, t)\boldsymbol{v}(\boldsymbol{k}, t)]}{\partial t} = \sum_{i=1}^{N} \frac{1}{\delta V}\left(m\boldsymbol{v}_{\mathrm{i}}(i\boldsymbol{k} \cdot \boldsymbol{v}_{\mathrm{i}})\, e^{i\boldsymbol{k}\cdot\boldsymbol{r}_{\mathrm{i}}} + \boldsymbol{F}_{\mathrm{i}}\, e^{i\boldsymbol{k}\cdot\boldsymbol{r}_{\mathrm{i}}} \right) \quad . \tag{2.83}$$

According to Evans and Morriss [49, p. 72], the second term on the right hand side can be rewritten by using $\boldsymbol{F}_{ij} = -\boldsymbol{F}_{ji}$ as

$$
\begin{aligned}
\sum_{i=1}^{N} \boldsymbol{F}_i \, e^{i\boldsymbol{k}\cdot\boldsymbol{r}_i} &= \frac{1}{2} \sum_{i=1}^{N} \sum_{\substack{j=1\\j\neq i}}^{N} \boldsymbol{F}_{ij} \left(e^{i\boldsymbol{k}\cdot\boldsymbol{r}_i} - e^{i\boldsymbol{k}\cdot\boldsymbol{r}_j} \right) \\
&= \frac{1}{2} \sum_{i=1}^{N} \sum_{\substack{j=1\\j\neq i}}^{N} \boldsymbol{F}_{ij} \left(e^{i\boldsymbol{k}\cdot\boldsymbol{r}_{ij}} - 1 \right) e^{i\boldsymbol{k}\cdot\boldsymbol{r}_j} \\
&= -\frac{i\boldsymbol{k}}{2} \cdot \sum_{i=1}^{N} \sum_{\substack{j=1\\j\neq i}}^{N} \boldsymbol{r}_{ij}\boldsymbol{F}_{ij} \frac{e^{i\boldsymbol{k}\cdot\boldsymbol{r}_{ij}} - 1}{-i\boldsymbol{k}\cdot\boldsymbol{r}_{ij}} \, e^{i\boldsymbol{k}\cdot\boldsymbol{r}_j} \quad .
\end{aligned}
\tag{2.84}
$$

When the exponential in the numerator is expanded in a Taylor series

$$
e^{i\boldsymbol{k}\cdot\boldsymbol{r}_{ij}} = 1 + i\boldsymbol{k}\cdot\boldsymbol{r}_{ij} + \frac{(i\boldsymbol{k}\cdot\boldsymbol{r}_{ij})^2}{2} + \dots
\tag{2.85}
$$

and terms of second and higher order are neglected, the fraction becomes -1 so that

$$
\sum_{i=1}^{N} \boldsymbol{F}_i \, e^{i\boldsymbol{k}\cdot\boldsymbol{r}_i} = \frac{i\boldsymbol{k}}{2} \cdot \sum_{i=1}^{N} \sum_{\substack{j=1\\j\neq i}}^{N} \boldsymbol{r}_{ij}\boldsymbol{F}_{ij} \, e^{i\boldsymbol{k}\cdot\boldsymbol{r}_j} = \frac{i\boldsymbol{k}}{2} \cdot \sum_{i=1}^{N} \sum_{\substack{j=1\\j\neq i}}^{N} \boldsymbol{r}_{ij}\boldsymbol{F}_{ij} \, e^{i\boldsymbol{k}\cdot\boldsymbol{r}_i} \quad .
\tag{2.86}
$$

The last identity follows from an exchange of i and j in the double sum and the subsequent application of Newton's second law $\boldsymbol{F}_{ji} = -\boldsymbol{F}_{ij}$ and of the identity $\boldsymbol{r}_{ji} = -\boldsymbol{r}_{ij}$. When this result is inserted into Eq. (2.83), the rate of change of the momentum density in reciprocal space becomes

$$
\frac{\partial[\rho_{\mathrm{m}}(\boldsymbol{k},t)\boldsymbol{v}(\boldsymbol{k},t)]}{\partial t} = i\boldsymbol{k}\cdot\left(\frac{1}{\delta V} \sum_{i=1}^{N} m\boldsymbol{v}_i\boldsymbol{v}_i + \frac{1}{2}\frac{1}{\delta V} \sum_{i=1}^{N} \sum_{\substack{j=1\\j\neq i}}^{N} \boldsymbol{r}_{ij}\boldsymbol{F}_{ij} \right) e^{i\boldsymbol{k}\cdot\boldsymbol{r}_i} \quad .
\tag{2.87}
$$

The real space representation of Eq. (2.87) is

$$
\frac{\partial[\rho_{\mathrm{m}}(\boldsymbol{r},t)\boldsymbol{v}(\boldsymbol{r},t)]}{\partial t} = -\nabla\cdot\Bigg(\sum_{i=1}^{N} m\boldsymbol{v}_i\boldsymbol{v}_i \, \delta(\boldsymbol{r}-\boldsymbol{r}_i)
$$

$$
+ \frac{1}{2} \sum_{i=1}^{N} \sum_{\substack{j=1\\j\neq i}}^{N} \boldsymbol{r}_{ij}\boldsymbol{F}_{ij} \, \delta(\boldsymbol{r}-\boldsymbol{r}_i) \Bigg) \quad .
\tag{2.88}
$$

In the final step of the derivation, peculiar particle velocities, that means particle velocities $\boldsymbol{v}_i - \boldsymbol{v}$ relative to the velocity of the volume element $\boldsymbol{v}$, are introduced to recover the convective term in the right hand side of Eq. (2.24). The first sum on the right hand side of Eq. (2.88) is rewritten as

$$\sum_{i=1}^{N} m\boldsymbol{v}_i\boldsymbol{v}_i\,\delta(\boldsymbol{r} - \boldsymbol{r}_i) = \sum_{i=1}^{N} m[(\boldsymbol{v}_i - \boldsymbol{v})(\boldsymbol{v}_i - \boldsymbol{v}) + 2m\boldsymbol{v}\boldsymbol{v}_i - m\boldsymbol{v}\boldsymbol{v}]\,\delta(\boldsymbol{r} - \boldsymbol{r}_i)$$

$$= \rho_m\boldsymbol{v}\boldsymbol{v} + \sum_{i=1}^{N} m(\boldsymbol{v}_i - \boldsymbol{v})(\boldsymbol{v}_i - \boldsymbol{v})\,\delta(\boldsymbol{r} - \boldsymbol{r}_i) \quad , \qquad (2.89)$$

where Eq. (2.81) has been used to combine the second and third term in the first line. Inserting this result into Eq. (2.88) yields the real space representation of the momentum conservation equation:

$$\frac{\partial[\rho_m(\boldsymbol{r}, t)\boldsymbol{v}(\boldsymbol{r}, t)]}{\partial t} = -\nabla \cdot \left(\rho_m\boldsymbol{v}\boldsymbol{v} + \sum_{i=1}^{N} m(\boldsymbol{v}_i - \boldsymbol{v})(\boldsymbol{v}_i - \boldsymbol{v})\,\delta(\boldsymbol{r} - \boldsymbol{r}_i) \right.$$

$$\left. + \frac{1}{2}\sum_{i=1}^{N}\sum_{\substack{j=1 \\ j\neq i}}^{N} \boldsymbol{r}_{ij}\boldsymbol{F}_{ij}\,\delta(\boldsymbol{r} - \boldsymbol{r}_i) \right) \quad . \quad (2.90)$$

The molecular expression for the pressure tensor in real space is obtained from the comparison of Eq. (2.90) with the momentum conservation equation, Eq. (2.24), as

$$\boldsymbol{P}(\boldsymbol{r}, t) = \sum_{i=1}^{N} \left(m(\boldsymbol{v}_i - \boldsymbol{v})(\boldsymbol{v}_i - \boldsymbol{v}) + \frac{1}{2}\sum_{\substack{j=1 \\ j\neq i}}^{N} \boldsymbol{r}_{ij}\boldsymbol{F}_{ij} \right) \delta(\boldsymbol{r} - \boldsymbol{r}_i) \quad , \qquad (2.91)$$

and with Eq. (2.29) the molecular expression for the viscous pressure tensor follows as

$$\boldsymbol{\Pi}(\boldsymbol{r}, t) = \sum_{i=1}^{N} \left(m(\boldsymbol{v}_i - \boldsymbol{v})(\boldsymbol{v}_i - \boldsymbol{v}) + \frac{1}{2}\sum_{\substack{j=1 \\ j\neq i}}^{N} \boldsymbol{r}_{ij}\boldsymbol{F}_{ij} \right) \delta(\boldsymbol{r} - \boldsymbol{r}_i) - p(\boldsymbol{r}, t)\,\boldsymbol{I} \quad . \quad (2.92)$$

The derivation of the expression for the energy flux vector starts from the energy density and proceeds analogously. The real space representation of the energy

density

$$\rho_{\mathrm{m}}(\boldsymbol{r}, t) e_{\mathrm{m}}(\boldsymbol{r}, t) = \sum_{i=1}^{N} \left(\frac{1}{2} m \boldsymbol{v}_{\mathrm{i}}^2 + \frac{1}{2} \sum_{\substack{j=1 \\ j \neq i}}^{N} u(r_{\mathrm{ij}}) \right) \delta(\boldsymbol{r} - \boldsymbol{r}_{\mathrm{i}}) \qquad (2.93)$$

becomes in reciprocal space

$$\rho_{\mathrm{m}}(\boldsymbol{k}, t) e_{\mathrm{m}}(\boldsymbol{k}, t) = \frac{1}{\delta V} \sum_{i=1}^{N} \left(\frac{1}{2} m \boldsymbol{v}_{\mathrm{i}}^2 + \frac{1}{2} \sum_{\substack{j=1 \\ j \neq i}}^{N} u(r_{\mathrm{ij}}) \right) e^{i\boldsymbol{k} \cdot \boldsymbol{r}_{\mathrm{i}}} \quad . \qquad (2.94)$$

The rate of change of the energy density is

$$\frac{\partial [\rho_{\mathrm{m}}(\boldsymbol{k}, t) e_{\mathrm{m}}(\boldsymbol{k}, t)]}{\partial t} = i\boldsymbol{k} \cdot \sum_{i=1}^{N} \frac{1}{\delta V} \left(\frac{1}{2} m \boldsymbol{v}_{\mathrm{i}}^2 + \frac{1}{2} \sum_{\substack{j=1 \\ j \neq i}}^{N} u(r_{\mathrm{ij}}) \right) \boldsymbol{v}_{\mathrm{i}} \, e^{i\boldsymbol{k} \cdot \boldsymbol{r}_{\mathrm{i}}}$$

$$+ \frac{1}{\delta V} \sum_{i=1}^{N} m \boldsymbol{a}_{\mathrm{i}} \cdot \boldsymbol{v}_{\mathrm{i}} \, e^{i\boldsymbol{k} \cdot \boldsymbol{r}_{\mathrm{i}}} + \frac{1}{2} \frac{1}{\delta V} \sum_{i=1}^{N} \sum_{\substack{j=1 \\ j \neq i}}^{N} \left(\frac{\partial u}{\partial \boldsymbol{r}_{\mathrm{ij}}} \cdot \frac{\partial \boldsymbol{r}_{\mathrm{ij}}}{\partial t} \right) e^{i\boldsymbol{k} \cdot \boldsymbol{r}_{\mathrm{i}}} \quad , \quad (2.95)$$

where $\boldsymbol{a}_{\mathrm{i}} = \dot{\boldsymbol{v}}_{\mathrm{i}}$ is the acceleration vector of particle i. With

$$\boldsymbol{F}_{\mathrm{i}} = m \boldsymbol{a}_{\mathrm{i}} \qquad , \qquad \boldsymbol{F}_{\mathrm{ij}} = -\frac{\partial u}{\partial \boldsymbol{r}_{\mathrm{ij}}} \qquad , \qquad \frac{\partial \boldsymbol{r}_{\mathrm{ij}}}{\partial t} = \frac{\partial \boldsymbol{r}_{\mathrm{i}}}{\partial t} - \frac{\partial \boldsymbol{r}_{\mathrm{j}}}{\partial t} = \boldsymbol{v}_{\mathrm{i}} - \boldsymbol{v}_{\mathrm{j}} \qquad (2.96)$$

and the abbreviation

$$e_{\mathrm{i}} = \frac{1}{2} m \boldsymbol{v}_{\mathrm{i}}^2 + \frac{1}{2} \sum_{\substack{j=1 \\ j \neq i}}^{N} u(r_{\mathrm{ij}}) \qquad (2.97)$$

for the energy per particle, it is found that

$$\frac{\partial [\rho_{\mathrm{m}}(\boldsymbol{k}, t) e_{\mathrm{m}}(\boldsymbol{k}, t)]}{\partial t} = i\boldsymbol{k} \cdot \sum_{i=1}^{N} \frac{\boldsymbol{v}_{\mathrm{i}} e_{\mathrm{i}}}{\delta V} \, e^{i\boldsymbol{k} \cdot \boldsymbol{r}_{\mathrm{i}}} + \frac{1}{\delta V} \sum_{i=1}^{N} \boldsymbol{v}_{\mathrm{i}} \cdot \boldsymbol{F}_{\mathrm{i}} \, e^{i\boldsymbol{k} \cdot \boldsymbol{r}_{\mathrm{i}}}$$

$$- \frac{1}{2} \frac{1}{\delta V} \sum_{i=1}^{N} \sum_{\substack{j=1 \\ j \neq i}}^{N} (\boldsymbol{v}_{\mathrm{i}} \cdot \boldsymbol{F}_{\mathrm{ij}} - \boldsymbol{v}_{\mathrm{j}} \cdot \boldsymbol{F}_{\mathrm{ij}}) \, e^{i\boldsymbol{k} \cdot \boldsymbol{r}_{\mathrm{i}}} \quad . \qquad (2.98)$$

The second and third term on the right hand side can be combined to yield

$$\frac{\partial[\rho_{\mathrm{m}}(\boldsymbol{k},t)e_{\mathrm{m}}(\boldsymbol{k},t)]}{\partial t} = i\boldsymbol{k}\cdot\sum_{i=1}^{N}\frac{\boldsymbol{v}_{\mathrm{i}}e_{\mathrm{i}}}{\delta V}\,e^{i\boldsymbol{k}\cdot\boldsymbol{r}_{\mathrm{i}}}$$

$$+\frac{1}{2}\frac{1}{\delta V}\sum_{i=1}^{N}\sum_{\substack{j=1\\j\neq i}}^{N}\boldsymbol{v}_{\mathrm{i}}\cdot\boldsymbol{F}_{\mathrm{ij}}\left(e^{i\boldsymbol{k}\cdot\boldsymbol{r}_{\mathrm{i}}}-e^{i\boldsymbol{k}\cdot\boldsymbol{r}_{\mathrm{j}}}\right)\quad.\qquad(2.99)$$

The difference between the two exponentials is the same as in Eq. (2.84). Hence, it can be evaluated analogously so that the rate of change of the energy density in reciprocal space becomes

$$\frac{\partial[\rho_{\mathrm{m}}(\boldsymbol{k},t)e_{\mathrm{m}}(\boldsymbol{k},t)]}{\partial t} = i\boldsymbol{k}\cdot\left(\frac{1}{\delta V}\sum_{i=1}^{N}\boldsymbol{v}_{\mathrm{i}}e_{\mathrm{i}}+\frac{1}{2}\frac{1}{\delta V}\sum_{i=1}^{N}\sum_{\substack{j=1\\j\neq i}}^{N}\boldsymbol{r}_{\mathrm{ij}}\left(\boldsymbol{v}_{\mathrm{i}}\cdot\boldsymbol{F}_{\mathrm{ij}}\right)\right)e^{i\boldsymbol{k}\cdot\boldsymbol{r}_{\mathrm{i}}}\quad.$$

$$(2.100)$$

In real space the rate of change of the energy density is

$$\frac{\partial[\rho_{\mathrm{m}}(\boldsymbol{r},t)e_{\mathrm{m}}(\boldsymbol{r},t)]}{\partial t} = -\nabla\cdot\left(\sum_{i=1}^{N}\frac{1}{2}m\boldsymbol{v}_{\mathrm{i}}^{2}\boldsymbol{v}_{\mathrm{i}}+\frac{1}{2}\sum_{i=1}^{N}\sum_{\substack{j=1\\j\neq i}}^{N}u(r_{\mathrm{ij}})\boldsymbol{v}_{\mathrm{i}}\right.$$

$$\left.+\frac{1}{2}\sum_{i=1}^{N}\sum_{\substack{j=1\\j\neq i}}^{N}(\boldsymbol{r}_{\mathrm{ij}}\boldsymbol{F}_{\mathrm{ij}})\cdot\boldsymbol{v}_{\mathrm{i}}\right)\delta(\boldsymbol{r}-\boldsymbol{r}_{\mathrm{i}})\quad,\qquad(2.101)$$

where it has been used that $\boldsymbol{r}_{\mathrm{ij}}\left(\boldsymbol{v}_{\mathrm{i}}\cdot\boldsymbol{F}_{\mathrm{ij}}\right)=(\boldsymbol{r}_{\mathrm{ij}}\boldsymbol{F}_{\mathrm{ij}})\cdot\boldsymbol{v}_{\mathrm{i}}$. The molecular expression for the energy flux vector is obtained by comparing Eq. (2.101) with the energy conservation equation, Eq. (2.32), as

$$\boldsymbol{J}^{\mathrm{e}}(\boldsymbol{r},t) = \sum_{i=1}^{N}\left(\frac{1}{2}m\boldsymbol{v}_{\mathrm{i}}^{2}\boldsymbol{v}_{\mathrm{i}}+\frac{1}{2}\sum_{\substack{j=1\\j\neq i}}^{N}u(r_{\mathrm{ij}})\boldsymbol{v}_{\mathrm{i}}+\frac{1}{2}\sum_{\substack{j=1\\j\neq i}}^{N}(\boldsymbol{r}_{\mathrm{ij}}\boldsymbol{F}_{\mathrm{ij}})\cdot\boldsymbol{v}_{\mathrm{i}}\right)\delta(\boldsymbol{r}-\boldsymbol{r}_{\mathrm{i}})\quad.$$

$$(2.102)$$

The corresponding molecular expression for the heat flux vector is found by inserting this result for the energy flux vector into

$$\boldsymbol{J}^{\mathrm{q}} = \boldsymbol{J}^{\mathrm{e}}-\rho_{\mathrm{m}}e_{\mathrm{m}}\boldsymbol{v}-\boldsymbol{P}\cdot\boldsymbol{v}\quad.\qquad(2.103)$$

When furthermore the identity

$$\boldsymbol{v}_i^2 \boldsymbol{v}_i = [\boldsymbol{v}_i - \boldsymbol{v}]^2 (\boldsymbol{v}_i - \boldsymbol{v}) + 2[(\boldsymbol{v}_i - \boldsymbol{v})(\boldsymbol{v}_i - \boldsymbol{v})] \cdot \boldsymbol{v} + \boldsymbol{v}_i^2 \boldsymbol{v} + \boldsymbol{v}^2 (\boldsymbol{v}_i - \boldsymbol{v}) \quad (2.104)$$

is used to introduce peculiar velocities, the molecular expressions for the pressure tensor, Eq. (2.91), and for the energy density, Eq. (2.93), can be used to recover two terms which exactly cancel the terms $\rho_m e_m \boldsymbol{v}$ and $\boldsymbol{P} \cdot \boldsymbol{v}$ in Eq. (2.103). The contribution from the last term in Eq. (2.104) vanishes because the average velocity of the particles in the volume element is the velocity of the volume element $\boldsymbol{v}$. Finally, the molecular expression for the heat flux vector is obtained as

$$\boldsymbol{J}^q(\boldsymbol{r}, t) = \sum_{i=1}^{N} \left(\frac{1}{2} m [\boldsymbol{v}_i - \boldsymbol{v}]^2 (\boldsymbol{v}_i - \boldsymbol{v}) + \frac{1}{2} \sum_{\substack{j=1 \\ j \neq i}}^{N} u(r_{ij})(\boldsymbol{v}_i - \boldsymbol{v}) \right.$$
$$\left. + \frac{1}{2} \sum_{\substack{j=1 \\ j \neq i}}^{N} (\boldsymbol{r}_{ij} \boldsymbol{F}_{ij}) \cdot (\boldsymbol{v}_i - \boldsymbol{v}) \right) \delta(\boldsymbol{r} - \boldsymbol{r}_i) \quad . \quad (2.105)$$

In molecular dynamics simulations where the total momentum of the system is kept constant, the expressions for the energy and heat flux vector become identical.

As the last point in this section, the molecular expression for the tagged particle flux vector is derived. The derivation starts from the real space representation of the instantaneous partial mass density of tagged particles

$$\rho_m^D(\boldsymbol{r}, t) = \sum_{i=1}^{N^D} m \delta(\boldsymbol{r}_i - \boldsymbol{r}) \quad . \quad (2.106)$$

The spatial Fourier transform of the tagged particle density is given by

$$\rho_m^D(\boldsymbol{k}, t) = \sum_{i=1}^{N^D} \frac{m}{\delta V} e^{i\boldsymbol{k} \cdot \boldsymbol{r}_i} \quad (2.107)$$

and its derivative with respect to time by

$$\frac{\partial \rho_m^D(\boldsymbol{k}, t)}{\partial t} = i\boldsymbol{k} \cdot \sum_{i=1}^{N^D} \frac{m\boldsymbol{v}_i}{\delta V} e^{i\boldsymbol{k} \cdot \boldsymbol{r}_i} \quad . \quad (2.108)$$

Transforming this result back into real space leads to

$$\frac{\partial \rho_m^D(\boldsymbol{r}, t)}{\partial t} = -\nabla \cdot \left(\sum_{i=1}^{N^D} m\boldsymbol{v}_i \delta(\boldsymbol{r} - \boldsymbol{r}_i) \right) \quad . \quad (2.109)$$

Using the relation

$$\sum_{i=1}^{N^{\mathrm{D}}} m\boldsymbol{v}_{\mathrm{i}}\delta(\boldsymbol{r} - \boldsymbol{r}_{\mathrm{i}}) = \rho_{\mathrm{m}}^{\mathrm{D}}\boldsymbol{v} + \sum_{i=1}^{N^{\mathrm{D}}} m(\boldsymbol{v}_{\mathrm{i}} - \boldsymbol{v})\delta(\boldsymbol{r} - \boldsymbol{r}_{\mathrm{i}}) \tag{2.110}$$

to introduce peculiar velocities yields

$$\frac{\partial \rho_{\mathrm{m}}^{\mathrm{D}}(\boldsymbol{r}, t)}{\partial t} = -\nabla\cdot\left(\rho_{\mathrm{m}}^{\mathrm{D}}\boldsymbol{v} + \sum_{i=1}^{N^{\mathrm{D}}} m(\boldsymbol{v}_{\mathrm{i}} - \boldsymbol{v})\delta(\boldsymbol{r} - \boldsymbol{r}_{\mathrm{i}})\right) \quad . \tag{2.111}$$

The molecular expression for the tagged particle flux in the centre of mass frame of the moving volume element is identified by comparing this result with Eq. (2.39) as

$$\boldsymbol{J}^{\mathrm{D}}(t) = \sum_{i=1}^{N^{\mathrm{D}}} m(\boldsymbol{v}_{\mathrm{i}}(t) - \boldsymbol{v})\delta(\boldsymbol{r} - \boldsymbol{r}_{\mathrm{i}}) \quad . \tag{2.112}$$

If there is only one tagged particle, for example particle i, the tagged particle flux becomes

$$\boldsymbol{J}^{\mathrm{D}}(t) = m(\boldsymbol{v}_{\mathrm{i}}(t) - \boldsymbol{v})\delta(\boldsymbol{r} - \boldsymbol{r}_{\mathrm{i}}) \quad . \tag{2.113}$$

When microscopic fluctuations of the fluxes in an ensemble representation of the volume element are examined, the macroscopic delta function becomes $1/V$, the inverse volume of the system, by its normalization, Eq. (2.74). Hence, the expressions for the viscous pressure tensor, heat flux vector and tagged particle flux vector applied in equilibrium molecular dynamics simulations are given by

$$\boldsymbol{\Pi} = \frac{1}{V}\sum_{i=1}^{N}\left(m\boldsymbol{v}_{\mathrm{i}}\boldsymbol{v}_{\mathrm{i}} + \frac{1}{2}\sum_{\substack{j=1 \\ j\neq i}}^{N}\boldsymbol{r}_{\mathrm{ij}}\boldsymbol{F}_{\mathrm{ij}}\right) - p\,\boldsymbol{I} \quad , \tag{2.114}$$

$$\boldsymbol{J}^{\mathrm{q}} = \frac{1}{V}\sum_{i=1}^{N}\left(\frac{1}{2}m\boldsymbol{v}_{\mathrm{i}}^{2}\boldsymbol{v}_{\mathrm{i}} + \frac{1}{2}\sum_{\substack{j=1 \\ j\neq i}}^{N} u(r_{\mathrm{ij}})\boldsymbol{v}_{\mathrm{i}} + \frac{1}{2}\sum_{\substack{j=1 \\ j\neq i}}^{N}(\boldsymbol{r}_{\mathrm{ij}}\boldsymbol{F}_{\mathrm{ij}})\cdot\boldsymbol{v}_{\mathrm{i}}\right) \tag{2.115}$$

and

$$\boldsymbol{J}^{\mathrm{D}}(t) = \frac{m\boldsymbol{v}_{\mathrm{i}}(t)}{V} \quad . \tag{2.116}$$

It is to be remembered that the system is at rest during the simulation and the velocity $\boldsymbol{v}_{\mathrm{i}}$ is the velocity of particle i in this reference frame.

It is noteworthy that sometimes a different molecular expression for the heat flux vector is reported in literature which results from a linearization of the energy balance, see for example [69, p. 281]. This expression reads

$$\boldsymbol{J}^{\mathrm{q}} = \frac{1}{V} \sum_{i=1}^{N} \left(\frac{1}{2} m \boldsymbol{v}_{\mathrm{i}}^{2} \boldsymbol{v}_{\mathrm{i}} + \frac{1}{2} \sum_{\substack{j=1 \\ j\neq i}}^{N} (u(r_{\mathrm{ij}}) - \langle h_{\mathrm{i}} \rangle) \boldsymbol{v}_{\mathrm{i}} + \frac{1}{2} \sum_{\substack{j=1 \\ j\neq i}}^{N} (\boldsymbol{r}_{\mathrm{ij}} \boldsymbol{F}_{\mathrm{ij}}) \cdot \boldsymbol{v}_{\mathrm{i}} \right) \quad , \quad (2.117)$$

where h_{i} is the enthalpy per particle. Here, the velocities $\boldsymbol{v}_{\mathrm{i}}$ refer to a space-fixed coordinate frame and the enthalpy term arises from the linearization of the energy balance. Again, this expression and the expression given by Eq. (2.115) become identical when the system is at rest.

2.5.3   Green-Kubo Integral Formulas

Transport processes that occur on length and time scales that are large compared to the molecular dimensions are described by the macroscopic hydrodynamic balance equations supplemented by the phenomenological equations that define the macroscopic transport coefficients. When the length and time scales of a transport process reach the molecular dimensions, this macroscopic continuum model does not provide a sufficient description of the process since the molecular structure of the fluid must be taken into account. An extension to the molecular scale is provided by generalized hydrodynamics where the continuum model is modified by introducing position and time dependent transport coefficients while retaining the form of the macroscopic balance equations [9, 69]. With this modification, transport processes at wave lengths of the order of a few intermolecular distances and frequencies of the order of magnitude of the collision frequencies can be described. In generalized hydrodynamics, the linear phenomenological equations are replaced by non-Markovian linear relations which have the form

$$\boldsymbol{J}^{\mathrm{i}}(\boldsymbol{r}, t) = - \int_{0}^{t} \int_{\boldsymbol{r}_{0}}^{\boldsymbol{r}} \boldsymbol{L}_{\mathrm{ij}}(\boldsymbol{r}', t') \cdot \boldsymbol{X}^{\mathrm{j}}(\boldsymbol{r} - \boldsymbol{r}', t - t') \, \mathrm{d}\boldsymbol{r}' \, \mathrm{d}t' \quad , \quad (2.118)$$

where $\boldsymbol{L}_{\mathrm{ij}}(\boldsymbol{r}', t')$ represents the generalized position and time dependent phenomenological coefficients. In this model, the thermodynamic flux $\boldsymbol{J}^{\mathrm{i}}$ is linearly proportional to the force $\boldsymbol{X}^{\mathrm{j}}$ at all previous times and all other positions. The fluid has a memory so that a disturbance at a position $\boldsymbol{r}'$ and a time t' has a delayed effect at a time t at another location $\boldsymbol{r}$. This delay arises because the fluid cannot respond

instantaneously to a change induced by a disturbance, but it takes some time for the particles to rearrange themselves. A rigorous justification of the generalized phenomenological equation was provided by Mori [156, 157]. Using the projection operator technique suggested by Zwanzig [218], Mori derived a generalized Langevin equation for an arbitrary phase variable directly from the microscopic equations of motion and showed that this result can be used to formulate phenomenological equations which have the functional form of Eq. (2.118). A discussion of memory effects from a different viewpoint was given by Zwanzig [219]. He showed how the Fokker-Planck equation approach on the basis of Markovian fluid behaviour by Green [58] can be extended to include non-Markovian behaviour.

The generalized phenomenological equation, Eq. (2.118), is the starting point for the derivation of Green-Kubo integral formulas for the macroscopic transport coefficients. They will be obtained as zero frequency and zero wave vector limit of the frequency and wave vector dependent generalized transport coefficients. First, the derivation is described for the viscosity and bulk viscosity in detail, while the relation for the thermal conductivity is subsequently given by a simple argument.

The generalized analog of the phenomenological equation relating the viscous pressure tensor to the strain rate tensor, Eq. (2.47), is given by

$$
\boldsymbol{\Pi}(\boldsymbol{r}, t) \;=\; -\int\limits_{0}^{t}\int\limits_{\boldsymbol{r}_0}^{\boldsymbol{r}} \left\{ 2\,\eta(\boldsymbol{r}', t')\,\widehat{\dot{\boldsymbol{\varepsilon}}}(\boldsymbol{r} - \boldsymbol{r}', t - t') \right.
$$
$$
\left. + \eta_{\mathrm{b}}(\boldsymbol{r}', t')\,\mathrm{tr}[\dot{\boldsymbol{\varepsilon}}(\boldsymbol{r} - \boldsymbol{r}', t - t')]\boldsymbol{I} \right\}\,\mathrm{d}\boldsymbol{r}'\,\mathrm{d}t' \quad . \quad (2.119)
$$

For the derivation of the Green-Kubo formulas for viscosity and bulk viscosity, Eq. (2.119) is Fourier transformed into reciprocal space and Fourier-Laplace transformed with respect to time into the frequency domain. The right hand side is a convolution with respect to both space and time. Application of the spatial Fourier transform on the strain rate tensor, Eq. (2.45), yields for the traceless part

$$
2\,\widehat{\dot{\boldsymbol{\varepsilon}}}(\boldsymbol{k}, t) = -i\left(\boldsymbol{k}\boldsymbol{v} + (\boldsymbol{k}\boldsymbol{v})^T - \frac{2}{3}\,\boldsymbol{k}\cdot\boldsymbol{v}\right) \tag{2.120}
$$

$$
= -\frac{i}{\rho_{\mathrm{m}}}\left(\boldsymbol{k}\boldsymbol{J}^{\mathrm{p}} + (\boldsymbol{k}\boldsymbol{J}^{\mathrm{p}})^T - \frac{2}{3}\,\boldsymbol{k}\cdot\boldsymbol{J}^{\mathrm{p}}\right) \tag{2.121}
$$

and for the trace

$$
\mathrm{tr}[\dot{\boldsymbol{\varepsilon}}(\boldsymbol{k}, t)] = -i\boldsymbol{k}\cdot\boldsymbol{v} = -i\frac{\boldsymbol{k}\cdot\boldsymbol{J}^{\mathrm{p}}}{\rho_{\mathrm{m}}} \quad , \tag{2.122}
$$

where the momentum density vector $\boldsymbol{J}^{\mathrm{p}}$ has been introduced as an abbreviation for the product of velocity and mass density. The result of the double transformation is

$$\boldsymbol{\Pi}(\boldsymbol{k}, i\omega) = i\,\frac{\eta(\boldsymbol{k}, i\omega)}{\rho_{\mathrm{m}}} \left[\boldsymbol{k}\boldsymbol{J}^{\mathrm{p}} + (\boldsymbol{k}\boldsymbol{J}^{\mathrm{p}})^{T} - \frac{2}{3}\,(\boldsymbol{k}\cdot\boldsymbol{J}^{\mathrm{p}})\,\boldsymbol{I} \right]$$
$$+ i\,\frac{\eta_{\mathrm{b}}(\boldsymbol{k}, i\omega)}{\rho_{\mathrm{m}}}\,(\boldsymbol{k}\cdot\boldsymbol{J}^{\mathrm{p}})\,\boldsymbol{I} \quad , \qquad (2.123)$$

in which $\eta(\boldsymbol{k}, i\omega)$ and $\eta_{\mathrm{b}}(\boldsymbol{k}, i\omega)$ are the wave vector and frequency dependent viscosity and bulk viscosity. The viscous pressure tensor is related to the time derivative of the momentum density vector by the linearized momentum balance, Eq. (2.31), which reads in reciprocal space

$$\frac{\partial \boldsymbol{J}^{\mathrm{p}}(\boldsymbol{k}, t)}{\partial t} = i\boldsymbol{k}\cdot\boldsymbol{\Pi}(\boldsymbol{k}, t) \quad . \qquad (2.124)$$

Additional transformation into the frequency domain and inserting the result for the viscous pressure tensor yields

$$\int\limits_{0}^{\infty} \frac{\partial \boldsymbol{J}^{\mathrm{p}}(\boldsymbol{k}, t)}{\partial t}\,e^{-i\omega t}\,\mathrm{d}t = -\frac{\eta(\boldsymbol{k}, i\omega)}{\rho_{\mathrm{m}}} \left[\boldsymbol{k}\cdot(\boldsymbol{k}\boldsymbol{J}^{\mathrm{p}}) + \boldsymbol{k}\cdot(\boldsymbol{k}\boldsymbol{J}^{\mathrm{p}})^{T} - \frac{2}{3}\,\boldsymbol{k}\,(\boldsymbol{k}\cdot\boldsymbol{J}^{\mathrm{p}}) \right]$$
$$-\frac{\eta_{\mathrm{b}}(\boldsymbol{k}, i\omega)}{\rho_{\mathrm{m}}}\,\boldsymbol{k}\,(\boldsymbol{k}\cdot\boldsymbol{J}^{\mathrm{p}}) \quad . \qquad (2.125)$$

In order to obtain separate equations for the viscosity and bulk viscosity, the momentum density vector is split into a transverse part,

$$\boldsymbol{J}^{\mathrm{p,t}} = -\frac{1}{\boldsymbol{k}^{2}}\,[\boldsymbol{k}\times(\boldsymbol{k}\times\boldsymbol{J}^{\mathrm{p}})] \quad , \qquad (2.126)$$

perpendicular to the wave vector $\boldsymbol{k}$ and a longitudinal part,

$$\boldsymbol{J}^{\mathrm{p,l}} = \frac{\boldsymbol{k}}{\boldsymbol{k}^{2}}\,(\boldsymbol{k}\cdot\boldsymbol{J}^{\mathrm{p}}) \quad , \qquad (2.127)$$

parallel to the wave vector $\boldsymbol{k}$. When this subdivision of the momentum density vector is inserted into Eq. (2.125), the relation

$$\int\limits_{0}^{\infty} \frac{\partial}{\partial t}(\boldsymbol{J}^{\mathrm{p,t}}(\boldsymbol{k}, t) + \boldsymbol{J}^{\mathrm{p,l}}(\boldsymbol{k}, t))\,e^{-i\omega t}\,\mathrm{d}t =$$
$$-\frac{\eta(\boldsymbol{k}, i\omega)}{\rho_{\mathrm{m}}} \left[\boldsymbol{k}^{2}\boldsymbol{J}^{\mathrm{p,t}} + \frac{4}{3}\,\boldsymbol{k}^{2}\boldsymbol{J}^{\mathrm{p,l}} \right] - \frac{\eta_{\mathrm{b}}(\boldsymbol{k}, i\omega)}{\rho_{\mathrm{m}}}\,\boldsymbol{k}^{2}\boldsymbol{J}^{\mathrm{p,l}} \qquad (2.128)$$

is obtained, where the identity

$$\boldsymbol{k}\cdot(\boldsymbol{k}\boldsymbol{J}^{\mathrm{p}}) + \boldsymbol{k}\cdot(\boldsymbol{k}\boldsymbol{J}^{\mathrm{p}})^{T} = 2\,\boldsymbol{k}\,(\boldsymbol{k}\cdot\boldsymbol{J}^{\mathrm{p}}) - \boldsymbol{k}\times(\boldsymbol{k}\times\boldsymbol{J}^{\mathrm{p}}) \tag{2.129}$$

has been used. Introducing the wave vector and frequency dependent longitudinal viscosity

$$\eta_{\mathrm{l}}(\boldsymbol{k},i\omega) = \frac{4}{3}\eta(\boldsymbol{k},i\omega) + \eta_{\mathrm{b}}(\boldsymbol{k},i\omega) \quad , \tag{2.130}$$

separating the transverse and longitudinal parts and evaluation of the Fourier-Laplace transform yields the two equations

$$i\omega\boldsymbol{J}^{\mathrm{p,t}}(\boldsymbol{k},i\omega) - \boldsymbol{J}^{\mathrm{p,t}}(\boldsymbol{k},0) = -\frac{\eta(\boldsymbol{k},i\omega)}{\rho_{\mathrm{m}}}\,\boldsymbol{k}^{2}\boldsymbol{J}^{\mathrm{p,t}}(\boldsymbol{k},i\omega) \tag{2.131}$$

and

$$i\omega\boldsymbol{J}^{\mathrm{p,l}}(\boldsymbol{k},i\omega) - \boldsymbol{J}^{\mathrm{p,l}}(\boldsymbol{k},0) = -\frac{\eta_{\mathrm{l}}(\boldsymbol{k},i\omega)}{\rho_{\mathrm{m}}}\,\boldsymbol{k}^{2}\boldsymbol{J}^{\mathrm{p,l}}(\boldsymbol{k},i\omega) \quad . \tag{2.132}$$

In the next step, Onsager's regression hypothesis is applied. The regression hypothesis provides a connection between the macroscopic transport coefficients and the temporal evolution of the microscopic fluctuations of the corresponding thermodynamic fluxes. It states that the microscopic fluctuations of the thermodynamic fluxes decay on the average according to the macroscopic transport relations. The average decay of the thermodynamic fluxes is measured by time-correlation functions. First, Eq. (2.131) is multiplied by $J^{\mathrm{p,t}}(-\boldsymbol{k},0)$ and Eq. (2.132) by $J^{\mathrm{p,l}}(-\boldsymbol{k},0)$. Then, autocorrelation functions are formed by taking the ensemble average over sections of the phase space trajectory of the system on both sides of the two equations. Introducing the abbreviations

$$C^{\mathrm{p,t}}(\boldsymbol{k},i\omega) = \langle \boldsymbol{J}^{\mathrm{p,t}}(-\boldsymbol{k},0)\cdot\boldsymbol{J}^{\mathrm{p,t}}(\boldsymbol{k},i\omega)\rangle \tag{2.133}$$

and

$$C^{\mathrm{p,l}}(\boldsymbol{k},i\omega) = \langle \boldsymbol{J}^{\mathrm{p,l}}(-\boldsymbol{k},0)\cdot\boldsymbol{J}^{\mathrm{p,l}}(\boldsymbol{k},i\omega)\rangle \tag{2.134}$$

for the wave vector and frequency dependent transverse and longitudinal momentum density autocorrelation functions yields

$$i\omega C^{\mathrm{p,t}}(\boldsymbol{k},i\omega) - C^{\mathrm{p,t}}(\boldsymbol{k},0) = -\frac{\boldsymbol{k}^{2}}{\rho_{\mathrm{m}}}\eta(\boldsymbol{k},i\omega)C^{\mathrm{p,t}}(\boldsymbol{k},i\omega) \tag{2.135}$$

and

$$i\omega C^{\mathrm{p,l}}(\boldsymbol{k}, i\omega) - C^{\mathrm{p,l}}(\boldsymbol{k}, 0) = -\frac{\boldsymbol{k}^2}{\rho_{\mathrm{m}}} \eta_{\mathrm{l}}(\boldsymbol{k}, i\omega) C^{\mathrm{p,l}}(\boldsymbol{k}, i\omega) \quad . \tag{2.136}$$

In order to establish a relation between the two transport coefficients and their corresponding fluxes, the momentum density autocorrelation functions must be related to correlation functions of the elements of the viscous pressure tensor. To identify which elements of the pressure tensor contribute to transverse and which to longitudinal momentum transport, the definitions of the transverse and longitudinal momentum density vector are inserted into the spatial Fourier transformed form of the linearized momentum balance, Eq. (2.31), and the vector and tensor products are evaluated:

$$\frac{1}{\boldsymbol{k}^2} \begin{pmatrix} k_{\mathrm{x}} \\ k_{\mathrm{y}} \\ k_{\mathrm{z}} \end{pmatrix} (\boldsymbol{k} \cdot \dot{\boldsymbol{J}}^{\mathrm{p}}) - \frac{1}{\boldsymbol{k}^2} \begin{pmatrix} k_{\mathrm{y}}(k_{\mathrm{x}}\dot{J}_{\mathrm{y}}^{\mathrm{p}} - k_{\mathrm{y}}\dot{J}_{\mathrm{x}}^{\mathrm{p}}) + k_{\mathrm{z}}(k_{\mathrm{x}}\dot{J}_{\mathrm{z}}^{\mathrm{p}} - k_{\mathrm{z}}\dot{J}_{\mathrm{x}}^{\mathrm{p}}) \\ k_{\mathrm{x}}(k_{\mathrm{y}}\dot{J}_{\mathrm{x}}^{\mathrm{p}} - k_{\mathrm{x}}\dot{J}_{\mathrm{y}}^{\mathrm{p}}) + k_{\mathrm{z}}(k_{\mathrm{y}}\dot{J}_{\mathrm{z}}^{\mathrm{p}} - k_{\mathrm{z}}\dot{J}_{\mathrm{y}}^{\mathrm{p}}) \\ k_{\mathrm{x}}(k_{\mathrm{z}}\dot{J}_{\mathrm{x}}^{\mathrm{p}} - k_{\mathrm{x}}\dot{J}_{\mathrm{z}}^{\mathrm{p}}) + k_{\mathrm{y}}(k_{\mathrm{z}}\dot{J}_{\mathrm{y}}^{\mathrm{p}} - k_{\mathrm{y}}\dot{J}_{\mathrm{z}}^{\mathrm{p}}) \end{pmatrix} =$$

$$i \begin{pmatrix} k_{\mathrm{x}}\Pi_{\mathrm{xx}} + k_{\mathrm{y}}\Pi_{\mathrm{yx}} + k_{\mathrm{z}}\Pi_{\mathrm{zx}} \\ k_{\mathrm{x}}\Pi_{\mathrm{xy}} + k_{\mathrm{y}}\Pi_{\mathrm{yy}} + k_{\mathrm{z}}\Pi_{\mathrm{zy}} \\ k_{\mathrm{x}}\Pi_{\mathrm{xz}} + k_{\mathrm{y}}\Pi_{\mathrm{yz}} + k_{\mathrm{z}}\Pi_{\mathrm{zz}} \end{pmatrix} \quad . \tag{2.137}$$

A comparison of the coefficients yields that

$$\dot{\boldsymbol{J}}^{\mathrm{p,t}} = i \begin{pmatrix} k_{\mathrm{y}}\Pi_{\mathrm{yx}} + k_{\mathrm{z}}\Pi_{\mathrm{zx}} \\ k_{\mathrm{x}}\Pi_{\mathrm{xy}} + k_{\mathrm{z}}\Pi_{\mathrm{zy}} \\ k_{\mathrm{x}}\Pi_{\mathrm{xz}} + k_{\mathrm{y}}\Pi_{\mathrm{yz}} \end{pmatrix} \tag{2.138}$$

and

$$\dot{\boldsymbol{J}}^{\mathrm{p,l}} = i \begin{pmatrix} k_{\mathrm{x}}\Pi_{\mathrm{xx}} \\ k_{\mathrm{y}}\Pi_{\mathrm{yy}} \\ k_{\mathrm{z}}\Pi_{\mathrm{zz}} \end{pmatrix} \quad . \tag{2.139}$$

With Eq. (2.124) and the second derivative of autocorrelation functions, Eq. (2.69),

the relation for the autocorrelation function of the transverse momentum density

$$
\begin{aligned}
\frac{\partial^2}{\partial t^2} C^{\mathrm{p,t}}(\boldsymbol{k}, t) &= \langle \boldsymbol{J}^{\mathrm{p,t}}(-\boldsymbol{k}, 0) \cdot \ddot{\boldsymbol{J}}^{\mathrm{p,t}}(\boldsymbol{k}, t) \rangle \\
&= -\langle \dot{\boldsymbol{J}}^{\mathrm{p,t}}(-\boldsymbol{k}, 0) \cdot \dot{\boldsymbol{J}}^{\mathrm{p,t}}(\boldsymbol{k}, t) \rangle \\
&= -k_{\mathrm{y}}^2 \langle \Pi_{\mathrm{yx}}(-\boldsymbol{k}, 0)\, \Pi_{\mathrm{yx}}(\boldsymbol{k}, t) \rangle - k_{\mathrm{z}}^2 \langle \Pi_{\mathrm{zx}}(-\boldsymbol{k}, 0)\, \Pi_{\mathrm{zx}}(\boldsymbol{k}, t) \rangle \\
&\quad - k_{\mathrm{x}}^2 \langle \Pi_{\mathrm{xy}}(-\boldsymbol{k}, 0)\, \Pi_{\mathrm{xy}}(\boldsymbol{k}, t) \rangle - k_{\mathrm{z}}^2 \langle \Pi_{\mathrm{zy}}(-\boldsymbol{k}, 0)\, \Pi_{\mathrm{zy}}(\boldsymbol{k}, t) \rangle \\
&\quad - k_{\mathrm{x}}^2 \langle \Pi_{\mathrm{xz}}(-\boldsymbol{k}, 0)\, \Pi_{\mathrm{xz}}(\boldsymbol{k}, t) \rangle - k_{\mathrm{y}}^2 \langle \Pi_{\mathrm{yz}}(-\boldsymbol{k}, 0)\, \Pi_{\mathrm{yz}}(\boldsymbol{k}, t) \rangle \\
&= -k_{\mathrm{y}}^2 N_{\mathrm{yx}}^{\Pi,\mathrm{t}}(\boldsymbol{k}, t) - k_{\mathrm{z}}^2 N_{\mathrm{zx}}^{\Pi,\mathrm{t}}(\boldsymbol{k}, t) - k_{\mathrm{x}}^2 N_{\mathrm{xy}}^{\Pi,\mathrm{t}}(\boldsymbol{k}, t) \\
&\quad - k_{\mathrm{z}}^2 N_{\mathrm{zy}}^{\Pi,\mathrm{t}}(\boldsymbol{k}, t) - k_{\mathrm{x}}^2 N_{\mathrm{xz}}^{\Pi,\mathrm{t}}(\boldsymbol{k}, t) - k_{\mathrm{y}}^2 N_{\mathrm{yz}}^{\Pi,\mathrm{t}}(\boldsymbol{k}, t)
\end{aligned}
\tag{2.140}
$$

is established. Correlations between different off-diagonal tensor elements vanish since the off-diagonal elements are independent. The autocorrelation functions of the tensor elements are denoted by $N_{\alpha\beta}^{\Pi,\mathrm{t}}$. In the following,

$$
\begin{aligned}
N^{\Pi,\mathrm{t}}(\boldsymbol{k}, t) &= k_{\mathrm{y}}^2 N_{\mathrm{yx}}^{\Pi,\mathrm{t}}(\boldsymbol{k}, t) + k_{\mathrm{z}}^2 N_{\mathrm{zx}}^{\Pi,\mathrm{t}}(\boldsymbol{k}, t) + k_{\mathrm{x}}^2 N_{\mathrm{xy}}^{\Pi,\mathrm{t}}(\boldsymbol{k}, t) \\
&\quad + k_{\mathrm{z}}^2 N_{\mathrm{zy}}^{\Pi,\mathrm{t}}(\boldsymbol{k}, t) + k_{\mathrm{x}}^2 N_{\mathrm{xz}}^{\Pi,\mathrm{t}}(\boldsymbol{k}, t) + k_{\mathrm{y}}^2 N_{\mathrm{yz}}^{\Pi,\mathrm{t}}(\boldsymbol{k}, t)
\end{aligned}
\tag{2.141}
$$

is used as an abbreviation for the sum of the autocorrelation functions weighted with squares of components of the wave vector. In the frequency domain, Eq. (2.140) becomes

$$
\omega^2 C^{\mathrm{p,t}}(\boldsymbol{k}, i\omega) + i\omega C^{\mathrm{p,t}}(\boldsymbol{k}, 0) = N^{\Pi,\mathrm{t}}(\boldsymbol{k}, i\omega) \quad .
\tag{2.142}
$$

Solving for $C^{\mathrm{p,t}}(\boldsymbol{k}, i\omega)$ yields

$$
C^{\mathrm{p,t}}(\boldsymbol{k}, i\omega) = \frac{1}{\omega^2} N^{\Pi,\mathrm{t}}(\boldsymbol{k}, i\omega) - \frac{i}{\omega} C^{\mathrm{p,t}}(\boldsymbol{k}, 0) \quad .
\tag{2.143}
$$

When this result is inserted into Eq. (2.135) and the resulting equation is solved for $\eta(\boldsymbol{k}, i\omega)$, the final expression for the frequency and wave vector dependent viscosity is obtained as

$$
\eta(\boldsymbol{k}, i\omega) = \frac{\rho_{\mathrm{m}} \dfrac{N^{\Pi,\mathrm{t}}(\boldsymbol{k}, i\omega)}{k^2}}{C^{\mathrm{p,t}}(\boldsymbol{k}, 0) - \dfrac{1}{i\omega} N^{\Pi,\mathrm{t}}(\boldsymbol{k}, i\omega)} \quad .
\tag{2.144}
$$

The macroscopic viscosity is given by the zero wave vector and zero frequency limit of the frequency and wave vector dependent viscosity. The zero wave vector limit is accompanied by the limits $V \to \infty$ and $N \to \infty$, while the density remains constant

because the zero wave vector limit implies that the volume of the system becomes
infinitely large.

In the limiting process, the zero wave vector limit must be taken before the zero
frequency limit because at zero frequency the autocorrelation function of an off-
diagonal element of the viscous pressure tensor element is a discontinuous function
of the wave vector [49, p. 89]. The autocorrelation function is non-zero at zero
frequency and zero wave vector, but identically zero at zero frequency and non-zero
wave vector. This behaviour is schematically illustrated in Figure 2.5. It arises
because there are no fluctuations of the the strain rate tensor at zero wave vector.
At zero wave vector, the strain rate tensor is only non-zero if boundary conditions
are imposed on the system. The frequency and wave vector dependent viscosity,
however, is a continuous function of both frequency and wave vector everywhere.
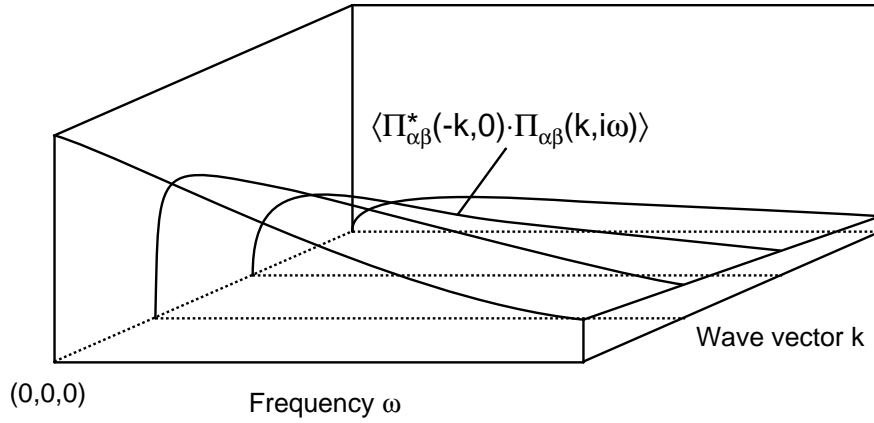
Figure 2.5. The autocorrelation function of an off-diagonal element of the viscous pres-
sure tensor as a function of frequency and wave vector [49].

The zero wave vector limit of Eq. (2.144) leads to the frequency dependent vis-
cosity:

$$
\eta(i\omega) = \frac{\rho_{\mathrm{m}}}{C^{\mathrm{p,t}}(0,0)} \left(\frac{1}{3}\, N_{\mathrm{yx}}^{\varPi,\mathrm{t}}(i\omega) + \frac{1}{3}\, N_{\mathrm{zx}}^{\varPi,\mathrm{t}}(i\omega) + \frac{1}{3}\, N_{\mathrm{xy}}^{\varPi,\mathrm{t}}(i\omega) \right.
$$
$$
\left. + \frac{1}{3}\, N_{\mathrm{zy}}^{\varPi,\mathrm{t}}(i\omega) + \frac{1}{3}\, N_{\mathrm{xz}}^{\varPi,\mathrm{t}}(i\omega) + \frac{1}{3}\, N_{\mathrm{yz}}^{\varPi,\mathrm{t}}(i\omega) \right) \quad . \quad (2.145)
$$

In the limiting process, the second term in the denominator of Eq. (2.144) vanishes
since its terms are proportional to squares of wave vector components. The numer-
ical factors 1/3 result from the zero wave vector limits of the coefficients $k_\alpha^2/\boldsymbol{k}^2$ of

the correlation functions of the viscous pressure tensor elements. For example,

$$\lim_{\boldsymbol{k}\to 0} \frac{k_{\mathrm{x}}^2}{\boldsymbol{k}^2} = \lim_{\boldsymbol{k}\to 0} \frac{k_{\mathrm{x}}^2}{k_{\mathrm{x}}^2 + k_{\mathrm{y}}^2 + k_{\mathrm{z}}^2} = \frac{1}{3} \quad . \tag{2.146}$$

The initial value of the transverse momentum density autocorrelation function at zero wavevector, $C^{\mathrm{p,t}}(0,0)$, can be related to the thermodynamic temperature. By using the definition of the transverse momentum density vector, Eq. (2.126), the contribution of an arbitrary component of the vector, for example the x-component

$$J_{\mathrm{x}}^{\mathrm{p,t}}(\boldsymbol{k},0) = -\frac{1}{\boldsymbol{k}^2} \left\{ -(k_{\mathrm{y}}^2 + k_{\mathrm{z}}^2)J_{\mathrm{x}}^{\mathrm{p}}(\boldsymbol{k},0) + k_{\mathrm{x}}k_{\mathrm{y}}J_{\mathrm{y}}^{\mathrm{p}}(\boldsymbol{k},0) + k_{\mathrm{x}}k_{\mathrm{z}}J_{\mathrm{z}}^{\mathrm{p}}(\boldsymbol{k},0) \right\} \ , \tag{2.147}$$

to the zero wave vector limit of the initial value of the transverse momentum density autocorrelation function is evaluated as

$$\langle J_{\mathrm{x}}^{\mathrm{p,t}}(-\boldsymbol{k},0)J_{\mathrm{x}}^{\mathrm{p,t}}(\boldsymbol{k},0)\rangle = \frac{1}{\boldsymbol{k}^4} \langle (k_{\mathrm{y}}^2 + k_{\mathrm{z}}^2)^2 J_{\mathrm{x}}^{\mathrm{p}}(-\boldsymbol{k},0)J_{\mathrm{x}}^{\mathrm{p}}(\boldsymbol{k},0)$$
$$+ k_{\mathrm{x}}^2 k_{\mathrm{y}}^2 J_{\mathrm{y}}^{\mathrm{p}}(-\boldsymbol{k},0)J_{\mathrm{y}}^{\mathrm{p}}(\boldsymbol{k},0) + k_{\mathrm{x}}^2 k_{\mathrm{z}}^2 J_{\mathrm{z}}^{\mathrm{p}}(-\boldsymbol{k},0)J_{\mathrm{z}}^{\mathrm{p}}(\boldsymbol{k},0)\rangle \quad . \tag{2.148}$$

Cross-correlations between different vector components vanish since components along different spatial directions are independent. Inserting the molecular expression for the momentum density vector, Eq. (2.82), yields

$$\langle J_{\mathrm{x}}^{\mathrm{p,t}}(-\boldsymbol{k},0)J_{\mathrm{x}}^{\mathrm{p,t}}(\boldsymbol{k},0)\rangle =$$

$$\frac{1}{\boldsymbol{k}^4} \left\langle (k_{\mathrm{y}}^4 + 2k_{\mathrm{y}}^2 k_{\mathrm{z}}^2 + k_{\mathrm{z}}^4) \left[\frac{1}{\delta V}\sum_{i=1}^{N} mv_{\mathrm{x,i}}e^{-i\boldsymbol{k}\cdot\boldsymbol{r}_{\mathrm{i}}} \right] \left[\frac{1}{\delta V}\sum_{i=1}^{N} mv_{\mathrm{x,i}}e^{i\boldsymbol{k}\cdot\boldsymbol{r}_{\mathrm{i}}} \right] \right.$$

$$+ k_{\mathrm{x}}^2 k_{\mathrm{y}}^2 \left[\frac{1}{\delta V}\sum_{i=1}^{N} mv_{\mathrm{y,i}}e^{-i\boldsymbol{k}\cdot\boldsymbol{r}_{\mathrm{i}}} \right] \left[\frac{1}{\delta V}\sum_{i=1}^{N} mv_{\mathrm{y,i}}e^{i\boldsymbol{k}\cdot\boldsymbol{r}_{\mathrm{i}}} \right]$$

$$\left. + k_{\mathrm{x}}^2 k_{\mathrm{z}}^2 \left[\frac{1}{\delta V}\sum_{i=1}^{N} mv_{\mathrm{z,i}}e^{-i\boldsymbol{k}\cdot\boldsymbol{r}_{\mathrm{i}}} \right] \left[\frac{1}{\delta V}\sum_{i=1}^{N} mv_{\mathrm{z,i}}e^{i\boldsymbol{k}\cdot\boldsymbol{r}_{\mathrm{i}}} \right] \right\rangle \quad . \tag{2.149}$$

By taking advantage of the fact that instantaneous correlations between different particles vanish, the zero wave vector limit of Eq. (2.149) becomes

$$\langle [J_{\mathrm{x}}^{\mathrm{p,t}}(0,0)]^2 \rangle = \left\langle \frac{1}{V^2}\sum_{i=1}^{N} \left(\frac{4}{9}m^2 v_{\mathrm{x,i}}^2 + \frac{1}{9}m^2 v_{\mathrm{y,i}}^2 + \frac{1}{9}m^2 v_{\mathrm{z,i}}^2 \right) \right\rangle \quad . \tag{2.150}$$

According to the equipartition theorem [29, p. 375][3], the contribution of an arbitrary translational degree of freedom to the kinetic energy of the system is given by

$$\sum_{i=1}^{N} \frac{1}{2}mv_{\alpha,\mathrm{i}}^2 = \frac{1}{2}NkT \quad . \tag{2.151}$$

---

[3] The reduction of the degrees of freedom by the mechanical constraints imposed on the system is neglected here.

Thus,

$$\langle [J_{\mathrm{x}}^{\mathrm{p,t}}(0,0)]^2 \rangle = \frac{2}{3} \frac{NmkT}{V^2} \quad . \tag{2.152}$$

As the evaluation of the contributions of the y- and z-component yields the same results, the initial value of the transverse momentum density autocorrelation function at zero wave vector is obtained as

$$C^{\mathrm{p,t}}(0,0) = 2 \frac{NmkT}{V^2} \quad . \tag{2.153}$$

When using this result and the symmetry of the viscous pressure tensor and explicitly writing the Fourier-Laplace transform, Eq. (2.145) becomes

$$\eta(i\omega) = \frac{V}{3kT} \int_0^\infty \langle \Pi_{\mathrm{xy}}(0)\Pi_{\mathrm{xy}}(t) + \Pi_{\mathrm{xz}}(0)\Pi_{\mathrm{xz}}(t) + \Pi_{\mathrm{yz}}(0)\Pi_{\mathrm{yz}}(t) \rangle \, e^{-i\omega t} \, \mathrm{d}t \quad . \tag{2.154}$$

The Green-Kubo integral representation of the viscosity is found by taking the zero frequency limit of Eq. (2.154) as

$$\begin{aligned}
\eta &= \frac{V}{3kT} \int_0^\infty \langle \Pi_{\mathrm{xy}}(0)\Pi_{\mathrm{xy}}(t) + \Pi_{\mathrm{xz}}(0)\Pi_{\mathrm{xz}}(t) + \Pi_{\mathrm{yz}}(0)\Pi_{\mathrm{yz}}(t) \rangle \, \mathrm{d}t \\
&= \frac{V}{3kT} \int_0^\infty \langle \tau_{\mathrm{xy}}(0)\,\tau_{\mathrm{xy}}(t) + \tau_{\mathrm{xz}}(0)\,\tau_{\mathrm{xz}}(t) + \tau_{\mathrm{yz}}(0)\,\tau_{\mathrm{yz}}(t) \rangle \, \mathrm{d}t \quad .
\end{aligned} \tag{2.155}$$

Hence, the viscosity is related to the time integral of the autocorrelation functions of off-diagonal elements of the viscous pressure tensor or, equivalently, the stress tensor. Additionally, the autocorrelation function is averaged over all independent off-diagonal tensor elements.

The derivation of the Green-Kubo formula for the longitudinal viscosity proceeds similarly. By using Eq. (2.139), the longitudinal momentum density autocorrelation function is related to the autocorrelation functions of the diagonal elements of the viscous pressure tensor:

$$\begin{aligned}
\frac{\partial^2}{\partial t^2} C^{\mathrm{p,l}}(\boldsymbol{k},t) &= - \langle \dot{\boldsymbol{J}}^{\mathrm{p,l}}(-\boldsymbol{k},0) \cdot \dot{\boldsymbol{J}}^{\mathrm{p,l}}(\boldsymbol{k},t) \rangle \\
&= -k_{\mathrm{x}}^2 \langle \Pi_{\mathrm{xx}}(0)\,\Pi_{\mathrm{xx}}(t) \rangle - k_{\mathrm{y}}^2 \langle \Pi_{\mathrm{yy}}(0)\,\Pi_{\mathrm{yy}}(t) \rangle - k_{\mathrm{z}}^2 \langle \Pi_{\mathrm{zz}}(0)\,\Pi_{\mathrm{zz}}(t) \rangle \\
&= -k_{\mathrm{x}}^2 N_{\mathrm{xx}}^{\Pi,\mathrm{l}}(\boldsymbol{k},t) - k_{\mathrm{y}}^2 N_{\mathrm{yy}}^{\Pi,\mathrm{l}}(\boldsymbol{k},t) - k_{\mathrm{z}}^2 N_{\mathrm{zz}}^{\Pi,\mathrm{l}}(\boldsymbol{k},t) \\
&= -N^{\Pi,\mathrm{l}}(\boldsymbol{k},t) \quad ,
\end{aligned} \tag{2.156}$$

which becomes in the frequency domain

$$\omega^2 C^{\mathrm{p,l}}(\boldsymbol{k}, i\omega) + i\omega C^{\mathrm{p,l}}(\boldsymbol{k}, 0) = N^{\varPi,\mathrm{l}}(\boldsymbol{k}, i\omega) \quad . \tag{2.157}$$

The quantity $N^{\varPi,\mathrm{l}}$ is introduced as an abbreviation for the sum of the autocorrelation functions weighted with squares of components of the wave vector. Solving for $C^{\mathrm{p,l}}(\boldsymbol{k}, i\omega)$, inserting the result into Eq. (2.136) and solving the resulting equation for $\eta_{\mathrm{l}}(\boldsymbol{k}, i\omega)$ yields

$$\eta_{\mathrm{l}}(\boldsymbol{k}, i\omega) = \frac{\rho_{\mathrm{m}} \dfrac{N^{\varPi,\mathrm{l}}(\boldsymbol{k}, i\omega)}{\boldsymbol{k}^2}}{C^{\mathrm{p,l}}(\boldsymbol{k}, 0) - \dfrac{1}{i\omega} N^{\varPi,\mathrm{l}}(\boldsymbol{k}, i\omega)} \quad . \tag{2.158}$$

The zero wavevector limit of Eq. (2.158) yields the frequency dependent longitudinal viscosity

$$\begin{aligned}
\eta_{\mathrm{l}}(i\omega) &= \frac{\rho_{\mathrm{m}}}{C^{\mathrm{p,l}}(0, 0)} \left[\frac{1}{3} N^{\varPi,\mathrm{l}}_{\mathrm{xx}}(i\omega) + \frac{1}{3} N^{\varPi,\mathrm{l}}_{\mathrm{yy}}(i\omega) + \frac{1}{3} N^{\varPi,\mathrm{l}}_{\mathrm{zz}}(i\omega) \right] \\
&= \frac{\rho_{\mathrm{m}}}{C^{\mathrm{p,l}}(0, 0)} \frac{1}{3} \left\langle \mathrm{tr}(\boldsymbol{\varPi}(0)\boldsymbol{\varPi}(i\omega)) \right\rangle \quad .
\end{aligned} \tag{2.159}$$

The initial value of the longitudinal momentum density autocorrelation function $C^{\mathrm{p,l}}(0, 0)$ can be evaluated by the same procedure as described above in detail for the transverse momentum density autocorrelation function. A lengthy calculation yields

$$C^{\mathrm{p,l}}(0, 0) = \frac{NmkT}{V^2} \quad . \tag{2.160}$$

The longitudinal viscosity is found as the zero frequency limit of

$$\eta_{\mathrm{l}} = \frac{V}{3kT} \int_0^\infty \left\langle \mathrm{tr}(\boldsymbol{\varPi}(0)\boldsymbol{\varPi}(t)) \right\rangle e^{-i\omega t} \, \mathrm{d}t \quad , \tag{2.161}$$

where the Fourier-Laplace transform is explicitly shown. The result is

$$\eta_{\mathrm{l}} = \frac{V}{3kT} \int_0^\infty \left\langle \mathrm{tr}(\boldsymbol{\varPi}(0)\boldsymbol{\varPi}(t)) \right\rangle \, \mathrm{d}t \quad . \tag{2.162}$$

To obtain an expression for the bulk viscosity rather than for the longitudinal viscosity, Eq. (2.162) must be separated into two equations for both the viscosity and bulk viscosity. A detailed description of the rigorous procedure leading to this

separation was outlined by Steele [203]. Since this part of the derivation is very involved, it is omitted here. Instead, a simple argument is used to extract the expression for the bulk viscosity from Eq. (2.162). The integrand in the Green-Kubo formula for the viscosity is the correlation function of the thermodynamic fluxes associated with transverse momentum transport, the off-diagonal elements of the viscous pressure tensor. As the hydrodynamic balance equations and the phenomenological transport relation have the same structure for every transport coefficient, every Green-Kubo formula has this form. Hence, a phenomenological coefficient of an isotropic fluid L_{ij} is in general determined by

$$L_{ij} = \frac{V}{k} \int\limits_0^\infty \langle J^j(0) J^i(t) \rangle \, \mathrm{d}t \quad , \tag{2.163}$$

where J^i and J^j represent the thermodynamic fluxes corresponding to the coefficient L_{ij}. If the fluxes have more than one independent component, time-correlation functions can be formed as averages of the time-correlation functions of the independent flux components.

Hence, the integrand in the expression for the bulk viscosity is the correlation function of the thermodynamic flux associated with the bulk viscosity. With Eq. (2.50), it is identified as the trace of the viscous pressure tensor divided by three. Thus, the Green-Kubo formula for the bulk viscosity reads

$$\eta_b = \frac{1}{9} \frac{V}{kT} \int\limits_0^\infty \langle \mathrm{tr}(\boldsymbol{\Pi}(0)) \mathrm{tr}(\boldsymbol{\Pi}(t)) \rangle \, \mathrm{d}t = \frac{V}{kT} \int\limits_0^\infty \langle \delta p(0) \delta p(t) \rangle \, \mathrm{d}t \quad . \tag{2.164}$$

Note that cross-correlations between different diagonal elements of the pressure tensor do not vanish. The quantity δp is the pressure fluctuation, i.e. the deviation of the instantaneous pressure from the thermodynamic pressure.

An additional expression for the viscosity is found by using the results for the bulk viscosity and longitudinal viscosity:

$$\eta = \frac{3}{4}(\eta_l - \eta_b) = \frac{V}{12kT} \int\limits_0^\infty \langle 3\,\mathrm{tr}(\boldsymbol{\Pi}(0)\boldsymbol{\Pi}(t)) - \mathrm{tr}(\boldsymbol{\Pi}(0))\mathrm{tr}(\boldsymbol{\Pi}(t)) \rangle \, \mathrm{d}t \quad . \tag{2.165}$$

This Green-Kubo formula for the viscosity supplements the expression derived earlier in this section. As longitudinal and transverse momentum flux are completely decoupled, it can be used as an alternative to Eq. (2.155) to calculate the viscosity. However, it is surprisingly little applied in molecular dynamics simulations to determine the viscosity.

The Green-Kubo formulas for the thermal conductivity and the self-diffusion coefficient are found analogously. Combining the relation of the thermal conductivity to its corresponding phenomenological coefficient, Eq. (2.42), and the general Green-Kubo formula, Eq. (2.163), yields

$$\lambda = \frac{V}{3kT^2} \int\limits_0^\infty \langle \boldsymbol{J}^{\mathrm{q}}(0) \cdot \boldsymbol{J}^{\mathrm{q}}(t) \rangle \, \mathrm{d}t \quad . \tag{2.166}$$

Similarly one finds for the self-diffusion coefficient

$$D = \frac{1}{3N} \sum_{i=1}^N \int\limits_0^\infty \langle \boldsymbol{v}_{\mathrm{i}}(t) \cdot \boldsymbol{v}_{\mathrm{i}}(0) \rangle \mathrm{d}t \quad . \tag{2.167}$$

Since all particles in a pure fluid have the same properties, every particle can be chosen as the tagged particle. Thus, the statistics can be improved by averaging over all N particles in the system. The self-diffusion coefficient differs from the hydrodynamic transport coefficients of pure fluids. Viscosity, bulk viscosity and thermal conductivity are collective transport coefficients. They are determined by the collective time-dependent behaviour of many molecules. In contrast, the self-diffusion coefficient is a single particle property and is determined by correlations of the motion of single particles. These results complete the derivation of the Green-Kubo formulas for the hydrodynamic transport coefficients.

Beside the method outlined in this section, other procedures are described in literature to derive the Green-Kubo integral formulas for the hydrodynamic transport coefficients. After the pioneering works of Green [58, 59, 60] and Kubo et al. [111, 112], Mori [155, 156, 157], McLennan [137, 138, 140], Kadanoff and Martin [104], Jackson and Mazur [101], Luttinger [131] and Zwanzig [221] among others presented derivations of the formulas. A summary of these methods and an exhaustive bibliography on this subject was provided in a review article by Zwanzig [222].

2.5.4   Generalized Einstein Relations

In this section, alternative expressions for the transport coefficients are derived. The resulting expressions are termed Einstein relations since Einstein first derived such a relation for the self-diffusion coefficient [37, 38]. It will be shown that the Einstein relations and Green-Kubo integral formulas for the transport coefficients are equivalent. The derivation is first carried out for an arbitrary phase variable.

Specific expressions for the transport coefficients are obtained afterwards in a simple way from the general result.

The general derivation [65, 69, 77, 222] starts by expressing the generalized displacement of an arbitrary phase variable

$$A(t) - A(0) = \int_0^t \dot{A}(t')\mathrm{d}t' \tag{2.168}$$

by the time integral of its derivative with respect to time. Squaring this equation and taking the ensemble average yields

$$\langle [A(t) - A(0)]^2 \rangle = \int_0^t \int_0^t \langle \dot{A}(t')\dot{A}(t'') \rangle \, \mathrm{d}t'' \, \mathrm{d}t' \quad . \tag{2.169}$$

In the next step, the double integral is rewritten. Since the integrand is symmetric with respect to t' and t'', the quadratic area of integration in the t',t''-plane can be changed into a triangular area with half of the size as shown in Figure 2.6.
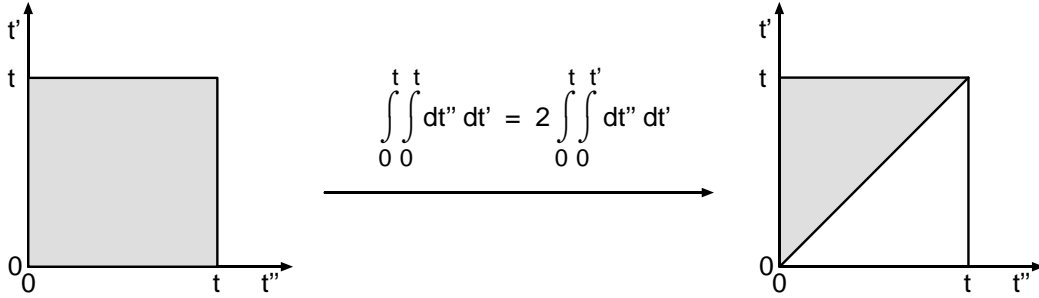
Figure 2.6. Illustration of changing the integration area in Eq. (2.169) from a square to a triangle in the t',t''-plane.

This transformation leads to

$$\langle [A(t) - A(0)]^2 \rangle = 2 \int_0^t \int_0^{t'} \langle \dot{A}(t')\dot{A}(t'') \rangle \, \mathrm{d}t'' \, \mathrm{d}t' \quad . \tag{2.170}$$

Since time-correlation functions are invariant to the shift of time origins, application of Eq. (2.59) yields

$$\langle [A(t) - A(0)]^2 \rangle = 2 \int_0^t \int_0^{t'} \langle \dot{A}(t' - t'')\dot{A}(0) \rangle \, \mathrm{d}t'' \, \mathrm{d}t' \quad . \tag{2.171}$$

Next, the inner integral is rewritten by the substitution $\tau = t' - t''$:

$$\langle [A(t) - A(0)]^2 \rangle = -2 \int\limits_0^t \int\limits_{t'}^0 \langle \dot{A}(\tau)\dot{A}(0) \rangle \, \mathrm{d}\tau \, \mathrm{d}t' \quad . \tag{2.172}$$

Reversing the limits of integration changes the sign of the integral:

$$\langle [A(t) - A(0)]^2 \rangle = 2 \int\limits_0^t \int\limits_0^{t'} \langle \dot{A}(0)\dot{A}(\tau) \rangle \, \mathrm{d}\tau \, \mathrm{d}t' \quad . \tag{2.173}$$

The outer integral is evaluated by integration by parts:

$$
\int\limits_0^t 1 \cdot \left[\int\limits_0^{t'} \langle \dot{A}(0)\dot{A}(\tau) \rangle \mathrm{d}\tau \right] \mathrm{d}t' = t' \cdot \int\limits_0^{t'} \langle \dot{A}(0)\dot{A}(\tau) \rangle \, \mathrm{d}\tau \Bigg|_0^t - \int\limits_0^t t' \cdot \langle \dot{A}(0)\dot{A}(t') \rangle \, \mathrm{d}t'
$$
$$
= \int\limits_0^t t \langle \dot{A}(0)\dot{A}(\tau) \rangle \mathrm{d}\tau - \int\limits_0^t \tau \langle \dot{A}(0)\dot{A}(\tau) \rangle \mathrm{d}\tau
$$
$$
= \int\limits_0^t (t - \tau)\langle \dot{A}(0)\dot{A}(\tau) \rangle \, \mathrm{d}\tau \quad . \tag{2.174}
$$

Inserting the result of the integration into Eq. (2.173) yields

$$\langle [A(t) - A(0)]^2 \rangle = 2 \int\limits_0^t \langle \dot{A}(0)\dot{A}(\tau) \rangle (t - \tau) \mathrm{d}\tau \quad . \tag{2.175}$$

The final expression is found by dividing by $2t$

$$\frac{1}{2t} \langle [A(t) - A(0)]^2 \rangle = \int\limits_0^t \langle \dot{A}(0)\dot{A}(\tau) \rangle \left(1 - \frac{\tau}{t}\right) \mathrm{d}\tau \quad . \tag{2.176}$$

and taking the long time limit, $t \to \infty$,

$$\lim_{t \to \infty} \frac{1}{2t} \langle [A(t) - A(0)]^2 \rangle = \int\limits_0^\infty \langle \dot{A}(0)\dot{A}(\tau) \rangle \mathrm{d}\tau \quad . \tag{2.177}$$

An alternative version of Eq. (2.177), which is easier to use for the evaluation of transport coefficients, is obtained by applying the Leibnitz rule for differentiation of

an integral [1, p. 11] to Eq. (2.175) as suggested by Haile [65, problem 7.12]:

$$
\begin{aligned}
\frac{\mathrm{d}}{\mathrm{d}t} \langle [A(t) - A(0)]^2 \rangle &= 2 \frac{\mathrm{d}}{\mathrm{d}t} \int_0^t \langle \dot{A}(0) \dot{A}(\tau) \rangle \, (t - \tau) \, \mathrm{d}\tau \\
&= 2 \int_0^t \langle \dot{A}(0) \dot{A}(\tau) \rangle \frac{\partial}{\partial t} (t - \tau) \, \mathrm{d}\tau + 2 \langle \dot{A}(0) \dot{A}(t) \rangle \\
&= 2 \int_0^t \langle \dot{A}(0) \dot{A}(\tau) \rangle \, \mathrm{d}\tau + 2 \langle \dot{A}(0) \dot{A}(t) \rangle
\end{aligned}
\tag{2.178}
$$

Taking the long time limit,

$$
\lim_{t \to \infty} \frac{\mathrm{d}}{\mathrm{d}t} \langle [A(t) - A(0)]^2 \rangle = \int_0^\infty \langle \dot{A}(0) \dot{A}(\tau) \rangle \mathrm{d}\tau
\tag{2.179}
$$

is obtained. The last term in Eq. (2.178) vanishes in the long time limit if $\dot{A}$ represents a thermodynamic flux whose ensemble average is zero. This expression relates the slope of the mean-squared displacement of the phase variable A to the time integral of the time derivative $\dot{A}$ in the long time limit. The derivation of the general Einstein relations shows that the Green-Kubo integral formulas and Einstein relations are completely equivalent from a mathematical point of view. Hence, both types of expressions yield the same results for the transport coefficients. The connection between the Green-Kubo formulas and Einstein relations can be utilized when analyzing time-correlation functions and generalized mean-squared displacement functions, as will be shown in Section 3.3.1.

The specific expressions for the hydrodynamic transport coefficients viscosity, bulk viscosity and thermal conductivity were first reported by Helfand [77]. Generalized mean-squared displacement functions are obtained by integration of the corresponding molecular expressions for the thermodynamic fluxes according to Eq. (2.168). For example, the generalized displacement corresponding to momentum transport is found by integration of the molecular expression for the viscous pressure tensor, Eq. (2.114). When employing the identity [10]

$$
\frac{1}{2} \sum_{i=1}^N \sum_{\substack{j=1 \\ j \neq i}}^N \boldsymbol{r}_{\mathrm{ij}} \boldsymbol{F}_{\mathrm{ij}} = \sum_{i=1}^N \boldsymbol{r}_{\mathrm{i}} \boldsymbol{F}_{\mathrm{i}}
\tag{2.180}
$$

for a system with pairwise interacting particles, integration by parts of Eq. (2.114)

yields

$$\int\limits_{t_0}^{t} \left\{ \frac{1}{V} \sum_{i=1}^{N} (m\boldsymbol{v}_\mathrm{i}\boldsymbol{v}_\mathrm{i} + \boldsymbol{r}_\mathrm{i}\boldsymbol{F}_\mathrm{i}) - p\,\boldsymbol{I} \right\} \mathrm{d}t = \left[\frac{1}{V} \sum_{i=1}^{N} m\boldsymbol{r}_\mathrm{i}(t)\boldsymbol{v}_\mathrm{i}(t) - p\,t\,\boldsymbol{I} \right]_{t_0}^{t} . \quad (2.181)$$

Individual Einstein relations for viscosity, bulk viscosity and longitudinal viscosity are constructed from the elements of the displacement tensor that correspond to the elements of the viscous pressure tensor appearing in the correlation functions of the Green-Kubo formulas. The Green-Kubo integral formulas and generalized Einstein relations for the viscosities are summarized in Table 2.2. It is obvious that there is an additional Einstein relation for the viscosity corresponding to the Green-Kubo relation (2.165) derived in Section 2.5.3. This relation is obtained by inserting the Einstein relations for the longitudinal and bulk viscosity into the zero wave vector and zero frequency version of Eq. (2.130).

Similarly, the generalized displacement function corresponding to heat conduction is derived by integrating the molecular expression of the heat flux vector. First, the relation

$$\sum_{i=1}^{N} \boldsymbol{r}_\mathrm{i} \frac{\mathrm{d}e_\mathrm{i}}{\mathrm{d}t} = \sum_{i=1}^{N} \boldsymbol{r}_\mathrm{i} \frac{\mathrm{d}}{\mathrm{d}t} \left(\frac{1}{2}m\boldsymbol{v}_\mathrm{i}^2 + \frac{1}{2} \sum_{\substack{j=1 \\ j \neq i}}^{N} u(r_\mathrm{ij}) \right) = \frac{1}{2} \sum_{i=1}^{N} \sum_{\substack{j=1 \\ j \neq i}}^{N} (\boldsymbol{r}_\mathrm{ij}\boldsymbol{F}_\mathrm{ij}) \cdot \boldsymbol{v}_\mathrm{i} \quad (2.182)$$

is established by explicit calculation of the time derivative of the energy per particle e_i, which was introduced by Eq. (2.93). Then, an integration by parts of the molecular expression for the heat flux vector, Eq. (2.115), can easily be carried out and yields

$$\frac{1}{V} \int\limits_{t_0}^{t} \left\{ \sum_{i=1}^{N} e_\mathrm{i}\boldsymbol{v}_\mathrm{i} + \frac{1}{2} \sum_{i=1}^{N} \sum_{\substack{j=1 \\ j \neq i}}^{N} (\boldsymbol{r}_\mathrm{ij}\boldsymbol{F}_\mathrm{ij}) \cdot \boldsymbol{v}_\mathrm{i} \right\} \mathrm{d}t = \frac{1}{V} \left[\sum_{i=1}^{N} \boldsymbol{r}_\mathrm{i}(t)e_\mathrm{i}(t) \right]_{t_0}^{t} . \quad (2.183)$$

The Einstein relation and Green-Kubo formula for the thermal conductivity are also given in Table 2.2.

The generalized displacements are related to the temporal evolution of the centre of the transported quantity in the system. For instance, the thermal conductivity is related to the displacement of the centre of energy of the system, while the viscosity is related to the displacement of the centre of transverse momentum. It is expected that the generalized mean-squared displacement functions are linear functions of time in the long time limit.

Table 2.2. Green-Kubo integral formulas and Einstein relations for the hydrodynamic transport coefficients.

	Green-Kubo Integral	Einstein Relation
D	$\dfrac{1}{3N}\displaystyle\sum_{i=1}^{N}\int_{0}^{\infty}\langle \boldsymbol{v}_{\mathrm{i}}(t)\cdot\boldsymbol{v}_{\mathrm{i}}(0)\rangle\,\mathrm{d}t$	$\displaystyle\lim_{t\to\infty}\dfrac{1}{6N}\sum_{i=1}^{N}\dfrac{\mathrm{d}}{\mathrm{d}t}\langle[\boldsymbol{r}_{\mathrm{i}}(t)-\boldsymbol{r}_{\mathrm{i}}(0)]^{2}\rangle$
η	$\dfrac{V}{kT}\displaystyle\int_{0}^{\infty}\langle\tau_{\alpha\beta}(t)\tau_{\alpha\beta}(0)\rangle\,\mathrm{d}t$	$\displaystyle\lim_{t\to\infty}\dfrac{V}{2kT}\dfrac{\mathrm{d}}{\mathrm{d}t}\left\langle\left[R_{\alpha\beta}^{\mathrm{p,t}}(t)-R_{\alpha\beta}^{\mathrm{p,t}}(0)\right]^{2}\right\rangle$
η_{l}	$\dfrac{V}{3kT}\displaystyle\int_{0}^{\infty}\langle\mathrm{tr}[\boldsymbol{\Pi}(t)\boldsymbol{\Pi}(0)]\rangle\,\mathrm{d}t$	$\displaystyle\lim_{t\to\infty}\dfrac{V}{6kT}\dfrac{\mathrm{d}}{\mathrm{d}t}\langle\mathrm{tr}([\boldsymbol{R}^{\mathrm{p}}(t)-\boldsymbol{R}^{\mathrm{p}}(0)][\boldsymbol{R}^{\mathrm{p}}(t)-\boldsymbol{R}^{\mathrm{p}}(0)])\rangle$
η_{b}	$\dfrac{V}{9kT}\displaystyle\int_{0}^{\infty}\langle\mathrm{tr}[\boldsymbol{\Pi}(t)]\,\mathrm{tr}[\boldsymbol{\Pi}(0)]\rangle\,\mathrm{d}t$	$\displaystyle\lim_{t\to\infty}\dfrac{V}{18kT}\dfrac{\mathrm{d}}{\mathrm{d}t}\left\langle[\mathrm{tr}(\boldsymbol{R}^{\mathrm{p}}(t)-\boldsymbol{R}^{\mathrm{p}}(0))]^{2}\right\rangle$
λ	$\dfrac{V}{3kT^{2}}\displaystyle\int_{0}^{\infty}\langle\boldsymbol{J}^{\mathrm{q}}(t)\cdot\boldsymbol{J}^{\mathrm{q}}(0)\rangle\,\mathrm{d}t$	$\displaystyle\lim_{t\to\infty}\dfrac{V}{6kT^{2}}\dfrac{\mathrm{d}}{\mathrm{d}t}\left\langle[\boldsymbol{R}^{\mathrm{e}}(t)-\boldsymbol{R}^{\mathrm{e}}(0)]^{2}\right\rangle$

Abbreviations:	related to:
$\boldsymbol{R}^{\mathrm{p}}(t)=\dfrac{m}{V}\displaystyle\sum_{i=1}^{N}\boldsymbol{v}_{\mathrm{i}}(t)\boldsymbol{r}_{\mathrm{i}}(t)-p\,t\,\boldsymbol{I}$	centre of momentum
$R_{\alpha\beta}^{\mathrm{p,t}}(t)=\dfrac{m}{V}\displaystyle\sum_{i=1}^{N}v_{\alpha,\mathrm{i}}(t)r_{\beta,\mathrm{i}}(t)$	centre of transverse momentum
$\boldsymbol{R}^{\mathrm{e}}(t)=\dfrac{1}{V}\displaystyle\sum_{i=1}^{N}\left[\dfrac{m}{2}[\boldsymbol{v}_{\mathrm{i}}(t)]^{2}+u_{\mathrm{i}}(t)\right]\boldsymbol{r}_{\mathrm{i}}(t)$	centre of energy

2.5.5   Subdivision of Transport Coefficients

In time-correlation function theory, a subdivision of the transport coefficients into three contributions arises, which is introduced in this section. In general, a thermodynamic flux J^{i} can be separated into a translational contribution $J_{\mathrm{t}}^{\mathrm{i}}$ and a configurational contribution $J_{\mathrm{c}}^{\mathrm{i}}$ so that

$$J^{\mathrm{i}} = J_{\mathrm{t}}^{\mathrm{i}} + J_{\mathrm{c}}^{\mathrm{i}} \quad . \tag{2.184}$$

The translational fluxes are defined by

$$J_{\alpha\beta,\mathrm{t}}^{\widehat{\Pi}} = -\tau_{\alpha\beta,\mathrm{t}} = \frac{1}{V}\sum_{i=1}^{N} m v_{\alpha,\mathrm{i}} v_{\beta,\mathrm{i}} \tag{2.185}$$

$$J_{\mathrm{t}}^{\mathrm{tr}(\Pi)} = 0 \tag{2.186}$$

$$\boldsymbol{J}_{\mathrm{t}}^{\mathrm{q}} = \frac{1}{V}\sum_{i=1}^{N} \frac{m}{2}\, \boldsymbol{v}_{\mathrm{i}}^2 \boldsymbol{v}_{\mathrm{i}} \tag{2.187}$$

$$\boldsymbol{J}_{\mathrm{t}}^{\mathrm{D}} = \boldsymbol{v}_{\mathrm{i}} \tag{2.188}$$

and the corresponding configurational fluxes follow from Eqs. (2.184) and (2.185) to (2.188) by using the molecular expressions for the fluxes as

$$J_{\alpha\beta,\mathrm{c}}^{\widehat{\Pi}} = -\tau_{\alpha\beta,\mathrm{c}} = \frac{1}{V}\sum_{i=1}^{N}\sum_{\substack{j=1 \\ j\neq i}}^{N} r_{\alpha,\mathrm{ij}} F_{\beta,\mathrm{ij}} \tag{2.189}$$

$$J_{\mathrm{c}}^{\mathrm{tr}(\Pi)} = P - p = \delta p = \frac{1}{3V}\left(\sum_{i=1}^{N} m\boldsymbol{v}_{\mathrm{i}}^2 + \frac{1}{2}\sum_{i=1}^{N}\sum_{\substack{j=1 \\ j\neq i}}^{N} \boldsymbol{r}_{\mathrm{ij}}\cdot\boldsymbol{F}_{\mathrm{ij}}\right) - \langle p\rangle \tag{2.190}$$

$$\boldsymbol{J}_{\mathrm{c}}^{\mathrm{q}} = \frac{1}{V}\left(\sum_{i=1}^{N} u_{\mathrm{i}}\boldsymbol{v}_{\mathrm{i}} + \frac{1}{2}\sum_{i=1}^{N}\sum_{\substack{j=1 \\ j\neq i}}^{N} (\boldsymbol{r}_{\mathrm{ij}}\boldsymbol{F}_{\mathrm{ij}})\cdot\boldsymbol{v}_{\mathrm{i}}\right) \tag{2.191}$$

$$\boldsymbol{J}_{\mathrm{c}}^{\mathrm{D}} = 0 \quad . \tag{2.192}$$

This subdivision is the same as that used by Ernst et al. [41] in their theoretical investigation of the long time behaviour of the time-correlation functions using mode-coupling theory. The subdivision of the fluxes introduces a separation of the time-correlation functions of the fluxes

$$N^{\mathrm{i}}(t) = N_{\mathrm{tt}}^{\mathrm{i}}(t) + N_{\mathrm{tc}}^{\mathrm{i}}(t) + N_{\mathrm{cc}}^{\mathrm{i}}(t) \tag{2.193}$$

with

$$N_{\mathrm{tt}}^{\mathrm{i}}(t) = \langle J_{\mathrm{t}}^{\mathrm{i}}(0) J_{\mathrm{t}}^{\mathrm{i}}(t)\rangle \tag{2.194}$$

$$N_{\mathrm{tc}}^{\mathrm{i}}(t) = \langle J_{\mathrm{t}}^{\mathrm{i}}(0) J_{\mathrm{c}}^{\mathrm{i}}(t)\rangle + \langle J_{\mathrm{c}}^{\mathrm{i}}(0) J_{\mathrm{t}}^{\mathrm{i}}(t)\rangle \tag{2.195}$$

$$N_{\mathrm{cc}}^{\mathrm{i}}(t) = \langle J_{\mathrm{c}}^{\mathrm{i}}(0) J_{\mathrm{c}}^{\mathrm{i}}(t)\rangle \quad . \tag{2.196}$$

Hence, correlation functions of thermodynamic fluxes are written as a sum of a translational-translational, a translational-configurational, and a configurational-configurational contribution. The subdivision of the fluxes is chosen so that the translational and configurational fluxes are instantaneously uncorrelated and the initial values of their cross correlation functions vanish:

$$N_{\text{tc}}^{\text{i}}(0) = 2\langle J_{\text{t}}^{\text{i}}(0) J_{\text{c}}^{\text{i}}(0) \rangle = 0 \quad . \tag{2.197}$$

Moreover, the subdivision ensures that the separated correlation functions contain no constant contributions and decay to zero in the long time limit.

When this subdivision of the correlation function is inserted into the Green-Kubo formulas (see Table 2.2), three contributions to every transport coefficient are found. For the viscosity and thermal conductivity, all three contributions are non-zero. Thus,

$$\eta(\rho, T) = \eta_{\text{tt}}(\rho, T) + \eta_{\text{tc}}(\rho, T) + \eta_{\text{cc}}(\rho, T) \tag{2.198}$$

and

$$\lambda(\rho, T) = \lambda_{\text{tt}}(\rho, T) + \lambda_{\text{tc}}(\rho, T) + \lambda_{\text{cc}}(\rho, T) \quad . \tag{2.199}$$

Since the translational fluxes for the bulk viscosity is zero, the bulk viscosity consists of a configurational-configurational contribution only:

$$\eta_{\text{b}}(\rho, T) = \eta_{\text{b,cc}}(\rho, T) \quad . \tag{2.200}$$

Similarly, the product of the self-diffusion coefficient and density contains a translational-translational contribution only:

$$D\rho(\rho, T) = (D\rho)_{\text{tt}}(\rho, T) \quad . \tag{2.201}$$

As the density approaches zero, the translational-configurational and configurational-configurational contributions vanish since the configurational fluxes become zero in this limiting case. In the zero density limit, the translational-translational contributions take the values

$$\lim_{\rho \to 0} \eta_{\text{tt}}(\rho, T) \quad = \eta_0(T) \tag{2.202}$$

$$\lim_{\rho \to 0} \lambda_{\text{tt}}(\rho, T) \quad = \lambda_0(T) \tag{2.203}$$

$$\lim_{\rho \to 0} (D\rho)_{\text{tt}}(\rho, T) = (D\rho)_0(T) \quad , \tag{2.204}$$

where $\eta_0(T)$ is the zero density viscosity, $\lambda_0(T)$ is the zero density thermal conductivity and $(D\rho)_0(T)$ is the zero density value for the product of the self-diffusion coefficient and density. For fluids of spherical particles, these limits are determined by the Chapman-Enskog solution to the Boltzmann equation [88] (see Appendix B). In fact, the zero density transport coefficients are the only accurately known values for the transport coefficients of an intermolecular potential model which were not obtained from molecular dynamics simulations. A validation of molecular dynamics simulation results can therefore only be conducted by comparing the extrapolation behaviour of the simulation results to zero density with the Chapman-Enskog values for the potential model.

In contrast to thermodynamic state variables of monatomic fluids, such as pressure or isochoric heat capacity, transport coefficients cannot be divided into pure translational and configurational parts, but also contain cross contributions. This is a consequence of the fact that translational and configurational fluxes are instantaneously uncorrelated, but at not too large time separations they are strongly correlated. Hence, in general there is a non-zero translational-configurational contribution to the transport coefficients.

In literature, other subdivisions of the transport coefficients were proposed. In empirical correlations for the transport coefficients viscosity and thermal conductivity the correlations are often split into three contributions [14]. For instance, the viscosity is written as

$$\eta(\rho, T) = \eta_0(T) + \eta_{\text{res}}(\rho, T) + \eta_{\text{cr}}(\rho, T) \quad . \tag{2.205}$$

The zero density contribution $\eta_0(T)$ corresponds to the zero density Chapman-Enskog values, $\eta_{\text{cr}}(\rho, T)$ accounts for the enhancement in the vicinity of the critical point and the residual contribution $\eta_{\text{res}}(\rho, T)$ describes the difference between the total transport coefficient and the sum of the other two contributions. In this subdivision, the zero density contribution is constant along isotherms over the whole density range and the critical enhancement contribution for the viscosity and thermal conductivity contributes significantly only in the immediate vicinity of the critical point. In general, the contributions found in this subdivision are different than those arising within time-correlation function theory.

Sharma [195] and Stassen and Steele [201, 202] suggested extensions of the subdivision of the shear stress correlation function introduced in this section. Sharma

defined a single particle shear stress as

$$\tau_{\alpha\beta,i} = -\frac{1}{V}mv_{\alpha,i}v_{\beta,i} - \frac{1}{V}\sum_{\substack{j=1\\j\neq i}}^{N}r_{\alpha,ij}F_{\beta,ij} = \tau_{\alpha\beta,t,i} + \tau_{\alpha\beta,c,i} \tag{2.206}$$

and separated the shear stress correlation function into auto- and cross-correlations

$$N_{\alpha\beta}^{\tau}(t) = N_{\alpha\beta}^{\tau,\mathrm{auto}}(t) + N_{\alpha\beta}^{\tau,\mathrm{cross}}(t) \quad, \tag{2.207}$$

where the autocorrelation part is given by

$$N_{\alpha\beta}^{\tau,\mathrm{auto}}(t) = \sum_{i=1}^{N}\langle\tau_{\alpha\beta,i}(0)\tau_{\alpha\beta,i}(t)\rangle \tag{2.208}$$

and the cross-correlation part by

$$N_{\alpha\beta}^{\tau,\mathrm{cross}}(t) = \sum_{i=1}^{N}\sum_{\substack{j=1\\j\neq i}}^{N}\langle\tau_{\alpha\beta,i}(0)\tau_{\alpha\beta,j}(t)\rangle \quad. \tag{2.209}$$

When the separation of the shear stress into single particle shear stresses is combined with the subdivision of the total shear stress into translational and configurational contributions, the total shear stress correlation function consists of six contributions:

$$N_{\alpha\beta,tt}^{\tau,\mathrm{auto}}(t) = \sum_{i=1}^{N}\langle\tau_{\alpha\beta,t,i}(0)\tau_{\alpha\beta,t,i}(t)\rangle \tag{2.210}$$

$$N_{\alpha\beta,tt}^{\tau,\mathrm{cross}}(t) = \sum_{i=1}^{N}\sum_{\substack{j=1\\j\neq i}}^{N}\langle\tau_{\alpha\beta,t,i}(0)\tau_{\alpha\beta,t,j}(t)\rangle \tag{2.211}$$

$$N_{\alpha\beta,tc}^{\tau,\mathrm{auto}}(t) = \sum_{i=1}^{N}\sum_{\substack{j=1\\j\neq i}}^{N}\langle\tau_{\alpha\beta,t,i}(0)\tau_{\alpha\beta,c,ij}(t) + \tau_{\alpha\beta,c,ij}(0)\tau_{\alpha\beta,t,i}(t)\rangle \tag{2.212}$$

$$N_{\alpha\beta,tc}^{\tau,\mathrm{cross}}(t) = \sum_{i=1}^{N}\sum_{\substack{j=1\\j\neq i}}^{N}\sum_{\substack{k=1\\k\neq j}}^{N}\langle\tau_{\alpha\beta,t,i}(0)\tau_{\alpha\beta,c,jk}(t) + \tau_{\alpha\beta,c,jk}(0)\tau_{\alpha\beta,t,i}(t)\rangle \tag{2.213}$$

$$N_{\alpha\beta,cc}^{\tau,\mathrm{auto}}(t) = \sum_{i=1}^{N}\sum_{\substack{j=1\\j\neq i}}^{N}\sum_{\substack{k=1\\k\neq i}}^{N}\langle\tau_{\alpha\beta,c,ij}(0)\tau_{\alpha\beta,c,ik}(t)\rangle \tag{2.214}$$

$$N_{\alpha\beta,cc}^{\tau,\mathrm{cross}}(t) = \sum_{i=1}^{N}\sum_{\substack{j=1\\j\neq i}}^{N}\sum_{k=1}^{N}\sum_{\substack{l=1\\l\neq k}}^{N}\langle\tau_{\alpha\beta,c,ij}(0)\tau_{\alpha\beta,c,kl}(t)\rangle \quad. \tag{2.215}$$

The number of terms in the translational-translational contribution N^2 is divided into N auto- and $N(N-1)$ cross-terms, while the number of terms in the translational-configurational contribution $N^2(N-1)$ separates into $N(N-1)$ auto- and $N(N-1)^2$ cross-terms. The $N^2(N-1)^2$ terms in the configurational-configurational contribution are partitioned into $N(N-1)^2$ auto- and $N(N-1)^3$ cross-terms. In this subdivision scheme, the viscosity is given as a sum of six contributions:

$$\eta(\rho, T) = (\eta_{\text{auto}} + \eta_{\text{cross}})_{\text{tt}} + (\eta_{\text{auto}} + \eta_{\text{cross}})_{\text{tc}} + (\eta_{\text{auto}} + \eta_{\text{cross}})_{\text{cc}} \quad . \tag{2.216}$$

Sharma investigated this subdivision at the reduced state point ($T^* = 0.72$, $\rho^* = 0.844$) close to the triple point of the Lennard-Jones model fluid.

Stassen and Steele suggested a separation of the translational-configurational and configurational-configurational part of the shear stress correlation function based on the number of particles involved in the correlations. For this purpose, the shear stress is separated according to

$$\tau_{\alpha\beta} = \sum_{i=1}^{N} \tau_{\alpha\beta,\text{t,i}} + \sum_{i=1}^{N} \sum_{\substack{j=1 \\ j \neq i}}^{N} \tau_{\alpha\beta,\text{c,ij}} \tag{2.217}$$

with

$$\tau_{\alpha\beta,\text{t,i}} = -\frac{1}{V} \, m v_{\alpha,\text{i}} v_{\beta,\text{i}} \tag{2.218}$$

and

$$\tau_{\alpha\beta,\text{c,ij}} = -\frac{1}{V}\frac{1}{2} \, r_{\alpha,\text{ij}} F_{\beta,\text{ij}} \quad . \tag{2.219}$$

Since this representation of the translational shear stress is identical to that found by using single particle shear stresses, the resulting one- and two-body contributions to the translational-translational shear stress correlation function are identical to the auto- and cross-contributions defined by Sharma.

The translational-configurational contribution is resolved into two- and three-body terms. Hence, it may be written as

$$N^{\tau}_{\alpha\beta,\text{tc}}(t) = N^{\tau,\text{2b}}_{\alpha\beta,\text{tc}}(t) + N^{\tau,\text{3b}}_{\alpha\beta,\text{tc}}(t) \tag{2.220}$$

with the two- and three-body contributions

$$N^{\tau,\text{2b}}_{\alpha\beta,\text{tc}}(t) = \left\langle 2 \sum_{i=1}^{N} \sum_{\substack{j=1 \\ j \neq i}}^{N} \{\tau_{\alpha\beta,\text{c,ij}}(0)\tau_{\alpha\beta,\text{t,i}}(t) + \tau_{\alpha\beta,\text{t,i}}(0)\tau_{\alpha\beta,\text{c,ij}}(t)\} \right\rangle \tag{2.221}$$

and

$$N_{\alpha\beta,\mathrm{tc}}^{\tau,\mathrm{3b}}(t) = \left\langle \sum_{i=1}^{N} \sum_{\substack{j=1 \\ j \neq i}}^{N} \sum_{\substack{k=1 \\ k \neq i,j}}^{N} \left\{ \tau_{\alpha\beta,\mathrm{c,jk}}(0)\tau_{\alpha\beta,\mathrm{t,i}}(t) + \tau_{\alpha\beta,\mathrm{t,i}}(0)\tau_{\alpha\beta,\mathrm{c,jk}}(t) \right\} \right\rangle \quad . \quad (2.222)$$

The factor of two accounts for permutations of the kind $[(i, jk)]; [(i, kj)]$ in the two-body contribution. The total number of terms $N^2(N-1)$ in the translational-configurational contribution separates into $2N(N-1)$ two- and $N(N-1)(N-2)$ three-body terms.

Similarly, the configurational-configurational contribution may be represented by two-, three- and four-body terms so that

$$N_{\alpha\beta,\mathrm{cc}}^{\tau}(t) = N_{\alpha\beta,\mathrm{cc}}^{\tau,\mathrm{2b}}(t) + N_{\alpha\beta,\mathrm{cc}}^{\tau,\mathrm{3b}}(t) + N_{\alpha\beta,\mathrm{cc}}^{\tau,\mathrm{4b}}(t) \quad , \quad\quad\quad (2.223)$$

where the three contributions are given by

$$N_{\alpha\beta,\mathrm{cc}}^{\tau,\mathrm{2b}}(t) = \left\langle 2 \sum_{i=1}^{N} \sum_{\substack{j=1 \\ j \neq i}}^{N} \tau_{\alpha\beta,\mathrm{c,ij}}(0)\tau_{\alpha\beta,\mathrm{c,ij}}(t) \right\rangle \quad , \quad\quad\quad (2.224)$$

$$N_{\alpha\beta,\mathrm{cc}}^{\tau,\mathrm{3b}}(t) = \left\langle 4 \sum_{i=1}^{N} \sum_{\substack{j=1 \\ j \neq i}}^{N} \sum_{\substack{k=1 \\ k \neq i,j}}^{N} \tau_{\alpha\beta,\mathrm{c,ij}}(0)\tau_{\alpha\beta,\mathrm{c,ik}}(t) \right\rangle \quad\quad\quad (2.225)$$

and

$$N_{\alpha\beta,\mathrm{cc}}^{\tau,\mathrm{4b}}(t) = \left\langle \sum_{i=1}^{N} \sum_{\substack{j=1 \\ j \neq i}}^{N} \sum_{\substack{k=1 \\ k \neq i,j}}^{N} \sum_{\substack{l=1 \\ l \neq i,j,k}}^{N} \tau_{\alpha\beta,\mathrm{c,ij}}(0)\tau_{\alpha\beta,\mathrm{c,kl}}(t) \right\rangle \quad , \quad\quad\quad (2.226)$$

respectively. The factors two and four take into account the permutations of the indices $[(ij, ij); (ji, ji)]$ in the two- and $[(ij, ik); (ij, ki); (ji, ik); (ji, ki)]$ in the three-body terms. There are $2N(N-1)$ two-body, $4N(N-1)(N-2)$ three-body terms and $N(N-1)(N-2)(N-3)$ four-body terms altogether, adding up to $N^2(N-1)^2$ terms in the total configurational-configurational correlation function. In this subdivision scheme, the viscosity is written as

$$\eta = (\eta_{\mathrm{1b}} + \eta_{\mathrm{2b}})_{\mathrm{tt}} + (\eta_{\mathrm{2b}} + \eta_{\mathrm{3b}})_{\mathrm{tc}} + (\eta_{\mathrm{2b}} + \eta_{\mathrm{3b}} + \eta_{\mathrm{4b}})_{\mathrm{cc}} \quad . \quad\quad\quad (2.227)$$

A comparison of the number of terms in the contributions arising in the subdivision schemes suggested by Sharma and Stassen and Steele shows that both schemes yield different separations of the viscosity.

The subdivision of the configurational-configurational viscosity contribution was examined by Stassen and Steele for the Lennard-Jones model fluid on five state points along the subcritical isotherm $T^* = 1.26$ and the same state point ($T^* = 0.722$, $\rho^* = 0.8442$) which was studied by Sharma [195]. Moreover, the short and long time behaviour of the two-, three- and four-body configurational-configurational shear stress correlation function was described by Stassen and Steele on these state points and revealed aspects of the transverse momentum transport mechanisms on the molecular scale. The results of both Sharma [195] and Stassen and Steele [201, 202] supplement the investigations on the subdivision of the transport coefficients undertaken in this work and will turn out to be useful when discussing the dependence of the shear stress correlation function on temperature and density in Section 5.4.

3 Molecular Dynamics Simulation Methodology

Molecular dynamics, first introduced by Alder and Wainright in 1956 [5], is a standard simulation method in computational statistical physics. By solving the classical equations of motion for a system of 100 to 10000 molecules numerically on a computer, the phase space trajectory of the system is generated over many thousands, up to millions, of time steps. These time periods correspond to some picoseconds up to some microseconds real time. At every simulated time step, the instantaneous properties of the system are calculated by their corresponding molecular expressions and stored on a hard disk. Subsequently, macroscopic properties of the system are calculated by analyzing the stored data. For the simulation study of this work, new software was developed and implemented on distributed memory parallel computers. This chapter describes the implementation of the simulation software and details of the simulations carried out in this work. Furthermore, the influence of the simulation parameters on the results is discussed and results for thermodynamic state variables of the Lennard-Jones model fluid are presented. Detailed descriptions of the molecular simulation methodology are given in the books of Allen and Tildesley [10], Frenkel and Smid [52], Haile [65], Rapaport [182] and Sadus [188].

3.1 Basic Simulation Algorithm

In a molecular dynamics simulation of spherical particles, Newton's classical equation of motion are solved by numerical integration. The equations of motion read

$$\boldsymbol{v}_i(t) = \dot{\boldsymbol{r}}_i(t) \tag{3.1}$$

$$\boldsymbol{a}_i(t) = \dot{\boldsymbol{v}}_i(t) \tag{3.2}$$

$$\boldsymbol{F}_i(t) = m\boldsymbol{a}_i(t) \tag{3.3}$$

for every molecule i. In this form, they form a set of first-order differential equations. Since the force acting upon on a particle depends in general on the positions of all other particles in the system, the equations for all particles are coupled. Due to the functional form of the intermolecular potential function, they are nonlinear.

In this work, the velocity-Verlet algorithm [206] was used to integrate the equations of motion. This algorithm proceeds in two steps. First, the new positions are

calculated by

$$\boldsymbol{r}_\text{i}(t + \Delta t) = \boldsymbol{r}_\text{i}(t) + \Delta t \boldsymbol{v}_\text{i}(t) + \frac{1}{2}\Delta t^2 \boldsymbol{a}_\text{i}(t) \quad , \tag{3.4}$$

where Δt denotes the size of the time step. In a second step, the velocities at $t + \Delta t$ are obtained by

$$\boldsymbol{v}_\text{i}(t + \Delta t) = \boldsymbol{v}_\text{i}(t) + \frac{1}{2}\Delta t [\boldsymbol{a}_\text{i}(t) + \boldsymbol{a}_\text{i}(t + \Delta t)] \quad . \tag{3.5}$$

Between the two steps, the forces at time $t + \Delta t$ are calculated. As the velocity-Verlet algorithm is a symplectic integrator, it conserves energy and total momentum of the system [213]. Hence, very stable phase space trajectories are generated. Moreover, the particle positions and velocities are evaluated at the same time $t + \Delta t$ so that numerical errors caused by interpolating velocities as required when applying the simple Verlet or leap-frog algorithm [10] are avoided.
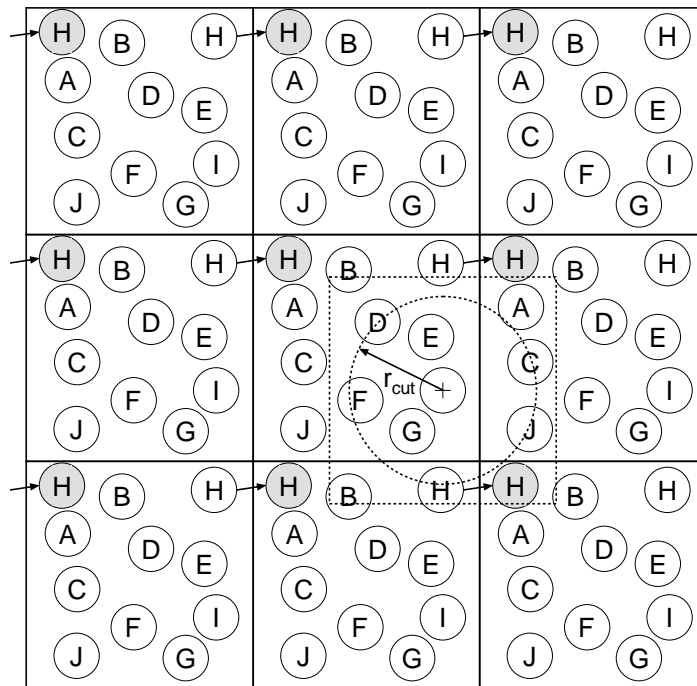
Figure 3.1. Illustration of periodic boundary conditions, minimum image convention and cutoff-radius.

Molecular dynamics simulations are performed within periodic boundary conditions [10, 52, 65, 182] as illustrated in Figure 3.1. Periodic boundary conditions

imply that the basic simulation box is infinitely repeated in all three spatial directions to form an infinite cubic lattice. Images of a particle in the basic box move in exactly the way in their boxes, as the original particle moves in the basic box. Whenever a particle leaves the box, its image in one of the neighbouring boxes enters the box in the same step at the opposite side. In principle, a particle in the basic simulation box interacts with all other particles in this box as well as infinitely many particles in the image boxes. Interactions between particles are calculated according to the minimum image convention. A particle interacts either with another particle in the basic simulation box or with this particle's nearest image in the neighbouring image boxes, whichever is closer. Hence, interactions are taken into account within a cubical region of the same size as the basic box whose centre is located at the centre of mass of the considered particle.

Moreover, when the intermolecular potential function is short ranged, a cutoff radius r_{cut} is introduced to reduce the number of interaction computations. Thus, the intermolecular potential function is truncated at the cutoff radius. Interactions of a particle with other particles are only calculated for particles that are within a sphere with the radius r_{cut} surrounding this particle. The value of the cutoff radius is chosen smaller than half of the box length. Interactions with particles outside the cutoff sphere are either neglected or are approximately taken into account by long range corrections. Simple long range corrections for ensemble averages that consist only of pair contributions are derived from the general relation [10]

$$\langle A \rangle = \left\langle \sum_{i=1}^{N} \sum_{j=i+1}^{N} a(r_{\text{ij}}) \right\rangle = \frac{1}{2} N \rho \int\limits_{0}^{\infty} a(r)\, g(r)\, 4\pi r^2 \mathrm{d}r \quad , \tag{3.6}$$

where $a(r)$ denotes the pair function corresponding to the phase variable A and $g(r)$ is the radial pair distribution function. Assuming vanishing instantaneous correlations of a particle with particles at distances greater than the cutoff radius, the radial pair distribution function is set to one for particle separations greater than the cutoff radius. When the integral is evaluated between r_{cut} and infinity for the pair contributions for the potential energy and its first and second volume derivative as given in Table 2.1 with the Lennard-Jones potential function, Eq. (2.13), the long

range corrections are obtained as

$$U_{\mathrm{LRC}} \qquad = \frac{8}{3}\,\pi N \rho\,\varepsilon\sigma^3 \left[\frac{1}{3}\left(\frac{\sigma}{r_{\mathrm{cut}}}\right)^9 - \left(\frac{\sigma}{r_{\mathrm{cut}}}\right)^3 \right] \qquad (3.7)$$

$$\left(\frac{\partial U}{\partial V}\right)_{\mathrm{LRC}} = -\frac{16}{3}\,\pi \rho^2 \varepsilon\sigma^3 \left[\frac{2}{3}\left(\frac{\sigma}{r_{\mathrm{cut}}}\right)^9 - \left(\frac{\sigma}{r_{\mathrm{cut}}}\right)^3 \right] \qquad (3.8)$$

$$\left(\frac{\partial^2 U}{\partial V^2}\right)_{\mathrm{LRC}} = \frac{32}{3}\,\pi\,\frac{\rho^2}{V}\,\varepsilon\sigma^3 \left[\frac{4}{3}\left(\frac{\sigma}{r_{\mathrm{cut}}}\right)^9 - \left(\frac{\sigma}{r_{\mathrm{cut}}}\right)^3 \right] \quad . \qquad (3.9)$$

Strictly, Eq. (3.7) to (3.9) represent corrections to ensemble averages of the volume derivatives. Here, they are applied to the instantaneous volume derivatives of the potential energy. Contributions of interactions from particles outside the cutoff sphere to the configurational contributions of the thermodynamic fluxes are neglected. Since relatively large cutoff-radii were used in the simulations of this work, this should have little influence on the results for the transport coefficients. To the best knowledge of the author, a method to carry out cutoff corrections for the thermodynamic fluxes has not yet been developed. Beside this simple corrections, other methods are available to account for the truncation of the intermolecular potential function at the cutoff radius. For example, Lustig [126, 127, 128, 129] suggested a more sophisticated method which yields instantaneous corrections to the volume derivatives of the potential energy.

A simulation starts by assigning initial positions and velocities to all particles and by calculating the forces acting upon the particles in the initial configuration. The particles are initially distributed on the sites of a face-centred cubic lattice within the simulation box. Initial velocities are drawn randomly from a Gaussian distribution so that they are compatible with the prescribed value for the total energy and the condition $\boldsymbol{M} = \boldsymbol{0}$. From this point on, the equations of motion are integrated with the velocity-Verlet algorithm according to Eqs. (3.4) and (3.5). Since the initial distribution of the particle coordinates and velocities is usually not conform with the thermodynamic equilibrium state corresponding to the constrained state variables, an equilibration phase of a few ten thousand up to several hundred thousand time steps precedes the actual simulation to relax the system to thermodynamic equilibrium. During the production phase of the simulation, instantaneous values for the phase variables are stored on a hard disk for later analysis.

3.2 Implementation of the Simulation Software on Distributed Memory Parallel Computers

One simulation run usually takes many hours up to several days of CPU-time and up to several gigabytes of hard disk space even on state-of-the-art high performance parallel computers. This large demand for computing resources requires an efficient implementation of the simulation and analysis software. The simulations of this work were performed on seven high performance parallel computers at four different locations. Computing resources were provided by the RRZN (Regionales Rechenzentrum für Niedersachen) at the Universität Hannover on a Cray T3E and SUN Enterprise 10000, by the Konrad-Zuse Zentrum für Informationstechnologie in Berlin on a Cray T3E, by the NIST Information Technology Laboratory in Gaithersburg (U.S.A) on three SGI Origin machines and by the Mechanical Engineering Department of the University of the Federal Armed Forces Hamburg on a Hewlett Packard Superdome. These parallel computers are multiple instruction multiple data (MIMD) machines with distributed memory architecture and employ the SPMD (same program multiple data) programming model. On this type of parallel computers, every processing element (PE) has its own copy of the program in its memory and processes it independently from all other PEs. If one PE needs data that reside in the memory of another PE, these data must be sent to that PE by the PE which controls the data. Such communications among the PEs are realized by the message passing software MPI, which is available as a FORTRAN subroutine library. The software developed in this work is based on FORTRAN codes provided as attachments to the book of Allen and Tildesley [10]. Assistance in the parallelization and optimization of the software was provided by the staff of the RRZN at the Universität Hannover.

Generally, there are several possible strategies for conducting molecular dynamics simulations on parallel computers [87, 182]. In the often applied geometric approach, the simulation region is partitioned into subregions and every PE is assigned a particular subregion for which it performs the simulation. Communications are required at the end of every time step, but every PE needs to exchange data only with PEs on which neighbouring subregions reside. This approach is best suitable if very large systems up to several million particles are investigated on massively parallel computers with several hundred PEs [175].

As systems with less than 1500 particles are examined on parallel computers with small numbers of PEs in this work, a different parallelization strategy is employed which distributes the computations among the PEs. Every PE controls the total

information about the system, for example all particle positions and velocities, and performs the computations for interacting pairs of particles assigned to it for the entire simulation. Since the computation of the forces and instantaneous values of the phase variables requires over 99 % of the total CPU-time of a simulation run, only this part of the program is parallelized. At the end of every time step, a communication phase is required to collect the contributions to the forces and phase variables and redistribute the information among all PEs. In this strategy, the performance is optimal if the computational load is equally partitioned among the PEs and the communication phase at the end of every time step is much shorter than the computation phase.

The evaluation of the forces and instantaneous phase variables, for instance A, is performed in a double sum,

$$\boldsymbol{F}_{i'} = \sum_{j=i'+1}^{N} \boldsymbol{F}_{i'j} - \sum_{i=1}^{i'-1} \boldsymbol{F}_{ii'} \qquad \text{for all particles } i' = 1, \ldots, N \qquad (3.10)$$

$$A = \sum_{i=1}^{N-1} \sum_{i=j+1}^{N} a(r_{ij}) \quad , \qquad (3.11)$$

since only pairwise interactions are considered in this work. In the force computation, Newton's third law $\boldsymbol{F}_{ij} = -\boldsymbol{F}_{ji}$ is utilized so that every pair contribution needs to be computed only once. In the inner j-loop, the contributions $\boldsymbol{F}_{ij}$ from the particles $i' + 1$ to N to the force $\boldsymbol{F}_{i'}$ upon particle i' are computed. The contributions $\boldsymbol{F}_{ij} = -\boldsymbol{F}_{ji}$ from the particles 1 to $i' - 1$ to $\boldsymbol{F}_{i'}$ are distributed among the outer i-loop iterations within the inner j-loop. The outer i-loop of the double loop force computation is distributed among the PEs. After completion of the loop, the computed contributions are collected by performing global sums over all PEs by the MPI subroutine `ALLREDUCE`.

The parallelization strategy is illustrated in Figure 3.2. Neglecting the potential truncation at the cutoff radius, the computation of the forces and phase variables can be interpreted as the computation of the elements of a triangular matrix, where every matrix element corresponds to a pair of particles ij. The double summation in Eqs. (3.10) and (3.11) extends over columns i and lines j of this matrix. If the computation is performed on a single processor, the double loop over i and j is executed sequentially. In a first parallelization step, consecutive outer loop iterations i are distributed among the PEs (Figure 3.2a). In every parallel outer loop iteration I, the force contributions $\boldsymbol{F}_{i'j}$ with $j = i' + 1, \ldots, N$ for particles $i' = (I - 1)n_{\mathrm{PE}} + k$ and $\boldsymbol{F}_{i',(I-1)n_{\mathrm{PE}}+k} = -\boldsymbol{F}_{(I-1)n_{\mathrm{PE}}+k,i'}$ for particles $i' = 1, \ldots, N - (I - 1)n_{\mathrm{PE}} - k + 1$
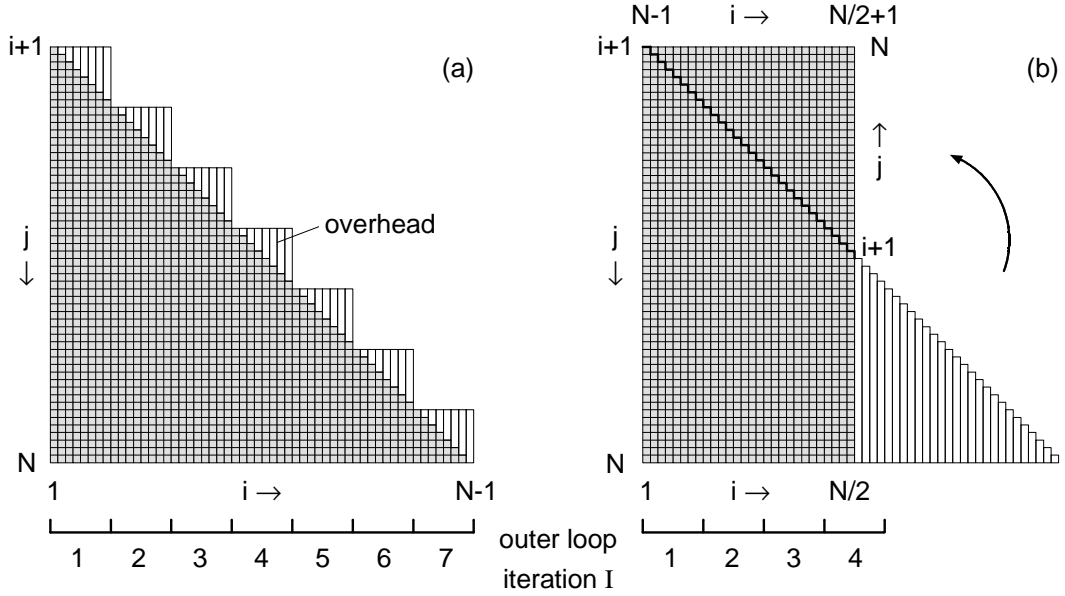
Figure 3.2. Illustration of parallelization strategy: a) Distribution of consecutive outer loop iterations among PEs and b) Rearrangement of inner loop iterations. Every square denotes the computation of one pair contribution.

are computed on PE $k = 1, \ldots, n_{\mathrm{PE}}$. Hence, Eqs. (3.10) and (3.11) read for parallel computation on n_{PE} PEs

$$\boldsymbol{F}_{\mathrm{i}'} = \sum_{j=i'+1}^{N} \boldsymbol{F}_{\mathrm{i'j}} - \sum_{I=1}^{(i'-1)/n_{\mathrm{PE}}} \sum_{\substack{k=1 \\ (I-1)n_{\mathrm{PE}}+k<i'}}^{n_{\mathrm{PE}}} \boldsymbol{F}_{(\mathrm{I}-1)\mathrm{n_{PE}}+\mathrm{k,i'}} \tag{3.12}$$

$$A = \sum_{I=1}^{(N-1)/n_{\mathrm{PE}}} \sum_{\substack{k=1 \\ (I-1)n_{\mathrm{PE}}+k<N}}^{n_{\mathrm{PE}}} \sum_{j=(I-1)n_{\mathrm{PE}}+k+1}^{N} a\big(r_{(I-1)\mathrm{n_{PE}}+k,j}\big) \quad, \tag{3.13}$$

where it is understood that quotients involving the integers i', n_{PE} and N are rounded to the next larger integer. Obviously, the load balancing is not yet optimal since the inner j-loops have different lengths. Further improvement is achieved by distributing outer loop iterations of equal length among the PEs. For this purpose, the i-loop iterations with indices between $N/2 + 1 \ldots N - 1$ are distributed in reverse order over iterations 1 to $N/2$ such that iteration $N - 1$ is performed after iteration 2 on PE 2, iteration $N - 2$ after 3 on PE 3, ... during the same outer loop iteration (Figure 3.2b). With this modification, the parallel force and phase variable

computation becomes

$$
\boldsymbol{F}_{\mathrm{i'}} = \sum_{j=i'+1}^{N} \boldsymbol{F}_{\mathrm{i'j}} - \sum_{\substack{I=1}}^{(i'-1)/n_{\mathrm{PE}}} \sum_{\substack{k=1 \\ (I-1)n_{\mathrm{PE}}+k<i'}}^{n_{\mathrm{PE}}} \boldsymbol{F}_{(\mathrm{I}-1)\mathrm{n_{PE}}+\mathrm{k,i'}} \qquad \text{for } i' \leq \frac{N}{2} \qquad (3.14)
$$

$$
\boldsymbol{F}_{\mathrm{i'}} = \sum_{j=i'+1}^{N} \boldsymbol{F}_{\mathrm{i'j}} - \sum_{I=1}^{(i'-1)/n_{\mathrm{PE}}} \left(\sum_{\substack{k=1 \\ (I-1)n_{\mathrm{PE}}+k\leq N/2}}^{n_{\mathrm{PE}}} \boldsymbol{F}_{(\mathrm{I}-1)\mathrm{n_{PE}}+\mathrm{k,i'}} \right.
$$

$$
\left. + \sum_{\substack{k=1 \\ N/2<N-(I-1)n_{\mathrm{PE}}-k<i'}}^{n_{\mathrm{PE}}} \boldsymbol{F}_{\mathrm{N}-(\mathrm{I}-1)\mathrm{n_{PE}}-\mathrm{k,i'}} \right) \qquad \text{for } i' > \frac{N}{2} \qquad (3.15)
$$

$$
A = \sum_{I=1}^{(N-1)/2n_{\mathrm{PE}}} \left(\sum_{\substack{k=1 \\ (I-1)n_{\mathrm{PE}}+k\leq N/2}}^{n_{\mathrm{PE}}} \sum_{j=(I-1)n_{\mathrm{PE}}+k+1}^{N} a\big(r_{(\mathrm{I}-1)\mathrm{n_{PE}}+\mathrm{k,j}}\big) \right.
$$

$$
\left. + \sum_{\substack{k=1 \\ N/2<N-(I-1)n_{\mathrm{PE}}-k<N}}^{n_{\mathrm{PE}}} \sum_{j=N-(I-1)n_{\mathrm{PE}}-k+1}^{N} a\big(r_{\mathrm{N}-(\mathrm{I}-1)\mathrm{n_{PE}}-\mathrm{k,j}}\big) \right) \qquad . \qquad (3.16)
$$

The performance is optimal, when $N/2$ is an integer multiple of the number of PEs, so that the last outer loop iteration distributes equal computational loads among the PEs. However, when the number of particles is much lower than the number of PEs, the overhead in the last outer loop is small. The lengths of the inner loops are not exactly equal since the number of particles within a cutoff radius of another particle varies around an average value. Since this variation is within narrow bounds of the average, this effect is negligible for simulations with large cutoff radii.

The performance of the parallelization can be measured by the speed-up

$$
S = \frac{t(1)}{t(n_{\mathrm{PE}})} \quad , \tag{3.17}
$$

where $t(1)$ is the real time needed for a sequential run on a single PE and $t(n_{\mathrm{PE}})$ the real time for a run on n_{PE} PEs. Figure 3.3 shows the speed-up of the parallelized simulation software on a Cray T3E with up to 16 PEs employing different particle numbers at the state point ($T^* = 1.8$, $\rho^* = 1.0$) of the Lennard-Jones fluid. At constant particle numbers, the speed-up increases with the number of PEs and is
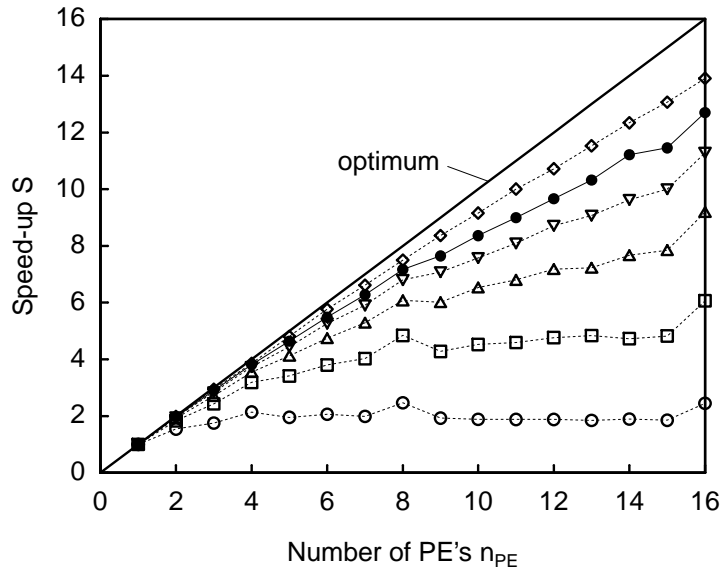
Figure 3.3. Speed-up of the parallelized simulation software as a function of the number of processing elements for different simulation parameters on a Cray T3E parallel computer at the state point ($T^* = 1.8$, $\rho^* = 1.0$) for the Lennard-Jones fluid. Legend: ($\bigcirc$) $N = 108$, $r^*_{\mathrm{cut}} = 2.35$, ($\square$) $N = 256$, $r^*_{\mathrm{cut}} = 3.1$, ($\triangle$) $N = 500$, $r^*_{\mathrm{cut}} = 3.9$, ($\triangledown$) $N = 864$, $r^*_{\mathrm{cut}} = 3.75$, ($\bullet$) $N = 1372$, $r^*_{\mathrm{cut}} = 5.5$ and ($\diamond$) $N = 2048$, $r^*_{\mathrm{cut}} = 6.3$.

almost optimal for runs on a few PEs. With increasing PE numbers, the curves becomes flatter and even reach saturation for the runs with 108 and 256 particles. At even PE numbers, the speed-up exhibits small peaks, which are most pronounced for 4, 8 and 16 PEs. It increases with the number of particles and is close to optimum for 2048 particles, where the peaks are not observed up to 16 PEs.

As the number of computations in the triangular matrix is proportional to the square of the number of particles, but the communication load increases linearly with the number of particles, the parallelization becomes more efficient with large particle numbers. Thus, the parallelization approach is communication bounded. The global sum in the MPI subroutine `ALLREDUCE` is carried out in a tree algorithm. Therefore, the communication is performed optimally if the number of PEs is a power of two. This explains the enhanced speed-up on 4, 8 or 16 PEs. The main body of simulations of this work were carried out with 1372 particles on 16 PEs. For this parameter constellation, a speed-up of 13 is achieved, showing that the chosen strategy works well for the target problem size. Even for simulation runs with 1372 particles on 32 PEs good performance was observed.

3.3 Simulation Analysis

After a simulation run, several separate analysis programs were used to compute thermodynamic state variables, time-correlation functions and generalized mean-squared displacements from the stored data on hard disk. In a subsequent analysis step, the transport coefficients were obtained from a careful analysis of the Einstein plots and time-correlation functions. Estimations of the uncertainties of the simulation data supplement a comprehensive simulation analysis.

3.3.1 Evaluation of Thermodynamic State Variables and Transport Coefficients

Thermodynamic state variables are related to phase space functions, which themselves are determined by combinations of ensemble averages of phase variables. In molecular dynamics simulations, ensemble averages are replaced by simulation averages over the production phase of the simulation. Simulation averages are calculated by

$$\langle A \rangle = \frac{1}{n_{\text{step}}} \sum_{i=1}^{n_{\text{step}}} A(i\Delta t) \tag{3.18}$$

from the instantaneous values of the phase variables stored on hard disk. The parameter n_{step} stands for the number of time steps of the production phase of the simulation. Phase space functions and thermodynamic state variables are then obtained by their molecular expressions in the molecular dynamics $NVE\boldsymbol{MG}$ ensemble as reported in Table 2.1.

Transport coefficients were deduced from their corresponding Einstein relations as the long time limit of the slopes of the generalized mean-squared displacements. In molecular dynamics simulations, the Einstein relations reported in Table 2.2 cannot be directly applied [46, 65, 190] because they implicitly assume continuous particle trajectories which are unaffected by periodic boundary conditions. Since the trajectories in a finite system simulation with periodic boundary conditions are discontinuous whenever a particle leaves or enters the simulation box, the generalized displacements must be calculated in a different way.

The modification for the self-diffusion Einstein relation is simple since only single particle trajectories are involved. Instead of the discontinuous particle trajectories, the unfolded trajectories, from which the periodic jumps are removed, termed

infinite-checkerboard form of the trajectories by Erpenbeck [46] are used to calculate the mean-squared displacements of the particles.

For the Einstein relations for the collective transport coefficients viscosity, bulk viscosity and thermal conductivity, this modification cannot be applied since their generalized displacements are functions of the coordinates of all particles in the system. An alternative way to calculate the generalized displacements was suggested by Haile [65] and used by Rowley and Painter [185] in their study on the viscosity of the Lennard-Jones fluid. A generalized displacement is related to the time integral of its corresponding flux by Eq. (2.168). As the molecular expressions for the thermodynamic fluxes are functions of the distances between all pairs of particles, their time evolution is, in fact, continuous if periodic boundary conditions and the minimum image convention are employed in a simulation. Therefore, Eq. (2.168) provides an indirect way to calculate the generalized displacements for the collective transport coefficients. A detailed discussion of this issue was given by Erpenbeck [46].
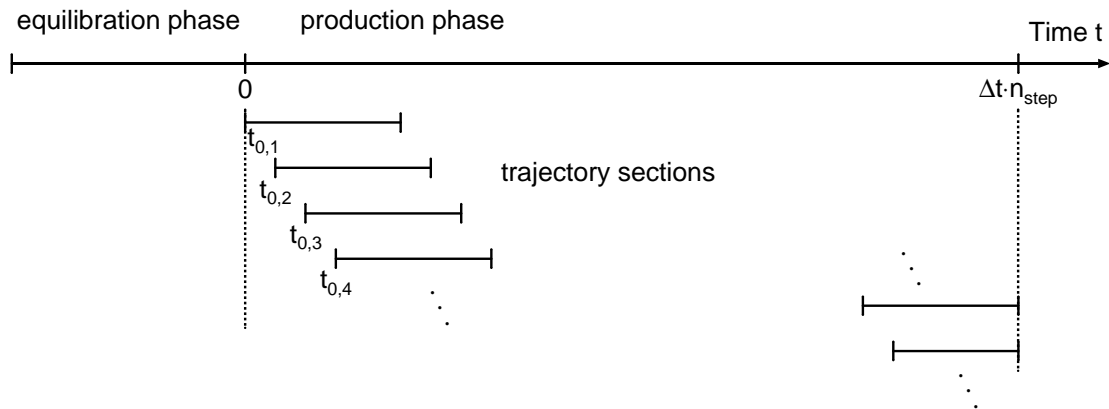
Figure 3.4. Choice of trajectory sections from simulated phase space trajectories.

For the determination of time-correlation functions and generalized displacement functions, time origins are taken at equally spaced intervals along the simulated phase space trajectory of the system as shown in Figure 3.4. Starting at the time origins, phase variables are correlated with their values at the origins and generalized displacement functions are calculated along short sections of the phase space trajectory. The length of the trajectory sections is chosen so that all relevant correlations decay to zero and the linear regime of the generalized displacement functions is evident within the length of the sections. The intervals between time origins and

the length of the trajectory sections depended on the transport coefficient and on the temperature and density of the state point.

In terms of simulation parameters, time-correlation functions are in general given by

$$\langle A(t)B(0)\rangle = \frac{1}{n_{\text{to}}} \sum_{i=1}^{n_{\text{to}}} A(t_{0,\text{i}} + t)B(t_{0,\text{i}}) \tag{3.19}$$

and their corresponding generalized displacement functions by

$$\langle [A(t) - A(0)][B(t) - B(0)]\rangle = \frac{1}{n_{\text{to}}} \sum_{i=1}^{n_{\text{to}}} \int_{t_{0,\text{i}}}^{t_{0,\text{i}}+t} A(t')\,\mathrm{d}t' \int_{t_{0,\text{i}}}^{t_{0,\text{i}}+t} B(t')\,\mathrm{d}t' \quad . \tag{3.20}$$

The parameter n_{to} denotes the number of time origins of trajectory sections along the phase space trajectory and $t_{0,\text{i}}$ is the ith time origin. Values of time-correlation functions are calculated at times t that are integer multiples of the time step size Δt. Autocorrelation functions and their corresponding mean-squared displacements are special cases of Eqs. (3.19) and (3.20) with $B = A$. Practically, the parameters for the calculation of time-correlation and generalized mean-squared displacement functions were chosen so that the available computing resources were optimally utilized.

Simulation averages of mean-squared displacements and time-correlation functions were computed by the algorithm described by Allen and Tildesley [10, p. 185]. The generalized displacements for the collective Einstein relations were evaluated according to Eq. (2.168) by numerical integration of their corresponding thermodynamic fluxes using Simpson's rule [1, p. 886]. The analysis software takes advantage of the parallelism provided by the independent components of the thermodynamic fluxes. For instance, time-correlation functions of the three independent off-diagonal elements of the stress tensor are computed in parallel on three PEs, while the pressure fluctuation autocorrelation function is computed on a fourth PE. The same parallelization strategy is applied for the computation of the heat flux vector and all generalized mean-squared displacements corresponding to these thermodynamic fluxes. Velocity autocorrelation functions and mean-squared particle displacements are averaged over all particles of the system. Thus, every particle is assigned to a particular PE, which performs all computations for its assigned particles. Averages over all particles are calculated at the end of the program run by performing global sums over all participating PEs.
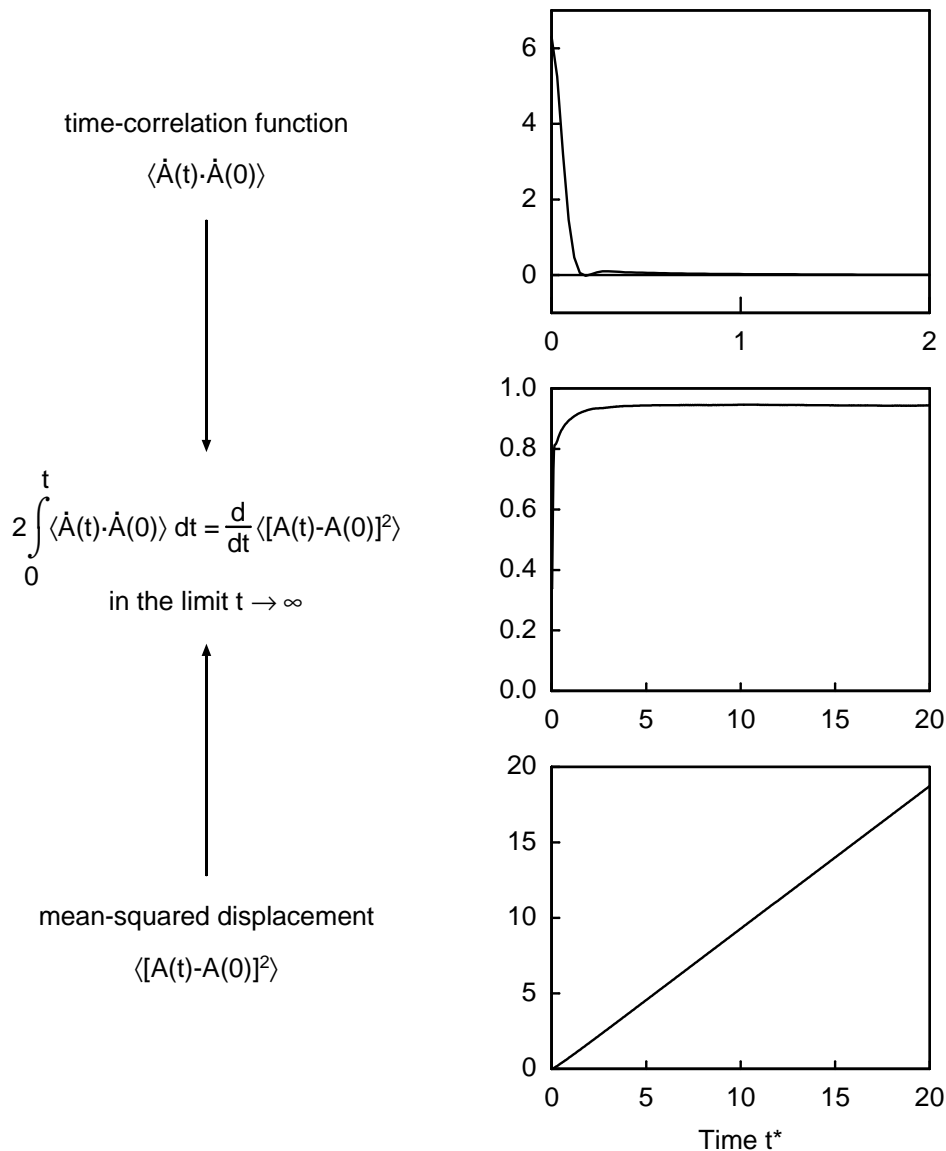
Figure 3.5. Illustration of the relation between a time-correlation function and its corresponding mean-squared displacement function. The depicted functions are results for self-diffusion at the state point ($T^* = 2.1$, $\rho^* = 0.8$) for the Lennard-Jones fluid.

To determine the long time limit of the slope of a mean-squared displacement function, it is plotted over time in a so-called Einstein plot. The long time limit of the slope is then obtained from a least-squares fit of a straight line to the linear regime of the plot. When inspecting an Einstein plot, on first sight, the linear regime is difficult to locate. From the derivation of the generalized Einstein relations in

Section 2.5.4, it is known that the mean-squared displacement, its corresponding time-correlation function and the derivative of the mean-squared displacement with respect to time are closely related to each other by simple mathematical operations. These relationships are illustrated in Figure 3.5 and can be utilized to locate the linear regime of the Einstein plot.

The linear regime of the plot starts, where the time-correlation function has decayed to zero. In the example in Figure 3.5, the time-correlation function appears to have decayed to zero within one reduced time unit. However, integration of the time-correlation function or differentiation of the mean-squared displacement reveals that there is a significant contribution from the interval between one and five to the value of the transport coefficient. If this contribution was neglected, the value for the transport coefficient would be much too low. The plateau of the integrated time-correlation function is reached after about five reduced time units. At this point, the linear regime of the mean-squared displacement starts and the straight line can for example be fitted in the interval between six and ten. For the choice of the fit interval, these three functions are inspected for every Einstein plot individually. By this procedure, it is ensured that the initial behaviour is discarded and the fit is done to that part of the plot where the linear regime is evident. The interval for the fit is chosen individually for the self-diffusion plots, the plots for the three viscosity and thermal conductivity contributions and the bulk viscosity plots for every simulation. The values for the total viscosity and thermal conductivity are then obtained as the sum of the three contributions according to Eqs. (2.198) and (2.199).

From the relationships between the three functions it is evident that the slope obtained by the fit of a straight line to the mean-squared displacement is equal to the value of a constant obtained from a fit to the time integral of the time-correlation function in the same interval. Thus, transport coefficients could have equally well be evaluated from time-correlation functions.

3.3.2   Estimation of Statistical Errors in Simulation Results

Any simulation result is subject to systematic and statistical errors. Systematic errors are for example caused by the potential truncation at the cutoff radius, finite-size effects due to the use of small particle numbers, numerical imprecisions in the integration of the equations of motion or insufficient equilibration of the system before the production phase of a simulation. Systematic errors can be eliminated to some extent by a careful choice of the simulation parameters. The influence of

the simulation parameters on the results is discussed in the next section. Here, the estimation of statistical errors is treated. Statistical errors arise because simulation averages are taken over phase space trajectories of finite length. To obtain precise simulation data with small uncertainties, the system must experience a large number of characteristic processes on the molecular scale, which are responsible for the macroscopic behaviour, throughout the simulation.

Statistical errors in simulation averages are estimated by a method described by Allen and Tildesley [10, p. 192], which is originally due to Friedberg and Cameron [53]. If all instantaneous values of a phase variable $A(i\Delta t)$ were statistically independent, their distribution would be Gaussian with the variance

$$\sigma^2(A) = \frac{1}{n_{\text{step}}} \sum_{i=1}^{n_{\text{step}}} (A(i\Delta t) - \langle A \rangle)^2 \tag{3.21}$$

and the variance of the simulation average could be estimated by

$$\sigma^2(\langle A \rangle_{\text{gauss}}) = \frac{\sigma^2(A)}{n_{\text{step}}} = \frac{1}{n_{\text{step}}^2} \sum_{i=1}^{n_{\text{step}}} (A(i\Delta t) - \langle A \rangle)^2 \quad . \tag{3.22}$$

In this case, the standard deviation $\sigma(\langle A \rangle_{\text{gauss}})$ would be a good measure for the statistical uncertainty of the simulation average. Since instantaneous phase variables at successive time steps are usually highly correlated, Gaussian statistics do not apply. To account for the correlation of successive phase variables, Friedberg and Cameron [53] introduced the statistical inefficiency S. A simulation of length n_{step} is broken into b blocks of length n_{b} so that $b\,n_{\text{b}} = n_{\text{step}}$. For every block j, the block average of A is given by

$$\langle A \rangle_{\text{b,j}} = \frac{1}{n_{\text{b}}} \sum_{i=1}^{n_{\text{b}}} A([j(n_{\text{b}} - 1) + i]\Delta t) \quad . \tag{3.23}$$

An estimate for the variance of the instantaneous values $A([j(n_{\text{b}} - 1) + i]\Delta t)$ in block j is

$$\sigma^2(A_{\text{b}}) = \frac{1}{n_{\text{b}}} \sum_{i=1}^{n_{\text{b}}} (A([j(n_{\text{b}} - 1) + i]\Delta t) - \langle A \rangle_{\text{b,j}})^2 \tag{3.24}$$

and an estimate for the variance of the block average $\langle A \rangle_{\text{b,j}}$ is

$$\sigma^2(\langle A \rangle_{\text{b}}) = \frac{1}{n_{\text{b}}^2} \sum_{i=1}^{n_{\text{b}}} (A([j(n_{\text{b}} - 1) + i]\Delta t) - \langle A \rangle_{\text{b,j}})^2 \quad . \tag{3.25}$$

On the other hand, the average of all block averages can be used to estimate the variance of the block average by

$$\sigma^2(\langle A \rangle_{\mathrm{b}}) = \frac{1}{b} \sum_{j=1}^{b} (\langle A \rangle_{\mathrm{b,j}} - \langle A \rangle)^2 \quad . \tag{3.26}$$

If the instantaneous values of A in a block were uncorrelated, their distribution would be Gaussian and the variance of the block average $\sigma^2(\langle A \rangle_{\mathrm{b}})$ according to Eq. (3.25) would be inversely proportional to the block length n_{b}. Thus, the product $n_{\mathrm{b}}\sigma^2(\langle A \rangle_{\mathrm{b}})$ would not depend on the block length. If, however, successive instantaneous phase variables are correlated, the product $n_{\mathrm{b}}\sigma^2(\langle A \rangle_{\mathrm{b}})$ will rise until it approaches a plateau value. The plateau indicates that the block length is so large that there are no correlations between successive blocks and the block averages obey Gaussian statistics.

This argument is used to define the statistical inefficiency in A as

$$S_{\mathrm{A}} = \lim_{n_{\mathrm{b}} \to \infty} \frac{n_{\mathrm{b}}\sigma^2(\langle A \rangle_{\mathrm{b}})}{\sigma^2(A)} \quad . \tag{3.27}$$

It is the factor by which the calculated variance of a simulation average must be multiplied to compensate for the correlation of successive instantaneous phase variables. An estimate for the statistical uncertainty of the simulation average is

$$\sigma(\langle A \rangle) = S_{\mathrm{A}}^{1/2}\sigma(\langle A \rangle_{\mathrm{gauss}}) \quad . \tag{3.28}$$

Hence, the uncertainty of the simulation average is by a factor of $S_{\mathrm{A}}^{1/2}$ larger than its standard deviation on the assumption of uncorrelated Gaussian statistics.

Practically, variances of block averages are calculated by Eq. (3.26) for different choices of the block length $n_{\mathrm{b}} = 1, 2, \ldots$ from the stored instantaneous phase variables on hard disk. Statistical inefficiencies are then derived from plots of the ratio $n_{\mathrm{b}}\sigma^2(\langle A \rangle_{\mathrm{b}})/\sigma^2(A)$ over the square root of the block length as shown in Figure 3.6 for four selected phase variables at the state point ($T^* = 3.0$, $\rho^* = 0.8$). The expected plateaus are evident for all four phase variables so that the statistical inefficiency can be unambiguously determined. In some instances, it was observed that the ratio $n_{\mathrm{b}}\sigma^2(\langle A \rangle_{\mathrm{b}})/\sigma^2(A)$ decreases after exhibiting a maximum without forming the expected plateau. In such cases, the value of the maximum was taken as an estimate for the statistical inefficiency.

Figure 3.7 depicts results for the estimation of uncertainties of simulation averages of the temperature, pressure and squared translational and configurational
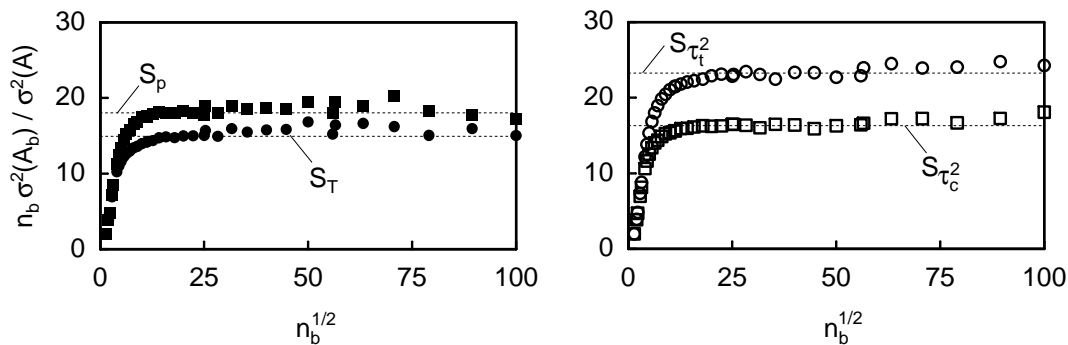
Figure 3.6. The ratio $n_{\mathrm{b}}\sigma^2(\langle A\rangle_{\mathrm{b}})/\sigma^2(A)$ for the temperature ($\bullet$), pressure($\blacksquare$), squared translational shear stress ($\bigcirc$) and squared configurational shear stress ($\square$) as a function of the square root of the block length n_{b} at the state point ($T^* = 3.0$, $\rho^* = 0.8$). The simulation was performed with 1372 particles and $r_{\mathrm{cut}}^* = 6.5$ and extended over 2 million time steps.

shear stresses along the supercritical isotherm $T^* = 3.0$. The relative standard deviation on the assumption of Gaussian statistics of the temperature simulation averages increases almost linearly with density, while the corresponding quantity for the pressure increases at low densities, exhibits a maximum close to the critical density and decreases at high densities. The relative standard deviations of the simulation averages of both squared shear stress contributions take values close to $(2/n_{\mathrm{step}})^{1/2} = (2/2\cdot 10^6)^{1/2} = 0.1\%$ along the isotherm. At low densities, the relative standard deviation of the squared configurational shear stress deviates from this value and becomes larger.

The occurrence of the value $(2/n_{\mathrm{step}})^{1/2}$ can be explained by statistical arguments. On the assumption that the instantaneous values of an arbitrary phase variable B_{i} whose ensemble average vanishes obey a Gaussian distribution, the average of the squared phase variable $\langle B^2\rangle$ is the second moment of the distribution of the instantaneous values. The standard deviation of the squared phase variable is given by

$$\sigma(B^2) = \sqrt{\langle B^4\rangle - \langle B^2\rangle^2} \quad, \tag{3.29}$$

where the ensemble average $\langle B^4\rangle$ is the fourth moment of the distribution of the B_{i}. For a Gaussian distribution, both moments can explicitly be calculated [1, p. 927]. With Eq. (3.29), the relative standard deviation $\sigma(\langle B^2\rangle)/\langle B^2\rangle$ then follows as $(2/n_{\mathrm{step}})^{1/2}$. Deviations from this value, as observed for the squared configura-
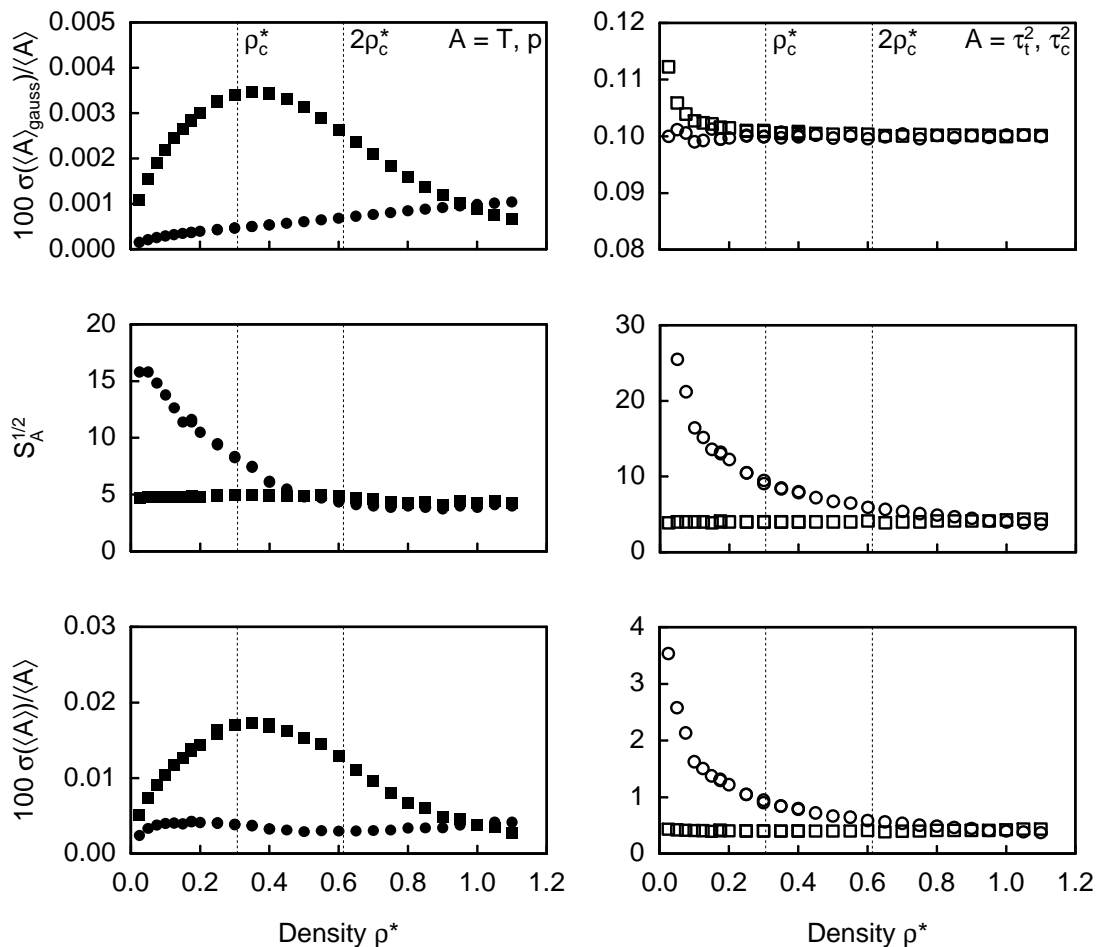
Figure 3.7. Relative standard deviation, square root of the statistical inefficiency and relative uncertainty of the temperature (●), pressure (■), squared translational shear stress (○) and squared configurational shear stress (□) as a function of density along the supercritical isotherm $T^* = 3.0$. The simulations were performed with 1372 particles and $r_{\mathrm{cut}}^* = 5.5$ or 6.5 and extended over 2 million time steps.

tional shear stress at low densities, indicate that the corresponding instantaneous phase variables, here the configurational shear stresses, do not obey a Gaussian distribution.

The statistical inefficiencies of the pressure and squared configurational shear stress are of similar magnitude and constant along the isotherm. Both quantities depend on the configuration of the system and are collective phase variables. On the other hand, the temperature and squared translational shear stress depend only on particle velocities. Since there are no instantaneous correlations between the

velocities of different particles, these quantities are single particle properties. Above two times the critical density, their inefficiencies are of similar magnitude as the inefficiencies of the pressure and configurational squared shear stress, but below this point they increase strongly with decreasing density. This behaviour can be explained by the frequency of events on the molecular scale. In gases, collisions between particles take place infrequently, whereas in liquids the particles are close-packed so that collisions occur continuously. Thus, the sampling of phase space is efficient at high density liquid states, but declines with decreasing density.

Combining the results for the relative standard deviations and statistical inefficiencies yields the relative uncertainties for the simulation averages of the four quantities. The relative statistical uncertainty of the pressure follows that of the standard deviation and never exceeds 0.02 %, while the uncertainty of the temperature is almost constant along the isotherm and remains below 0.005 %. The uncertainties of the two squared shear stress contributions resemble the behaviour of their corresponding statistical inefficiencies. For the squared configurational shear stress, the uncertainty is lower than 0.5 % and constant along the isotherm, whereas for the squared translational shear stress it increases from 0.4 % at liquid densities up to almost 4 % in the gas region. To decrease this quite high uncertainty of the data in the gas region, the simulation length must be increased.

Uncertainties of thermodynamic state variables that are determined by combinations of phase space functions which themselves are combinations of several simulation averages, such as the isochoric heat capacity, isochoric pressure coefficient or the speed of sound (see Table 2.1), were estimated by the method suggested by Lustig [126, p. 174]. In principle, the uncertainties of the simulation averages can be estimated by the method of Allen and Tildesley as described above. Then, the error propagation law [26, p. 38] can be used to estimate the uncertainties of the phase space functions and thermodynamic state variables. This procedure yields unreasonable estimates for the uncertainties because the error propagation law strictly applies only to statistically independent quantities. However, the simulation averages required to calculate the thermodynamic state variables are highly correlated.

The method of Lustig defines fictitious instantaneous values for the thermodynamic state variables. The simulation result for a thermodynamic state variable Z after n_{step} time steps is given by

$$\langle Z \rangle_{n_{\text{step}}} = f(\Omega_{\text{ij}}) \quad , \tag{3.30}$$

in which the phase space functions are obtained from simulation averages after n_{step}

time steps. A fictitious instantaneous value Z_i is defined by

$$\langle Z \rangle_{n_{step}} \overset{!}{=} \frac{1}{n_{step}} \sum_{i=1}^{n_{step}} Z_i = \frac{1}{n_{step}} \left[(n_{step} - 1)\langle Z \rangle_{n_{step}-1} + Z_{n_{step}} \right] \quad , \tag{3.31}$$

where it has been used that the average after $n_{step} - 1$ time steps is

$$\langle Z \rangle_{n_{step}-1} = \frac{1}{n_{step} - 1} \sum_{i=1}^{n_{step}-1} Z_i \quad . \tag{3.32}$$

An expression for the instantaneous value $\langle Z \rangle_i$ is obtained from the second equality in Eq. (3.31) by setting $n_{step} = i$ so that

$$Z_i = i\langle Z \rangle_i - (i-1)\langle Z \rangle_{i-1} \quad . \tag{3.33}$$

Hence, the fictitious instantaneous value Z_i is the difference of the simulation averages after i and $i-1$ time steps, each weighted with the number of time steps i and $i-1$. On the fictitious instantaneous values, the method of Friedberg and Cameron can be applied as described above to determine the uncertainty of the simulation result for Z.

This method was applied to determine the uncertainties of the simulation results for the isochoric heat capacity, isothermal pressure coefficient and zero frequency speed of sound. It was found that it yields reliable estimates for the uncertainties of these thermodynamic state variables which resemble the scatter of the data.

Uncertainties of simulation results for transport coefficients are determined by the uncertainties of all quantities entering into the Einstein relations. These are the slopes of the generalized mean-squared displacements and, additionally, for the viscosity, bulk viscosity and thermal conductivity the simulation averages of the temperature. Since for the present simulations the uncertainties of temperature simulation averages are by several orders of magnitude smaller than the uncertainties of the slopes of the generalized mean-squared displacements, the influence of the uncertainty of the temperature simulation averages is neglected. Thus, the uncertainties of the transport coefficients are solely determined by the uncertainties of the slopes of the generalized mean-squared displacements.

A procedure for estimating the uncertainty of the slope of a generalized mean-squared displacement involves two steps. First, the uncertainty of the simulation average of the generalized mean-squared displacement function is estimated for every data point of the function. Then, the error propagation law is used to estimate how the uncertainty of the mean-squared displacement function propagates through the

least-squares fit into the slope of the linear part of the function. Brandt [26] for example describes a method for estimating the uncertainty of the slope of a straight line fitted to statistically independent data points. This method was applied to estimate the uncertainty of the slopes of the mean-squared displacement functions. It was found that the resulting uncertainties for the transport coefficient data were much too low when compared with the scatter of the data along isotherms and isochors. The reason for the underestimation of the uncertainties is that successive data points of the mean-squared displacement functions are not independent, but highly correlated. In this case, the error propagation law does not apply. A rigorous method to estimate the propagation of uncertainties of correlated data into the slope of the fitted straight line is not available.
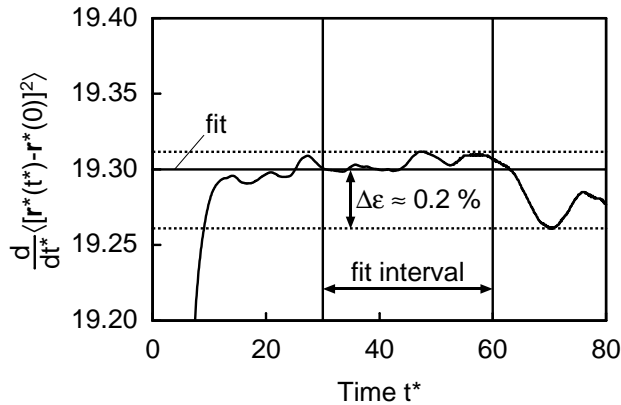

Figure 3.8. Derivative of the mean-squared particle displacement with respect to time as a function of time at the state point ($T^* = 2.5$, $\rho^* = 0.1$). The simulation was carried out with 1372 particles and $r^*_{\mathrm{cut}} = 6.5$ and extended over $2 \cdot 10^6$ time steps.

For this reason, the statistical uncertainties of the simulation results for the transport coefficients were estimated from the scatter of the data along isotherms and isochors and from intensive comparisons with literature data. Moreover, the generalized mean-squared displacement functions were inspected by the following method to estimate the uncertainty of the slope of the fitted straight line. The derivative of the generalized mean-squared displacement with respect to time together with the corresponding derivative of the fitted straight line is plotted over time. An example for such a plot for self-diffusion at the state ($T^* = 2.5$, $\rho^* = 0.1$) is depicted in Figure 3.8. In this plot, the slope of the fitted straight line appears as a horizontal line. An estimate of the uncertainty of the slope is provided by the difference between

the largest deviation of the mean-squared displacement function from the horizontal line.

In this work, uncertainties of the simulation results are not reported for every single state point, but are summarized for characteristic parts of the fluid region of the phase diagram.

3.4   Influence of Simulation Parameters

In this work, molecular dynamics simulations are carried out to determine macroscopic properties of the Lennard-Jones model fluid. To ensure that the simulated system is a representative model of the macroscopic system, the influence of the simulation parameters on the results of the simulation must be minimized. Since it is not *a priori* known how the simulation parameters must be chosen, a systematic investigation of their influence on the results for macroscopic properties is required.

Results of a simulation can depend on the number of particles in the simulated system, the cutoff radius, at which the intermolecular potential function is truncated, the time step size for the algorithm used to integrate the equations of motion, the length of the equilibration phase and the time period covered by the production phase of the simulation.

In all simulations of this work, the velocity-Verlet algorithm was used to integrate the equations of motion with the step size $\Delta t^* = 0.003$. Even extremely long simulations over 50 million time steps at gaseous states could be run without rescaling the velocities in order to correct for small energy drifts as sometimes done by other authors in literature [10]. The total energy of the system was always kept constant within two parts in 10^5. All simulations were equilibrated over at least 100000 time steps before starting the production phase to attain thermodynamic equilibrium in the system. With these choices, it is ensured that both parameters do not significantly influence the results for the macroscopic properties of the system.

For a prescribed density, the number of particles determines the size of the simulation box by the relation $L = (N/\rho)^{1/3}$. As the Green-Kubo integrals and Einstein relations determine the transport coefficients in the zero wave vector and zero frequency limit, the number of particles must be chosen so large that the full wave length and frequency spectrum of the fluctuations is present in the simulated system. Fluctuations with wave lengths larger than the box length are suppressed and low frequency fluctuations whose decay takes longer than the transit time of a disturbance through the system are not correctly sampled. Moreover, the sufficient

sampling of low frequency fluctuations must be ensured by an appropriate choice of the length of the production phase of the simulation.

The cutoff radius influences the results of a simulation in two ways. First, contributions to the instantaneous configurational contributions of the phase variables from pairs of particles whose distance is larger than the cutoff radius are neglected. Second, contributions to the force on a particle from particles at distances larger than the cutoff radius are not considered. The latter small systematic errors are propagated into the particle trajectories by the numerical integration of the equations of motion.
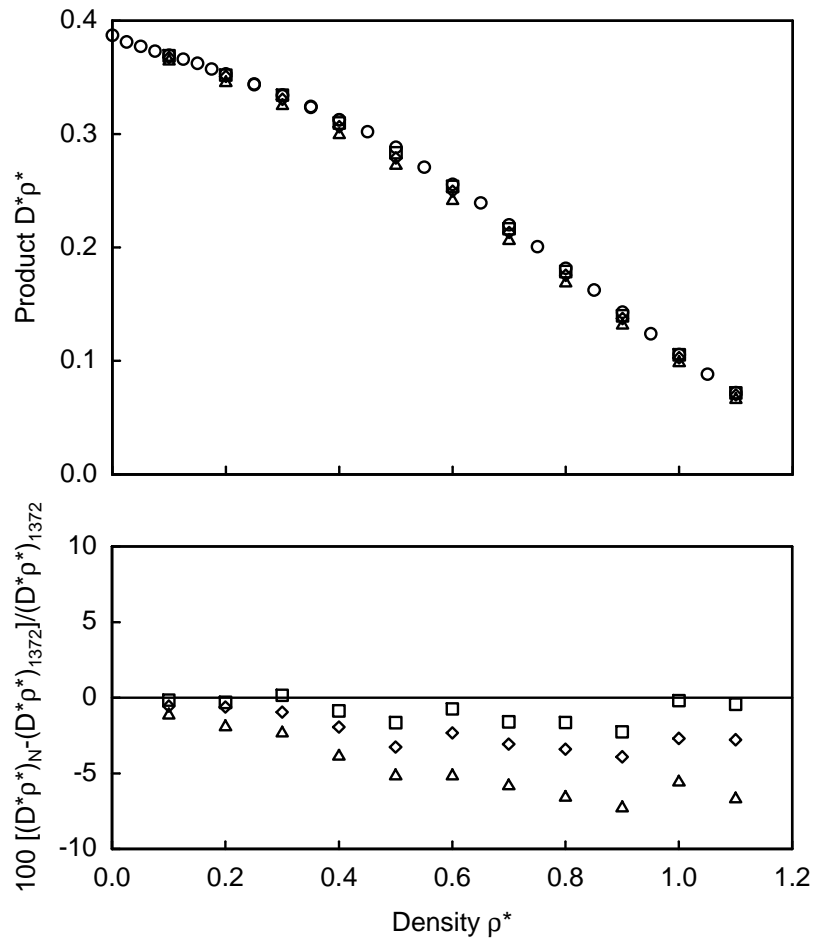
Figure 3.9. The product $D^*\rho^*$ along the isotherm $T^* = 3.0$ as a function of the density for different numbers of particles N. Simulation parameters: ($\bigcirc$) $N = 1372$, $r^*_{\mathrm{cut}} = 5.0$ to 6.5, 10^6 time steps; ($\square$) $N = 864$, $r^*_{\mathrm{cut}} = 3.0$, $3 \cdot 10^6$ time steps; ($\diamond$) $N = 500$, $r^*_{\mathrm{cut}} = 3.0$, $6 \cdot 10^6$ time steps; ($\triangle$) $N = 256$, $r^*_{\mathrm{cut}} = 3.0$, $10 \cdot 10^6$ time steps.

Several simulation series were carried out to examine the dependence of results for the transport coefficients on the number of particles and cutoff radius. In Figure 3.9, the influence of the number of particles on the product $D^*\rho^*$ is shown for the supercritical isotherm $T^* = 3.0$. The product $D^*\rho^*$ shows a strong dependence on the number of particles between from the density $\rho^* = 0.2$ up to the highest simulated density close to the freezing line. The largest effect with up to 8 % difference between the results for 256 and 1372 particles is observed at intermediate densities. At gaseous densities below $\rho^* = 0.3$, the dependence of the number of particles decreases and good agreement between the results for 864 and 1372 particles is found. Consequently, with 1372 particles the results for $D^*\rho^*$ at densities $\rho^* \leq 0.3$ represent the product $D^*\rho^*$ for the macroscopic Lennard-Jones model fluid well. However, at higher densities the macroscopic products $D^*\rho^*$ are expected to be higher than the results for 1372 particles.

The influence of the number of particles on the viscosity, its three contributions and the bulk viscosity was investigated at the state point ($T^* = 0.722$, $\rho^* = 0.8442$). This state point is very close to the triple point of the Lennard-Jones fluid ($T^*_{tr} = 0.67$, $\rho^*_{tr} = 0.8442$) [2]. The viscosity at this state was subject of many simulations studies in literature (see Table 3.1 below) since it was first studied by Levesque et al. [118]. At this lowest temperature where a liquid state exists, the correlation functions decay extremely slowly and, thus, the viscosity should be most difficult to obtain. Altogether, 7 simulations were carried out with 108 to 4000 particles. In simulations with 1372 or more particles, the cutoff radius was set to $r^*_{cut} = 5.5$, while in simulations with less particles it was chosen slightly smaller than the half box length. All 7 simulations extended over 10 million time steps. After 10 million time steps, the simulation with 4000 particles was continued up to 25 million time steps.

The results of this simulation series are reported in Table D.7, while details of the literature viscosity data are collected in Table 3.1. Data for the viscosity contributions were reported by Erpenbeck [45] and Stassen and Steele [201]. Erpenbeck [44] reported six data which were derived from simulations with a modified Lennard-Jones potential. In order to minimize the influence of the cutoff radius, the long range attractive part of the Lennard-Jones potential was replaced by a cubic polynomial function that decays continuously to zero. Evans et al. [48] pointed out that the modification of the intermolecular potential function results in macroscopic thermodynamic state variables and transport coefficients that deviate significantly from the corresponding properties of the original potential. Hence, these data cannot be

compared with those data sets obtained with the original Lennard-Jones potential and are excluded from further considerations. Sharma and Woodcock [194] and Sharma [195] presented additional data, which were obtained by the Green-Kubo integral formulas, but they used a different cutoff model to compute the shear stress correlation functions. These data are also not taken into account in the following discussion. Heyes [81] provided 17 nonequilibrium data which were not extrapolated to zero shear rate and can therefore not be compared with the present data.

Bulk viscosity data are reported in six literature sources. The details of the bulk viscosity data are provided in Table 6.1 together with the details of further bulk viscosity data sets. Levesque et al. [118], Levesque and Verlet [119] and Schoen [190] derived bulk viscosity data from the same simulations as described in Table 3.1 for the viscosity. Heyes [80, 82] and Hoover et al. [96] employed nonequilibrium techniques to determine the bulk viscosity at this state point.

All figures to be discussed in the remainder of this chapter are collected at the end of the chapter. Figure 3.10 depicts the results for the viscosity, the viscosity contributions and the bulk viscosity as a function of the inverse number of particles at this state point and includes literature data for these quantities. At this state point, the viscosity is dominated by the η_{cc}^*-contribution so that η^* closely resembles the behaviour of η_{cc}^*. All three contributions increase with the number of particles. The contribution η_{tt}^* yields the smallest contribution to the viscosity and shows the weakest dependence on the number of particles. The cross contribution η_{tc}^* shows the highest scatter, but the overall tendency to increase with the number of particles is evident. It is about 20 % larger than η_{tt}^*. Altogether, both contributions amount to less than 5 % of the total viscosity.

The comparison of the present data with literature data starts by observing that the literature data can be divided into two groups. The first group contains the data of Ashurst and Hoover [13], Evans [47], Heyes et al. [78, 79, 82, 84, 85], Hoover [96], Levesque et al. [118], Levesque and Verlet [119], Pollock [177], Schoen and Hoheisel [189], Sharma and Woodcock [194], Sharma [195], Singer et al. [197], Stassen and Steele [201] and Trozzi and Cicotti [211]. These data are in part relatively old and were often derived from short simulation runs. Therefore, the uncertainty and scatter of the data is quite high. In some instances, single data agree well with the data of this work. A second group summarizes data sets which are more recent and derived from long simulation runs. These are the data of Erpenbeck [45], Evans [48] and Ferrario et al. [50]. The data of the second group agree well with the data of this work. The few literature data for the viscosity contributions yield only little

Table 3.1. Literature data for the viscosity of the Lennard-Jones fluid close to its triple point. Abbreviations: DT: difference in trajectories method, ER: Einstein relation method, GK: Green-Kubo integral method, TS: trajectory segments, WR: wall reservoir boundary conditions, MC-GO: Monte Carlo generated time origins. OS: oscillating shear perturbed Hamiltonian method, LE: Lees-Edwards shear boundary conditions. Remarks: 1): not reported by the authors.

Author		Year	Data	Symbol	Method	Ensemble	N	r^*_{cut}	T^*	ρ^*	Simul. Length
This work		2002	20	●	ER	*NVEMG*	256-4000	2.5-5.5	0.717-0.733	0.8442	30000-75000
Ashurst	[13]	1975	3	⋈	WR	-	108-324	1)	0.722	0.8442	464
Erpenbeck	[45]	1988	2	⋈	GK	*NVT*	108, 864	2.5	0.722	0.8442	MC-GO
Evans	[47]	1981	1	⋈	LE	*NVT*	108, 256	2.5	0.722	0.8442	-3640
Evans	[48]	1989	1	×	LE	*NVT*	2048	3.5	0.722	0.8442	120-560
Ferrario	[50]	1991	7	□	GK	*NVT*	500-4000	2.5	0.725	0.8442	1600-18000
Heyes	[78]	1980	1	◨	DT	*NVT*	108	2.5	0.722	0.8442	20 TS
Heyes	[79]	1983	1	◪	DT	*NVEMG*	256	2.5	0.73	0.8442	150
Heyes	[82]	1986	1	⧅	DT	*NVT*	256	2.5	0.722	0.8442	200 TS
Heyes	[84]	1988	3	◑	GK	*NVT*	108-500	1)	0.72	0.848	3295-8780
Heyes	[85]	1990	1	◧	GK	*NVT*	256	2.5	0.722	0.8442	1500
Hoover	[96]	1980	1	▶	WR	-	864	2.5	0.715	0.8442	700
Levesque	[118]	1973	1	▲	OS	-	108	2.5	0.722	0.8442	0.03-7.7
Levesque	[119]	1987	5	✳	GK	*NVEMG*	108-864	1)	0.715-0.728	0.8442	11-88
Pollock	[177]	1980	2	○	GK	1)	256, 500	1)	0.722	0.8442	1)
Schoen	[189]	1985	1	▽	GK	*NVEMG*	500	2.5	0.73	0.8442	232
Sharma	[194]	1991	4	+	GK	*NVT*	32-500	1.6, 2.5	0.72	0.844	80-400
Sharma	[195]	1994	5	◇	GK	*NVT*	32-864	1.6, 2.5	0.72	0.84	80-400
Singer	[197]	1980	1	▣	DT	*NVE*	256	1)	0.722	0.8442	100 TS
Stassen	[201]	1995	1	⧓	GK	*NVEMG*	256	3.4	0.72	0.8445	325
Trozzi	[211]	1984	2	■	WR	-	180, 384	2.5, 3.5	0.722	0.8442	1)

additional insight. The configurational-configurational contribution η_{cc}^* follows the corresponding data for the total viscosity, while the data for the cross-contribution η_{tc}^* are much lower than the present data for this contribution. Good agreement is found between the present and the literature data for the translational-translational contribution η_{tt}^*.

For the extrapolation of the data for the viscosity and viscosity contributions at $(T^* = 0.722, \rho^* = 0.8442)$ to infinite system size $(N^{-1} \to 0)$, a linear dependence on the inverse number of particles is assumed. From a weighted linear least-squares fit to the present data, the estimates for the infinite system size limit

$$\eta^* = 3.258 \pm 0.033$$
$$\eta_{tt}^* = 0.05079 \pm 0.00033$$
$$\eta_{tc}^* = 0.06023 \pm 0.0042$$
$$\eta_{cc}^* = 3.147 \pm 0.028 \quad .$$

are derived. Erpenbeck [45] estimated the value $\eta^* = 3.345 \pm 0.068$ for the infinite system size viscosity from a weighted linear least-squares fit to his data for a modified Lennard-Jones potential. To account for the difference in the potential function, a correction was applied to the data before the fit. Schoen and Hoheisel [189, 190] reported the value $\eta^* = 3.18 \pm 0.15$ for a simulation with 500 particles. They observed no dependence of their data on the number of particles within the uncertainty of the data for systems of more than 256 particles. Therefore, this value represents the infinite system size viscosity within the quoted uncertainty. The present value agrees with these two literature results within the combined uncertainties.

The present bulk viscosity data show higher scatter than the viscosity data, but are more consistent than the literature data. Good agreement is found between the present data and two data reported by Levesque and Verlet for 864 particles [119] and with the datum published by Schoen [190] for 500 particles. The other data of Levesque [118] and Levesque and Verlet [119] are lower than the present data. The data of Hoover [96] and Heyes [80, 82] $\eta_b^* = 1.55$ and $\eta_b^* = 1.47$ are much higher than all other data and lie outside the range of Figure 3.10. This large difference may be due to use of nonequilibrium simulations by the two authors.

As for the viscosity, an estimate for the bulk viscosity for the infinite system size limit was derived from a weighted linear least-squares fit to the present data, yielding

$$\eta_b^* = 1.161 \pm 0.019 \quad .$$

The value for 108 particles was excluded from the fit because it appears to be too high compared with the other data.

To conclude, for the target system size of 1372 particles employed in the present simulations the statistical uncertainty of the data is larger than their dependence on the number of particles, even for long simulation runs over ten million time steps. Therefore, the dependence of the simulation data on the number of particles for the viscosity and bulk viscosity is negligible.

The influence of the cutoff radius on the simulation results was investigated at the same state point ($T^* = 0.722$, $\rho^* = 0.8442$) with a series of 12 simulations employing different cutoff radii between $r_{\text{cut}}^* = 2.5$ and 5.5 in steps of $\Delta r_{\text{cut}}^* = 0.25$. These simulations extended over 10 million time steps each. The results for selected thermodynamic state variables, the product $D^*\rho^*$, the bulk viscosity, the viscosity and the viscosity contributions are shown in Figures 3.11 and 3.12. The uncertainties of the bulk viscosity data and viscosity data and the data for the three viscosity contributions are indicated by the error bars. For all other quantities, the uncertainty is in most cases smaller than the size of the symbols.

Every simulation of this series was started from a cubic face-centred lattice configuration with the initial energy $e^* = $ -5.0. As the number of particles which are initially within the cutoff radius of a particle differs in general from its simulation average, the simulation averages of the total energy deviate slightly from the initial value. Due to this small energy difference, slightly different state points are simulated. The results for the temperature, configurational internal energy, configurational pressure, isochoric heat capacity, the product $D^*\rho^*$, the quantities $V^*/T^* \cdot \langle (\tau_{\text{t}}^*)^2 \rangle$ and $V^*/T^* \cdot \langle (\tau_{\text{c}}^*)^2 \rangle$ and the translational-translational viscosity contribution reflect this influence for small values of the cutoff radius. Above $r_{\text{cut}}^* = 4.5$ these simulation data show no dependence on the cutoff radius. The data for the isochoric heat capacity, the quantities $V^*/T^* \cdot \langle (\tau_{\text{t}}^*)^2 \rangle$ and $V^*/T^* \cdot \langle (\tau_{\text{c}}^*)^2 \rangle$ and the translational-translational viscosity contribution scatter more than the data for the other quantities.

Even higher scatter is found for the viscosity data, the translational-configurational and configurational-configurational viscosity contributions and the bulk viscosity data. As in the investigation of the particle number influence, the viscosity reflects the scatter pattern of the configurational-configurational viscosity contribution. At small cutoff radii, the uncertainty of the data is larger than the influence of the initial energy. For cutoff radii above $r_{\text{cut}}^* = 3.25$, the agreement of almost all data is within the combined uncertainties. A systematic dependence of any of the thermodynamic

state variables and transport coefficients on the cutoff radius is not observable. Consequently, the influence of the cutoff radius is negligible if it is chosen larger than 4.5. The accuracy of the simulation data is determined by their statistical uncertainty. Therefore, the length of the production phase of the simulation determines as the leading parameter the accuracy of the present simulation data for the viscosity and bulk viscosity.

The influence of the length of the production phase on the results for the viscosity in the gas region was examined for the subcritical isotherm $T^* = 1.2$. Figure 3.13 displays data for the viscosity and the viscosity contributions obtained from simulations over 2, 15 and 50 million time steps. It is evident that the scatter of the data reduces considerably with increasing simulation length. Thus, extremely long simulations are required to determine accurate transport coefficients in the gas region.

3.5   Simulation Details

For the determination of the transport coefficients of the Lennard-Jones model fluid, extensive equilibrium molecular dynamics simulations were carried out along 16 isotherms on 351 state points. The simulations were carried out in the classical molecular dynamics ensemble at constant $NVE\boldsymbol{MG}$ as described in Section 3.1. Input internal energies for a given temperature T^* and density ρ^* were calculated from the fundamental equation of state of Mecke et al. [142]. All simulations were performed with 1372 particles and a time step size $\Delta t^* = 0.003$. After an equilibration phase of 100000 up to 300000 time steps, the production phase of the simulations proceeded over 1.5 to 2 million time steps. The cutoff radius r^*_{cut} depended on the density of the state point. It was set to $r^*_{\mathrm{cut}} = 5.0$ for $\rho^* > 1.0$, 5.5 for $0.6 < \rho^* \leq 1.0$, and 6.5 for $\rho^* \leq 0.6$. With this parameter constellation, one simulation run typically required about 10 hours real time on a Cray T3E employing 16 PEs.

The distribution of the simulated state points in relation to the phase boundaries is given in Figure 3.14. The simulations extend over a wide range of the fluid region of the phase diagram from the low density gas to the compressed liquid close to the freezing line. The simulated state points cover the temperature range between $T^* = 0.7$ to 6.0. Metastable vapour and liquid states were also included. However, state points which apparently lie in the unstable region were not considered. Unstable states were identified by inspection of simulated heat capacities and isentropic compressibilities. If these thermodynamic state variables showed unphysical

behaviour or values, e.g., either negative or very large positive values, a state point was considered to lie in the unstable region. At every simulated state point, several thermodynamic state variables and the transport coefficients viscosity, bulk viscosity and the self-diffusion coefficient were evaluated as described in Section 3.3.1. The simulations on the gaseous parts of the isotherms $T^* = 0.8$, 0.9, 1.0 and 1.1 and on the liquid part of the isotherm $T^* = 1.1$ were carried out by Dr. Laesecke on SGI Origin Computers at the NIST Information Technology Laboratory in Gaithersburg (U.S.A.) as part of a collaborative project between the Institut für Themodynamik at the Universtät Hannover and the Physical and Chemical Properties of Fluids Division at the National Institute of Standards and Technology in Boulder (U.S.A.) with the simulation and analysis software developed by the author. Results for thermodynamic state variables, time-correlation functions and generalized mean-squared displacement functions were communicated to the author and analyzed at the Institute of Thermodynamics in Hannover.

In addition to this large body of simulations, two further simulation series were carried out. The first series repeated simulations at low temperature gaseous states between the temperatures $T^* = 0.7$ and 1.2 on 39 state points. The production phases of these simulations extended over 50 million time steps. These simulations were performed to determine the behaviour of the viscosity and bulk viscosity in this state region.

The second additional series was conducted to determine the shape of the thermal conductivity and bulk viscosity close-critical isotherm $T^* = 1.35$ in the vicinity of the critical density. The production phases of these 20 simulations extended over 2 million time steps. With input internal energies calculated from the fundamental equation of state of Mecke et al. [142], the simulations averages of the temperatures were slightly higher than 1.35 at states in the vicinity of the critical density. Therefore, 11 simulations were repeated with corrected input internal energies derived from the results of the first simulations. The production phases of these simulations extended over 10 million time steps. The thermal conductivity was calculated on the isotherm $T^* = 1.35$ only because of the higher demand for computational resources required for the computation of the instantaneous heat flux vectors.

The results for the transport coefficients are discussed in detail in the next chapters. A brief discussion of the results for thermodynamic state variables follows in the next section.

3.6   Simulation Results for Thermodynamic State Variables

The thermodynamic state variables of the Lennard-Jones model fluid were subject of many simulation studies, see for example [2, 102, 109, 122]. These works concentrated on the internal energy, pressure or the determination of the phase boundaries. Wide ranging data sets for higher thermodynamic derivatives, such as the isochoric heat capacity c_V, the thermal pressure coefficient γ_V or the zero frequency speed of sound w_0 are rarely reported in literature although they can be calculated with little additional computational effort in molecular dynamics simulations. For this reason, the thermodynamic state variables temperature T^*, potential energy u^*, pressure p^*, isochoric heat capacity c_V^*, isothermal pressure coefficient γ_V^* and zero frequency speed of sound w_0^* were evaluated at almost every simulated state point and are reported in Table D.1. These data supplement literature data sets for thermodynamic state variables and provide interesting insights into the thermodynamic behaviour of the Lennard-Jones model fluid. Instead of the total internal energies, the potential internal energies are reported in Table D.1 since internal energy data for the Lennard-Jones model fluid are usually reported in this form.

Statistical uncertainties of the data were estimated by the methods described in Section 3.3.2. The temperature data have the highest uncertainty of 0.06 % on subcritical isotherms. On supercritical isotherms, the uncertainty decreases from 0.04 % at $T^* = 1.3$ to 0.005 % at $T^* = 6.0$. The uncertainty of the pressure data is estimated to be 0.1 % at subcritical temperatures. In the vicinity of the critical density, larger uncertainties of up to 0.25 % are observed, while on supercritical isotherms the uncertainty decreases from 0.06 % at $T^* = 1.8$ to 0.01 % at $T^* = 6.0$. Data for the configurational internal energy have uncertainties of up to 0.6 % at subcritical gaseous states, whereas data in the liquid region are by at least one order of magnitude more accurate with an uncertainty of 0.01 %. With increasing temperature, the uncertainties of the configurational internal energy data on supercritical isotherms decrease from 0.09 % at $T^* = 1.3$ to 0.05 % at $T^* = 6.0$.

The uncertainties of the higher thermodynamic derivatives isochoric heat capacity c_V^*, isothermal pressure coefficient γ_V^* and zero frequency speed of sound w_0^* are generally larger than those of the pressure and potential internal energy. The largest uncertainties were observed at the highest densities close to the freezing line with 0.5 % for the isochoric heat capacity and 0.7 % for the isothermal pressure coefficient and zero frequency speed of sound data. With decreasing density, the uncertainties decline and are lower than 0.05 % at the lowest simulated densities. In the vicinity

of the critical point and at metastable states, the data for these three state variables have higher uncertainties up to 1.5 % and 5 %, respectively.

With the two recent fundamental equations of state of Mecke et al. [142] and of Kolafa and Nezbeda [110], accurate models are available, from which thermodynamic state variables can be calculated with high precision. Both models represent the thermodynamic state variables in terms of the Helmholtz free energy as a function of temperature and density. The present data are compared with the fundamental equation of state of Mecke et al.,which is slightly more accurate than the equation of Kolafa and Nezbeda. Although the simulation data were obtained as a function of density and internal energy in the $NVE\boldsymbol{MG}$-ensemble, the density and the simulation average for the temperature were taken as independent variables for this comparison.

Figure 3.15 shows the percentage deviations of the pressure, configurational internal energy and isochoric heat capacity data from the fundamental equation of state. At gaseous densities, the pressure data agree with the equation of state within 0.1 % over the whole temperature range. Slightly higher deviations up to 0.2 % are observed at intermediate densities on supercritical isotherms outside the critical region and close to the freezing line. In the critical region and on subcritical liquid states, the deviations increase to up to 1 %.

The data for the configurational internal energy at gaseous states agree with the equation of state within 0.1 % at supercritical temperatures and within 1 % at subcritical temperatures. At high density liquid states, the deviations are smaller than 0.1 %, except at high temperatures, where deviations up to almost 5 % at $T^* = 6.0$ are found. This large deviations are probably due to the fundamental equation of state because $T^* = 6.0$ is the highest temperature at which it was fitted to high density data close to the freezing line [142]. In the critical region, the deviations increase up to 1 %. For the majority of the pressure and configurational internal energy data, the deviations from the fundamental equation of state are larger than the statistical uncertainties of the data.

Due to larger uncertainties, the isochoric heat capacity data show higher scatter in the liquid region than the pressure and the configurational internal energy data, but still agree with the fundamental equation of state within 0.5 % over almost the whole range of thermodynamic state conditions. Higher systematic deviations are observed in the critical region.

Furthermore, the data for all three state variables p^*, u^* and c_V^* at metastable states on the gas and liquid parts of the subcritical isotherms show high systematic

deviations. Metastable pressure data lie below the equation of state, whereas configurational internal energy and isochoric heat capacity data show positive deviations.

In Figure 3.16, the percentage deviations for the thermal pressure coefficient and zero frequency speed of sound data data are depicted. The largest part of the thermal pressure coefficient data agrees with the fundamental equation of state within 1 %. Higher deviations up to several percent are found in the critical region and at metastable states.

The speed of sound data show large systematic deviations from the fundamental equation of state up to almost 20 %, which exceed the uncertainty of the data. This result is surprising because the data for all other thermodynamic state variables calculated by the expressions in terms of phase space functions reported in Table 2.1 agreed well with the equation of state.

To examine this problem, several possible sources of error were checked. First, the data were compared with an additional set of speed of sound data which was calculated by the expression for the isentropic compressibility in the NVE ensemble reported by Allen and Tildesley [10, p. 53]. This expression was derived by the transformation technique introduced by Lebowitz et al. [114]. The corresponding expression for the zero frequency speed of sound reads

$$w_0^\dagger = \left[\frac{1}{\rho_\mathrm{m}} \left(\frac{2NkT}{3V} + \langle p \rangle + \frac{1}{V} \left\langle \frac{\partial^2 U}{\partial V^2} \right\rangle - \frac{V}{kT} \langle (\delta p)^2 \rangle \right) \right]^{1/2} \quad . \tag{3.34}$$

It is expected that systematic differences between speed of sound data calculated by both methods are of the order of $\mathcal{O}(N^{-1})$. Since the simulations were carried out with 1372 particles, systematic errors of the data calculated by Eq. (3.34) should be smaller than 0.1 %. The data for the speed of sound calculated by Eq. (3.34) are also reported in Table D.1. The percentage deviations of this additional speed of sound data from the fundamental equation of state are shown in the last subfigure of Figure 3.16. It is evident that these data agree with the fundamental equation of state to the same degree as the results for the other state variables. Thus, the equation of state predicts the speed of sound correctly and the discrepancy must be due to systematic errors of the data calculated by the phase space function expression.

The influence of the number of particles and cutoff radius on the speed of sound data was checked by repeating simulations at selected state points with different values for the cutoff radius and with 256 particles. The results for the speed of sound obtained by both methods agreed with the corresponding 1372 particle data within their uncertainties. Hence, the influence of both simulation parameters can be excluded as a possible source for the large systematic deviations.

A similar problem was encountered by Lustig [130] who computed isothermal compressibilities β_T for the Lennard-Jones model fluid by *NVE* Monte Carlo simulations. In that work, phase space function expressions derived from the two possible entropy definitions $S = k \ln \Omega$ and $S = k \ln \omega$ were applied to determine the isothermal compressibility data. Lustig found that the data from both entropy definitions agreed within their uncertainties, but showed large systematic deviations from the fundamental equation of state of Mecke et al. Since the isothermal compressibility is closely related to the speed of sound by thermodynamic relations, Eqs. (C.18) and (C.24), it is likely that the deviations from the equation of state have the same origin as those observed in this work for the speed of sound.

To conclude, it is not unreasonable to assume that the origin for the systematic deviations of the speed of sound data from the fundamental equation of state lies in the expression for the speed of sound given in Table 2.1. However, the problem could not be solved during this work. At present, the data calculated by Eq. (3.34) provide the best estimates for the speed of sound of the Lennard-Jones model fluid.
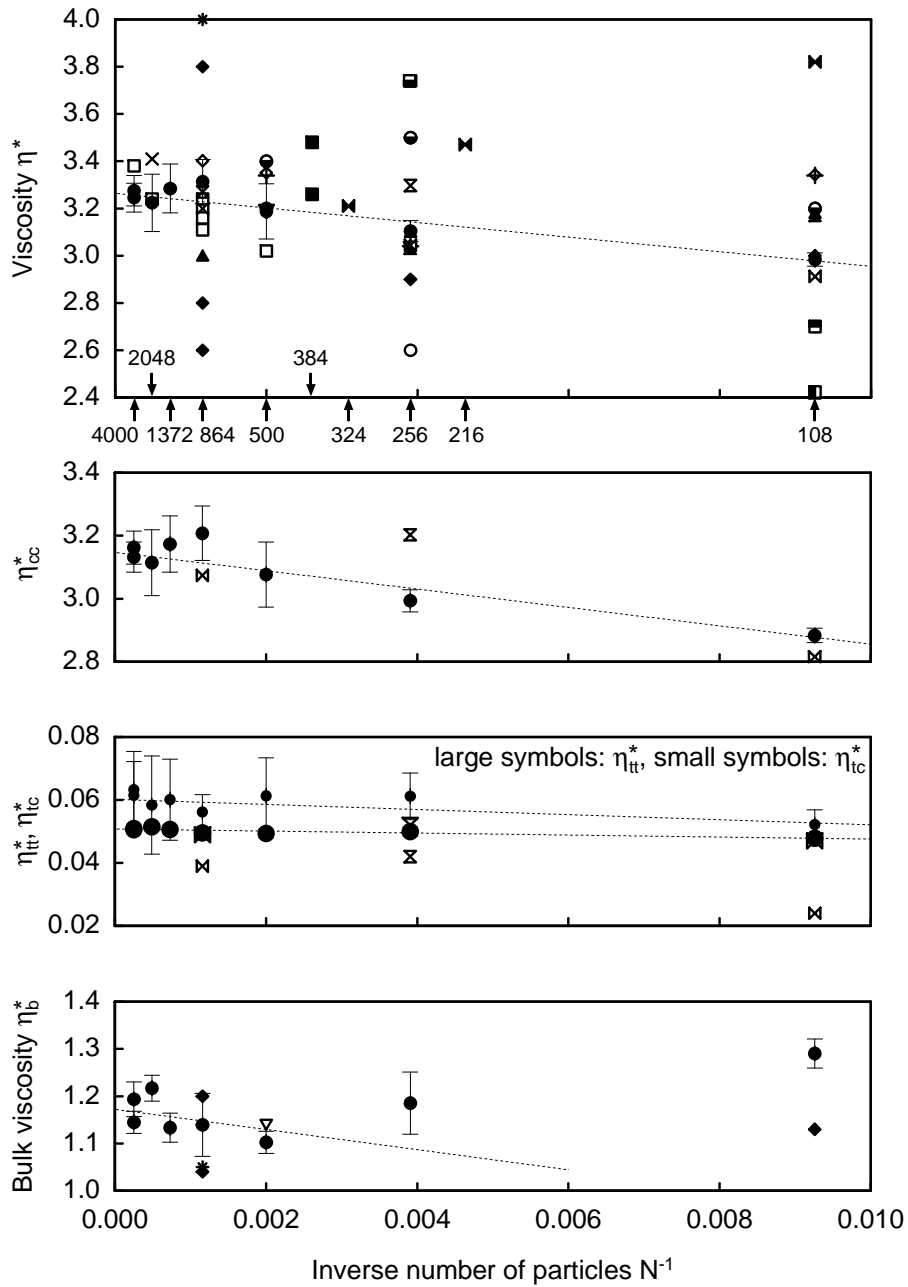
Figure 3.10. Present simulation data and literature data for the viscosity contributions η_{tt}^*, η_{tc}^*, and η_{cc}^*, the viscosity η^* and the bulk viscosity η_{b}^* at the state point ($T^* = 0.722$, $\rho^* = 0.8442$) as a function of the inverse number of particles. Error bars designate the uncertainty of the present data. The dashed lines represent weighted linear least-squares fits to the present data. Legend: Symbols for the viscosity are given in Table 3.1. Symbols for the bulk viscosity: (●) This work, (✳) Levesque et al. [118], (◆) Levesque and Verlet [119] and (▽) Schoen [190].
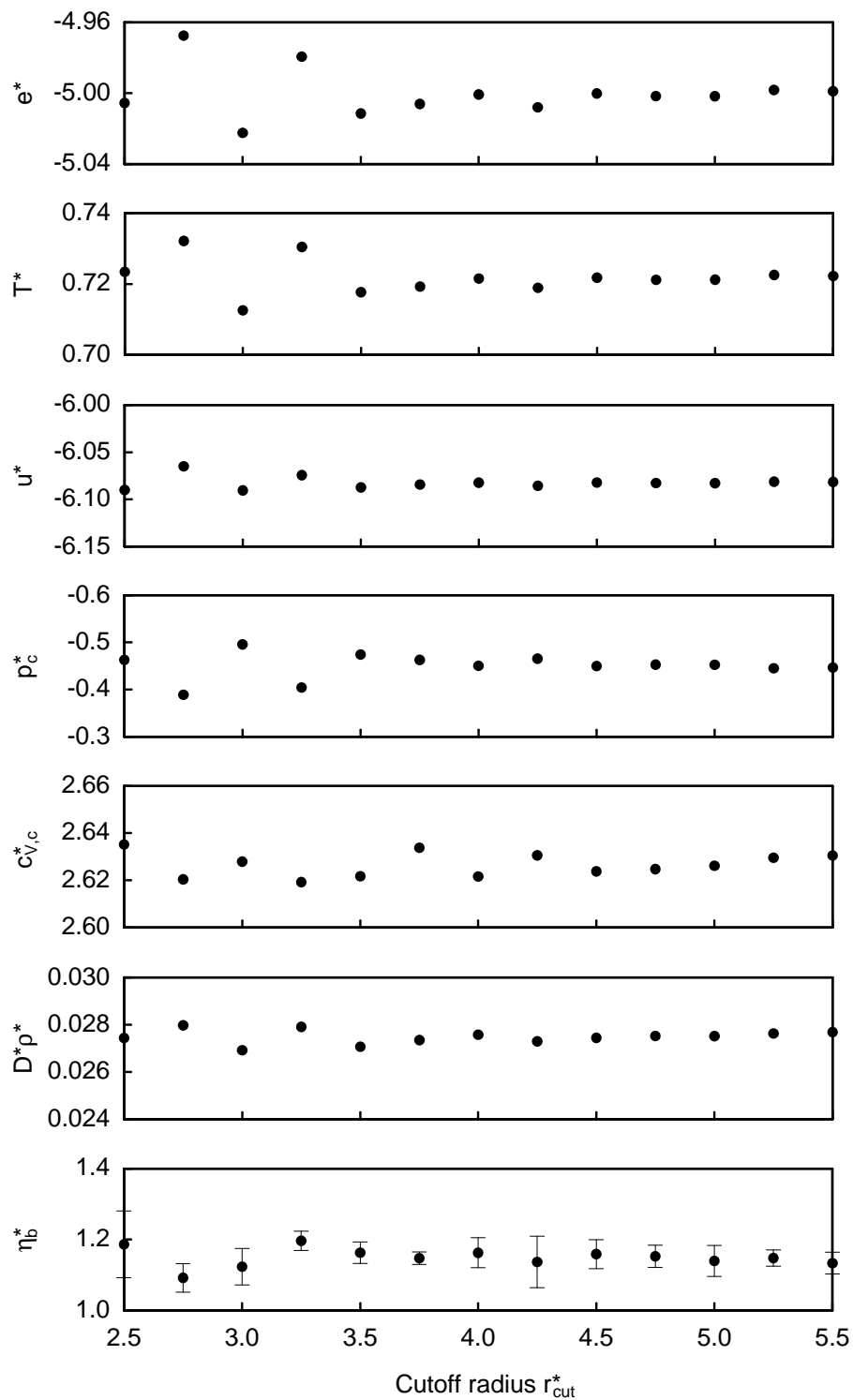
Figure 3.11. The thermodynamic state variables e^*, T^*, u^*, p_c^*, c_V^*, the product $D^*\rho^*$ and the bulk viscosity η_b^* at the state point ($T^* = 0.722$, $\rho^* = 0.8442$) as a function of the cutoff radius r_{cut}^*.
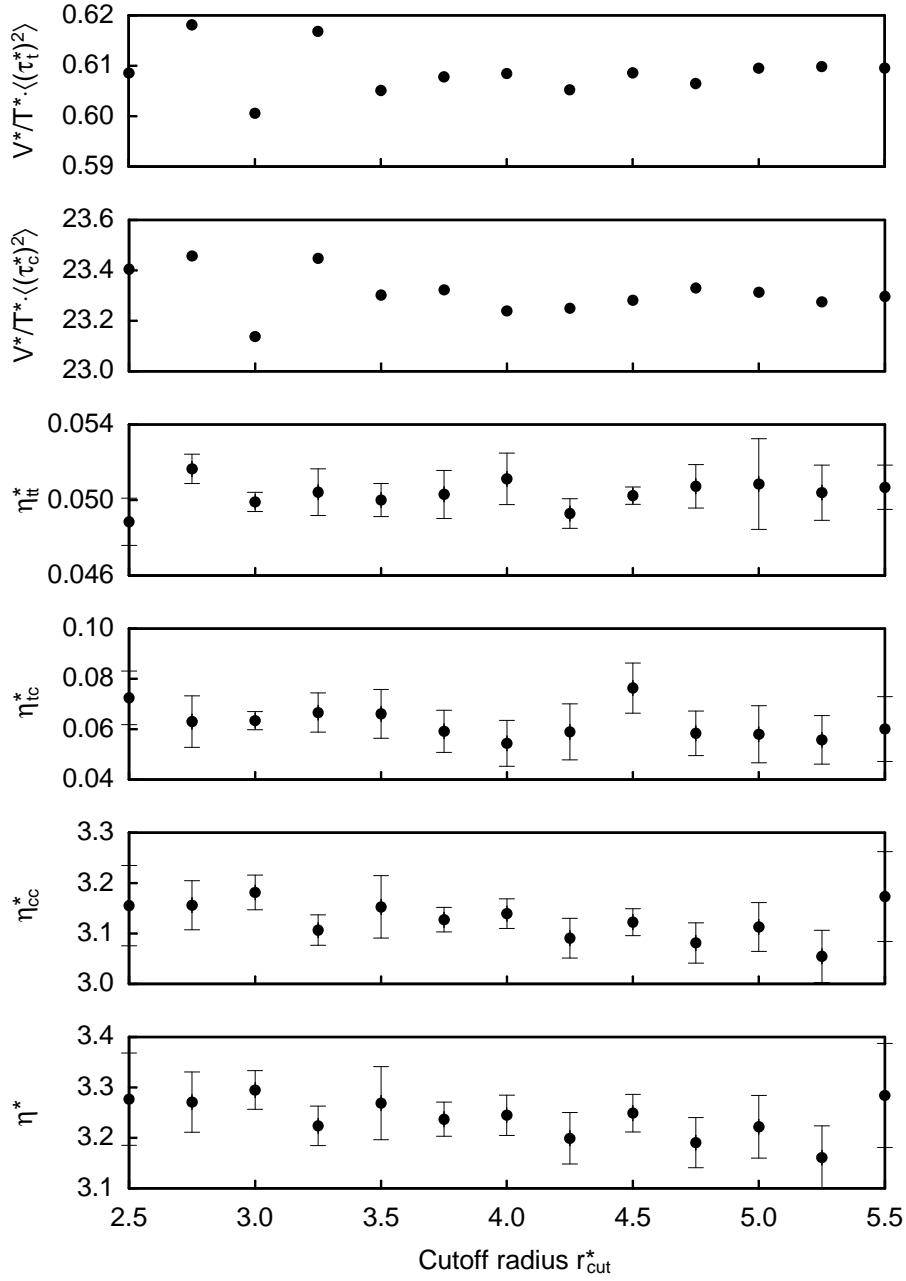
Figure 3.12. The quantities $V^*/T^* \cdot \langle [\tau_{\mathrm{t}}^*]^2 \rangle$ and $V^*/T^* \cdot \langle [\tau_{\mathrm{c}}^*]^2 \rangle$, the viscosity contributions η_{tt}^*, η_{tc}^*, and η_{cc}^* and the viscosity η^* at the state point ($T^* = 0.722$, $\rho^* = 0.8442$) as a function of the cutoff radius r_{cut}^*.
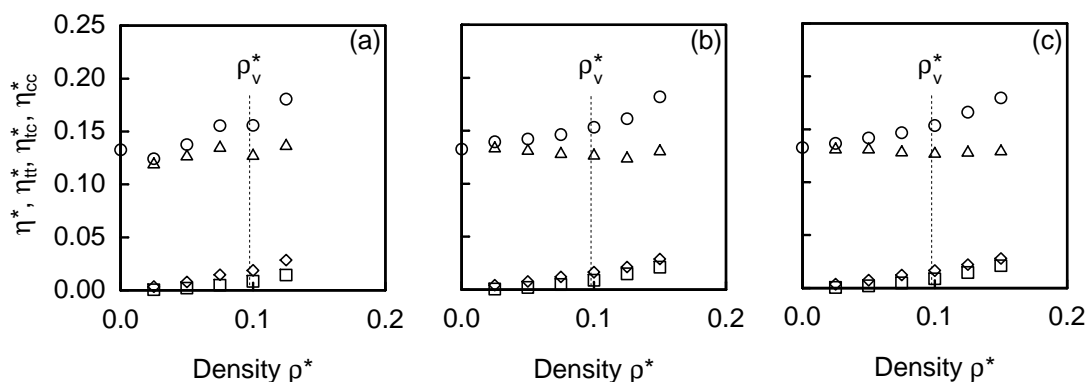
Figure 3.13. Influence of the length of the production phase of the simulation on the viscosity η^* (○) and the viscosity contributions η_{tt}^* (△), η_{tc}^* (◇), η_{cc}^* (□) at low density gaseous states on the subcritical isotherm $T^* = 1.2$. The production phases of the simulations extended over (a) $2 \cdot 10^6$, (b) $15 \cdot 10^6$ and (c) $50 \cdot 10^6$ time steps. Symbols at zero density denote the Chapman-Enskog solution to the Boltzmann equation.
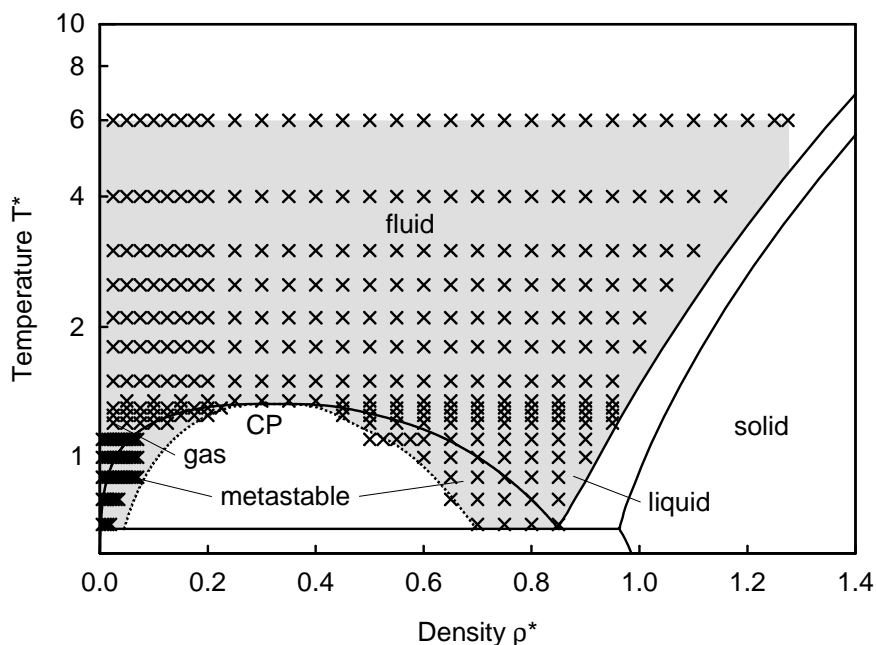
Figure 3.14. Distribution of simulated state points in the T^*, ρ^*-plane.
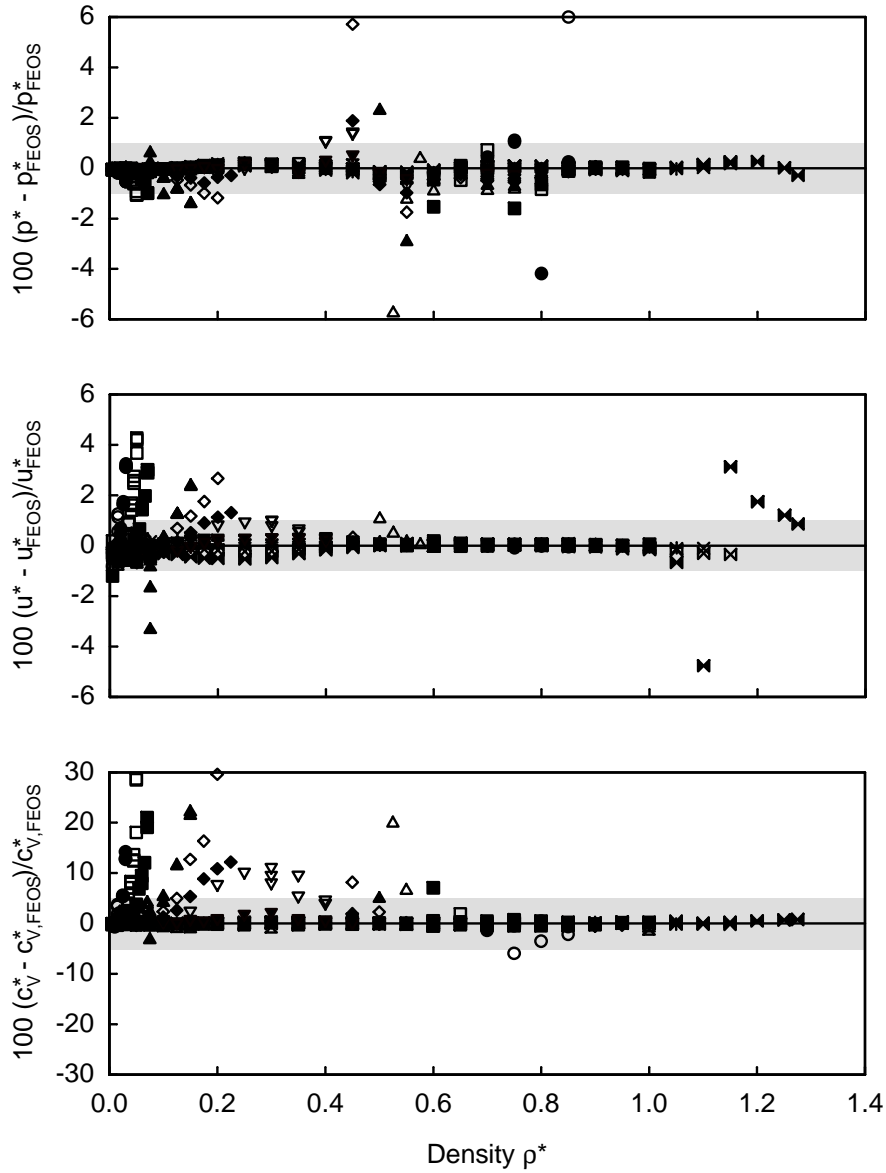
Figure 3.15. Percentage deviations of the simulated pressures p^*, potential energies u^* and isochoric heat capacities c_V^* from the fundamental equation of state of Mecke et al. [142]. Legend: ($\bigcirc$) $T^* = 0.7$, ($\bullet$) $T^* = 0.8$, ($\square$) $T^* = 0.9$, ($\blacksquare$) $T^* = 1.0$, ($\triangle$) $T^* = 1.1$, ($\blacktriangle$) $T^* = 1.2$, ($\diamond$) $T^* = 1.25$, ($\blacklozenge$) $T^* = 1.3$, ($\triangledown$) $T^* = 1.35$, ($\blacktriangledown$) $T^* = 1.5$, ($\boxtimes$) $T^* = 1.8$, ($\mathbf{\Xbar}$) $T^* = 2.1$, ($+$) $T^* = 2.5$, ($\times$) $T^* = 3.0$, ($\bowtie$) $T^* = 4.0$ and ($\blacktriangleright\!\blacktriangleleft$) $T^* = 6.0$.

Figure 3.16. Percentage deviations of the simulated isothermal pressure coefficients γ_V^* and zero frequency speeds of sound w_0^* calculated by the expressions in terms of phase space functions (see Table 2.1) and $w_0^{\dagger*}$ calculated by Eq. (3.34) from the fundamental equation of state of Mecke et al. [142]. Symbols are the same as in the legend to Figure 3.15.

4 Self-Diffusion in the Lennard-Jones Model Fluid

Experimental studies on the self-diffusion coefficient of real fluids are scarce since it is difficult to measure the diffusion of a tagged particle which is of the same species as the other particles in a fluid. Available data sets are restricted to few substances and cover only limited portions of the fluid region of the phase diagram. On the other hand, self-diffusion coefficients can be determined with high accuracy in molecular dynamics simulations. Therefore, this transport coefficient was the subject of many simulations studies. A review of available literature data for the Lennard-Jones model fluid was given by Liu et al. [121]. Many literature data are subject to systematic errors because they were obtained from simulations of relatively small systems. This chapter describes new self-diffusion data that were derived from the first series of simulations carried out during the course of this work.

4.1 Simulation Data for the Self-Diffusion Coefficient

At every simulated state point, mean-squared particle displacement and velocity autocorrelation functions were computed. The parameters for the computation of these functions depend on the state point. At densities above $\rho^* = 0.2$, the coordinates and velocities of the molecules were stored on a hard disk every tenth time step during the first million time steps of the production phase of the simulation. Time origins were taken at every twentieth time step. At lower densities, the coordinates and velocities were stored every 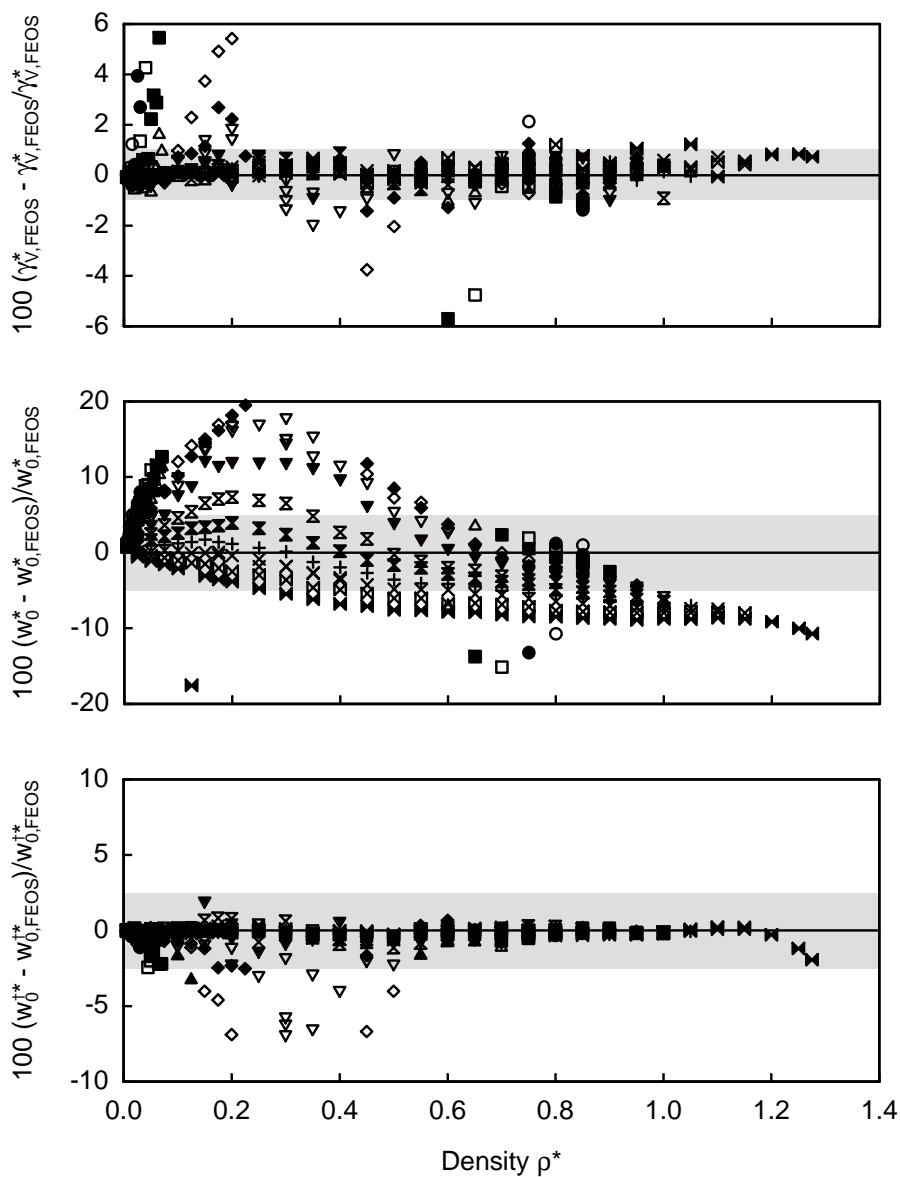twentieth time step during the first 1.5 million time steps for the isotherm $T^* = 1.2$ and higher temperatures. At lower temperatures, they were stored during the whole production phase of the simulation over two million time steps. Every fortieth time step was taken as a time origin in these cases. The self-diffusion coefficients were determined from the Einstein relations as described in Section 3.3.1 and are reported in Table D.2. The statistical uncertainty of the data is estimated to be 0.5 % at densities larger than $\rho^* = 0.2$ and 1 % at lower gaseous densities.

Figure 4.1 depicts the data for the self-diffusion coefficient for all sixteen simulated isotherms in semi-logarithmic representation. It is evident from the plot that all isotherms diverge when they approach the zero density limit. In the discussion of the data in the remainder of this chapter, the product self-diffusion coefficient
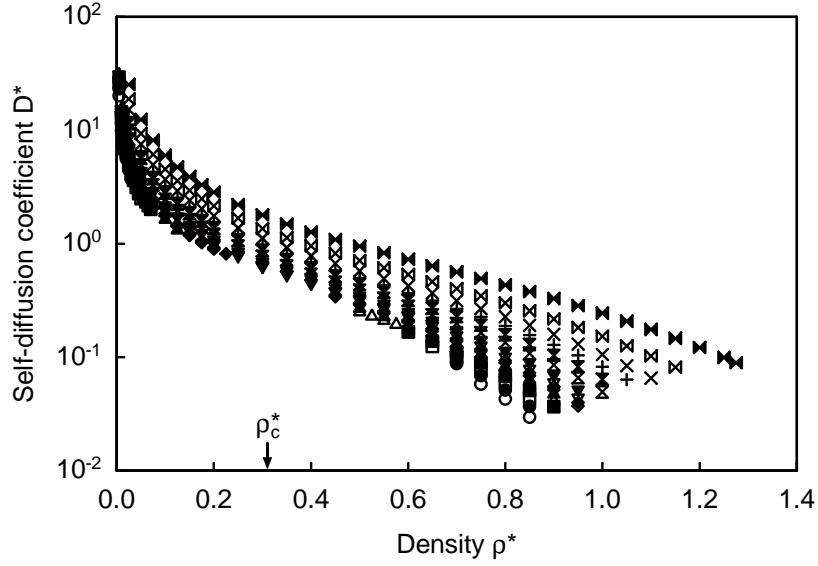
Figure 4.1. The self-diffusion coefficient D^* for all simulated isotherms as a function of density in semi-logarithmic representation. Legend: ($\bigcirc$) $T =^* 0.7$, ($\bullet$) $T^* = 0.8$, ($\square$) $T^* = 0.9$, ($\blacksquare$) $T^* = 1.0$, ($\triangle$) $T^* = 1.1$, ($\blacktriangle$) $T^* = 1.2$, ($\diamond$) $T^* = 1.25$, ($\blacklozenge$) $T^* = 1.3$, ($\triangledown$) $T^* = 1.35$, ($\blacktriangledown$) $T^* = 1.5$, ($\boxtimes$) $T^* = 1.8$, ($\mathbf{\Xi}$) $T^* = 2.1$, ($+$) $T^* = 2.5$, ($\times$) $T^* = 3.0$, ($\bowtie$) $T^* = 4.0$ and ($\blacktriangleright\!\blacktriangleleft$) $T^* = 6.0$.

times density $D^*\rho^*$ rather than the self-diffusion coefficient itself is considered as the multiplication with density removes the singularity of the self-diffusion coefficient in the zero density limit.

Table 4.1 summarizes details of literature data sets for the self-diffusion coefficient of the Lennard-Jones model fluid. In an additional study, Heyes [82] determined the self-diffusion coefficient by equilibrium molecular dynamics simulations using the Einstein relation method, but the data were not reported in the publication. A critical assessment of the quality of the data sets must take into account the simulation method and parameters employed by the authors.

Most data sets were determined from simulations of systems with 108-500 particles. Exceptions are the data sets of Erpenbeck [44] and Kincaid [106] which were obtained from simulations of systems with up to 4000 or 1372 particles, respectively. In Section 3.4, it was shown that self-diffusion data depend strongly on the number of particles in the simulated system. It must be expected that the literature data are also subject to this effect.

The data sets of Erpenbeck [44] and Kincaid [106] were derived from simulations

Table 4.1. Literature data sets for the self-diffusion coefficient of the Lennard-Jones model fluid. Abbreviations: CC: constant colour current method, CG: constant colour current gradient method, ER: Einstein relation method, GK: Green-Kubo integral method, MC-GO: Monte Carlo generated time origins. Remarks: [1]: modified Lennard-Jones potential, [2]: not reported by the authors, [3]: according to Figure 1 in Ref. [66].

Author		Year	Data	Method	Ensemble	N	r^*_{cut}	T^*	ρ^*	Simul. Length
This work		2002	334	ER	*NVEMG*	1372	5.5-6.5	0.7-6.0	0.005-1.275	4500-6000
Borgelt	[25]	1990	46	GK	*NVEMG*	108	2.5	0.66-2.94	0.78-0.84	371
Canales	[30]	1999	3	GK/ER	*NVT*	668	2.71-3.11	0.53, 1.89	0.756, 1.143	554-1203
Chen	[32]	1977	6	ER	*NVEMG*	500	2.5	0.679-2.16	0.3-0.8442	23-35
Erpenbeck	[44]	1987	4	GK	*NVT*	108-1372	1.74[1]	1.08	0.85	MC-GO
			3	CC	*NVT*	108-1372	1.74[1]	1.08	0.85	MC-GO
Erpenbeck	[45]	1988	6	GK	*NVT*	108-4000	2.75[1]	0.722	0.8442	MC-GO
			2	GK	*NVT*	108, 864	2.75[1]	0.722	0.8442	MC-GO
Gardner	[55]	1991	22	ER	*NVEMG*	108, 256	$L/2$	1.3, 2.49	0.01-0.3	10000
Hammonds	[66]	1988	53	GK	*NVEMG/T*	108-500	2.5[3]	0.72-10.0	0.4-1.18	3000-14000
Heyes	[79]	1983	54	ER	*NVEMG*	256	2.5	0.68-4.58	0.2-1.13	150
Heyes	[83]	1987	16	ER	*NVT*	108-2048	2)	1.4562	0.1-1.0	100-9000
Heyes	[84]	1988	213	ER	*NVT*	108-500	2)	0.72-10.0	0.2-1.22	417-9500
Heyes	[85]	1990	26	GK	*NVT*	256	2.5	0.722-6.0	0.4-1.4	1500
Heyes	[86]	1993	4	GK	*NVEMG*	256	2.5	0.707-6.0	0.5-1.0	655-17082
Kincaid	[106]	1994	6	CG/ER	*NVE*	256-1372	1.24[1]	2.0	0.05-0.5	ER: 2200-30000
Leegwater	[116]	1991	7	GK	2)	500	2)	0.84-1.96	0.2-0.85	2)
Michels	[145]	1975	22	GK	*NVEMG*	125	2.5	1.5-3.0	0.04-0.35	$>250\,t^*(C_{\mathrm{D}}(0))$
Michels	[146]	1978	43	GK	*NVEMG*	108, 125	2.5	1.3-5.56	0.01-0.3	306-28850
Rowley	[185]	1997	141	ER	*NVT*	256	3.5	0.8-4.0	0.05-1.0	182-6063
Schofield	[191]	1973	4	GK	*NVEMG*	2)	2.25	1.0	0.626-0.845	2)
Sharma	[195]	1994	5	GK	*NVT*	32-864	1.6, 2.5	0.72	0.84	80-400
Straub	[205]	1992	35	ER	*NVEMG*	512	2.5	0.75-4	0.3-1.05	150

with a modified Lennard-Jones potential. For the reasons given in the discussion of the viscosity near the triple point in Section 3.4, these two data sets cannot be compared with those data sets obtained with the original Lennard-Jones potential and are excluded from further considerations.

In the majority of studies, equilibrium molecular dynamics simulations were employed and the Einstein relation or Green-Kubo integral methods were used to determine the self-diffusion data. Indicators for the accuracy of the data obtained by these methods are the lengths of the production phases of the simulations and the number of time origins that are used in the calculation of the velocity autocorrelation and mean-squared displacement functions. Since both functions are single particle properties, they are usually averaged over all particles in the system to increase the accuracy of the results. Thus, simulations of large systems with many particles yield data with smaller uncertainties than those carried out with small systems, provided that the simulations extend over comparable time periods and that time origins are taken sufficiently frequent and at equally spaced intervals from the simulated phase space trajectory. Beside the present data, the data sets of Hammonds and Heyes [66], Heyes [84, 86], Michels and Trappeniers [146] and Rowley and Painter [185] were obtained from relatively long simulation runs.

Figure 4.2 shows the distribution of the data sets for $D^*\rho^*$ in relation to the phase boundaries in the T^*,ρ^*-plane. The present data cover the temperature range between $T^* = 0.7$ up to 6.0 and the density range from low density gaseous states up the compressed liquid close to the freezing line. The literature data sets concentrate in the high density liquid region. Similar temperature ranges are covered by the data sets of Hammonds and Heyes [66], Heyes [79, 84], Heyes and Powles [85] and Rowley and Painter [185]. Hammonds and Heyes [66] as well as Heyes [84] data sets extend up to the temperature $T^* = 10$. Data at low density gaseous states were reported by Gardner [55], Michels and Trappeniers [145, 146] and Rowley and Painter [185].

In Figure 4.3, the present simulation results for the product $D^*\rho^*$ are shown for two selected isotherms, the subcritical isotherm $T^* = 1.2$ and the supercritical isotherm $T^* = 3.0$. Also included are literature data [145, 146, 185, 205] and the recent correlation by Rowley and Painter [185]. The present data appear very consistent and extrapolate well into the zero density limit. On the isotherm $T^* = 1.2$, a shallow minimum is observed at the approximate reduced density $\rho^* = 0.1$ in the gas region. Isotherm $T^* = 3.0$, however, does not show such a minimum. The data of Rowley and Painter also give a consistent picture, but are systematically lower
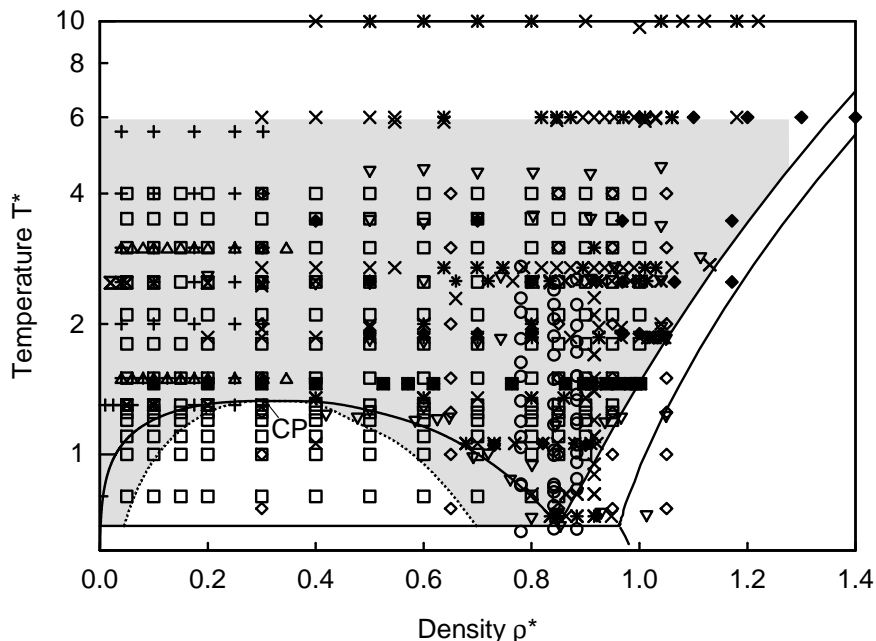
Figure 4.2. The distribution of literature data sets for the product $D^*\rho^*$ in the T^*,ρ^*-plane. The grey shaded area is the state region considered in this work. Legend: ($\bigcirc$) Borgelt et al. [25], ($\ast$) Hammonds and Heyes [66], ($\boxtimes$) Gardner et al. [55], ($\triangledown$) Heyes [79], ($\blacksquare$) Heyes [83] ($\times$) Heyes [84], ($\blacklozenge$) Heyes [85], ($\triangle$) Michels and Trappeniers [145], (+) Michels and Trappeniers [146], ($\square$) Rowley and Painter [185] and ($\diamondsuit$) Straub [205].

than the present data in the liquid region. Since their simulations were performed with 256 particles and the present simulation with 1372 particles, these systematic deviations are probably due to finite size effects. On the isotherm $T^* = 3.0$, the literature data sets of Straub [205] and Michels and Trappeniers [145, 146] scatter more than the data of this work. At low gaseous densities, the Michels and Trappeniers data lie below the data of this work. As their simulations were carried out with 108 and 125 particles, these systematic deviations may also be attributed to finite size effects. The correlation of Rowley and Painter follows their data well at high densities, but fails to describe the correct physical behaviour in the gas region. This discussion shows that the present comprehensive self-diffusion data are substantially more accurate than the literature data on the two isotherms. Similar observations were made in comparisons of the present data with literature data on other isotherms.
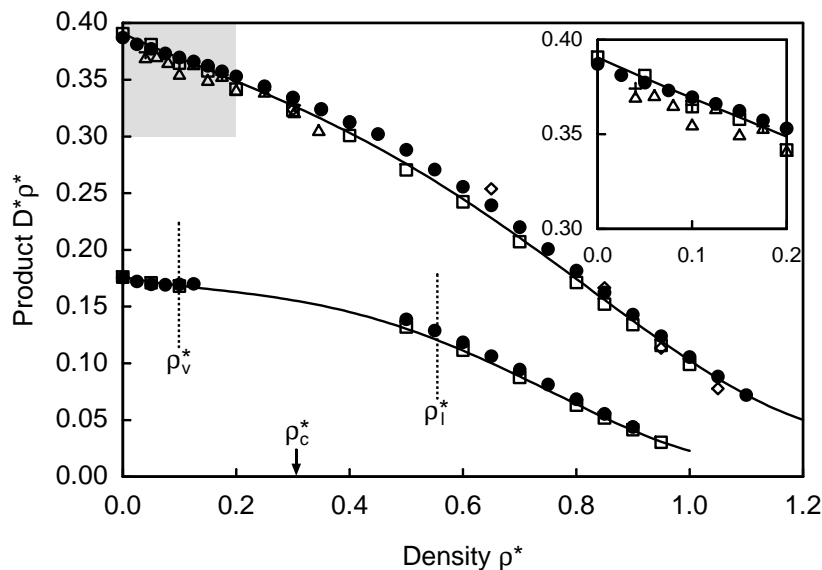
Figure 4.3. The product $D^*\rho^*$ on the subcritical isotherm $T^* = 1.2$ and supercritical isotherm $T^* = 3.0$ as a function of density. The shaded area is enlarged in the insert. Symbols at zero density denote the Chapman-Enskog solution to the Boltzmann equation. Legend: ($\bullet$) This work, ($\triangle$) Michels and Trappeniers [145], ($+$) Michels and Trappeniers [146], ($\square$) Rowley and Painter [185] and ($\diamond$) Straub [205].

4.2   Temperature and Density Dependence of the Product $D^*\rho^*$

Figures 4.4 and 4.5 display the product $D^*\rho^*$ for all sixteen simulated sub- and supercritical isotherms, respectively. All sixteen isotherms extrapolate well into the zero density limit. The initial slope of the isotherms is always negative at sub- as well as supercritical temperatures. The isotherms between $T^* = 1.0$ and 1.5 in the vicinity of the critical temperature exhibit shallow minima in the gas region as already observed for the isotherm $T^* = 1.2$ in the last section. These results suggest that the minima are real physical effects. At lower temperatures, the gaseous isotherms become shorter since the dew density decreases with temperature and they decrease monotonically with density. On higher supercritical isotherms, the minima vanish so that the product $D^*\rho^*$ decreases monotonically. Along an isotherm, $D^*\rho^*$ never exceeds the zero density value. At high density liquid states, the isotherms decrease over the whole temperature range. Below the critical density, the isotherms have concave curvature, whereas in the high density region the curvature is convex.

Figure 4.4. The product $D^*\rho^*$ for all simulated subcritical isotherms as a function of density. Symbols at zero density denote the Chapman-Enskog solution to the Boltzmann equation. Legend: (○) $T =^* 0.7$, (●) $T^* = 0.8$, (□) $T^* = 0.9$, (■) $T^* = 1.0$, (△) $T^* = 1.1$, (▲) $T^* = 1.2$, (◇) $T^* = 1.25$, (◆) $T^* = 1.3$ and (▽) $T^* = 1.35$ (supercritical).

Figure 4.6 shows the product $D^*\rho^*$ along selected isochors as a function of temperature. In this representation, the range of the isochors is limited by the zero density values from above and the values of the product $D^*\rho^*$ on the freezing line from below. The dependence of the product $D^*\rho^*$ on temperature is monotonic over the entire density range between the zero density limit and the freezing line. $D^*\rho^*$ increases with temperature, and thus, resembles the increased mobility of the molecules at high temperatures due to their larger average velocities. The zero density isochor is the steepest isochor. With increasing density the slope of the isochors declines.

For a detailed investigation of the initial behaviour of the isotherms, estimates for the initial slopes were derived from the present simulation data on 15 isotherms. The isotherm $T^* = 1.35$ was excluded because the data at this temperature do not extend close enough to the zero density limit. The slopes were determined from a linear least-squares fit to the first few state points of every isotherm including the zero density theoretical Chapman-Enskog value. Since these initial slopes are derived in a very simple way from the simulation data, they are of qualitative nature and might be subject to future adjustment.

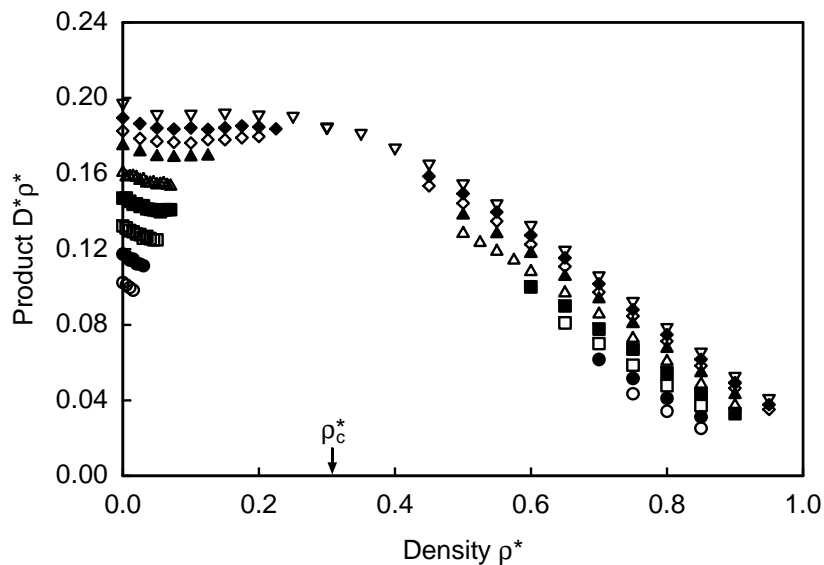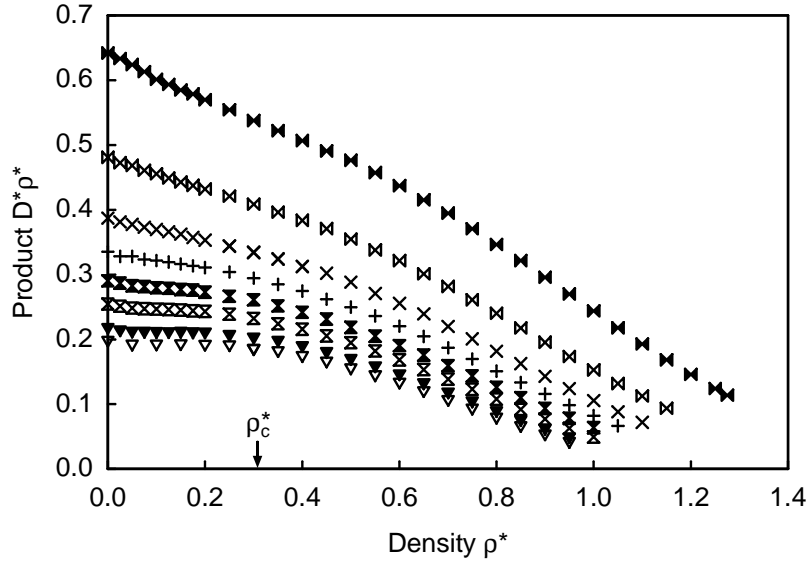**Figure 4.5.** The product $D^*\rho^*$ for all simulated supercritical isotherms as a function of density. Symbols at zero density denote the Chapman-Enskog solution to the Boltzmann equation. Legend: ($\triangledown$) $T^* = 1.35$, ($\blacktriangledown$) $T^* = 1.5$, ($\boxtimes$) $T^* = 1.8$, ($\blacksquare$) $T^* = 2.1$, (+) $T^* = 2.5$, ($\times$) $T^* = 3.0$, ($\bowtie$) $T^* = 4.0$ and ($\blacktriangleright\hspace{-0.5em}\blacktriangleleft$) $T^* = 6.0$.

The initial slopes correspond to the second self-diffusion virial coefficients that appear as coefficients of the linear term in a series expansion of the product $D^*\rho^*$ in terms of the density at low densities [105, 220]:

$$D^*\rho^* = (D^*\rho^*)_0 + B_{\mathrm{D}}^*(T^*)\rho^* + \dots \quad . \tag{4.1}$$

Figure 4.7 depicts the second self-diffusion virial coefficient as a function of temperature. Despite of the scatter of the data, the qualitative temperature dependence of B_{D}^* is evident. The second self-diffusion virial coefficients are negative over the whole temperature range between $T^* = 0.7$ and $T^* = 6.0$. At subcritical temperatures, B_{D}^* increases with temperature, reaches a maximum at approximately $T^* = 1.5$ and decreases at higher temperatures. This temperature dependence is similar to that of the second viscosity virial coefficients of real fluids [20, 164, 180, 181].

Bennett and Curtiss [19] calculated the second self-diffusion virial coefficient for the Lennard-Jones model fluid numerically from the solution of a modified Boltzmann equation. They found that B_{D}^* is negative at all temperatures, approaching zero in the high temperature limit, and reported the values $B_{\mathrm{D}}^* = $ -3.982, -0.9536 and -0.7240 at the temperatures $T^* = 1$, 2 and 8, respectively. Within their approximative theory, B_{D}^* has a monotonic temperature dependence. However, the
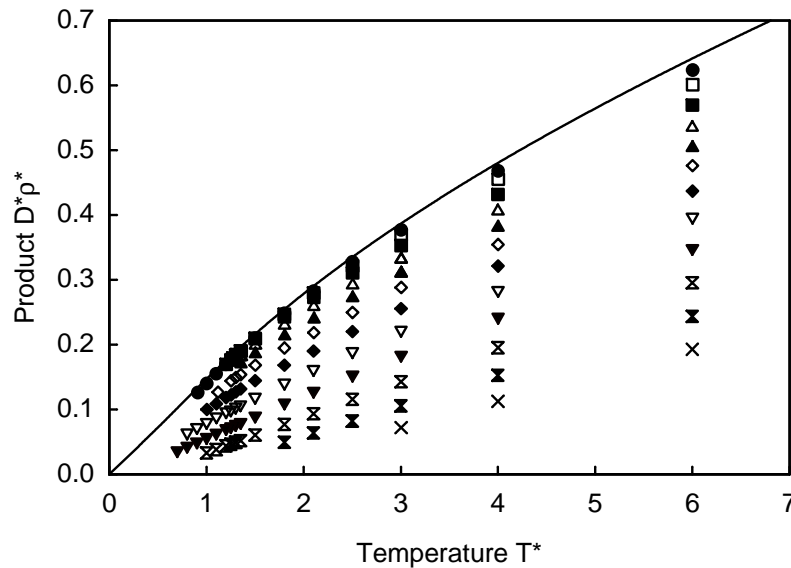
Figure 4.6. The product $D^*\rho^*$ on selected isochors as a function of temperature. Legend: (●) $\rho^* = 0.05$, (□) $\rho^* = 0.1$, (■) $\rho^* = 0.2$, (△) $\rho^* = 0.3$, (▲) $\rho^* = 0.4$, (◇) $\rho^* = 0.5$, (◆) $\rho^* = 0.6$, (▽) $\rho^* = 0.7$, (▼) $\rho^* = 0.8$, (⊠) $\rho^* = 0.9$, (⊠) $\rho^* = 1.0$ and (×) $\rho^* = 1.1$; (——) Chapman-Enskog solution to the Boltzmann equation.

treatment of Bennett and Curtiss lacks more recent contributions to the theory by Rainwater and Friend [180, 181], which improve the description of several effects previously treated less rigorously. This might be the reason for the discrepancy to the present results.

Experimental self-diffusion data for real substances are reviewed by Dymond et al. [36], Harris [72], van der Gulik [63], Liu et al. [121], Silva et al. [196], Ruckenstein and Liu [186] and Speedy et al. [200]. Often, experimental studies focus on the liquid region such as those reviewed by Speedy et al. [200] for several halogenated methane derivatives. Investigations extending into the supercritical region and to low densities were carried out by Peereboom et al. [172, 173] for the noble gas xenon, by Harris [70], Harris and Trappeniers [71] and Oosting and Trappeniers [170] for methane and by Arends et al. [11] and Peereboom et al. [172] for ethene. The experimental data for these three substances are compared with the present results for the Lennard-Jones model fluid.
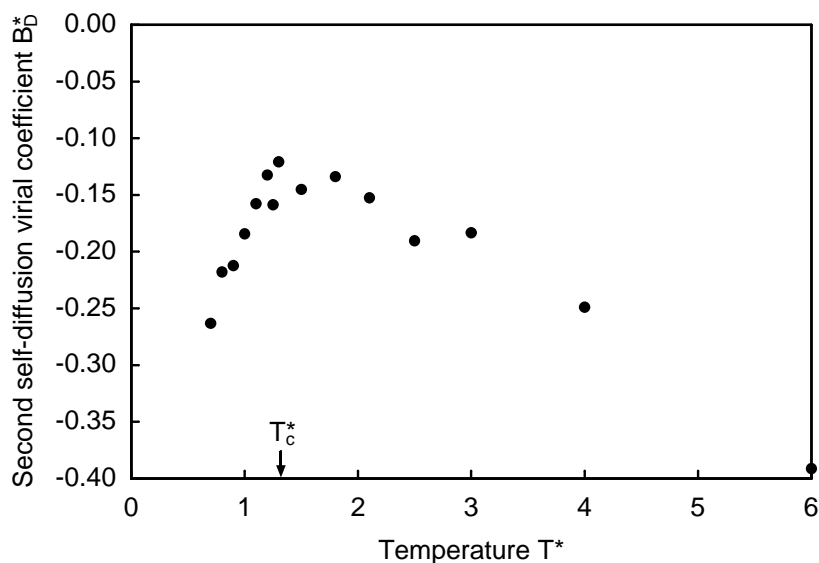
Figure 4.7. The second self-diffusion virial coefficients B_{D}^* for the Lennard-Jones model fluid as a function of temperature.

The experimental data of Peereboom et al. [172, 173] for the two xenon isotopes ^{129}Xe and ^{131}Xe are shown in Figure 4.8. Two isotherms at $T = 248$ K and $T = 273$ K are subcritical, while the two highest isotherms at $T = 298$ K and $T = 343$ K lie above the critical temperature $T_{\mathrm{c}} = 290$ K. Zero density values for $D\rho_{\mathrm{m}}$ are derived from zero density values for the Lennard-Jones potential with the potential parameters $\sigma = 0.3924$ nm and $\varepsilon/k = 257.4$ K which were reported by Peereboom et al. [173]. The xenon isotherms show a different behaviour than isotherms of the Lennard-Jones model fluid in this temperature range. They start with positive or almost zero initial slopes at the zero density limit and exhibit maxima close to the critical density before decreasing at high density liquid states. At the maxima, the values of $D\rho_{\mathrm{m}}$ are larger than the zero density values.

The experimental data for methane are displayed in Figure 4.9. Beside the isothermal data of Oosting and Trappeniers [170] at the supercritical temperatures $T = 194.75$ K, $T = 273.15$ K and 298.15 K, their data on the dew and bubble line and the data sets of Harris [70] at the supercritical temperatures $T = 223.15$ K, $T = 298.15$ K, and $T = 323.15$ K and Harris and Trappeniers [71] at the subcritical temperatures $T = 110$ K, $T = 140$ K, and $T = 160$ K in the liquid region are shown. Zero density values for the three supercritical isotherms of Oosting and Trappeniers were derived from the zero density products $D^*\rho^*$ of the Lennard-Jones model fluid
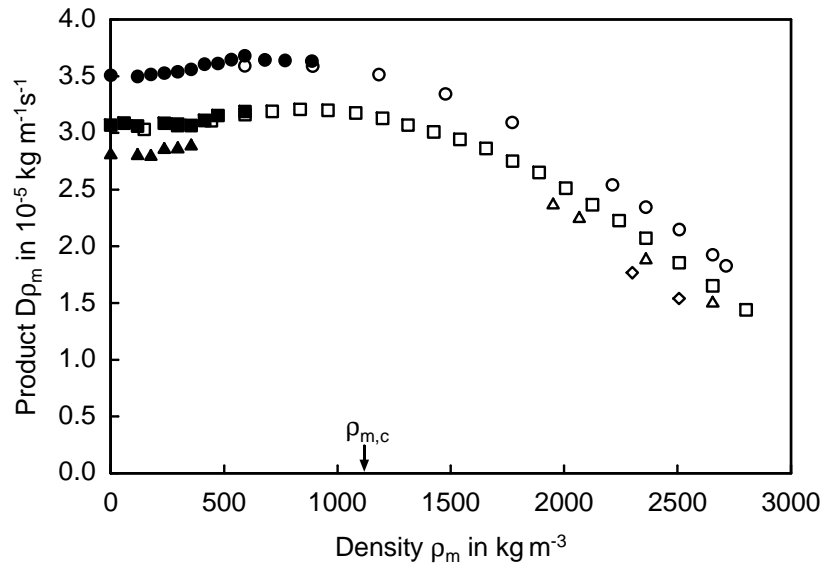
Figure 4.8. Experimental data of Peereboom et al. [173] for the product $D\rho_m$ for the noble gas xenon. Critical parameters of xenon: $T_c = 290$ K, $\rho_{m,c} = 1120.8$ kg m^{-3}. Legend: Isotope ^{129}Xe: ($\diamond$) 248 K, ($\triangle$) 273 K, ($\square$) 298 K and ($\circ$) 343 K; isotope ^{131}Xe: ($\blacktriangle$) 273.15 K, ($\blacksquare$) 298 K and ($\bullet$) 343 K.

using the potential parameters $\sigma = 0.371$ nm and $\varepsilon/k = 147$ K given by Oosting and Trappeniers [170]. The zero density values for the three supercritical isotherms of Harris are the values published by Harris together with his experimental data [70]. Some data at low densities were interpolated from additional isochoric data of Oosting and Trappeniers [170] to match the temperatures of the isotherms.

The supercritical data of Oosting and Trappeniers scatter more than the data of Harris in this states region. On the isotherm $T = 298.15$ K, they are up to 10 % higher than the data of Harris on the same isotherm. Moreover, the lowest supercritical isotherm of Oosting and Trappeniers cuts the bubble line. Therefore, this data set is probably in error and the discussion is focused on the data sets of Harris and Harris and Trappeniers. In the gas region, the isotherm of Harris at $T = 223.15$ K is almost horizontal, while the two higher isotherms have negative initial slopes. These two isotherms decrease monotonically over the whole density range of the measurements. The isotherm $T = 223.15$ K has a maximum in the vicinity of the critical density before decreasing in the liquid region. The data of Harris and Trappeniers on the three subcritical liquid isotherms show the typical behaviour for the liquid region.
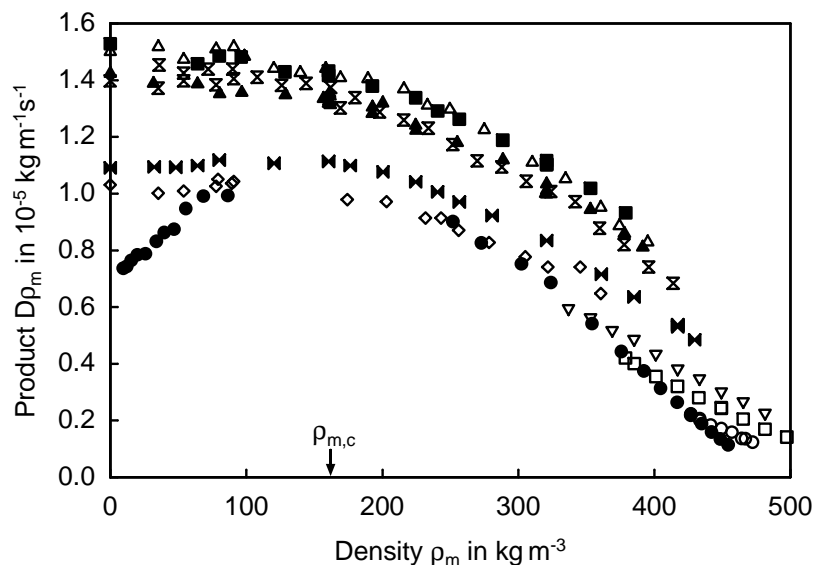
Figure 4.9. Experimental data for the product $D\rho_m$ for methane. Critical parameters of methane: $T_c = 190.6$ K, $\rho_{m,c} = 162.7$ kg m^{-3}. Legend: Oosting and Trappeniers [170]: ($\diamond$) 194.75 K, ($\boxtimes$) 273.15 K, ($\triangle$) 298.15 K and ($\bullet$) saturated vapour and liquid; Harris [70]: ($\bowtie$) 223.15 K, ($\blacktriangle$) 298.15 K and ($\blacksquare$) 323.15 K; Harris and Trappeniers [71]: ($\circ$) 110 K, ($\square$) 140 K and ($\triangledown$) 160 K.

Figure 4.10 depicts the data of Arends et al. [11] for ethene along three subcritical isotherms with the temperatures $T = 123.15$ K, 173.15 K and 223.15 K and two supercritical isotherms with the temperatures 273.15 K and 298.15 K. Also shown are the low density data of Peereboom et al. [172] at the five temperatures $T = 273$ K, 279 K, 298 K, 323 K and 348 K. The zero density values were derived from the zero density product $D^*\rho^*$ for the Lennard-Jones potential with the parameters $\sigma = 0.410$ nm and $\varepsilon/k = 220$ K reported by Peereboom et al. [172]. The behaviour of the product $D\rho_m$ for ethene closely follows that of $D\rho_m$ for xenon. All isotherms have positive initial slopes, exhibit maxima close to the critical density and decrease in the liquid region.

A comparison of the behaviour of the product $D^*\rho^*$ for the Lennard-Jones model fluid with the experimental data for xenon, methane and ethene yields the following insights. In the liquid region, the shape of the isotherms for all three real fluids is similar to the shape of the Lennard-Jones isotherms in this state region. Supercritical isotherms close to the critical temperature exhibit maxima in the vicinity of the critical density with maximum values of $D\rho_m$ being larger than the zero density val-
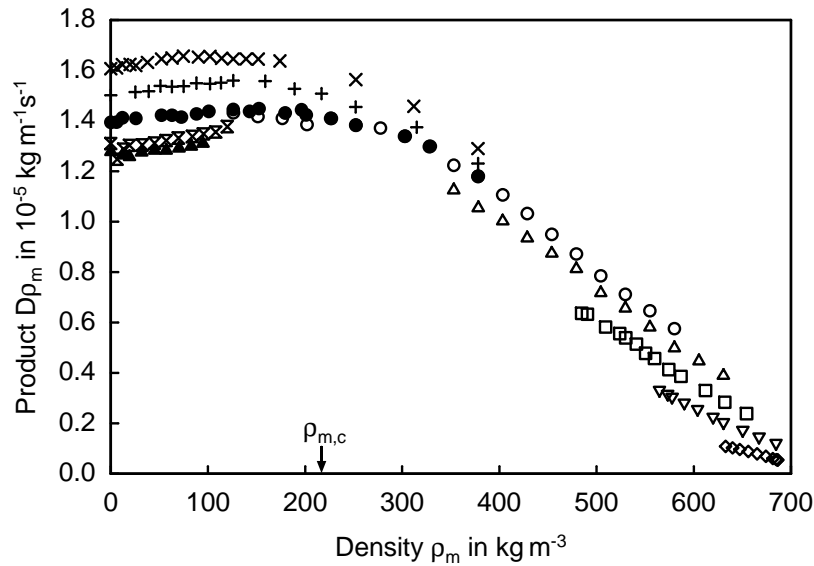
Figure 4.10. Experimental data for the product $D\rho_\mathrm{m}$ for ethene. Critical parameters of ethene: $T_\mathrm{c} = 282.4$ K, $\rho_\mathrm{m,c} = 218.0$ kg m^{-3}. Legend: Arends et al. [11]: ($\diamond$) 123.15 K, ($\triangledown$) 173.15 K, ($\square$) 223.15 K, ($\triangle$) 273.15 K and ($\circ$) 298.15 K; Peereboom et al. [172]: ($\blacktriangle$) 273 K, ($\boxtimes$) 279 K, ($\bullet$) 298 K, ($+$) 323 K and ($\times$) 348 K.

ues. Isotherms of the Lennard-Jones model fluid in this state region have a similar shape, but at intermediate densities they do not show such pronounced maxima and never exceed the zero density values. In this context, it is interesting to consider the influence of the number of particles on the simulation results for the product $D^*\rho^*$ again (see Section 3.4). If the data at intermediate densities were subject to finite size effects in spite of the use of large systems of 1372 particles in the present simulations, the isotherms would certainly be higher than the present results and their shape would be closer to the shape of the real fluid isotherms. However, such an effect is not expected to be so large that it compensates for the difference. Therefore, the discrepancy is at least partly due to the Lennard-Jones potential function. On the other hand, the scatter and uncertainty of the experimental data at low and intermediate densities is quite large. This effect might also contribute to the discrepancy between the experimental and simulated isotherms.

The initial slopes of the real fluid isotherms are positive or almost horizontal in the vicinity of the critical temperature and decrease with increasing temperature. At higher temperatures, they are negative. This behaviour is qualitatively similar to that of the initial slopes of the Lennard-Jones isotherms, but the curve $B_\mathrm{D}(T)$ for

real fluids lies above the Lennard-Jones self-diffusion virial coefficients. From the results for the Lennard-Jones model fluid, it is expected that real fluid isotherms at low subcritical temperatures have negative initial slopes. Due to the lack of experimental data in this state region, this behaviour has not yet been established. It is important to note that in some instances the experimental data do not extend as close to the zero density limit as the present simulation data. Since the initial slope of the isotherms is determined by the data below the density $\rho^* = 0.05$, it is possible that the experimental data for such isotherms do not yet show the correct initial behaviour.

4.3   Molecular Aspects of Self-Diffusion

The decay of velocity autocorrelation functions provides insights into the diffusion mechanisms on the molecular scale. Since the self-diffusion coefficient is related to the time integral of the velocity autocorrelation function, the details of the decay have an influence on the temperature and density dependence of the macroscopic product $D^*\rho^*$.

Figure 4.11 shows the initial behaviour of normalized velocity autocorrelation functions and their time derivatives at low densities in the gas region. At low temperatures, the decay of the autocorrelation functions is superimposed by small oscillations, which decay after a few cycles. The oscillations are clearly evident in the time derivatives of the velocity autocorrelation functions. The strongest effect is observed for the temperature $T^* = 0.7$ close to the triple point temperature. The magnitude of the oscillations increases with density, while the overall decay of the autocorrelation function becomes faster. Along the isochor $\rho^* = 0.025$, the oscillations become smaller with increasing temperature and vanish for the highest temperatures displayed in Figure 4.11. Moreover, the velocity autocorrelation functions decay more rapidly with increasing temperature.

Similar observations were reported by Michels and Trappeniers [145] for velocity autocorrelation functions of the Lennard-Jones model fluid at the temperatures $T^* = 1.0$ and 1.5. Additionally, Michels and Trappeniers found the same effect in the velocity autocorrelation function for a system of particles interacting by a square-well potential. They attributed the oscillations to the formation of bound states at low temperatures since the effect was only observed for intermolecular potential functions with attractive forces.

Michels and Trappeniers [145] explained the occurrence of oscillations by using
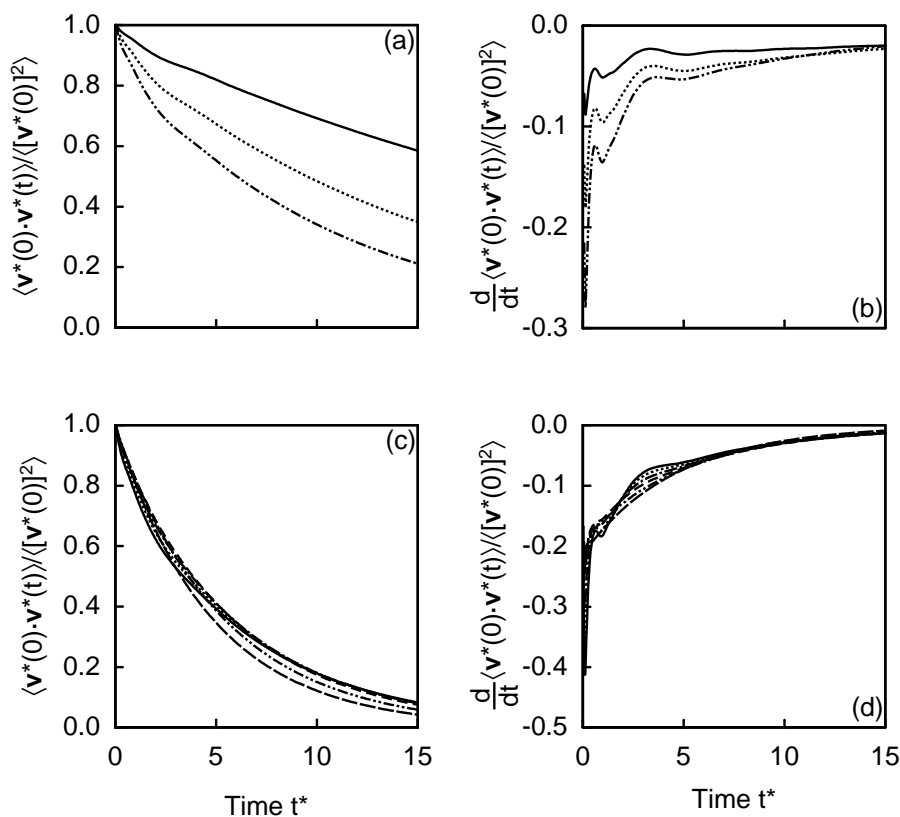
Figure 4.11. Short time behaviour of the normalized velocity autocorrelation function and its time derivative at gaseous densities. (a) and (b): Density dependence on the lowest isotherm $T^* = 0.7$. Legend: (———) $\rho^* = 0.005$, (············) $\rho^* = 0.01$ and (–·––·–) $\rho^* = 0.015$. (c) and (d): Temperature dependence along the isochor $\rho^* = 0.025$. Legend: (———) $T^* = 0.8$, (············) $T^* = 0.9$, (–·––·–) $T^* = 1.1$, (- - - -) $T^* = 1.5$, (–···––) $T^* = 2.5$ and (–––·) $T^* = 4.0$.

that the velocity autocorrelation function is the scalar product of the velocity vector at the time origin and the velocity vector at a later time t and, thus, closely related to the angle between the two vectors. For example, in the case of dimers, internal vibrations and rotations of the dimer relative to its centre of mass introduce periodic components into the motions of the particles that superimpose their translational motion. In an undisturbed vibrating dimer, the relative velocity of the two molecules is reversed within half of an oscillation period resulting in a negative contribution to the velocity autocorrelation function. In the following half period, the relative velocities return to their initial value, yielding a positive contribution. Due to the permanent creation and destruction of bound states by collisions with other particles

and the existence of a whole spectrum of rotational and vibrational frequencies, the oscillations in the velocity autocorrelation functions are damped out rapidly.

Dufty and Gubbins [35] and Marchetti and Dufty [134, 135] calculated the short time behaviour of the velocity autocorrelation function at low densities by means of kinetic theory for the square-well fluid. In their theory, the correlation function was separated into contributions due to scattering and bound states. The bound state contribution showed damped oscillations, whereas the scattering contribution decayed monotonically. The superimposed result was in excellent agreement with the simulation results of Michels and Trappeniers [145].

Since the integral of the velocity autocorrelation function determines the self-diffusion coefficient, the latter is influenced by the formation of bound states. Michels and Trappeniers [145] suggested that the formation of bound states also has an influence on the second self-diffusion virial coefficients because at low densities the number of dimers is proportional to density [204]. This hypothesis is supported by the well established fact that bound states have an influence on the second viscosity and thermal conductivity virial coefficient [54, 180, 181]. A quantification of the effect would require an extension of the Rainwater-Friend theory to self-diffusion and is not anticipated here.
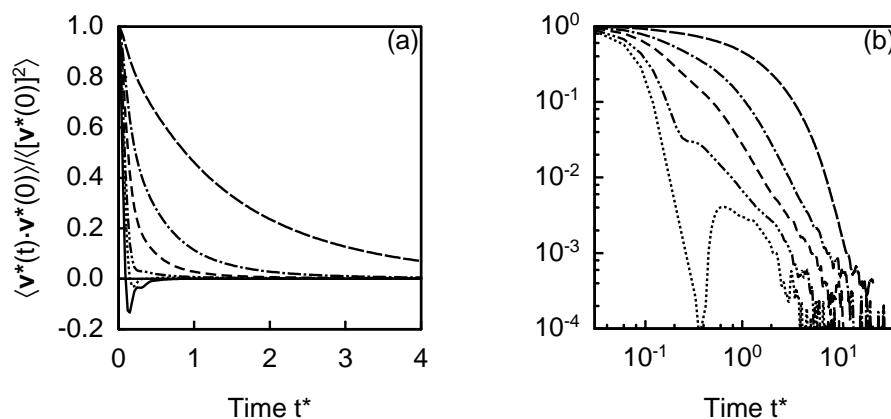
Figure 4.12. Dependence of the normalized velocity autocorrelation function on density along the close-critical isotherm $T^* = 1.35$ in (a) linear and (b) double logarithmic representation. Legend: (——) $\rho^* = 0.95$, (··········) $\rho^* = 0.8$, (—··—··—) $\rho^* = 0.7$, (– – – –) $\rho^* = 0.5$, (–··–··–·) $\rho^* = 0.3$ and (– – – –·) $\rho^* = 0.1$.

Figure 4.12 shows the dependence of the normalized velocity autocorrelation function on density for the supercritical isotherm $T^* = 1.35$. At low and intermediate

densities, the velocity autocorrelation function decays slowly, whereas in the liquid region it decays rapidly to negative values, exhibits a minimum and increases to positive values. Close to the freezing line at the density $\rho^* = 0.95$, several oscillations are observed in the negative regime. This behaviour is known as backscattering effect, see for example [113, 24]. At liquid densities, the free forward movement of a particles is hindered by the surrounding particles. They form a cage-like structure from which it is difficult for a particle to escape. The particle is reflected backwards at particles in front of it so that its velocity is inverted. Close to the freezing line, a particle may oscillate several times back and forth before it escapes from its cage.

The long time behaviour of the autocorrelation functions is better assessed in the double logarithmic representation. It is evident that the velocity autocorrelation function always approaches the time axis asymptotically from above. At long times, the decay is linear in double logarithmic representation before it ends in random noise for values of the autocorrelation functions below 0.001. This linear long time behaviour corresponds to hyperbolic decay of the type $\sim t^{-m}$ in the linear representation. The exponent $-m$ is the slope of the linear decay in the double logarithmic representation. The slope depends on the density of the state point and increases towards lower densities. Numerical values of the slopes were determined by linear least-squares fits to the linear long time parts of the velocity autocorrelation functions in the double logarithmic representation. The slopes are -1.4, -1.95, -2.5 and -4.8 at the reduced densities $\rho^* = 0.7$, 0.5, 0.3 and 0.1, respectively.

The hyperbolic long time tails in the velocity autocorrelation functions were first observed by Alder and Wainwright [6, 8] for a hard sphere fluid and, subsequently, explained by theoretical investigations using mode coupling approaches and kinetic theory [40, 178]. In contrast to the present results for the long time tail exponents, Alder and Wainwright found the value -3/2 for the hard sphere fluid independent from the density of the state point. Alder and Wainwright [8, 9] explained the long time decay of the velocity autocorrelation function by a simple hydrodynamic model. This hydrodynamic model treats the motion of a spherical particle with a prescribed initial velocity through a continuum liquid which represents the surrounding particles. The forward movement of the spherical particle creates a vortex. After about ten collisions, the vortex has the size of three particle diameters and feeds the velocity of the spherical particle back into itself via the surrounding medium. This effect leads to the long time correlations.

Figure 4.13 depicts the normalized velocity autocorrelation functions for the two isochors $\rho^* = 0.3$ and $\rho^* = 0.85$ for several temperatures. Along the close-critical
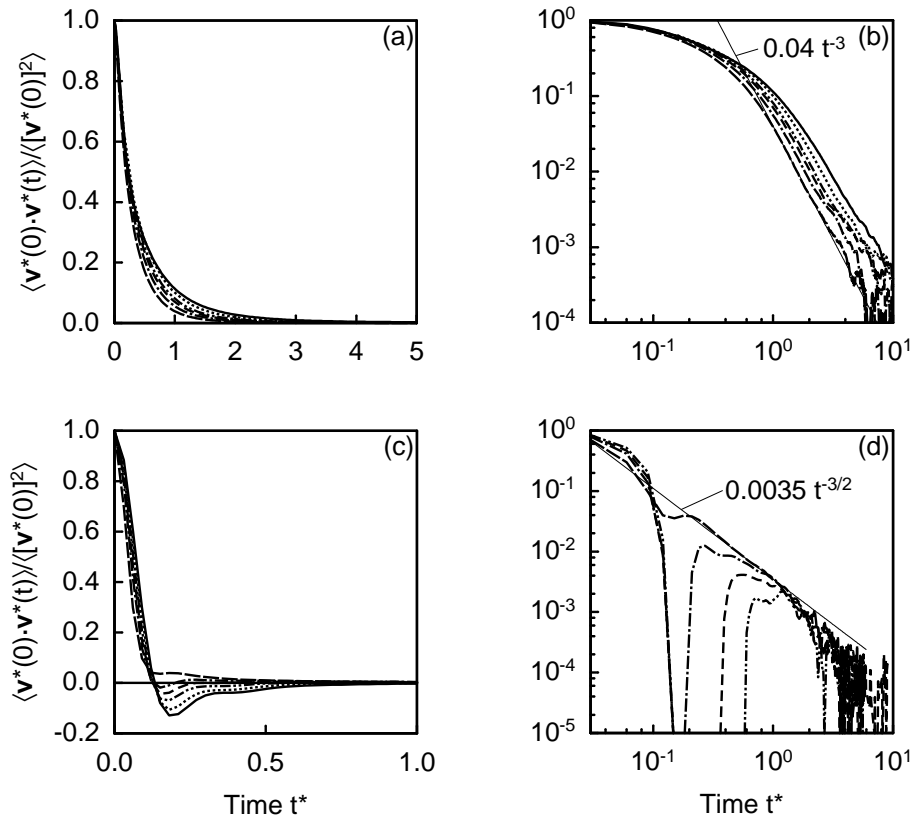
Figure 4.13. Dependence of the normalized velocity autocorrelation function on temperature in linear and double logarithmic representation. (a) and (b): Along the isochor $\rho^* = 0.3$ close to the critical density. Legend: (———) $T^* = 1.358$, (·············) $T^* = 1.8$, (—·····—) $T^* = 2.5$, (————) $T^* = 3.0$, (—·—··—·) $T^* = 4.0$ and (————) $T^* = 6.0$. (c) and (d): Along the liquid isochor $\rho^* = 0.85$. Legend: (———) $T^* = 0.7$, (·············) $T^* = 0.9$, (—·····—) $T^* = 1.3$, (————) $T^* = 1.8$, (—·—··—·) $T^* = 2.5$ and (————) $T^* = 6.0$. Negative values of the autocorrelation functions are not shown in the double logarithmic plots.

isochor $\rho^* = 0.3$, the decay becomes faster with increasing temperature. Due to the higher average velocity of the particles, collisions occur more frequently, which causes the correlations to decay more rapidly. Therefore, the integral of the normalized velocity autocorrelation function decreases with temperature and the increase of the product $D^*\rho^*$ is caused by the initial value of the correlation function $\langle \boldsymbol{v}_i^2 \rangle$. As $\langle \boldsymbol{v}_i^2 \rangle$ is related to the temperature by the equipartition theorem [29, p. 375], the temperature itself is the cause for the increase of $D^*\rho^*$. In double logarithmic representation, the linear long time regime is evident for every displayed temperature at this isochor. The long time tails are almost parallel with exponents of about -3.

At the higher liquid isochor $\rho^* = 0.85$, the behaviour is different. The negative region at intermediate times is shifted above the time axis with increasing temperature, thus, increasing the integral under the normalized autocorrelation function. At this density, the increase of the product $D^*\rho^*$ is due to temperature as well as to the slower decay of the normalized autocorrelation function. In double logarithmic representation, the autocorrelation function at the highest displayed temperature $T^* = 6.0$ reaches the linear long time behaviour after the negative regime and follows closely the curve $0.0035\,t^{-3/2}$. The exponent from a linear least-squares fit to the double logarithmic representation is -1.54. At lower temperatures, the linear long time tails are not observable before the autocorrelation functions vanish in the noise. However, a consequent continuation of the previously described behaviour to low temperatures would support the existence of the long time tails after the negative regime.

The results of this section for the long time behaviour of the velocity autocorrelation functions suggest that the exponent of the long time tail depends on the density of the state point. Only at liquid densities, the present results agree with the theoretically predicted value -3/2. With decreasing density, the hyperbolic decay at long times persists, but the exponent becomes larger. This behaviour is not unreasonable because it is expected that there is a continuous transition to the zero density limit.

Very recently, McDonough et al. [136] investigated the long time behaviour of the velocity autocorrelation functions of the Lennard-Jones and soft sphere model fluid with systems of 4000 particles at the reduced temperature $T^* = 2.17$ for the reduced densities $\rho^* = 0.35$, 0.45 and 0.55. They concluded that long time tails with the exponent -3/2 are observable for the soft sphere fluid after 2.57 and 2.1 reduced time units at the reduced densities $\rho^* = 0.35$ and $\rho^* = 0.55$, respectively. However, a closer inspection of their double logarithmic plots (Figures 1 and 3 in Ref. [136]) leads to the conclusion that in this time regime noise dominates the velocity autocorrelation functions so that their conclusions appear questionable.

The results for the long time behaviour of the velocity autocorrelation function rise the question if the slow decay has an impact on the accuracy of the self-diffusion data. Since the fit interval in the Einstein plots is always chosen in the linear regime, it is ensured that all correlations have decayed to a negligible level. For example, at densities above $\rho^* = 0.7$ the start of the fit interval was usually chosen at $t^* = 6.0$ or later, where the long time tails have vanished in the noise. Therefore, systematic errors of the present data due to long time tails are not expected.

5   The Viscosity of the Lennard-Jones Model Fluid

This chapter describes the simulation results for the viscosity of the Lennard-Jones model fluid. Besides the self-diffusion coefficient, the viscosity is the best investigated transport coefficient in molecular dynamics simulations. However, the uncertainty of literature data is often up to two orders of magnitude larger than those commonly achieved in experiments for real fluids. The present simulations differ from previous studies in two respects. First, it is attempted to simulate the viscosity at near-experimental uncertainties. By performing very long simulation runs, the statistical uncertainty of the data is decreased to a few percent. Second, the three viscosity contributions η_{tt}^*, η_{tc}^* and η_{cc}^* are calculated at every simulated state point. These results characterize the behaviour of the three viscosity contributions over a wide range of fluid states. An interpretation of the viscosity and its three contributions in the last section of this chapter in terms of shear stress correlation functions provides insights into the momentum transport mechanisms on the molecular scale.

5.1   Simulation Data for the Viscosity

The present viscosity data were determined from the three simulation series described in Section 3.5. In addition to the large body of simulations covering the entire fluid region with 343 new viscosity data, the series of extremely long simulations with production phases of 50 million times steps provides 39 data at low temperatures between $T^* = 0.7$ and $T^* = 1.2$ in the gas region. 11 additional data at the close-critical temperature $T^* = 1.35$ were obtained from the simulations with production phases of 10 million time steps.

For every simulated state point, the generalized mean-squared displacements and shear stress autocorrelation functions were computed. The parameters for the computation of both functions were the same at every simulated state point. Every fifth time step was taken as a new time origin. The data for the viscosity contributions were derived from the generalized displacement functions as described in Section 3.3.1 and the total viscosity was then obtained as the sum of the three contributions. The data are summarized in Appendix D in Tables D.3 and D.4 for the two simulation series.

The uncertainties of the viscosity data of the first simulation series are estimated to be 3 % at high densities above $\rho^* = 0.6$, 5 % for densities between $\rho^* = 0.3$ and $\rho^* = 0.6$ and 10 % for densities below $\rho^* = 0.3$. The uncertainties of the viscosity contributions depend on the contribution as well as on density. The η_{tt}^*- and η_{cc}^*-data have uncertainties of 3 % at high densities, while at densities below $\rho^* = 0.3$ in the gas region the uncertainties increase up to 10 %. The η_{tc}^*-data have higher uncertainties of about 20 % over almost the entire density and temperature range. At low temperatures in the gas region, the uncertainty of the data is even higher with up to 50 %.

The uncertainty of the data of the second simulation series at gaseous densities is lower. The viscosity data and η_{tt}^*-data have uncertainties of about 4 %, whereas the uncertainties of the η_{tc}^*- and η_{cc}^*-data are estimated to be 30 % and 1 %, respectively.

Table 5.1 provides a summary of the available literature data sets with its characteristic simulation parameters. Holian and Evans [95] applied a modified Lennard-Jones potential in their simulations, which results in different macroscopic properties as the application of the original Lennard-Jones potential. Thus, their data are excluded from further considerations. In most studies, the viscosity was obtained from the time integral of the shear stress correlation function using the Green-Kubo integral formula. Beside the data of this work, only the data of Rowley and Painter were obtained by application of the Einstein relation. Nonequilibrium molecular dynamics was used by Ashurst and Hoover [13] and Heyes [83, 84]. Additionally, Heyes [82] carried out nonequilibrium simulations using the difference in trajectories method, but the data were not reported in the publication. Almost all literature simulation studies applied small cutoff radii between $r_{cut}^* = 2.5$ and 3.5 and only very few simulations were conducted with more than 500 particles, whereas the present simulations were performed with cutoff radii between $r_{cut}^* = 5.0$ and 6.5 and 1372 particles. An important indicator for the quality of simulation data is the simulation length since it determines the statistical uncertainty of the data. The simulations of Hammonds and Heyes [66], Heyes [83, 84, 86], Michels and Trappeniers [153] and Rowley and Painter [185] extend over similar or longer time periods as the simulations of this work.

The distribution of the literature viscosity data in the T^*,ρ^*-plane is given in Figure 5.1. As the self-diffusion literature data, the available literature data for the viscosity concentrate in the high density liquid region below the $T^* = 3.0$ isotherm. The data sets of Heyes [84] and Rowley and Painter [185] are the most comprehensive and cover a similar state region as the data of this work. The data of Heyes

Table 5.1. Literature data sets for the viscosity of the Lennard-Jones model fluid. Abbreviations: DT: difference in trajectories method, ER: Einstein relation, GK: Green-Kubo integral, LE: Lees-Edwards shear boundary conditions, WR: wall reservoir boundary conditions. Remarks: [1]: modified Lennard-Jones potential, [2]: not reported by the authors, [3]: according to Figure 1 in Ref. [30], [4]: according to Figure 1 in Ref. [66], [5]: Nonequilibrium data not extrapolated to zero shear rate. Literature data for the viscosity already listed in Table 3.1 are not considered here.

Author	Year	Data	Method	Ensemble	N	r^*_{cut}	T^*	ρ^*	Simul. Length
This work	2002	343	ER	*NVEMG*	1372	5.0-6.5	0.7-6.0	0.005-1.275	4500-6000
This work	2002	39	ER	*NVEMG*	1372	6.5	0.7-1.2	0.005-0.15	150000
This work	2002	11	ER	*NVEMG*	1372	6.5	1.35	0.05-0.45	30000
Ashurst[5] [13]	1975	39	WR	*NVE*	108-324	2)	0.7-30.0	0.25-1.4	464
Borgelt [25]	1990	46	GK	*NVEMG*	108	2.5	0.66-2.94	0.78-0.8415	371
Canales [30]	1999	3	GK/ER	*NVT*	668	2.71, 3.11[4]	0.53, 1.89	0.756, 1.143	554-1203
Hammonds [66]	1988	51	GK	*NVEMG/T*	108-500	3)	0.72-10.0	0.4-1.18	3000-14000
Heyes [79]	1983	49	DT	*NVEMG*	256	2.5	0.68-4.58	0.2-1.13	150
Heyes [83]	1987	16	LE	*NVT*	108-2048	2)	1.4562	0.1-1.0	100-9000
Heyes [84]	1988	208	GK	*NVT*	108-500	2)	0.72-10.0	0.2-1.22	417-9500
Heyes [85]	1990	87	LE	*NVT*	256	2)	1.45-10.0	0.3-1.22	278, 1460
Heyes [85]	1990	25	GK	*NVT*	256	2.5	0.722-6.0	0.4-1.4	1500
Heyes [86]	1993	4	GK	*NVEMG*	256	2.5	0.707-6.02	0.5-1.0	655-17082
Holian [95]	1983	1	LE	*NVT*	108	1.24[1]	2.75	0.7	60-900
Holian [95]	1983	3	LE	*NVT*	108-4000	1.24[1]	2.75	0.7	45-98
Levesque [119]	1987	4	GK	*NVEMG*	108, 864	2)	2.725-2.803	0.962-1.113	11-88
Michels [153]	1985	36	GK	*NVEMG*	108	2.5	1.3-10.0	0.05-0.3	9120-151200
Rowley [185]	1997	171	ER	*NVT*	256	3.5	0.8-4.0	0.05-1.0	182-6063
Schoen [189]	1985	13	GK	*NVEMG*	32-2048	2.5	0.68-4.42	0.5-1.113	232-928
Schoen [190]	1986	32	GK	*NVEMG*	500	2.5	0.68-4.0	0.45-0.85	464
Sharma [195]	1994	2	GK	*NVT*	108	2.5	0.59, 0.61	1.0, 1.21	320
Stassen [201]	1995	5	GK	*NVEMG*	256	3.4-5.3	1.26	0.211-0.8445	325
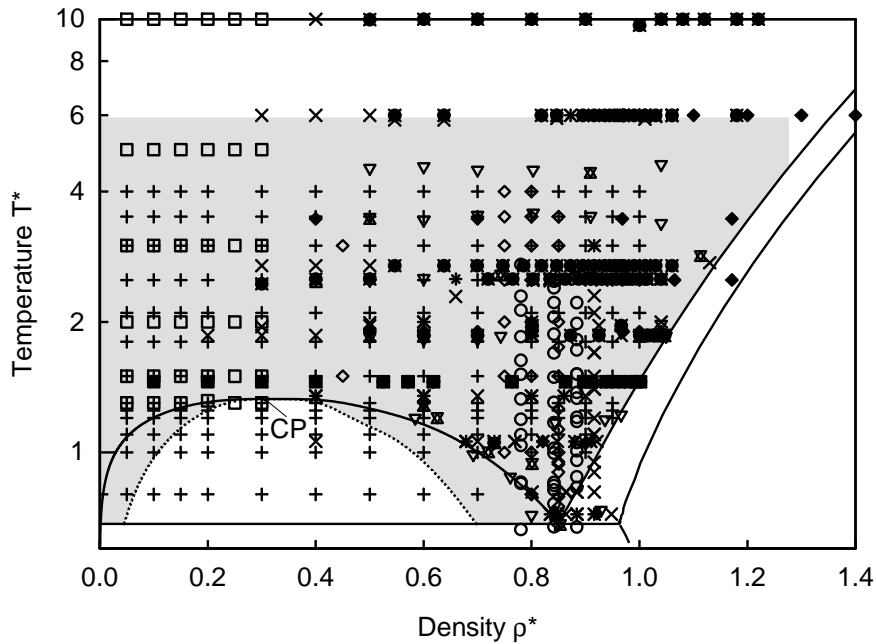
Figure 5.1. The distribution of literature data for the viscosity η^* in the T^*,ρ^*-plane. The shaded area is the state region considered in this work. Legend: (○) Borgelt et al. [25], (✳) Hammonds and Heyes [66], (▽) Heyes [79], (■) Heyes [83], (×) GK data of Heyes [84], (●) nonequilibrium data of Heyes [84], (◆) Heyes [85], (□) Michels and Trappeniers [153], (+) Rowley and Painter [185], (◇) Schoen [190] and (△) Schoen and Hoheisel [189].

extend to higher temperatures, but do not cover low density gaseous states. The simulations of Rowley and Painter cover the temperature range from $T^* = 0.8$ to 4.0 and extend from low density gaseous states to the density $\rho^* = 1.0$. Rowley and Painter included state points in the metastable and unstable region of the phase diagram. Data in the gas region at supercritical temperatures were reported by Michels and Trappeniers [153]. They also investigated the subdivision of viscosity into the three contributions. These data were obtained from very long simulations extending over 150000 reduced time units and supplement the subcritical low density data from the second simulation series of this work. Schoen [190] explored the temperature dependence of viscosity isochors at high densities.

In the remainder of this section, the selected viscosity data of this work are discussed and compared with literature data, whereas the characteristic behaviour of the viscosity and viscosity contributions in the fluid region of the phase diagram is treated in the next two sections. Figures 5.2 and 5.3 show the results for the viscosity
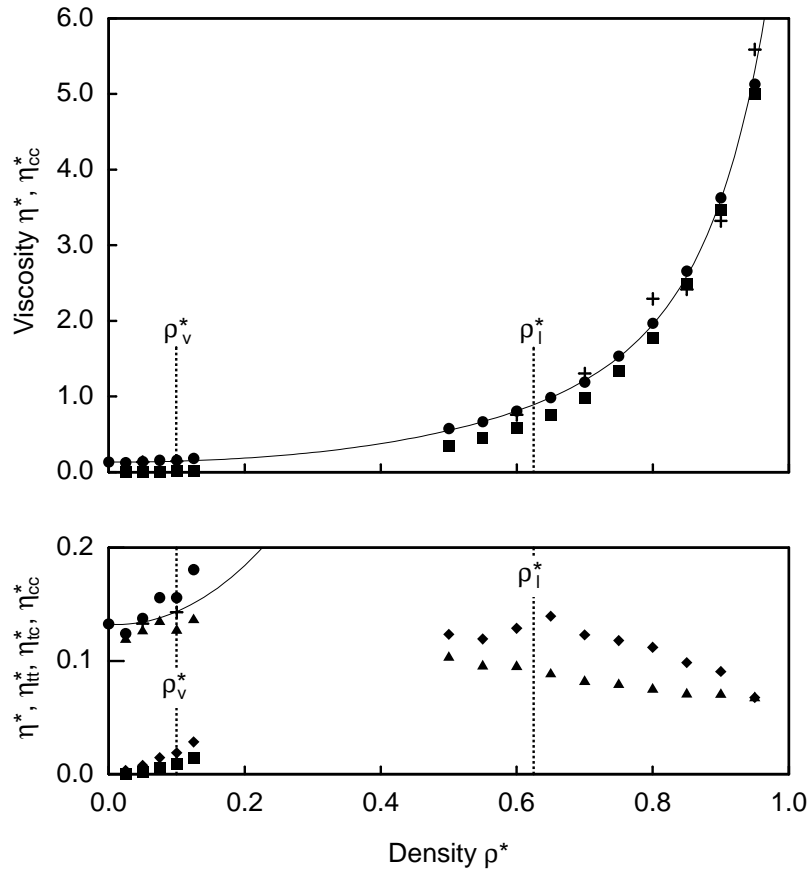
Figure 5.2. The viscosity η^* ($\bullet$) and the viscosity contributions η_{tt}^* ($\blacktriangle$), η_{tc}^* ($\blacklozenge$) and η_{cc}^* ($\blacksquare$) for the subcritical isotherm $T^* = 1.2$ as a function of density. Symbols at zero density denote the Chapman-Enskog solution to the Boltzmann equation. Legend: (+) data of Rowley and Painter [185] and (——) correlation of Rowley and Painter [185].

and the three viscosity contributions for the same selected isotherms $T^* = 1.2$ and $T^* = 3.0$ which were already discussed in Section 4.1 for the self-diffusion data. Included are literature data from different sources discussed above. At high densities, the viscosity is dominated by the configurational-configurational contribution η_{cc}^*, whereas η_{tt}^* and η_{tc}^* contribute little to the total viscosity. At low densities, the η_{cc}^* isotherms are relatively flat, but with increasing densities they become steeper and increase exponentially at high densities. The data for η_{cc}^* are very consistent over the whole density range. The translational-translational contribution η_{tt}^* yields the largest contribution to the total viscosity at low densities in the gas region, decreases with density and becomes flat close to the freezing line. The data for
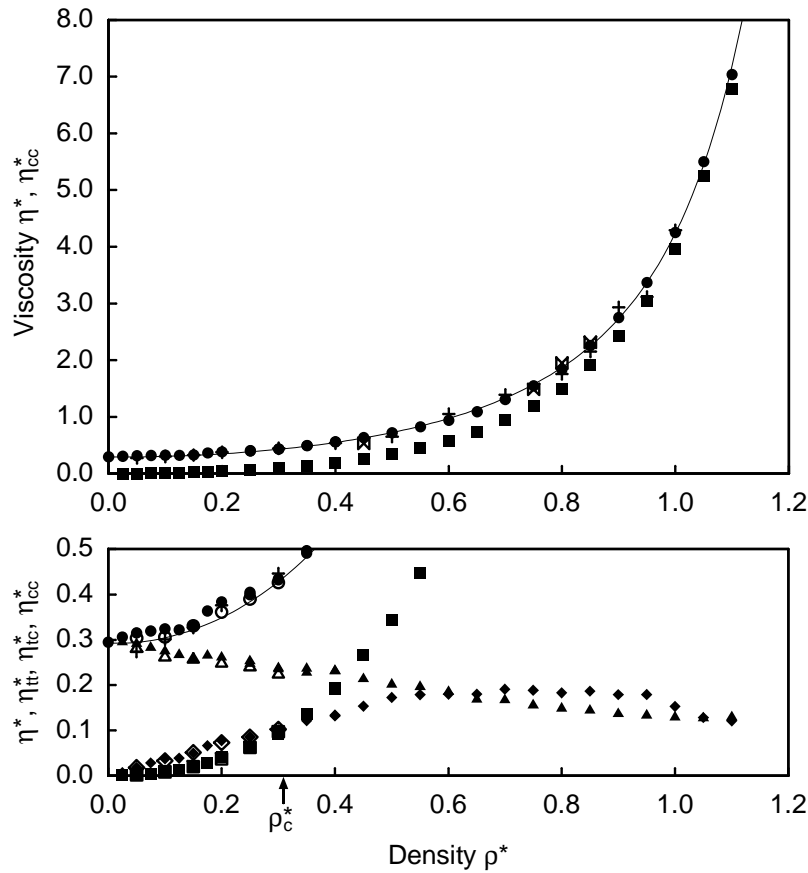
Figure 5.3. The viscosity η^* ($\bullet$) and the viscosity contributions η^*_{tt} ($\blacktriangle$), η^*_{tc} ($\blacklozenge$) and η^*_{cc} ($\blacksquare$) for the supercritical isotherm $T^* = 3.0$ as a function of density. Symbols at zero density denote the Chapman-Enskog solution to the Boltzmann equation. Legend: ($\circ$) data of Michels and Trappeniers [153], (+) Rowley and Painter [185], ($\bowtie$) Schoen [190] and (———) correlation of Rowley and Painter [185]; ($\triangle$), ($\diamond$) and ($\square$) denote the results of Michels and Trappeniers [153] for the viscosity contributions η^*_{tt}, η^*_{tc} and η^*_{cc}.

this contribution are fairly consistent at intermediate and high densities, but show some scatter in the gas region. The translational-configurational contribution η^*_{tc} shows a different behavior. At gaseous densities, it increases, reaches a maximum at intermediate densities and decreases in the high density region. On the subcritical isotherm $T^* = 1.2$, the maximum is partly covered by the two-phase region. The cross contribution η^*_{tc} shows the largest scatter of the three viscosity contributions and is the most difficult to simulate accurately.

At liquid densities, the viscosity data of this work show less scatter than the data of Rowley and Painter [185] and the data of Schoen [190]. Michels and Trappeniers

[153] investigated the behaviour of the three viscosity contributions on supercritical isotherms up to the density $\rho^* = 0.3$. On the isotherm $T^* = 3.0$, their data are more consistent and systematically lower than the present data. However, they used different simulation parameters: a cutoff radius of $r_{\mathrm{cut}}^* = 2.5$, 108 particles and their simulations extended over up to 150000 reduced time units. The systematic deviations are due to the translational-translational contribution, which yields the largest contribution to the total viscosity. The contributions η_{tc}^* and η_{cc}^* agree well with the data of this work. The correlation of Rowley and Painter [185] follows the present data well at high densities. However, this is surprising since it was fitted to only their own data. In the gas region, the data of this work lie above the correlation on both isotherms, suggesting that the correlation predicts gas viscosities that are too low.

5.2   Temperature and Density Dependence of the Viscosity

Figure 5.4 gives an overview over all 16 simulated viscosity isotherms. The viscosity of the Lennard-Jones model fluid shows the typical temperature and density dependence known for real fluids. The isotherms intersect in the density range between $\rho^* = 0.75$ and 0.8, which corresponds to approximately 2.5 times the critical density. This intersection point marks a change in the temperature dependence of the viscosity. At lower densities, the viscosity increases with temperature, while it decreases at higher densities in the liquid region.

   Another viewpoint is explored when the viscosity is plotted along isochors as a function of temperature. Figure 5.5 shows the viscosity for eight selected isochors between $\rho^* = 0.45$ and 0.95 and the data of Schoen [190] on four isochors between $\rho^* = 0.45$ and 0.85. The two lowest displayed isochors $\rho^* = 0.45$ and 0.6 are almost parallel to the zero density viscosity at supercritical temperatures. If the viscosity is separated using the empirical subdivision given by Eq. (2.205), the residual viscosity, i.e. the viscosity minus the zero density viscosity, depends only weakly on temperature. This observation is in agreement with the behaviour of the viscosity of real fluids in this state region [64].

   On the isochors $\rho^* = 0.7$, 0.75 and 0.8, the temperature dependence changes. The viscosity decreases at low temperatures, reaches a minimum and increases in the high temperature region. This is the density range where the viscosity isotherms in Figure 5.4 intersect. The temperature T_{I}^* for which $\partial\eta^*/\partial T_{\mathrm{I}}^* = 0$ is the inversion temperature. It marks a transition from gas-like ($T^* > T_{\mathrm{I}}^*$) to liquid-like ($T^* < T_{\mathrm{I}}^*$)
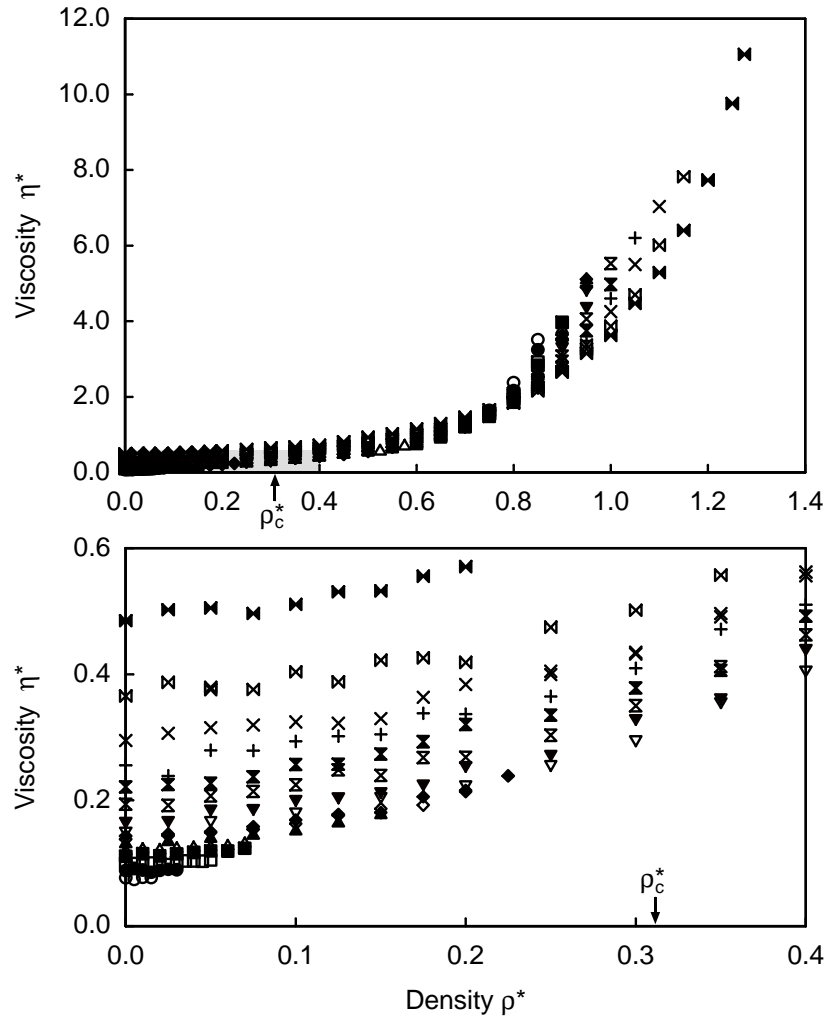
Figure 5.4. The viscosity η^* for all simulated isotherms as a function of density. Symbols at zero density denote the Chapman-Enskog solution to the Boltzmann equation. The shaded area is enlarged in the bottom plot. Legend: ($\bigcirc$) $T^* = 0.7$, ($\bullet$) $T^* = 0.8$, ($\square$) $T^* = 0.9$, ($\blacksquare$) $T^* = 1.0$, ($\triangle$) $T^* = 1.1$, ($\blacktriangle$) $T^* = 1.2$, ($\diamond$) $T^* = 1.25$, ($\blacklozenge$) $T^* = 1.3$, ($\triangledown$) $T^* = 1.35$, ($\blacktriangledown$) $T^* = 1.5$, ($\boxtimes$) $T^* = 1.8$, ($\boxtimes$) $T^* = 2.1$, ($+$) $T^* = 2.5$, ($\times$) $T^* = 3.0$, ($\bowtie$) $T^* = 4.0$ and ($\blacktriangleright\!\!\blacktriangleleft$) $T^* = 6.0$.

viscous behaviour. The inversion temperature increases with density from approximately the critical temperature on the isochor $\rho^* = 0.7$ to about $T_\mathrm{I}^* = 2.0$ on the isochor $\rho^* = 0.8$. From the density $\rho^* = 0.85$ on, the isochors show the typical behaviour for the liquid region and decrease monotonically with temperature.

The data of Schoen show higher scatter than the present data on the isochors
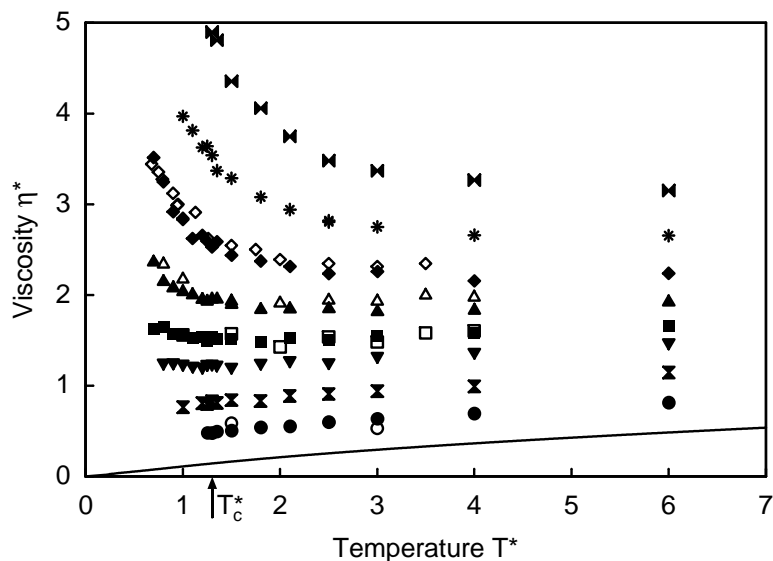
Figure 5.5. The viscosity η^* for selected isochors as a function of temperature. Legend: This work: ($\bullet$) $\rho^* = 0.45$, ($\mathbf{X}$) $\rho^* = 0.6$, ($\blacktriangledown$) $\rho^* = 0.7$, ($\blacksquare$) $\rho^* = 0.75$, ($\blacktriangle$) $\rho^* = 0.8$, ($\blacklozenge$) $\rho^* = 0.85$, ($\divideontimes$) $\rho^* = 0.9$ and ($\bowtie$) $\rho^* = 0.95$; Schoen: ($\bigcirc$) $\rho^* = 0.45$, ($\square$) $\rho^* = 0.75$, ($\triangle$) $\rho^* = 0.8$ and ($\diamond$) $\rho^* = 0.85$; (———) Chapman-Enskog solution to the Boltzmann equation.

$\rho^* = 0.45$ and 0.75. On the two higher isochors $\rho^* = 0.8$ and 0.85, the data of Schoen lie above the data of this work. Schoen's data suggest that the isochors $\rho^* = 0.8$ and 0.85 exhibit minima [190], but the present data support only the minimum on the isochor $\rho^* = 0.8$. Comparing the parameters of Schoen's simulations and the present simulations (see Table 5.1), the present data are expected to be more accurate. Schoen reports the statistical uncertainty of his data to be about 3 % to 5 %, while the present data have an uncertainty of 3 %.

Figure 5.6 shows selected experimental data for the viscosity of the noble gas argon along several isotherms in the temperature range between $T = 107.7$ K and 348.15 K. This range extends from 0.72 to 2.3 times the critical temperature of argon, while the present simulation data extend from 0.53 to 4.5 times the critical temperature of the Lennard-Jones model fluid. The viscosity of argon shows the same characteristics and qualitative dependence on density and temperature as observed for the viscosity of the Lennard-Jones model fluid in Figure 5.4.
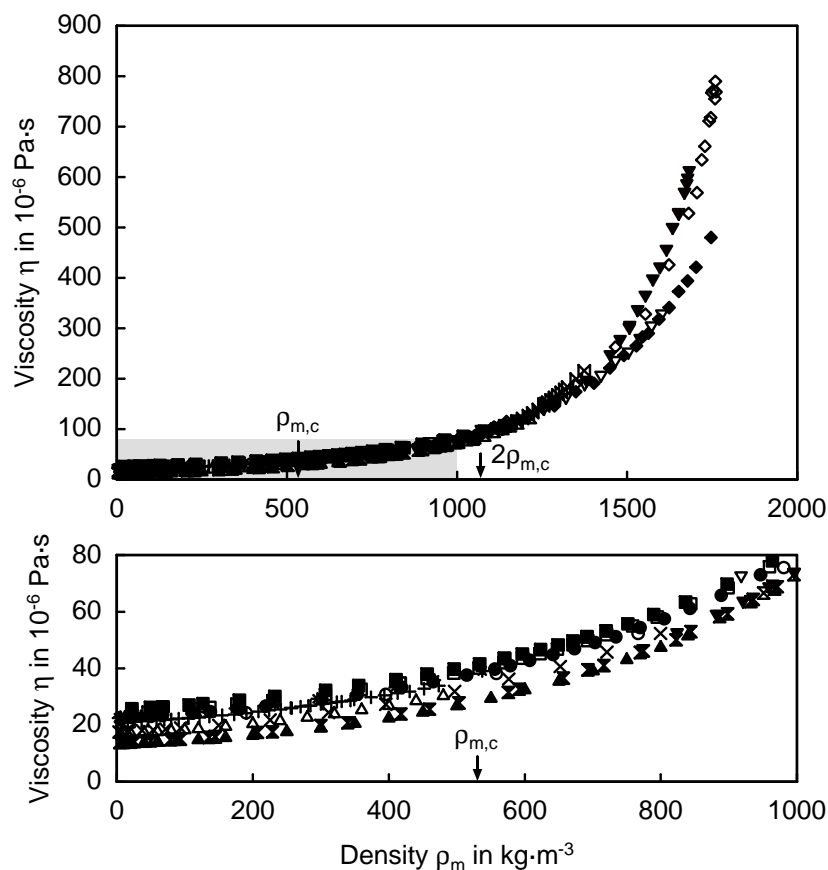
Figure 5.6. Experimental data for the viscosity of the noble gas argon. Critical parameters of argon: $T_c = 150.7$ K, $\rho_{m,c} = 530.9$ kg m^{-3}. The shaded area is enlarged in the bottom figure. Legend: Gracki et al. [56]: ($\blacktriangle$) $T = 173.15$ K, ($\triangle$) $T = 223.15$ K; van der Gulik [62]: ($\blacktriangledown$) $T = 174.45$ K; Haynes [73]: ($\bowtie$) $T = 107.7$ K, ($\blacktriangleright\hspace{-0.3em}\blacktriangleleft$) $T = 125$ K, ($\boxtimes$) $T = 139.7$ K, ($\mathbf{\Xmark}$) $T = 173$ K, ($\times$) $T = 223$ K, ($+$) $T = 270$ K, ($\ast$) $T = 298$ K; Michels et al. [143]: ($\circ$) $T = 273.15$ K, ($\bullet$) $T = 298.15$ K, ($\square$) $T = 323.15$ K, ($\blacksquare$) $T = 348.15$ K; Trappeniers et al. [209]: ($\diamond$) $T = 223.15$ K, ($\blacklozenge$) $T = 301.15$ K, ($\triangledown$) $T = 323.15$ K.

5.3   The Viscosity Contributions

In this section, the temperature and density dependence of the three viscosity contributions η_{tt}, η_{tc} and η_{cc} is discussed. In terms of Einstein relations, the three contributions are determined by

$$\eta_{\mathrm{tt}} = \lim_{t\to\infty} \frac{V}{2kT} \frac{\mathrm{d}}{\mathrm{d}t} \left\langle \left[\int_{t_0}^{t} \tau_{\mathrm{xy,t}}(t)\,\mathrm{d}t \right]^2 \right\rangle \tag{5.1}$$

$$\eta_{\mathrm{tc}} = \lim_{t\to\infty} \frac{V}{kT} \frac{\mathrm{d}}{\mathrm{d}t} \left\langle \left[\int_{t_0}^{t} \tau_{\mathrm{xy,t}}(t)\,\mathrm{d}t \right] \left[\int_{t_0}^{t} \tau_{\mathrm{xy,c}}(t)\,\mathrm{d}t \right] \right\rangle \tag{5.2}$$

$$\eta_{\mathrm{cc}} = \lim_{t\to\infty} \frac{V}{2kT} \frac{\mathrm{d}}{\mathrm{d}t} \left\langle \left[\int_{t_0}^{t} \tau_{\mathrm{xy,c}}(t)\,\mathrm{d}t \right]^2 \right\rangle \tag{5.3}$$

and the total viscosity is given by the sum of the three contributions, see Eq. (2.198).
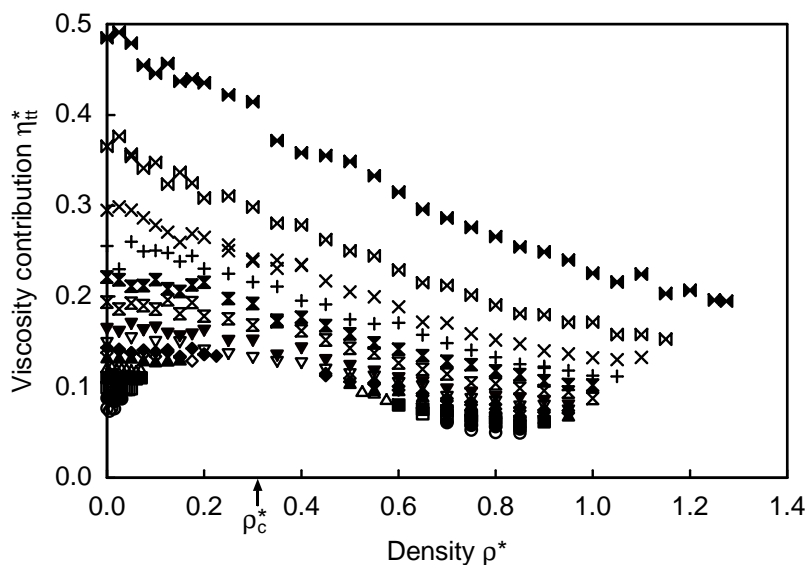
Figure 5.7. The translational-translational viscosity contribution η_{tt}^* for all simulated isotherms as a function of density. Symbols are the same as in the legend to Figure 5.4.

Figure 5.7 displays the results for the translational-translational viscosity contribution η_{tt}^* for all 16 simulated isotherms. The isotherms are clearly distinguishable and do not intersect. At subcritical and supercritical temperatures not too far above the critical temperature, the isotherms are almost horizontal in the gas region in

this representation. In the liquid region, the decrease first becomes steeper, but flattens again close to the freezing line. The highest isotherms decline strongly over almost the whole density range before becoming flatter near the freezing line. The dependence of η_{tt}^* on temperature is monotonic over the whole density range from the low density gas up to the compressed liquid, increasing with temperature. At low and intermediate densities, it closely resembles the behaviour of the product $D^*\rho^*$ (see Figures 4.4 and 4.5). However, close to the freezing line the behaviour is different. The curvature of the η_{tt}^* isotherms is concave, while the $D^*\rho^*$ isotherms are convex in this state region. Due to the higher scatter of the η_{tt}^* data, the fine details of the isotherms in the gas region, such as the initial slope and the curvature, cannot be resolved as for the $D^*\rho^*$ isotherms.
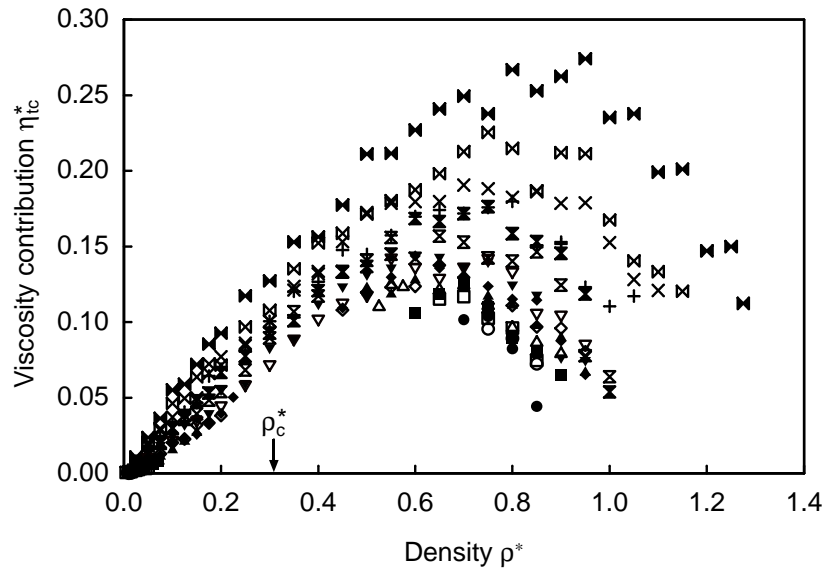
Figure 5.8. The translational-configurational viscosity contribution η_{tc}^* for all simulated isotherms as a function of density. Symbols are the same as in the legend to Figure 5.4.

The isotherms of the translational-configurational contribution are depicted in Figure 5.8. Due to larger scatter of the data, the isotherms are not as clearly distinguishable as for the translational-translational contribution. However, some trends can be observed from Figure 5.8. The isotherms start from zero in the zero density limit, increase and reach a maximum at approximately 2.0 to 2.5 times the critical density. At higher liquid densities, the isotherms decrease. This contribution also shows a monotonic temperature dependence, increasing with temperature over the whole density range. The maximum of the isotherms is shifted to higher densities

as the temperature increases. It occurs in that density range where the viscosity isotherms intersect.
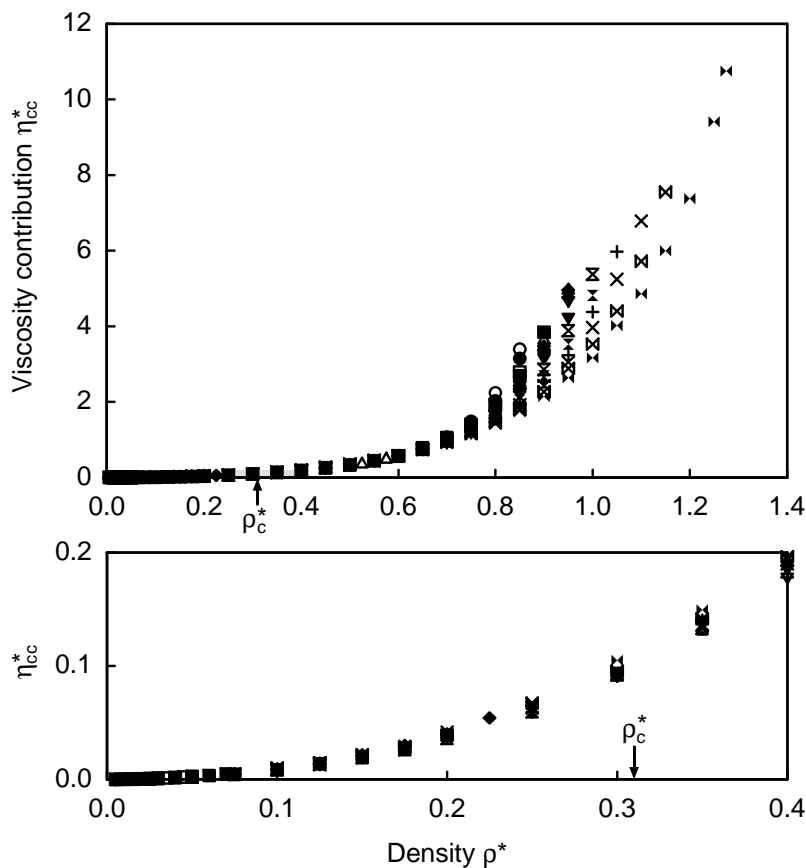
Figure 5.9. The configurational-configurational viscosity contribution η_{cc}^* for all simulated isotherms as a function of reduced density. The shaded area is enlarged in the bottom plot. Symbols are the same as in the legend to Figure 5.4.

Figure 5.9 shows the isotherms of the configurational-configurational viscosity contribution η_{cc}^*. The behaviour is more complex than that of η_{tt}^* and η_{tc}^*. This contribution depends only weakly on temperature up to densities of about $\rho^* = 0.7$. From this point, the isotherms split and diverge. The splitting occurs in the same density range where η_{tc}^*-isotherms exhibit their maxima and the viscosity isotherms intersect. In the high density region, η_{cc}^* decreases with temperature.

Figure 5.10 displays the configurational-configurational viscosity contribution η_{cc}^* for selected isochors. Since the values of η_{cc}^* extend over several orders of magnitude, its temperature dependence is difficult to visualize in one plot. Therefore, the isochors for liquid densities are displayed in a linear scale. The gaseous isochors
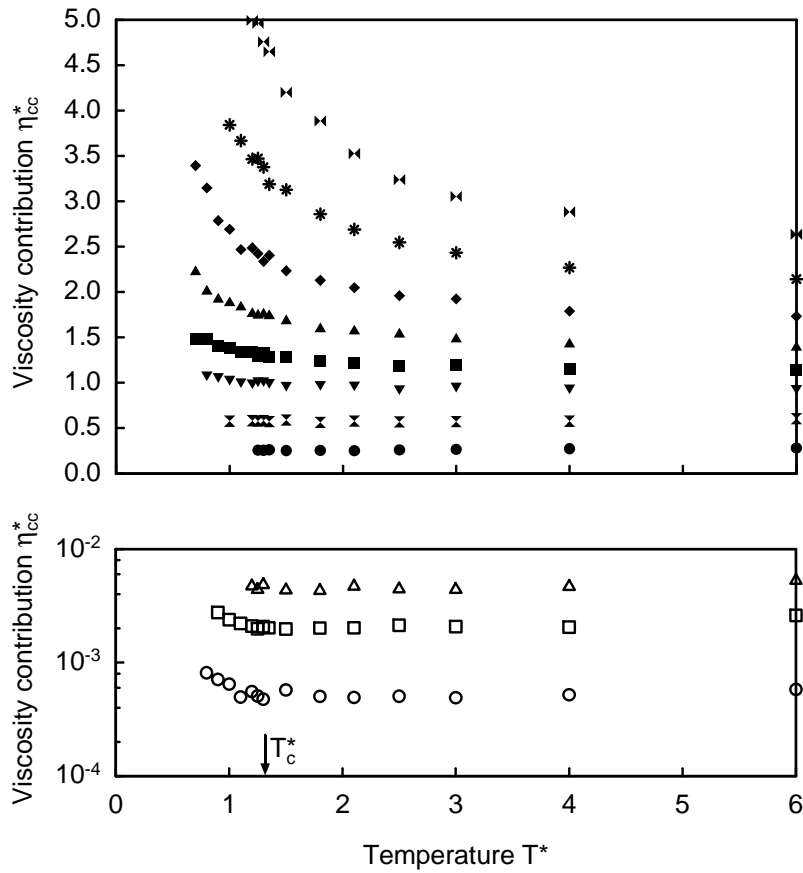
Figure 5.10. The configurational-configurational viscosity contribution η_{cc}^* for selected isochors as a function of temperature. Legend: (○) $\rho^* = 0.025$, (□) $\rho^* = 0.05$, (△) $\rho^* = 0.075$, (●) $\rho^* = 0.45$, (✗) $\rho^* = 0.6$, (▼) $\rho^* = 0.7$, (■) $\rho^* = 0.75$, (▲) $\rho^* = 0.8$, (◆) $\rho^* = 0.85$, (✳) $\rho^* = 0.9$ and (⋈) $\rho^* = 0.95$.

are given in semi-logarithmic representation. The isochoric representation reveals that the temperature dependence of η_{cc}^* up to the point where the isotherms split is more complex than the isothermal representation, Figure 5.9, indicates. Above the critical density, the isochors $\rho^* = 0.45$ and 0.6 are indeed almost constant in this representation. Increasing the resolution (not shown here) reveals that they increase slightly with temperature. In the gas region, the isochors decrease steeply at sub-critical temperatures, but show little dependence on temperature at supercritical temperatures.

With the observed rather different and complex behaviour of the three viscosity contributions, the viscosity surface in Figures 5.4 and 5.5 can now be constructed

by superposition of the contributions. At high liquid densities, the configurational-configurational contribution η_{cc}^* dominates, in the gas region the translational-translational contribution η_{tt}^* yields the largest contribution to the viscosity. The temperature dependence of the viscosity follows that of the dominating contribution. The minima on the viscosity isochors are caused by the superposition of the opposite temperature dependencies of η_{cc}^*, on the one hand, and η_{tt}^* and η_{tc}^*, on the other hand.
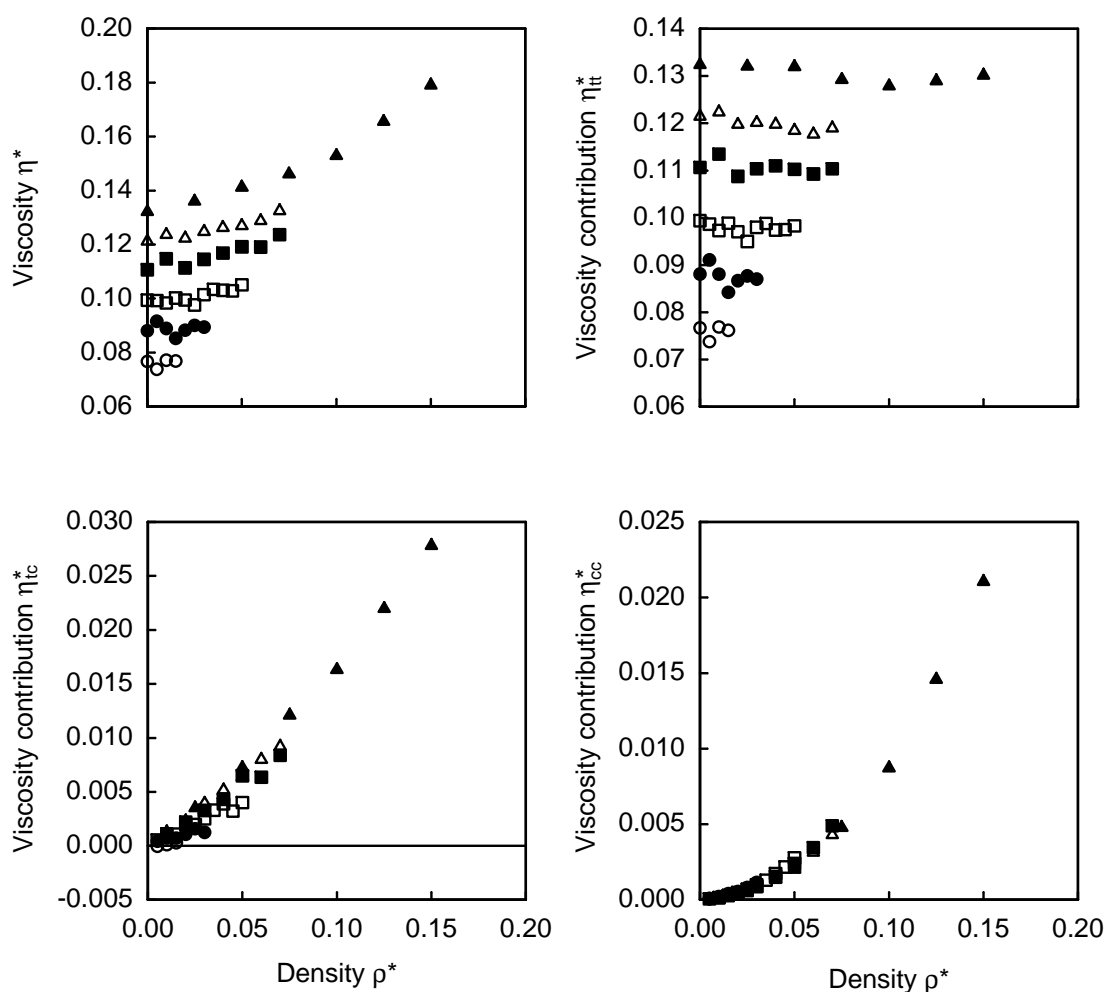
Figure 5.11. The viscosity η^* and the viscosity contributions η_{tt}^*, η_{tc}^* and η_{cc}^* for subcritical isotherms as a function of density. Symbols at zero density denote the Chapman-Enskog solution to the Boltzmann equation. Legend: (○) $T^* = 0.7$, (●) $T^* = 0.8$, (□) $T^* = 0.9$, (■) $T^* = 1.0$, (△) $T^* = 1.1$ and (▲) $T^* = 1.2$.

In Figure 5.11, the results for the viscosity and its three contributions are depicted for the second simulation series at subcritical gaseous states. Due to the much longer production phases of 150000 reduced time units, the data are far more accurate than the data at the same state point of the first series, whose simulations extended over 6000 reduced time units. Beside the data of this work, only the data set of Rowley and Painter [185] provides six viscosity data in this state region. They are not shown in Figure 5.11 because their uncertainty is much higher than the uncertainty of the present data. The present simulations were carried out to determine the behaviour of the viscosity in the gas region at low temperatures. It is a well established fact that the initial slope of the isotherms becomes negative at reduced temperatures below about $T^* = 1.0$ for real fluids [20, 54, 180, 181]. Moreover, the isotherms exhibit minima in a small temperature range below this temperature. For instance, for propane a minimum is observed on the isotherm $T = 280$ K between the densities $\rho = 0.11$ to 0.14 mol dm^{-3} [216]. With the scaling parameters $\sigma = 0.49748$ nm and $\varepsilon/k = 263.88$ K reported by Vogel et al. [216] for the Lennard-Jones potential, these states correspond to the reduced density range between $\rho^* = 0.008$ and 0.01 on the isotherm $T^* = 0.942$ of the Lennard-Jones model fluid.

The two highest isotherms $T^* = 1.1$ and 1.2 increase with density. The isotherms $T^* = 0.9$ and 1.0 increase near the dew line. However, if the initial slope is negative and if a minimum exists on these isotherms cannot be unambiguously decided because the scatter of the data is too high at the lowest densities. For the two lowest isotherms $T^* = 0.7$ and 0.8, the density dependence cannot be assessed due to the scatter of the data. In spite of the extensive simulation lengths, the scatter of the data is still too high to determine the shape of the isotherms unambiguously. For a definite determination of the initial slopes of the viscosity isotherms and their shape, even longer simulation runs than those of the present simulations are required. Provided that the statistics are comparable for self-diffusion and viscosity, simulations extending over at least two billion time steps are needed to obtain viscosity data at the accuracy level of the self-diffusion data presented in Chapter 4. Such simulations are at present even on the fastest high performance computers not feasible. Thus, this issue remains unsolved.

In Figure 5.9, the isotherms of the configurational-configurational viscosity contribution are extremely flat at low densities. This rises the question wether the initial slope of the isotherms is zero or takes small non-zero values. Negative initial slopes are not possible as η_{cc}^* is zero at zero density and must always be positive at
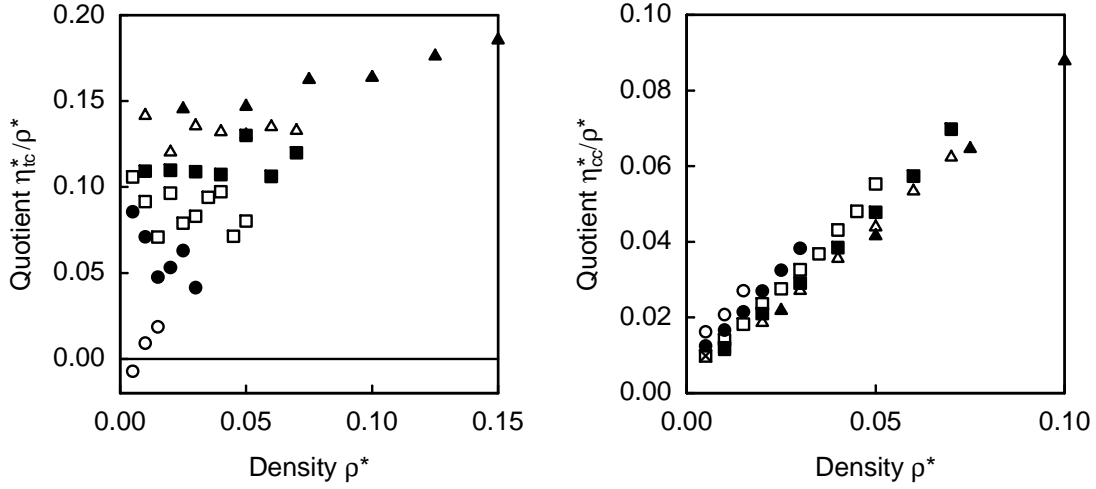
Figure 5.12. The quotients $\eta_{\text{tc}}^*/\rho^*$ and $\eta_{\text{cc}}^*/\rho^*$ at gaseous states on subcritical isotherms as a function of density. Legend: (○) $T^* = 0.7$, (●) $T^* = 0.8$, (□) $T^* = 0.9$ and $N = 1372$, (×) $T^* = 0.9$ and $N = 256$, (■) $T^* = 1.0$, (△) $T^* = 1.1$ and (▲) $T^* = 1.2$.

higher densities. At low densities, η_{cc}^* can be expressed by the series expansion

$$\eta_{\text{cc}}^* = B_{\eta_{\text{cc}}}^*(T^*)\rho^* + \dots \quad , \tag{5.4}$$

where the second configurational-configurational viscosity virial coefficient $B_{\eta_{\text{cc}}}^*$ is the initial slope at the temperature T^*. To determine the value of the initial slope, a method suggest by Prausnitz et al. [179] for the derivation of thermal second virial coefficients from experimental pvT-data is adopted. If the simulation data for η_{cc}^* are divided by density and the results are plotted over density, $B_{\eta_{\text{cc}}}^*(T^*)$ is found by extrapolating the $\eta_{\text{cc}}^*/\rho^*$-isotherm to zero density. This can be verified by

$$\lim_{\rho \to 0} \frac{\eta_{\text{cc}}}{\rho} = \frac{\text{``0''}}{\text{``0''}} = \lim_{\rho \to 0} \frac{\partial \eta_{\text{cc}}}{\partial \rho} \quad , \tag{5.5}$$

in which the rule of de l'Hospital has been applied to evaluate the limit. This method can be used to determine the initial slope of the η_{tc}^*-isotherms, $B_{\eta_{\text{tc}}}^*(T^*)$, since η_{tc}^* also becomes zero in the zero density limit.

Figure 5.12 depicts the calculated quotients $\eta_{\text{tc}}^*/\rho^*$ and $\eta_{\text{cc}}^*/\rho^*$ for the six sub-critical isotherms of the second simulation series. The data for the translational-configurational viscosity contribution scatter, but it is evident that $B_{\eta_{\text{tc}}}^*$ increases with temperature as could be expected from the discussion of Figure 5.8. Moreover, the extrapolation of the $\eta_{\text{cc}}^*/\rho^*$-isotherms shows that the second configurational-

configurational viscosity virial coefficient $B^*_{\eta_{cc}}$ is non-zero and that it decreases with temperature between $T^* = 0.7$ and 1.2.

Since the mean free path between collisions might become as large as the length of the simulation cube at low densities, one might suspect that the simulation data are subject to systematic errors. To check the data for this effect, one simulation at the state point ($T^* = 0.9$, $\rho^* = 0.005$) was repeated with 256 instead of 1372 particles, but otherwise unchanged simulation parameters. Since the simulation cube is smaller with less particles, a systematic effect is expected to be stronger. However, the result for η^*_{cc} agreed with that obtained with 1372 particles within 0.1 %. Therefore, the size of the simulation cube appears to have no influence on the present investigation. Probably, the application of periodic boundary conditions reduces the influence of the system size.

5.4 Shear Stress Correlation Functions

When using the Green-Kubo integral formulas instead of the Einstein relations,

$$\eta_{tt} = \frac{V}{2kT} \int_0^\infty \langle \tau_{xy,t}(0)\tau_{xy,t}(t) \rangle \, \mathrm{d}t \tag{5.6}$$

$$\eta_{tc} = \frac{V}{2kT} \int_0^\infty \langle \tau_{xy,c}(0)\tau_{xy,t}(t) + \tau_{xy,t}(0)\tau_{xy,c}(t) \rangle \, \mathrm{d}t \tag{5.7}$$

$$\eta_{cc} = \frac{V}{2kT} \int_0^\infty \langle \tau_{xy,c}(0)\tau_{xy,c}(t) \rangle \, \mathrm{d}t \quad , \tag{5.8}$$

the viscosity contributions are related to the integrals of the shear stress correlation functions. Therefore, their temperature and density dependence can be interpreted by the decay behaviour of the correlation functions. For this purpose, the total correlation functions are separated into the three contributions $\langle \tau^*_t(0)\cdot\tau^*_t(t) \rangle$, $\langle \tau^*_c(0)\cdot\tau^*_t(t) + \tau^*_t(0)\cdot\tau^*_c(t) \rangle$ and $\langle \tau^*_c(0)\cdot\tau^*_c(t) \rangle$ that correspond to the viscosity contributions η^*_{tt}, η^*_{tc} and η^*_{cc}. The discussion focuses on the normalized shear stress correlation function at the same state points for which the normalized velocity autocorrelation function was discussed in Section 4.3. In some instances, time derivatives, time integrals or double logarithmic representations of the correlation functions are given to illustrate their decay behaviour. The representation is chosen so that the effects are optimally visible.

Figures 5.13 and 5.14 show the three contributions to the shear stress correlation function at low densities on the isotherm $T^* = 0.7$ and the isochor $\rho^* = 0.025$. The translational-translational contribution closely resembles the behaviour observed for the velocity autocorrelation functions in this state region. At short times, oscillations superimpose the decay of the correlation functions. These oscillations become stronger with increasing density, but disappear at high supercritical temperatures. The observed similarities between translational-translational shear stress correlation functions and velocity autocorrelation functions are not surprising since both functions measure correlations between particle velocities. Moreover, the dependence of the product $D^* \rho^*$ and η_{tt}^* on density and temperature at low densities is similar.

The cross contributions show a completely different behaviour. At low temperatures, they start from zero, exhibit maxima, decrease to negative values, reach a minimum and increase to a second maximum before approaching the time axis. This complex behaviour at short times is superimposed by small oscillations. Details of the long time behaviour cannot be assessed since it is hidden in stochastic noise. With increasing temperature, the minimum as well as the superimposed oscillations vanish and the correlation function decreases monotonically from the first maximum to zero.

On the isotherm $T^* = 0.7$, the configurational-configurational shear stress correlation function appears to be almost independent of density. It decreases rapidly to negative values, reaches a minimum, then increases and oscillates several times before decaying monotonically to the time axis from above. This short time behaviour is similar to the oscillations observed in the short time behaviour of the translational-translational and translational-configurational contributions. The corresponding time integrals reveal that the short time behaviour is indeed density independent on this isotherm. However, the long time behaviour depends strongly on density and yields a significant contribution to η_{cc}^*. With increasing temperature, the first minimum on the isochor $\rho^* = 0.025$ is lifted and shifted to earlier times. Furthermore, the contribution of the long time decay to the integral of the configurational-configurational shear stress correlation function decreases at high temperatures.

Oscillations in the configurational-configurational contribution to shear stress correlation functions were also reported by Michels and Trappeniers [151] for square-well model fluids and attributed to the formation of bound states. The same effect was already observed for the velocity autocorrelation functions at low densities and explained in detail by the formation of bound states in Section 4.3. The present

results for the contributions to the shear stress correlation functions provide further evidence for the existence of oscillations in the short time behaviour of all three contributions and, thus, for the existence of bound states at low temperatures.

Figure 5.15 shows the influence of density on the three contributions to the shear stress autocorrelation function along the supercritical isotherm $T^* = 1.35$ close to the critical temperature. The shape of the translational-translational shear stress correlation functions is similar at all densities with the decay becoming slower at low densities. At high densities, the translational-translational correlation function does not show the negative regime at intermediate times found for the velocity autocorrelation functions in this state region. This difference yields the explanation for the different behaviour of the isotherms of the product $D^* \rho^*$ and the viscosity contribution η_{tt}^* at high densities in Figures 4.4, 4.5 and 5.7. The negative regime of the velocity autocorrelation functions lowers the values of the product $D^* \rho^*$ so that the isotherms are relatively steep at high densities. On the other hand, the η_{tt}^*-isotherms are flat in this state region, which is a consequence of the monotonic decay of the translational-translational shear stress correlation functions.

Similarly, the decrease of the η_{tc}^*-isotherms at high densities can be explained by the decay behaviour of the translational-configurational stress correlation functions. All cross-correlation functions have a maximum at short times. At low densities, the correlation functions decrease monotonically towards zero from this maximum. At high densities, however, the maximum is followed by a steep decrease to negative values and a pronounced negative region. This yields a significant negative contribution to the value of η_{tc}^*, causing the isotherm to decrease at high densities.

The decay of the configurational-configurational shear stress correlation function also changes along the isotherm. With increasing density, the characteristic minimum observed at low densities vanishes and the correlation function decay monotonically. At the highest density $\rho^* = 0.95$, the rapid decay at short times is followed by a pronounced slow decay up to at least one reduced time unit. The slow decay occurs in that time regime where the negative regions for the cross correlation function and velocity autocorrelation function are found. This observation indicates a close relation between the responsible molecular mass and momentum molecular transport mechanisms.

Stassen and Steele [201, 202] examined the decay of the contributions to the shear stress correlation functions at the subcritical isotherm $T^* = 1.26$ at five state points between $\rho^* = 0.211$ and $\rho^* = 0.844$. Moreover, they calculated the two-, three- and four-body contributions to the configurational-configurational shear stress correla-

tion functions as defined in Section 2.5.5. At low densities, the three- and four-body contributions are very small and cancel each other so that the configurational-configurational shear stress correlation function is dominated by the two-body contribution. At high densities, the short time behaviour of all contributions was found to be relatively complex. Both, the three- and four-body contributions yield larger contributions to the configurational-configurational shear stress correlation function. Surprisingly, the behaviour of the two-body contribution found at low densities is almost unchanged at high densities with the minimum being lifted to positive values. The monotonic decay of the configurational-configurational shear stress correlation function at high densities results from the superposition of the three contributions.

The influence of temperature on the decay of shear stress correlation functions is shown in Figures 5.16 and 5.17 for the isochors $\rho^* = 0.3$ and $\rho^* = 0.85$. On the isochor $\rho^* = 0.3$, the characteristic decay behaviour depends only weakly on temperature for all three viscosity contributions. Due to increased scattering, the decay of the translational-translational contribution becomes faster at high temperatures. This effect lowers the time integral of the normalized correlation function. The configurational-configurational contribution shows the minimum typical for low densities at short times at all displayed temperatures. At high temperatures, the minimum is lifted and shifted to earlier times as already observed for the isochor $\rho^* = 0.025$. At this density, the constant plateau values of the integrated time-correlation functions are reached within a few reduced time units.

Along the isochor $\rho^* = 0.85$, the influence of temperature on the translational-translational and cross-contribution is similar. At all temperatures, the cross-contribution shows the negative region at intermediate times that causes the decay of the isotherms at high densities. The decay behaviour of the configurational-configurational contribution depends strongly on temperature. At low temperatures, a pronounced slow decay at intermediate times is observed. This effect becomes smaller with increasing temperature. Again, the slow decay occurs in the same time regime where the cross correlation function and the velocity autocorrelation function take negative values.

As a final point, the question is addressed wether the contributions to the shear stress correlation functions show long time tails as found for the velocity autocorrelation function. Theoretical calculations of the long time behaviour by mode coupling approaches support the existence of long time tails of the form $\sim t^{-3/2}$ for all three contributions [40, 41, 42]. This issue has previously been investigated by molecular dynamics simulations [45, 50]. However, due to the large demand for computational

resources for an accurate determination of the correlation functions at long times the problem has not yet been solved.

The translational-translational contributions to the correlation functions at both densities, $\rho^* = 0.3$ and $\rho^* = 0.85$, and the configurational-configurational contributions at $\rho^* = 0.85$ are depicted in Figures 5.16 and 5.17 in double logarithmic representation. In this representation, the long time tails should appear as straight lines with the slope -1.5. From the results for the velocity autocorrelation functions in Section 4.3, it is expected that the predicted behaviour is preferably observable at high densities and temperatures.

On the isochor $\rho^* = 0.85$, linear decay appears to exist for the translational-translational contribution at the lowest displayed temperature $T^* = 0.7$ between $t^* = 0.2$ and 0.5. The exponent from a linear least-squares fit is approximately -2.2. At the higher temperatures $T^* = 0.9$, 1.3 and 1.8, the 'linear' decay starts slightly earlier with increasing temperature. At the two highest temperatures, the decay is certainly faster than linear. For the configurational-configurational contribution, the expected straight lines with the slope -1.5 appear to exist for the two lowest displayed temperatures $T^* = 0.7$ and 0.9 at about one reduced time unit. However, from the results for the velocity autocorrelation functions the linear decay is expected to start later. At higher temperatures, the decay is faster, becoming exponentially at the highest temperatures. On the isochor $\rho^* = 0.3$, the translational-translational contribution does not show the expected linear decay.

The time periods in which the linear decay is observed are relatively short so that the existence of the long time tails in shear stress correlation functions cannot be unambiguously proved with the present simulation results. The analysis of the shear stress correlation functions at longer times is hindered by the high noise level, which is by almost an order of magnitude larger than for the velocity autocorrelation functions. Much longer than the present simulations are required for the precise determination of the long time behaviour of the shear stress correlation functions.
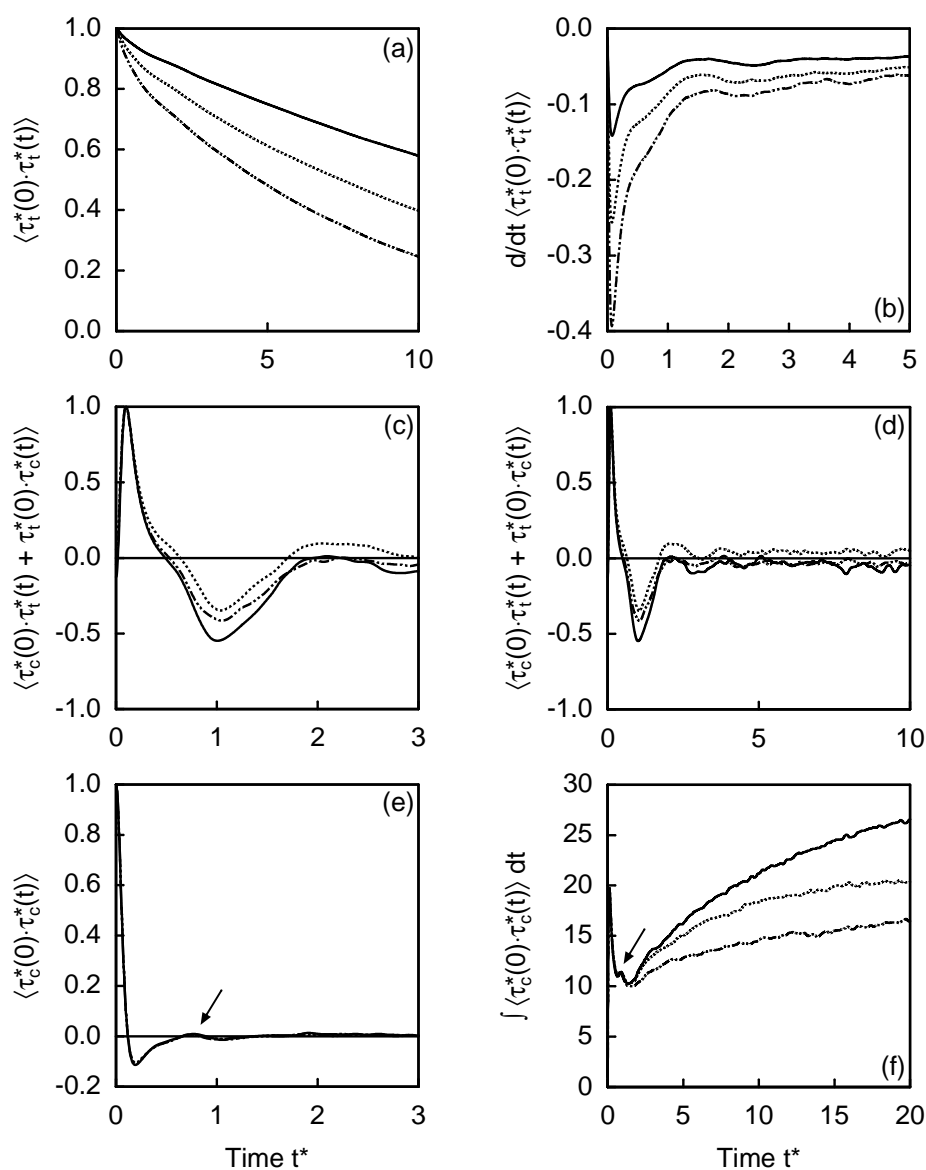
Figure 5.13. *Normalized* shear stress correlation function for selected densities on the lowest simulated isotherm $T^* = 0.7$ close to the triple point. (a) short time behaviour of translational-translational contribution; (b) time derivative of the translational-translational contribution; (c) short time behaviour of translational-configurational contribution; (d) long time behaviour of translational-configurational contribution; (e) configurational-configurational contribution and (f) time integral function of configurational-configurational contribution. Note the different abscissa scale in the subfigures. The arrow points at special features of the correlation functions addressed in the text. Legend: (———) $\rho^* = 0.005$, (·········) $\rho^* = 0.01$ and (–·–·–) $\rho^* = 0.015$.
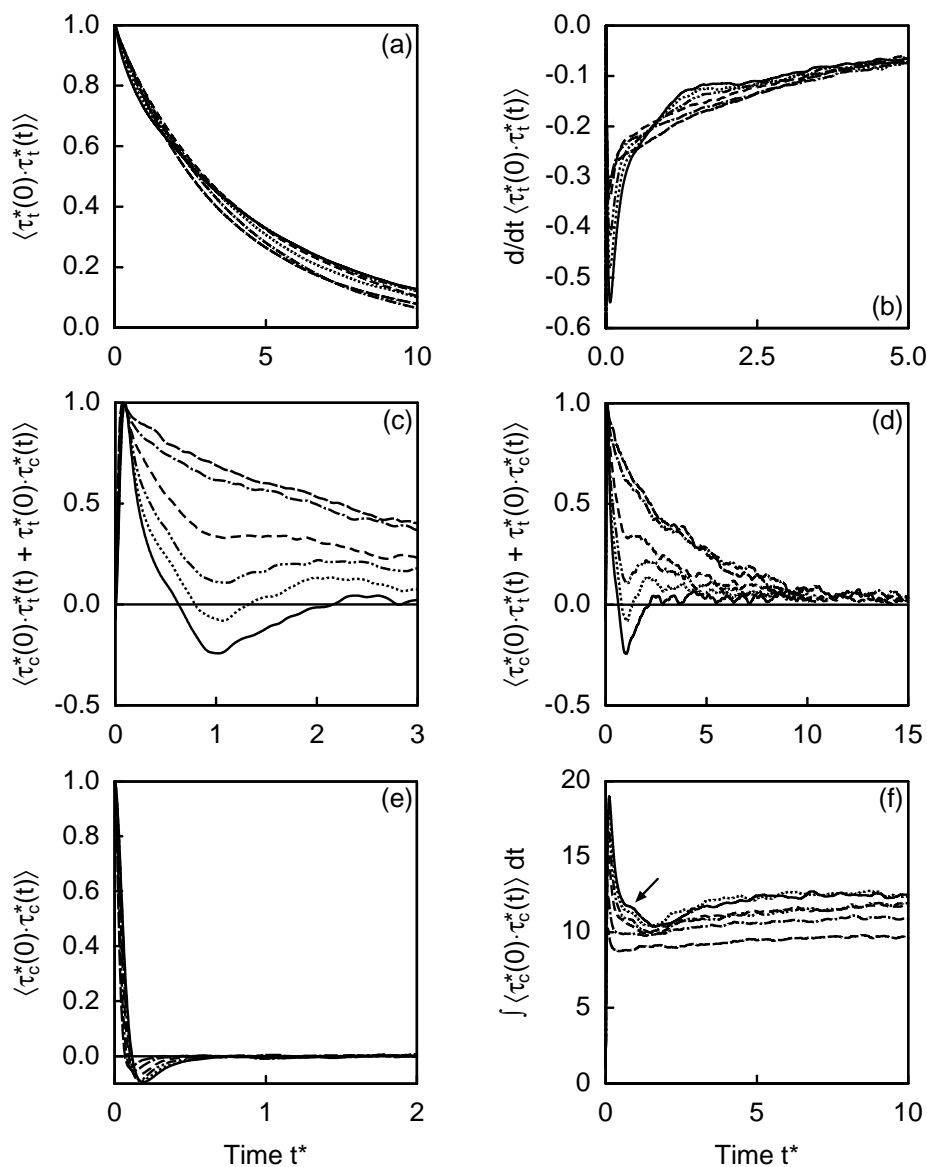
Figure 5.14. *Normalized* shear stress correlation function for selected temperatures on the isochor $\rho^* = 0.025$. (a) short time behaviour of translational-translational contribution; (b) time derivative of translational-translational contribution; (c) short time behaviour of translational-configurational contribution; (d) long time behaviour of translational-configurational contribution; (e) configurational-configurational contribution and (f) time integral function of configurational-configurational contribution. Note the different abscissa scale in the subfigures. The arrow points at special features of the correlation functions addressed in the text. Legend: (———) $T^* = 0.8$, ($\cdots\cdots\cdots$) $T^* = 0.9$, ($\text{—}\cdots\text{—}\cdots\text{—}$) $T^* = 1.1$, (– – – –) $T^* = 1.5$, ($\text{—}\cdot\text{—}\cdot\text{—}$) $T^* = 2.5$ and (— — —) $T^* = 4.0$.
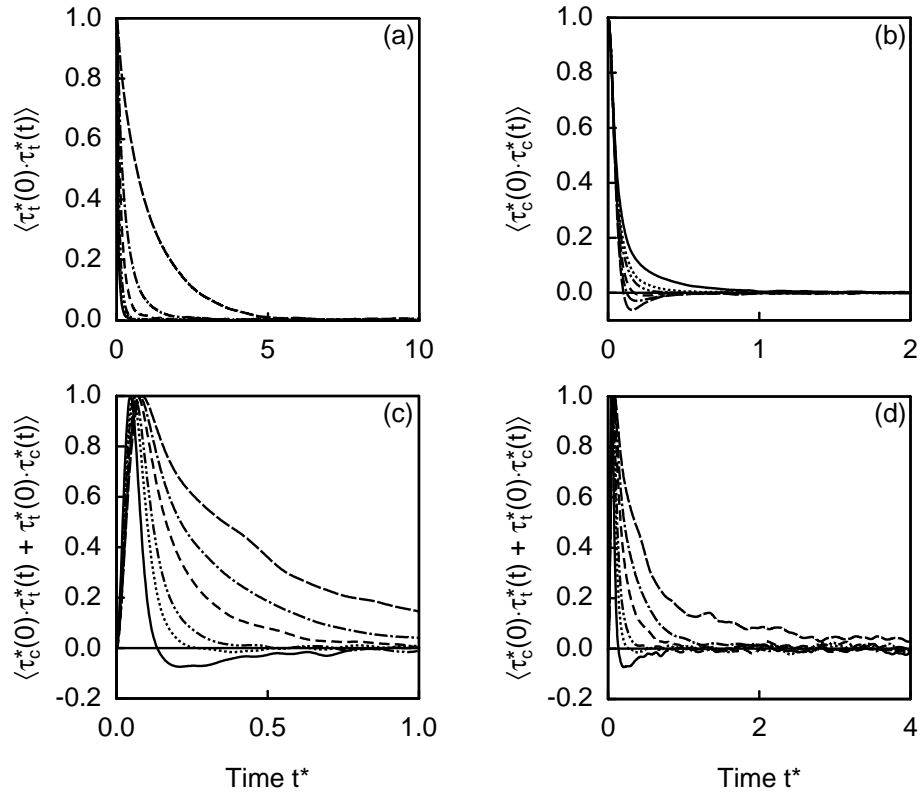
Figure 5.15. *Normalized* shear stress correlation function for selected densities on the isotherm $T^* = 1.35$. (a) translational-translational contribution; (b) configurational-configurational contribution; (c) short time behaviour of translational-configurational contribution and (d) long time behaviour of translational-configurational contribution. Note the different abscissa scale in the subfigures. Legend: ($---\cdot$) $\rho^* = 0.1$, ($-\cdot-\cdot-$) $\rho^* = 0.3$, ($----$) $\rho^* = 0.5$, ($-\cdots-$) $\rho^* = 0.7$, ($\cdots\cdots\cdots$) $\rho^* = 0.8$ and ($---$) $\rho^* = 0.95$.
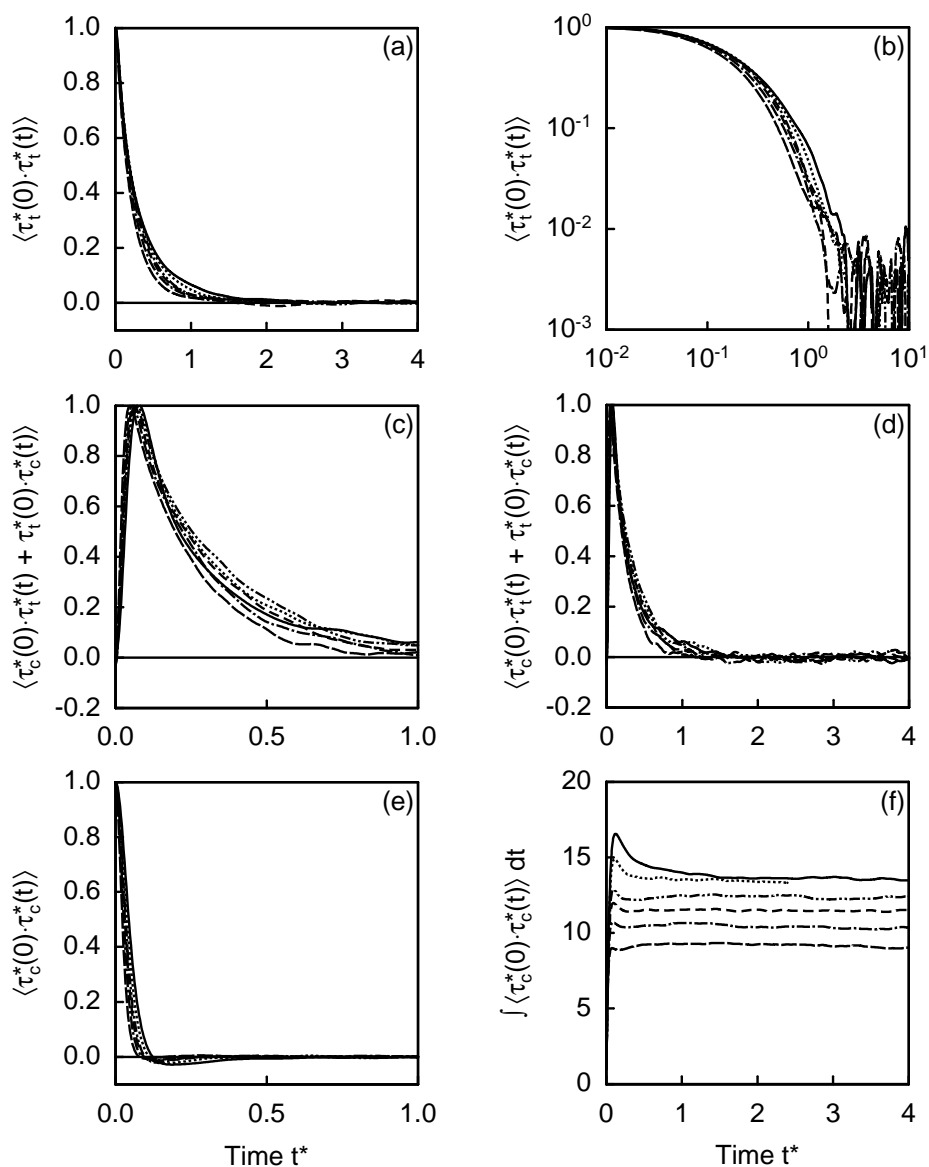
Figure 5.16. *Normalized* shear stress correlation function for selected temperatures on the isochor $\rho^* = 0.3$ close to the critical density. (a) translational-translational contribution; (b) translational-translational contribution in double logarithmic representation; (c) short time behaviour of translational-configurational contribution; (d) long time behaviour of translational-configurational contribution; (e) configurational-configurational contribution and (f) time integral function of configurational-configurational contribution. Note the different abscissa scale in the subfigures. Legend: (———) $T^* = 1.35$, (··········) $T^* = 1.8$, (—··—··—) $T^* = 2.5$, (————) $T^* = 3.0$, (—·—·—·) $T^* = 4.0$ and (————) $T^* = 6.0$.
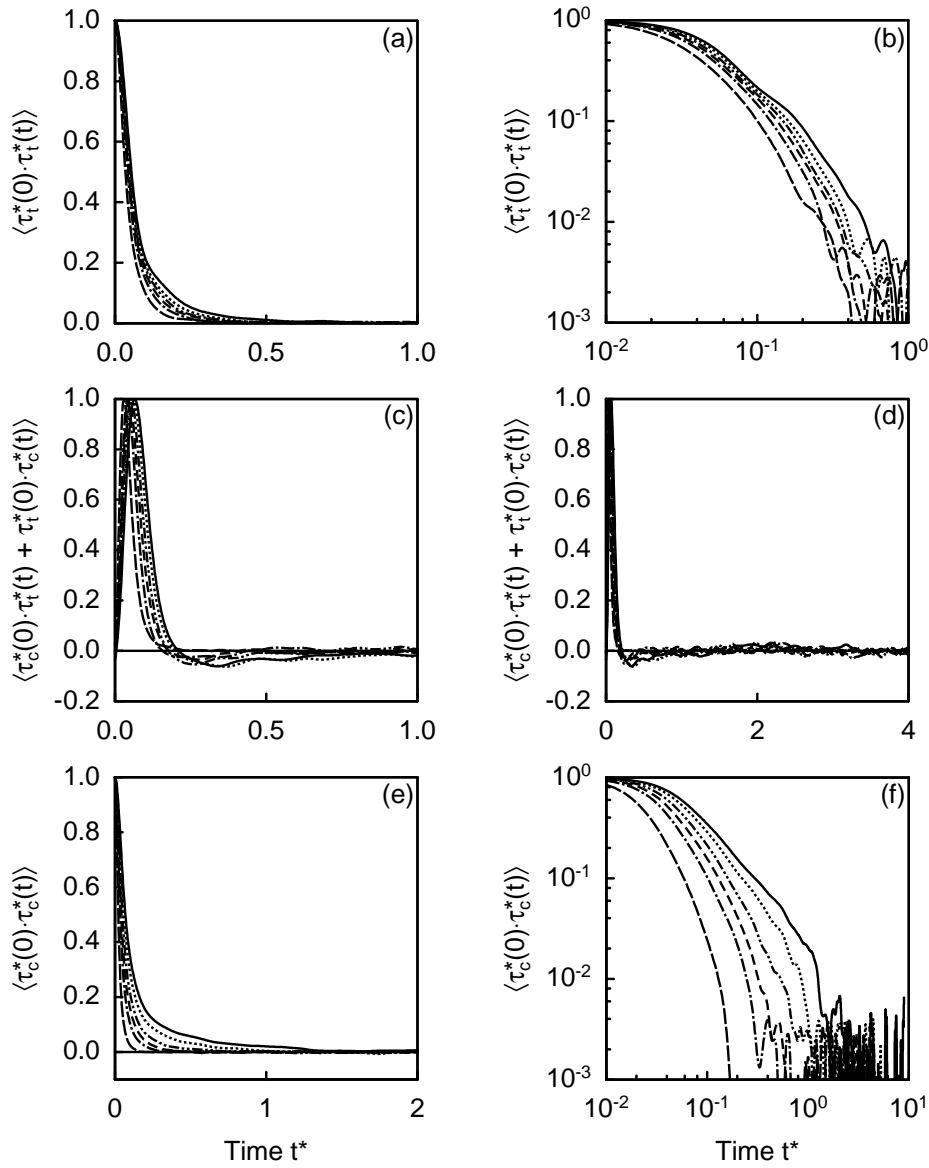
Figure 5.17. *Normalized* shear stress correlation function for selected temperatures on the liquid isochor $\rho^* = 0.85$. (a) translational-translational contribution; (b) translational-translational contribution in double logarithmic representation; (c) short time behaviour of translational-configurational contribution; (d) long time behaviour of translational-configurational contribution; (e) configurational-configurational contribution and (f) configurational-configurational contribution in double logarithmic representation. Note the different abscissa scale in the subfigures. Legend: (———) $T^* = 0.7$, (············) $T^* = 0.9$, (—··—··—) $T^* = 1.3$, (— — — —) $T^* = 1.8$, (—·—·—·) $T^* = 2.5$ and (— — — —·) $T^* = 6.0$.

6 The Bulk Viscosity of the Lennard-Jones Model Fluid

The hydrodynamic transport coefficient bulk viscosity describes viscous effects associated with the change of the volume of an infinitesimal volume element of a fluid at constant shape of the volume element. Almost nothing is known about the bulk viscosity. In fluid mechanics, bulk viscosity effects are often neglected. This is correct if the fluid is an ideal monatomic gas or if it is treated as an incompressible fluid. Only in these cases, the bulk viscosity is exactly zero. However, in some applications, such as the spread of shock wave fronts or the attenuation of sound waves, dilatation and compression of the fluid are important effects. Hence, knowledge of the bulk viscosity is required in these applications.

Experimental bulk viscosity data are available for a few fluids, but are often restricted to some state points. Reviews of experimental data are given by Hanley and Cohen [68] and in the recent survey article of Graves and Argrow [57]. Presently, comprehensive data sets characterizing the bulk viscosity over a wide range of fluid states are not available.

Bulk viscosities are usually determined from experimental data of the sound absorption coefficient α, which in classical acoustics is given by

$$\frac{\alpha}{f^2} = \frac{2\pi^2}{\rho_{\mathrm{m}} w_0^3} \left[\frac{c_{\mathrm{p,m}} - c_{\mathrm{v,m}}}{c_{\mathrm{p,m}} c_{\mathrm{v,m}}} \; \lambda + \frac{4}{3}\eta + \eta_{\mathrm{b}} \right] \quad . \tag{6.1}$$

Eq. (6.1) shows that the isochoric and isobaric heat capacity, zero frequency speed of sound, thermal conductivity and viscosity must be known accurately at the state point of the measurement to obtain precise values for the bulk viscosity. As such data sets data are rarely available, experimental bulk viscosity data are often associated with large uncertainties.

However, bulk viscosities can be determined with little additional computational cost together with the viscosity in molecular dynamics simulations. Therefore, data for the Lennard-Jones model fluid were determined from the present simulations. With these results, the temperature and density dependence of the bulk viscosity is characterized.

6.1   Simulation Data for the Bulk Viscosity

As the self-diffusion and viscosity data, the bulk viscosity data were determined by the Einstein relation method as described in Section 3.3.1. The parameters used for the calculation of the generalized displacement functions were the same as for the viscosity. From the first simulation series, 344 bulk viscosity data were derived that cover the same region of states as the self-diffusion and viscosity data. Further 39 data were determined from the second simulation series at subcritical temperatures in the gas region. Additionally, 11 data were obtained from the simulations with production phases over 10 million time steps on the close-critical isotherm $T^* = 1.35$. The data are reported Tables D.5 and D.6.

The uncertainty of the bulk viscosity data is estimated to be 5 % in the liquid at high densities above $\rho^* = 0.3$. At lower densities and in the vicinity of the critical point, the uncertainty is higher, amounting up to 30 %. The low temperature gas data of the second series of extremely long simulations over 50 million time steps have uncertainties of 10 % increasing up to 20 % at the lowest densities.

Eight literature sources report simulation data for the bulk viscosity of the Lennard-Jones model fluid. The details of these data sets and of the present data are summarized in Table 6.1. Only in two sources, the works of Heyes [80] and of Borgelt et al. [25], data at more than 10 state points are reported. In a further article, Heyes [82] reported simulations at 45 states from which 36 states coincide with those of Ref. [80]. Unfortunately, the bulk viscosity data were not reported in the publication. Instead, the data were regressed and the parameters of the resulting equation were published. With only few exceptions, the literature data were derived from simulations with less than 500 molecules. In most literature studies, the cutoff radius was set to $r_{\text{cut}}^* = 2.5$. Furthermore, the production phases of the literature simulations are in most cases much shorter than those of the present simulations.

The distribution of the state points of the two largest literature data sets in the fluid region is shown in Figure 6.1 in the T^*,ρ^*-plane. The data of Borgelt et al. [25] are distributed along three isochors in the liquid region and extend up to the temperature $T^* = 3.0$. The data set of Heyes covers a larger density range and extends up to $T^* = 4.5$ [80]. Both data sets concentrate in the liquid region. Data in the vicinity of the critical density at supercritical temperatures and at low densities in the gas region are reported in this work for the first time.

Figure 6.2 shows the isochoric data of Borgelt et al. [25] at the densities $\rho^* = 0.7801$, $\rho^* = 0.8415$ and $\rho^* = 0.8836$ and data of this work along the three closest

Table 6.1. Data sets for the bulk viscosity of the Lennard-Jones model fluid. Included are data at the state point ($T^* = 0.722$, $\rho^* = 0.8442$) close to the triple point, which are discussed in Section 3.4. Abbreviations: DT: difference in trajectories method, ER: Einstein relation, GK: Green-Kubo integrals, OS: oscillating strain perturbed Hamiltonian method, TS: trajectory segments. Remarks: [1]: not reported by the authors.

Author		Year	Data	Method	Ensemble	N	r^*_{cut}	T^*	ρ^*	Simul. Length
This work		2002	344	ER	*NVE**MG***	1372	5.5-6.5	0.7-6.0	0.005-1.275	4500-6000
This work		2002	39	ER	*NVE**MG***	1372	6.5	0.7-1.2	0.005-0.15	150000
Borgelt	[25]	1990	46	GK	*NVE**MG***	108	2.5	0.66-2.93	0.78-0.883	371
Canales	[30]	1999	3	GK/ER	*NVT*	668	2.71-3.11	0.53-1.893	0.756, 1.143	550-1200
Heyes	[80]	1984	39	DT	-	256	2.5	0.71-4.56	0.5-1.05	180 TS
Heyes	[86]	1993	4	GK	*NVE**MG***	256	2.5	0.7-6.0	0.5-1.0	655-17100
Hoover	[96]	1980	1	OS	-	54	1)	0.722	0.8442	126-5027
Levesque	[118]	1973	1	GK	*NVE**MG***	864	1)	0.722	0.8442	465.6
Levesque	[119]	1987	9	GK	*NVE**MG***	108-864	1)	0.715-2.8	0.8442-1.113	11.04-88.32
Schoen	[190]	1986	1	GK	*NVE**MG***	500	2.5	0.73	0.8442	464
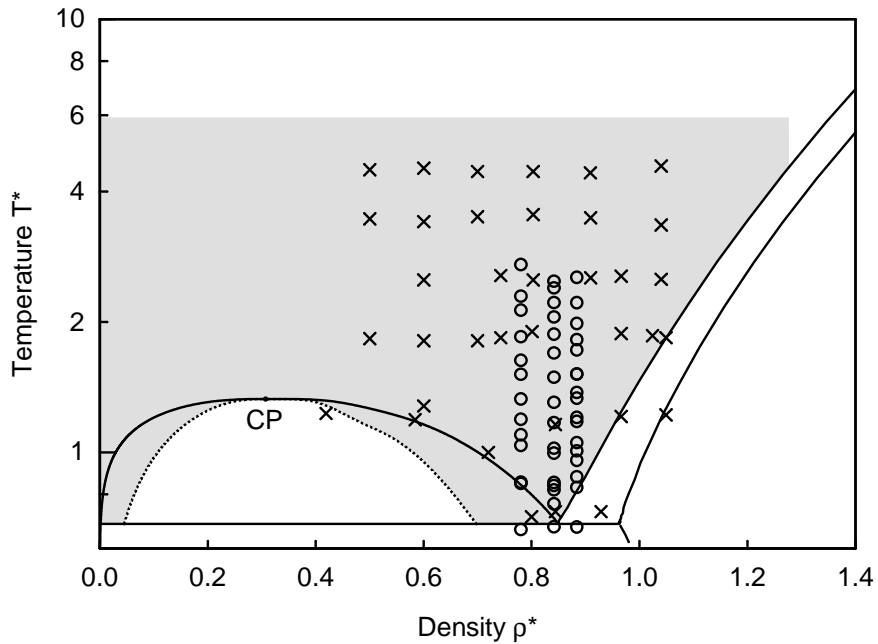
Figure 6.1. The distribution of literature data for the bulk viscosity η_b^* in the T^*, ρ^*-plane. The shaded area is the state region considered in this work. Legend: ($\bigcirc$) Borgelt et al. [25] and ($\times$) nonequilibrium molecular dynamics data of Heyes [80].

isochors $\rho^* = 0.8$, $\rho^* = 0.85$ and $\rho^* = 0.9$. At the displayed liquid densities, the bulk viscosity decreases steeply at subcritical temperatures, but shows little temperature dependence at supercritical temperatures. The data of this work give a consistent picture for the three isochors, whereas the data of Borgelt et al. show large scatter so that the individual isochors cannot be distinguished. However, the temperature dependence of both data sets is similar.

A comprehensive comparison with the data of Heyes [80] is difficult to perform because there are only a few state points which coincide with states of the present simulation. For example, Heyes reports $\eta_b^* = 1.05$ for the state ($T^* = 1.81$, $\rho^* = 0.6$) and $\eta_b^* = 0.77$ for the ($T^* = 2.5$, $\rho^* = 0.7$). The results of this work at ($T^* = 1.8$, $\rho^* = 0.6$) and ($T^* = 2.5$, $\rho^* = 0.7$) are $\eta_b^* = 0.5861$ and $\eta_b^* = 0.5835$, respectively. The magnitude of the difference between the data is similar to that observed at the state point close to the triple point before. Therefore, the discrepancy must also be due to the different simulation methods used.

The comparison with the literature data allows the conclusion that the present data are far more accurate than any previously published data for the bulk viscosity.
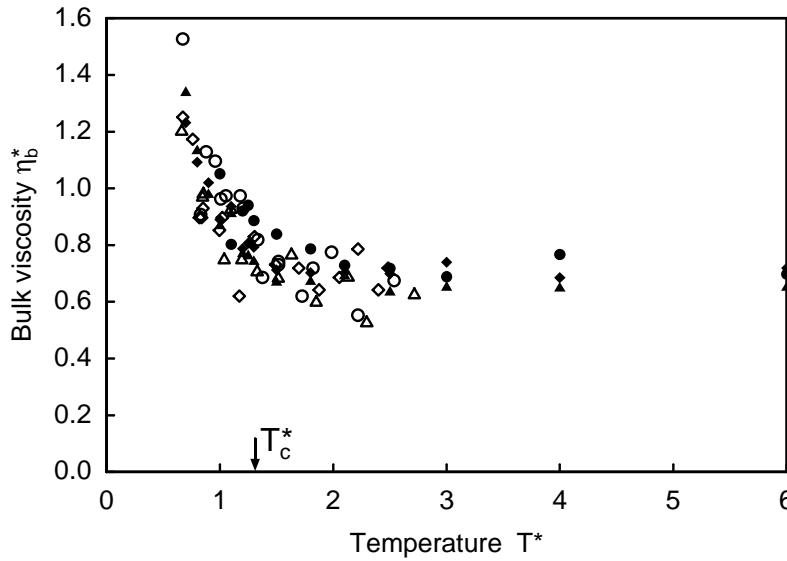
Figure 6.2. Bulk viscosity data along isochors at high densities. This work: ($\blacktriangle$) $\rho^* = 0.8$, ($\blacklozenge$) $\rho^* = 0.85$, ($\bullet$) $\rho^* = 0.9$; Borgelt et al. [25]: ($\triangle$) $\rho^* = 0.7801$, ($\diamond$) $\rho^* = 0.8415$, ($\circ$) $\rho^* = 0.8836$.

6.2 Temperature and Density Dependence of the Bulk Viscosity

With the present simulation data, the behaviour of the bulk viscosity is characterized in the fluid region. Figure 6.3 displays the results for gaseous and liquid subcritical isotherms and Figure 6.4 presents the gas data of the second simulation series. In the zero density limit, the bulk viscosity is zero since the Lennard-Jones model fluid is a monatomic fluid (see Appendix B). Close to the zero density limit, the isotherms are flat, but increase more strongly as they enter the metastable region. When the isotherms approach the stability limit in the metastable region, they diverge. The low temperature liquid isotherms increase monotonically with decreasing density. At higher, but still subcritical temperatures, the liquid isotherms decrease close to the freezing line, exhibit minima and then increase strongly when entering the metastable region. As the gaseous isotherms, the liquid isotherms diverge in the metastable region when they approach the stability limit.

Figure 6.5 depicts the data on supercritical isotherms. The behaviour observed for subcritical isotherms continues into the supercritical region. The close-critical isotherm $T^* = 1.35$ increases in the gas region, exhibits a maximum close to the crit-
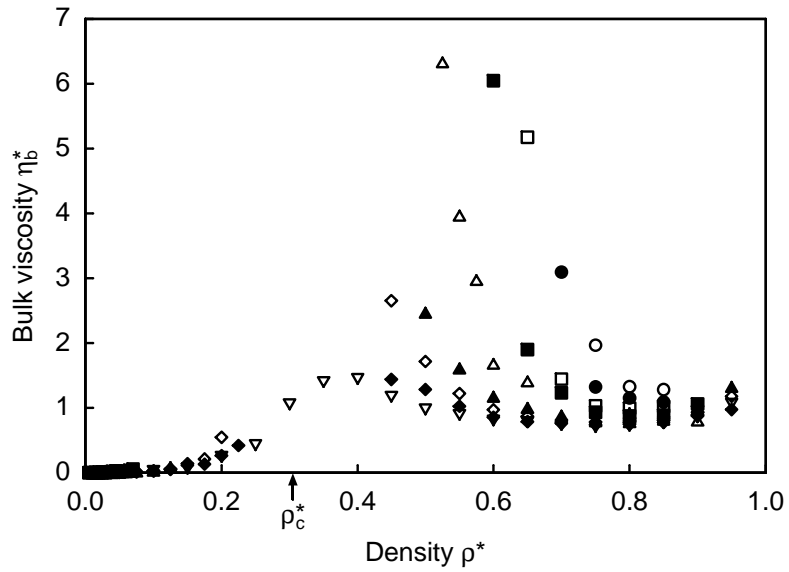
Figure 6.3. The bulk viscosity for all simulated subcritical isotherms as a function of density. Legend: ($\bigcirc$) $T^* = 0.7$, ($\bullet$) $T^* = 0.8$, ($\square$) $T^* = 0.9$, ($\blacksquare$) $T^* = 1.0$, ($\triangle$) $T^* = 1.1$, ($\blacktriangle$) $T^* = 1.2$, ($\diamondsuit$) $T^* = 1.25$, ($\blacklozenge$) $T^* = 1.3$ and ($\triangledown$) $T^* = 1.35$ (supercritical).
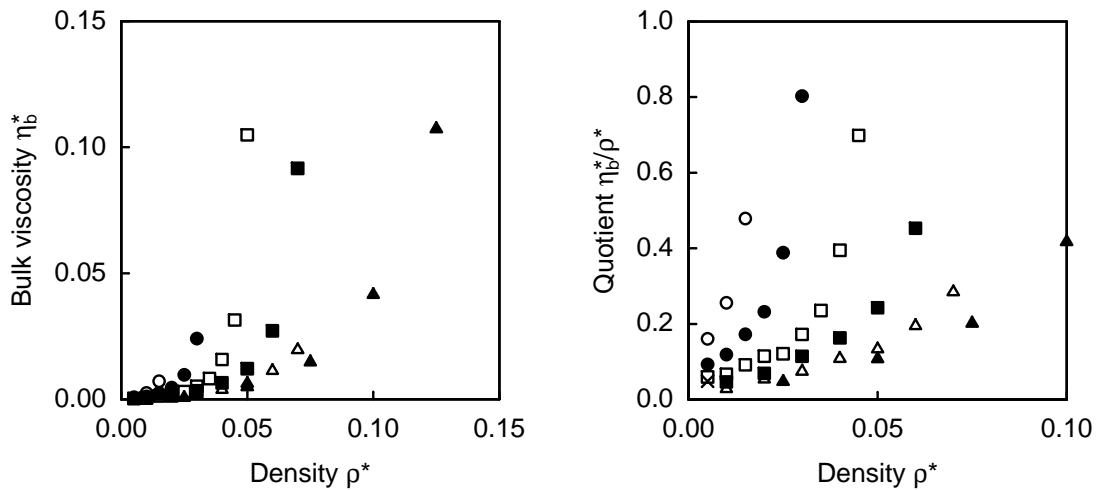
Figure 6.4. The bulk viscosity and the quotient of bulk viscosity and density at gaseous states on subcritical isotherms as a function of density. Legend: ($\bigcirc$) $T^* = 0.7$, ($\bullet$) $T^* = 0.8$, ($\square$) $T^* = 0.9$ and $N = 1372$, ($\times$) $T^* = 0.9$ and $N = 256$, ($\blacksquare$) $T^* = 1.0$, ($\triangle$) $T^* = 1.1$ and ($\blacktriangle$) $T^* = 1.2$.
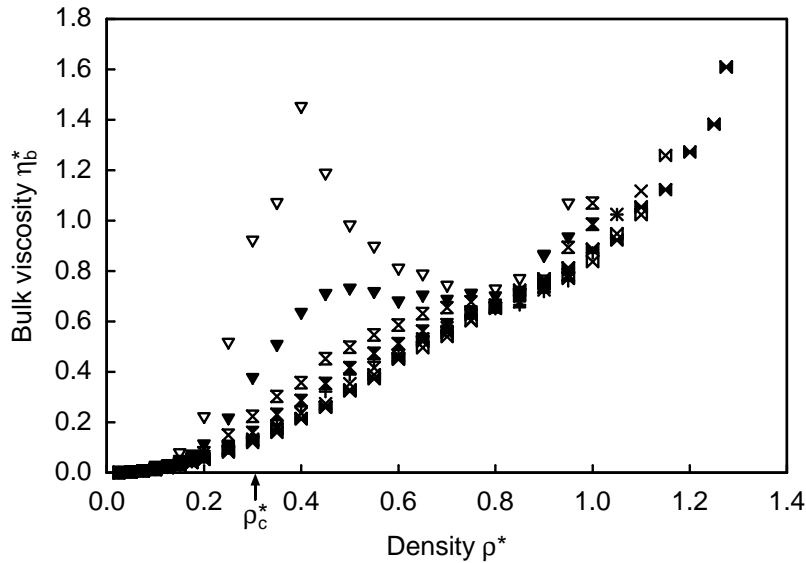
Figure 6.5. The bulk viscosity for all simulated supercritical isotherms as a function of density. Legend: ($\triangledown$) $T^* = 1.35$, ($\blacktriangledown$) $T^* = 1.5$, ($\boxtimes$) $T^* = 1.8$, ($\pmb{\times}$) $T^* = 2.1$, ($+$) $T^* = 2.5$, ($\times$) $T^* = 3.0$, ($\bowtie$) $T^* = 4.0$ and ($\blacktriangleright\!\blacktriangleleft$) $T^* = 6.0$.

ical density, decreases and reaches a minimum before increasing towards the freezing line. In the vicinity of the critical density, the bulk viscosity shows a large enhancement. With increasing temperature, the enhancement becomes broader and smaller in magnitude. Moreover, it is shifted to higher densities. When the temperature is further increased, the maximum vanishes and the isotherms increase monotonically. Nevertheless, the enhancement is still observed on the highest isotherm $T^* = 6.0$ at about 4.5 times the critical temperature. This effect is similar to the enhancement of the thermal conductivity in the vicinity of the critical point, which is experimentally observed for real fluids [144, 208]. In contrast to the critical enhancement of the thermal conductivity, the enhancement of the bulk viscosity is not restricted to a small region close to the critical point, but dominates the bulk viscosity over a far wider range of fluid states.

As the bulk viscosity isotherms are very flat close to the zero density limit, the question remains if the initial slope, i.e. the second bulk viscosity virial coefficient $B_{\eta_b}^*$, is zero or if it takes small positive non-zero values. Negative bulk viscosity virial coefficients are not allowed since the bulk viscosity is zero at zero density and it must always be positive at higher densities so that the entropy source strength, Eq. (2.54), is positive. This issue can be examined by the same method used in

Section 5.3 to assess the initial slope of the configurational-configurational viscosity contribution isotherms. Figure 6.4 shows the quotient of the bulk viscosity and density for the gas data of the second simulation series. In this representation, the second bulk viscosity virial coefficient for a selected temperature is given by the intersection of the extrapolated isotherm with the ordinate. The isotherms between $T^* = 0.7$ and 1.0 extrapolate to non-zero values in the zero density limit, suggesting that the second bulk viscosity virial coefficient is non-zero. Moreover, $B_{\eta_b}^*$ takes the largest value at the lowest simulated temperature and decreases with temperature. For the two highest temperatures, the extrapolation is complicated by the fact the effect is much weaker. At the isotherm $T^* = 1.1$, the scatter of the data at the lowest densities is too large for an unambiguous extrapolation to zero density and on the isotherm $T^* = 1.2$ the data do not extend close enough to zero density.

The theory of the second transport virial coefficients as developed by Curtiss et al. [19, 34, 89, 90, 91] predicts that the bulk viscosity virial coefficient is identically zero. However, as for the second self-diffusion virial coefficient, this treatment of the second bulk viscosity virial coefficient lacks the recent improvements of the theory by Rainwater and Friend [180, 54, 181] and might therefore be in error.
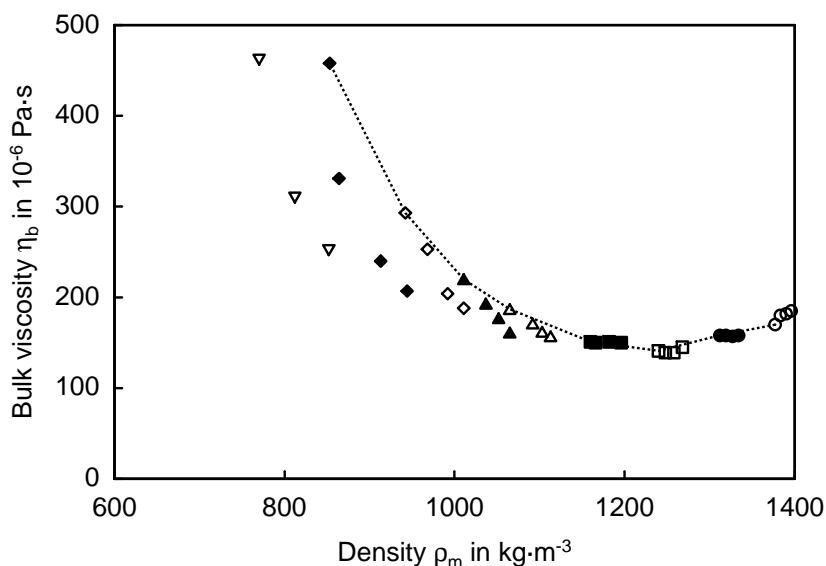
Figure 6.6. The bulk viscosity of liquid argon as a function of density as measured by Cowan and Ball [33]. Critical parameters of argon: $T_c = 150.7$ K, $\rho_{m,c} = 530.9$ kg m^{-3}. Legend: (⋯⋯⋯) Saturated liquid, (○) $T = 90$ K, (●) $T = 100$ K, (□) $T = 110$ K, (■) $T = 120$ K, (△) $T = 130$ K, (▲) $T = 135$ K, (◇) $T = 140$ K, (◆) $T = 145$ K and (▽) $T = 150$ K.

The simulation results for the bulk viscosity of the Lennard-Jones fluid can only be compared with experimental data for monatomic fluids, i.e. noble gases, since internal degrees of freedom in molecular fluids yield contributions to the bulk viscosity that cannot be described by the simple Lennard-Jones potential. Experimental bulk viscosity data for noble gases are only available at a few state points at moderate pressures not too far above ambient pressure, see for example [33, 132, 165, 166, 207]. The most comprehensive investigation is the work of Cowan and Ball [33], who determined the bulk viscosity of liquid argon in the temperature range between $T = 90$ K and 150 K from the vapour pressure up to 7 MPa from measurements of the sound absorption coefficient.

Their results for nine isotherms are displayed in Figure 6.6. The lowest isotherm is slightly higher than the triple point temperature of argon $T_{tr} = 83.8$ K, while the highest isotherm at 150 K is very close to the critical temperature $T_c = 150.7$ K. The experimental data lie in a small density region close to the bubble line, whereas the present simulation data in the liquid region extend from the stability limit to the freezing line. At high temperatures, the qualitative behaviour of the experimental and simulated isotherms is similar. They increase strongly as the bubble density is approached. Between $T = 100$ K and 120 K, the bulk viscosity of argon is almost constant close to the bubble line. The constant portion of the isotherms is also found for the simulation data in the range of the minima. On the lowest isotherm $T = 90$ K close to the triple point, the bulk viscosity increases with density. The simulation data on the lowest isotherm $T^* = 0.7$ decline with density. However, the three data of this isotherm lie in the metastable region so that it cannot be conclusively decided if the density dependence of the simulation data on this isotherm is physically correct.

The comparison shows that the behaviour of the bulk viscosity of the Lennard-Jones model fluid in the liquid region agrees qualitatively with that found for liquid argon. Particularly, the enhancement of the bulk viscosity close to the critical point is also observed for argon. Thus, the strong enhancement observed for the Lennard-Jones model fluid must be a real physical effect. Often, the bulk viscosity is compared with the viscosity [57]. However, the results of this section show that the bulk viscosity behaves completely different than the viscosity over the fluid region of the phase diagram.

6.3   Pressure Fluctuation Autocorrelation Functions

In the Green-Kubo integral representation, the bulk viscosity is determined by the time integral of the pressure fluctuation autocorrelation function. Therefore, the temperature and density dependence of the bulk viscosity can be interpreted by the analyzing the decay behaviour of the pressure fluctuation autocorrelation functions. The state points for which the pressure autocorrelation function will be discussed are the same as those considered in Sections 4.3 and 5.4 for the velocity and shear stress correlation functions. For the following discussion, it is interesting to compare the reduced Lennard-Jones time scale with a time scale corresponding to a real fluid. To represent the properties of the noble gas argon, the potential parameters $\sigma = 3.405 \cdot 10^{-10}$ m and $\varepsilon/k = 119.8$ K are often employed, see for example Ref. [25]. With these parameters, one reduced time unit corresponds to about 0.34 ps real time.

In Figure 6.7, the short time behaviour of the pressure fluctuation autocorrelation function at low gaseous densities is shown for three states on the lowest isotherm $T^* = 0.7$ and for six states along the isochor $\rho^* = 0.025$. The decay behaviour of the autocorrelation function closely resembles that of the configurational-configurational shear stress correlation function. At short times, the autocorrelation function decays rapidly to negative values, exhibits a minimum, then increases to reach a maximum and approaches the time axis from above. At low temperatures, the minimum is followed by several oscillations as the time integrals of the autocorrelation functions clearly reveal. With increasing temperature, the effect becomes smaller and it vanishes at the highest displayed temperatures. This effect was already observed for the velocity autocorrelation function and the three contributions to the shear stress correlation functions and interpreted by the formation of bound states at low temperatures. The formation of bound states also explains the oscillations in the pressure fluctuation autocorrelation functions. Furthermore, it can be concluded that the formation of bound states has an influence on the second bulk viscosity virial coefficient, yielding a non-zero contribution.

Figure 6.8 depicts the pressure fluctuation autocorrelation function for selected state points on the close-critical isotherm $T^* = 1.35$ and along the two isochors $\rho^* = 0.3$ and 0.85. On the isotherm $T^* = 1.35$ at the highest density near the freezing line, the autocorrelation function shows a rapid decrease at short times, which suddenly becomes flatter at about $t^* = 0.1$. At the transition between the two characteristic regions, small oscillations are observed. This behaviour is neither found for shear

stress, nor for energy flux correlation functions (see Sections 5.4 and 7.4). At lower, but still liquid densities, the pressure fluctuation autocorrelation function decays much faster at long times. At gaseous states, the decay of the autocorrelation function is similar to that of the configurational-configurational shear stress correlation function as described above. In all these cases, the autocorrelation function has decayed to zero within a few reduced time units. Close to the critical density, the decay is much slower: Even within twenty reduced time units the pressure fluctuation autocorrelation function has not reached zero. Hence, the enhancement of the bulk viscosity in the vicinity of the critical point is caused by extremely slowly decaying pressure fluctuations.

On both isochors $\rho^* = 0.3$ and 0.85, the decay of the pressure fluctuation autocorrelation function becomes much faster with increasing temperature. At the highest temperatures, the autocorrelation function has rapidly decayed to zero within less than 0.1 reduced time unit at both densities. The slowest decay is again observed close to critical point on the isochor $\rho^* = 0.3$. At the liquid density $\rho^* = 0.85$, the decay in the intermediate time regime at the lowest temperatures is similar to that of the configurational-configurational shear stress correlation functions in this state region, suggesting a close relation between the responsible molecular transport mechanisms.
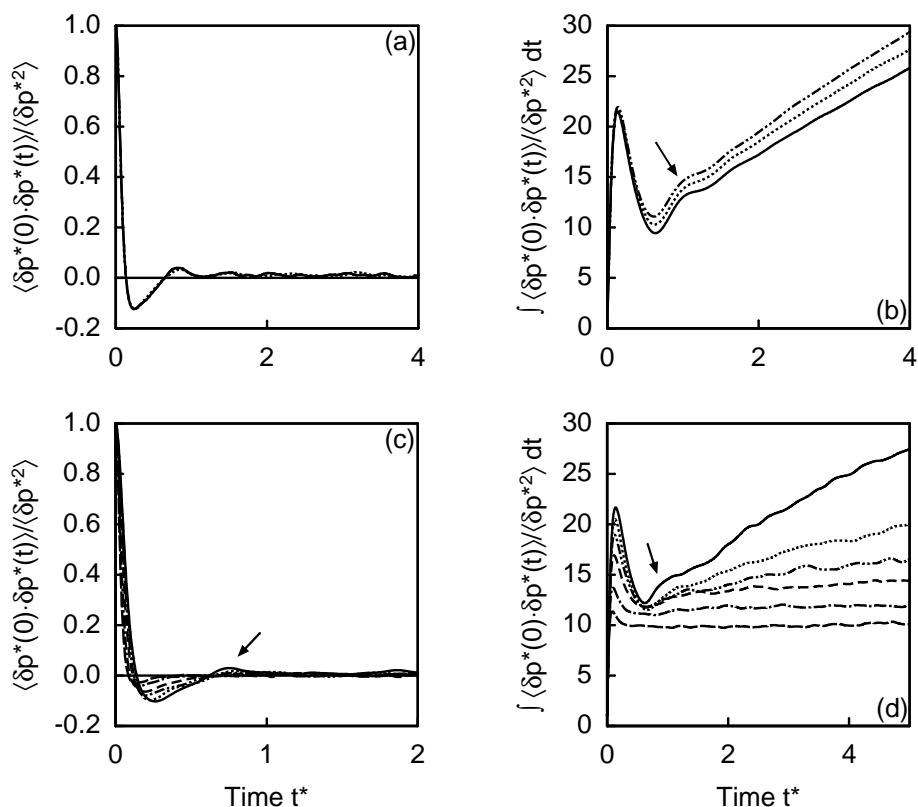
Figure 6.7. Short time behaviour of the normalized pressure fluctuation autocorrelation function and its time integral at gaseous densities. Note the different abscissa scale in the subfigures. The arrow points at special features of the correlation functions addressed in the text. (a) and (b): Density dependence on the lowest isotherm $T^* = 0.7$. Legend: (——) $\rho^* = 0.005$, (··········) $\rho^* = 0.01$ and (—··—··—) $\rho^* = 0.015$. (c) and (d): Temperature dependence along the isochor $\rho^* = 0.025$. Legend: (——) $T^* = 0.8$, (··········) $T^* = 0.9$, (—··—··—) $T^* = 1.1$, (————) $T^* = 1.5$, (—··—··—) $T^* = 2.5$ and (————) $T^* = 4.0$.
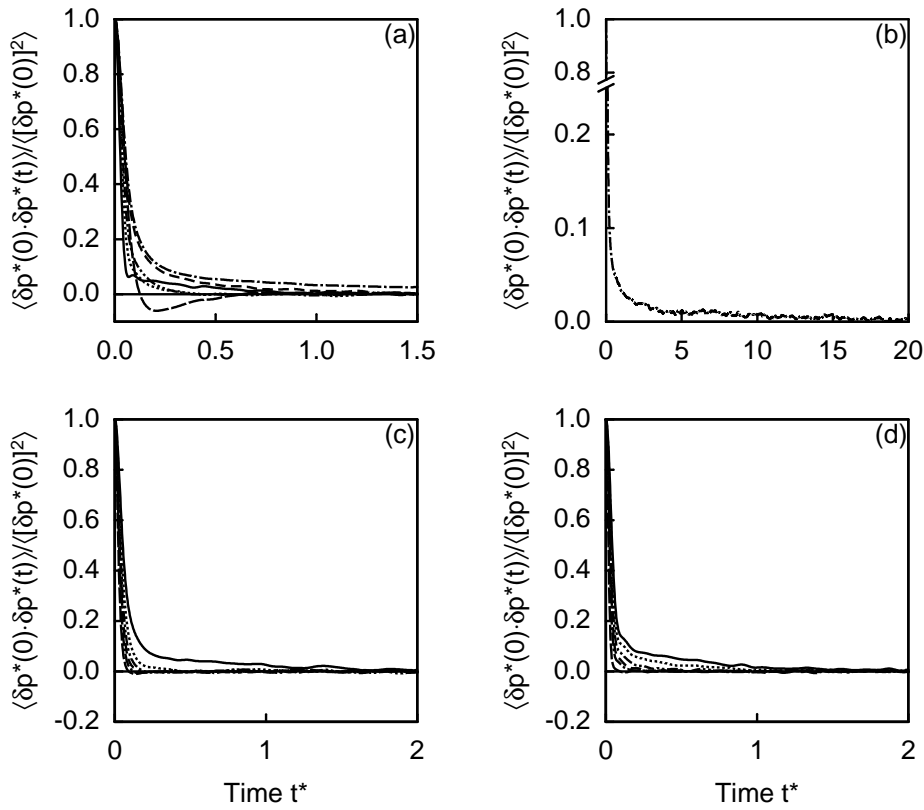
Figure 6.8. Dependence of the normalized pressure fluctuation autocorrelation function on density and temperature. Note the different abscissa scale in the subfigures. (a) and (b): On the supercritical isotherm $T^* = 1.35$ close to the critical temperature. Legend: (——) $\rho^* = 0.95$, (············) $\rho^* = 0.8$, (–···–···–) $\rho^* = 0.7$, (– – – –) $\rho^* = 0.5$, (–··–··–) $\rho^* = 0.35$, and (– – – –·) $\rho^* = 0.05$. (c): Along the isochor $\rho^* = 0.3$ close to the critical density. Legend: (——) $T^* = 1.358$, (············) $T^* = 1.8$, (–···–···–) $T^* = 2.5$, (– – – –) $T^* = 3.0$, (–··–··–·) $T^* = 4.0$ and (– – – –·) $T^* = 6.0$. (d) Along the liquid isochor $\rho^* = 0.85$. Legend: (——) $T^* = 0.7$, (············) $T^* = 0.9$, (–···–···–) $T^* = 1.3$, (– – – –) $T^* = 1.8$, (–··–··–·) $T^* = 2.5$ and (– – – –·) $T^* = 6.0$.

7   Interpretation of Transport Coefficients Within the Relaxation Time Concept

In this final chapter, the transport coefficients are analyzed within the relaxation time concept introduced by Zwanzig and Mountain [158, 223] in their work on the high frequency elastic moduli of simple liquids. After a brief introduction to the theory, its application to the self-diffusion coefficient, viscosity and bulk viscosity is described. In a second step, an extension of the relaxation time concept is suggested. Based on the subdivision of the viscosity, separate relaxation times are introduced for the three viscosity contributions. It is shown how the temperature and density dependence of the viscosity is built up from the three viscosity contributions within the relaxation time concept. Finally, the relaxation time concept is utilized to examine the question if the critical enhancement of the thermal conductivity found in experiments of real fluids is also observed in molecular dynamics simulations of the Lennard-Jones model fluid.

7.1   Elastic Moduli and Relaxation Times

When a sudden mechanical disturbance is applied to a fluid, it responds elastically at first instance as if it were a solid. The elastic response of the fluid is described by two quantities, the shear modulus at infinite frequency, G_∞, and bulk modulus at infinite frequency, K_∞. At low frequencies, the response of the fluid to the perturbation is entirely viscous.

According to Zwanzig and Mountain [223], a relation between the frequency dependent viscosity and bulk viscosity and the frequency dependent elastic moduli can be established by using the similarity between the Newtonian stress tensor (see Section 2.4.3),

$$\boldsymbol{\tau} = 2\eta\,\widehat{\dot{\boldsymbol{\varepsilon}}} + \eta_{\mathrm{b}}\,\mathrm{tr}(\dot{\boldsymbol{\varepsilon}})\boldsymbol{I} \quad , \tag{7.1}$$

and the stress tensor for ideal isotropic elastic solids,

$$\boldsymbol{\tau} = 2G\,\widehat{\boldsymbol{\varepsilon}} + K\,\mathrm{tr}(\boldsymbol{\varepsilon})\boldsymbol{I} \quad . \tag{7.2}$$

For instance, the viscous response of an off-diagonal element of the stress tensor to a sinusoidal disturbance with the frequency ω is given by

$$\tau_{\mathrm{xy}}(\omega) = 2\eta(i\omega)\, i\omega\, \varepsilon_{\mathrm{xy}} \tag{7.3}$$

and the elastic response by

$$\tau_{\mathrm{xy}}(i\omega) = 2G(i\omega)\, \varepsilon_{\mathrm{xy}} \quad . \tag{7.4}$$

An expression for the frequency dependent shear modulus is obtained from a comparison of both equations:

$$G(i\omega) = i\omega\eta(i\omega) \quad . \tag{7.5}$$

Analogously, the frequency dependent bulk modulus can be related to the frequency dependent bulk viscosity by

$$K(i\omega) - K_0 = i\omega\eta_{\mathrm{b}}(i\omega) \quad . \tag{7.6}$$

At zero frequency, the shear modulus vanishes, but the zero frequency bulk modulus is related to the zero frequency speed of sound by

$$K_0 = \rho_{\mathrm{m}} w_0^2 \quad . \tag{7.7}$$

Therefore, it is a thermodynamic state variable. The infinite frequency elastic moduli are determined by the infinite frequency viscosity and bulk viscosity.

Taking again an off-diagonal element of the stress tensor as an example, the expression for the frequency dependent shear modulus reads

$$G(i\omega) = i\omega\, \frac{V}{kT} \int\limits_0^\infty e^{-i\omega t} \langle \tau_{\mathrm{xy}}(0)\tau_{\mathrm{xy}}(t)\rangle\, \mathrm{d}t \quad , \tag{7.8}$$

when the frequency dependent viscosity, Eq. (2.145), is inserted. Before the infinite frequency limit is taken, the shear stress is expanded in a Taylor series

$$\tau_{\mathrm{xy}}(t) = \tau_{\mathrm{xy}}(0) + \dot{\tau}_{\mathrm{xy}}(0)\, t + \ddot{\tau}_{\mathrm{xy}}(0)\, \frac{t^2}{2} + \dots \tag{7.9}$$

and the substitution $\tau = \omega t$ is applied to the Fourier integral in Eq. (7.8), yielding

$$G(i\omega) = \frac{V}{kT} \int\limits_0^\infty i\, e^{-i\tau} \langle \tau_{\mathrm{xy}}(0)\tau_{\mathrm{xy}}(0) + \frac{\tau}{\omega}\, \tau_{\mathrm{xy}}(0)\dot{\tau}_{\mathrm{xy}}(0) + \dots \rangle\, \mathrm{d}\tau \quad . \tag{7.10}$$

In the infinite frequency limit, terms of first and higher order vanish and the integral over the remaining first term of the series is $\langle [\tau_{\mathrm{xy}}(0)]^2 \rangle$ so that the infinite frequency shear modulus becomes

$$G_\infty = \frac{V}{kT} \langle [\tau_{\mathrm{xy}}(0)]^2 \rangle \quad . \tag{7.11}$$

Similarly, the result for the bulk modulus

$$K_\infty = K_0 + \frac{V}{kT} \langle [\delta p(0)]^2 \rangle \tag{7.12}$$

can be established. Thus, the infinite frequency elastic moduli are determined by the initial values of the shear stress and pressure fluctuation correlation functions.

Both, G_∞ and K_∞ are equilibrium properties, but, in general, they are no thermodynamic state variables. When only pairwise interactions are taken into account, both infinite frequency elastic moduli can be expressed in terms of integrals of the radial distribution function and intermolecular pair potential function [223]. These relations read

$$G_\infty = \rho kT + \frac{2}{15}\pi\rho^2 \int\limits_0^\infty g(r) \frac{\mathrm{d}}{\mathrm{d}r}\left[r^4 \frac{\mathrm{d}u(r)}{\mathrm{d}r} \right] \mathrm{d}r \tag{7.13}$$

and

$$K_\infty = \frac{5}{3}\rho kT + p_{\mathrm{c}} + \frac{2}{9}\pi\rho^2 \int\limits_0^\infty g(r) r^3 \frac{\mathrm{d}}{\mathrm{d}r}\left[r \frac{\mathrm{d}u(r)}{\mathrm{d}r} \right] \mathrm{d}r \quad . \tag{7.14}$$

For the Lennard-Jones potential, the integrals can be explicitly evaluated [223] so that the final expressions for the infinite frequency elastic moduli read

$$G_\infty = \rho kT + 3p_{\mathrm{c}} - \frac{24}{5}\rho u \tag{7.15}$$

and

$$K_\infty = \frac{5}{3}G_\infty + 2p_{\mathrm{c}} \quad . \tag{7.16}$$

With these results, G_∞ and $K_\infty - K_0$ can be calculated in two different ways: Either directly by Eqs. (7.11) and (7.12), or by means of Eqs. (7.15), (7.7) and (7.16) using the simulation data for the configurational pressure, configurational internal energy and speed of sound.

The infinite frequency shear modulus can be separated into a translational and a configurational contribution as

$$G_\infty = \underbrace{\rho k T}_{G_{\mathrm{t},\infty}} + \underbrace{3 p^{\mathrm{c}} - \frac{24}{5} \rho u}_{G_{\mathrm{c},\infty}} \quad , \tag{7.17}$$

whereas the difference $K_\infty - K_0$ cannot be further separated into instantaneously uncorrelated contributions. The speed of sound appearing in the relation for the zero frequency bulk modulus, Eq. (7.7), is given by a nonlinear combination of the phase space functions (see Table 2.1). For this reason, the bulk viscosity cannot be partitioned into different contributions as the viscosity.

The Green-Kubo integral formulas for the viscosity and bulk viscosity can be written as a product of the initial values of the correlation functions and the integral of the normalized correlation functions. For example, the Green-Kubo formula for the viscosity is then given by

$$\eta = \frac{V}{kT} \langle [\tau_{\mathrm{xy}}(0)]^2 \rangle \underbrace{\int_0^\infty \frac{\langle \tau_{\mathrm{xy}}(0) \tau_{\mathrm{xy}}(t) \rangle}{\langle [\tau_{\mathrm{xy}}(0)]^2 \rangle} \, \mathrm{d}t}_{\tau_\eta} \quad . \tag{7.18}$$

Analogously, the Green-Kubo formula for the bulk viscosity can be written as

$$\eta_{\mathrm{b}} = \frac{V}{kT} \langle [\delta p(0)]^2 \rangle \underbrace{\int_0^\infty \frac{\langle \delta p(0) \delta p(t) \rangle}{\langle [\delta p(0)]^2 \rangle} \, \mathrm{d}t}_{\tau_{\eta\mathrm{b}}} \quad . \tag{7.19}$$

The normalized integrals have the unit of time and may be interpreted as relaxation times. They are measures of the duration of the decay of the correlation functions to zero. Hence, the viscosity and bulk viscosity can be expressed as

$$\eta = G_\infty \cdot \tau_\eta \tag{7.20}$$

and

$$\eta_{\mathrm{b}} = (K_\infty - K_0) \cdot \tau_{\eta_{\mathrm{b}}} \quad , \tag{7.21}$$

where the quantities τ_η and $\tau_{\eta_{\mathrm{b}}}$ are the shear and bulk relaxation times.

In the zero density limit, both relaxation times possess first order singularities. It is therefore more convenient to discuss the products of the relaxation times and

density instead of the relaxation times. Thus, Eqs. (7.20) and (7.21) are rewritten as

$$\eta = \frac{G_\infty}{\rho} \cdot (\tau_\eta \rho) \tag{7.22}$$

and

$$\eta_\mathrm{b} = \frac{K_\infty - K_0}{\rho} \cdot (\tau_{\eta_\mathrm{b}} \rho) \quad . \tag{7.23}$$

The initial value of the velocity autocorrelation function $\langle [\boldsymbol{v}_\mathrm{i}(0)]^2 \rangle$ is related to the thermodynamic temperature by the equipartition theorem [29, p. 375]:

$$\frac{1}{2} m \langle [\boldsymbol{v}_\mathrm{i}(0)]^2 \rangle = \frac{3}{2} kT \quad . \tag{7.24}$$

Thus, in analogy to the viscosity and bulk viscosity the product $D\rho$ can be written as

$$D\rho = \rho \frac{kT}{m} \underbrace{\frac{1}{N} \sum_{i=1}^{N} \int_0^\infty \frac{\langle \boldsymbol{v}_\mathrm{i}(t) \cdot \boldsymbol{v}_\mathrm{i}(0) \rangle}{\langle [\boldsymbol{v}_\mathrm{i}(0)]^2 \rangle} \, \mathrm{d}t}_{\tau_\mathrm{D}} = \frac{kT}{m} (\tau_\mathrm{D} \rho) \quad , \tag{7.25}$$

where τ_D is the self-diffusion relaxation time, which represents the normalized integral of the velocity autocorrelation function. The quantity $\rho kT/m$ is the analogue of the elastic moduli for self-diffusion and is termed self-diffusion modulus. In reduced quantities, Eq. (7.25) reads

$$D^* \rho^* = T^* (\tau_\mathrm{D}^* \rho^*) \quad . \tag{7.26}$$

Hence, the reduced self-diffusion modulus is the product of reduced density and reduced temperature.

In fact, the self-diffusion modulus and the first terms in the expressions for the infinite frequency elastic moduli, Eqs. (7.13) and (7.14), evaluated from Eqs. (7.11) and (7.12) differ from the correct thermodynamic temperature by the factor $(N-1)/N$ (see Section 2.3). These small differences arise because the reduction of the number of degrees of freedom by the mechanical constrains imposed on the system was neglected in the derivation of the molecular expressions for the thermodynamic fluxes in Section 2.5.2. However, they amount to less than 0.1 % for systems of 1372 particles and are negligible for the purposes of this chapter.

7.2 Application to Self-diffusion, Viscosity and Bulk Viscosity

The simulation data for the thermodynamic state variables and transport coefficients presented in the previous chapters were used to calculate moduli and relaxation times at every simulated state point. This section presents a discussion of the results for the self-diffusion coefficient, the viscosity and bulk viscosity, respectively.
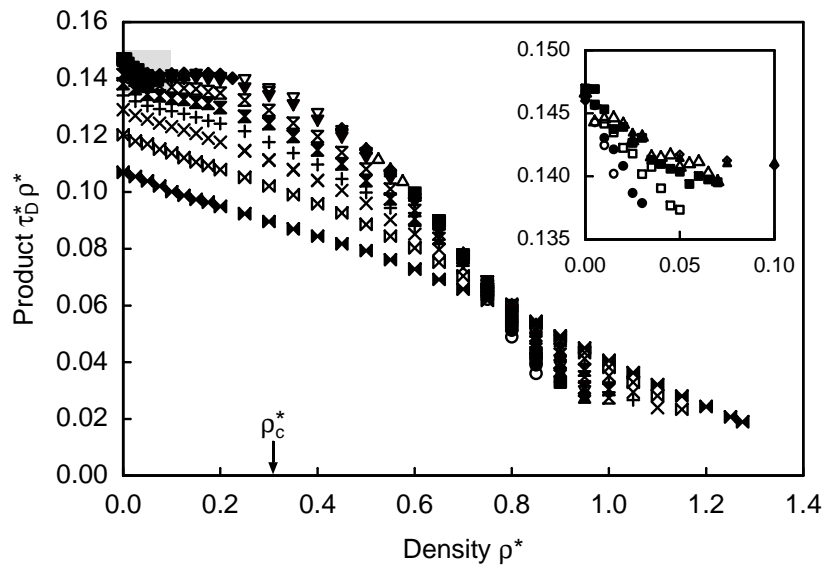
Figure 7.1. The product of self-diffusion relaxation time and density $\tau_{\mathrm{D}}^*\rho^*$ as a function of density for all simulated isotherms. The shaded area is enlarged in the insert. Symbols at zero density denote the Chapman-Enskog solution to the Boltzmann equation. Legend: (○) $T^* = 0.7$, (●) $T^* = 0.8$, (□) $T^* = 0.9$, (■) $T^* = 1.0$, (△) $T^* = 1.1$, (▲) $T^* = 1.2$, (◇) $T^* = 1.25$, (◆) $T^* = 1.3$, (▽) $T^* = 1.35$, (▼) $T^* = 1.5$, (⊠) $T^* = 1.8$, (⊠) $T^* = 2.1$, (+) $T^* = 2.5$, (×) $T^* = 3.0$, (⋈) $T^* = 4.0$ and (⋈) $T^* = 6.0$.

Figure 7.1 depicts the results for the product $\tau_{\mathrm{D}}^*\rho^*$ for all sixteen simulated isotherms. The self-diffusion relaxation times were calculated by Eq. (7.26) from the data for the product $D^*\rho^*$ and temperature T^* reported in Table D.2. Since $D^*\rho^*$ is only divided by temperature, the shape of the isotherms remains unchanged. In the gas region below the critical density, the temperature dependence of $\tau_{\mathrm{D}}^*\rho^*$ is not monotonic. At low temperatures, $\tau_{\mathrm{D}}^*\rho^*$ increases with temperature, above the temperature $T^* = 1.0$ it decreases. Above the critical density, $\tau_{\mathrm{D}}^*\rho^*$ decreases monotonically with temperature before the isotherms intersect at approximately

$\rho^* = 0.75$. In the high density liquid, the backscattering effect governs the decay of the velocity autocorrelation function at intermediate times. This effect is most pronounced at low temperatures and lowers the normalized integrals of the velocity autocorrelation function. Therefore, the temperature dependence of $\tau_D^* \rho^*$ is reversed in this state region. The intersection of the $\tau_D^* \rho^*$-isotherms lies in the same density range where the viscosity isotherms intersect (see Figure 5.4) and the isotherms of the viscosity contribution η_{cc}^* split (see Figure 5.9). This similarity again indicates a close relation between the molecular mass and momentum transport mechanisms.
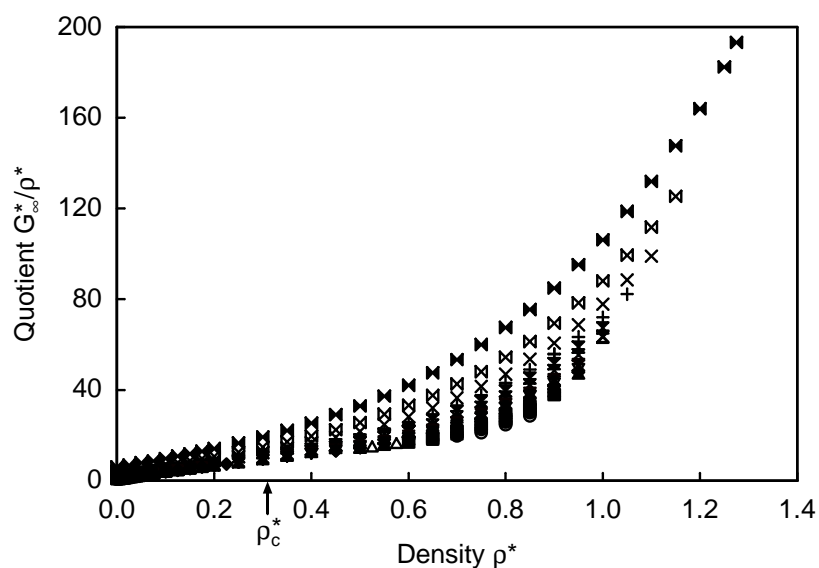
Figure 7.2. The quotient of infinite frequency shear modulus and density G_∞^*/ρ^* as a function of density for all simulated isotherms. Symbols are the same as in the legend to Figure 7.1.

Zwanzig and Mountain [223] used the expressions (7.15) and (7.16) together with tabulated pressure and internal energy data for argon to estimate values for the infinite frequency shear and bulk moduli over a wide range of fluid states. However, strictly Eqs. (7.15) and (7.16) apply only to model fluids in which the particles interact by the Lennard-Jones potential. In a second paper on this topic, Mountain and Zwanzig [158] used experimental viscosity data for argon to calculate shear relaxation times. Their results provided a picture of the characteristic behaviour of the elastic moduli and shear relaxation time. An evaluation of bulk relaxation times was not possible up to now due to the lack of bulk viscosity data. With the present comprehensive data for thermodynamic state variables and transport coefficients,
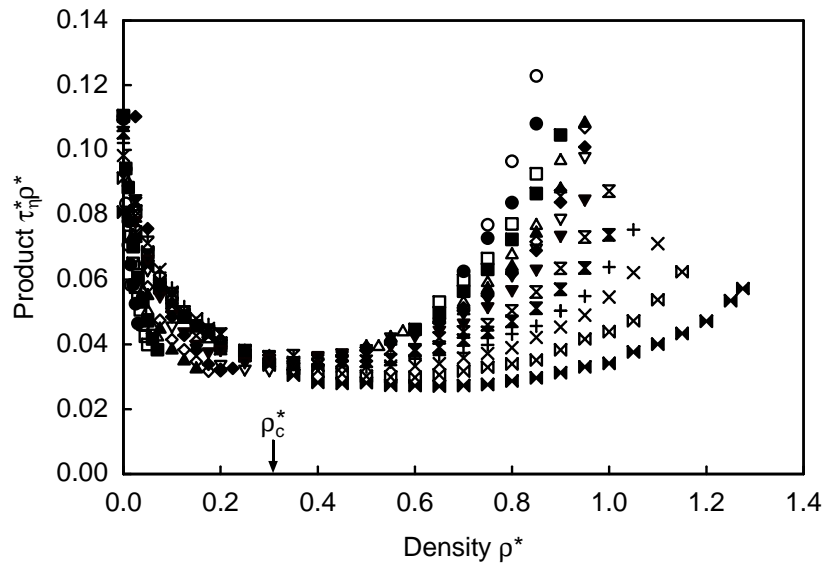
Figure 7.3. The product of shear relaxation time and density $\tau_\eta^* \rho^*$ as a function of density for all simulated isotherms. Symbols are the same as in the legend to Figure 7.1.

a self-consistent analysis of the viscosity and bulk viscosity in the relaxation time concept is possible. To retain maximum consistency with the data for the transport coefficients, the first method of the last section was chosen here to evaluate $G_{c,\infty}$ and $K_\infty - K_0$ for the simulations of the first simulation series. As the translational shear modulus is in a simple way related to the temperature, it it sufficient to consider only the configurational shear modulus. The results are reported together with the viscosity and bulk viscosity data in Tables D.3 and D.5.

Figures 7.2 and 7.3 display the results for G_∞^*/ρ^* and $\tau_\eta^* \rho^*$. The zero density limit of G_∞^*/ρ^* is the temperature T^*. In the gas region, the slope of the isotherms is small, in the liquid region they increase exponentially. G_∞^*/ρ^* increases monotonically with temperature over the whole density range from the zero density limit to the compressed liquid near the freezing line. At high densities, this temperature dependence is opposite to that of the viscosity.

The zero density values of the product $\tau_\eta^* \rho^*$ are determined by the zero density viscosity η_0^* divided by temperature T^*. On supercritical isotherms, three characteristic regions can be distinguished. The first region extends from zero density to the critical density. In this region, the $\tau_\eta^* \rho^*$-isotherms decrease strongly. The second region between the critical and 2.5 times the critical density is governed by a flat plateau, where the isotherms increase only moderately. The third region at

higher densities is characterized by strongly increasing isotherms. The temperature dependence changes at about the critical density. Below the critical density, the temperature dependence of $\tau_\eta^* \rho^*$ follows that of the zero density values η_0^*/T^*. At low temperatures, $\tau_\eta^* \rho^*$ increases, reaches a maximum and then decreases at high temperatures. In the gas region, the monotonic temperature dependence of the viscosity arises mainly from the temperature dependence of G_∞^*/ρ^*. Above the critical density, $\tau_\eta^* \rho^*$ decreases with temperature. Between the critical density and the point where the viscosity isotherms intersect (see Figure 5.4), the temperature dependence of the viscosity follows that of the quotient G_∞^*/ρ^*, while at higher liquid densities the temperature dependence of the viscosity results from the product $\tau_\eta^* \rho^*$.
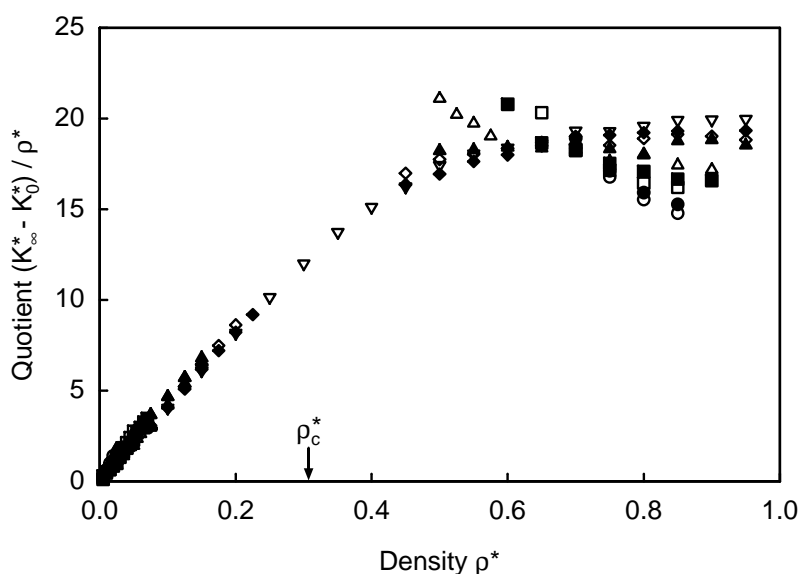
Figure 7.4. The quotient $(K_\infty^* - K_0^*)/\rho^*$ as a function of density for all simulated sub-critical isotherms. Symbols are the same as in the legend to Figure 7.1.

The results for the bulk modulus and relaxation time are shown in separate figures for sub- and supercritical isotherms. Figures 7.4 and 7.5 depict the quotients $(K_\infty^* - K_0^*)/\rho^*$, the products $\tau_{\eta b}^* \rho$ are displayed in Figures 7.6 and 7.7. The quotient $(K_\infty^* - K_0^*)/\rho^*$ shows a different behaviour than G_∞^*/ρ^*. At zero density, $(K_\infty^* - K_0^*)/\rho^*$ vanishes. This can be verified by the explicit evaluation of the zero density limit. For this purpose, the configurational pressure and configurational internal
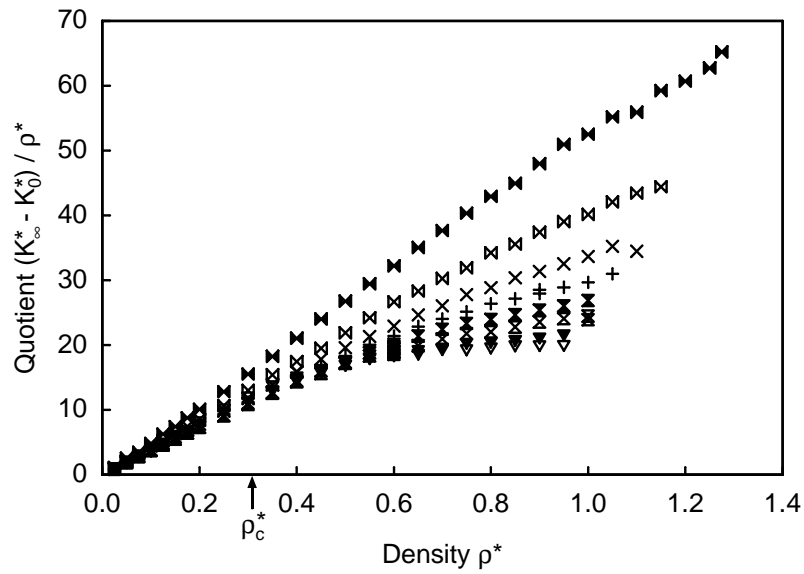
Figure 7.5. The quotient $(K_\infty^* - K_0^*)/\rho^*$ as a function of density for all simulated supercritical isotherms. Symbols are the same as in the legend to Figure 7.1.
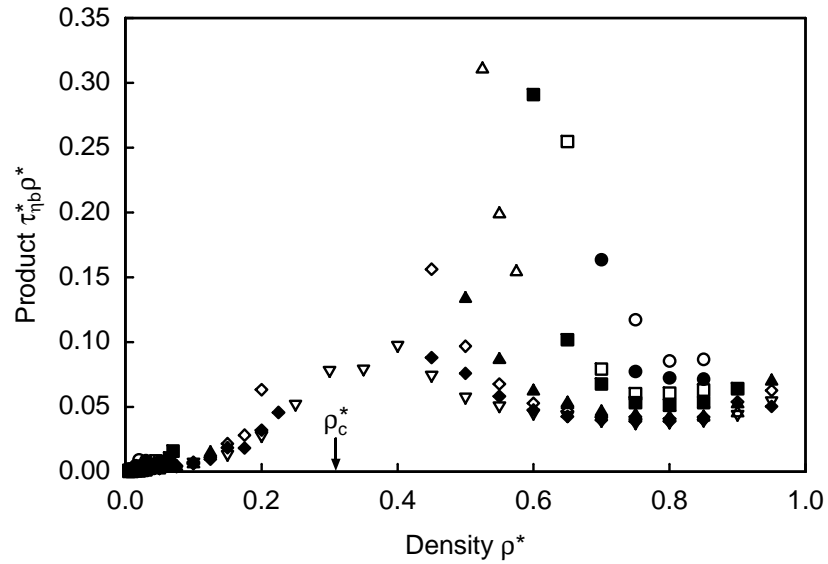
Figure 7.6. The product of bulk relaxation time and density $\tau_{\eta b}^* \rho^*$ as a function of density for all simulated subcritical isotherms. Symbols are the same as in the legend to Figure 7.1.
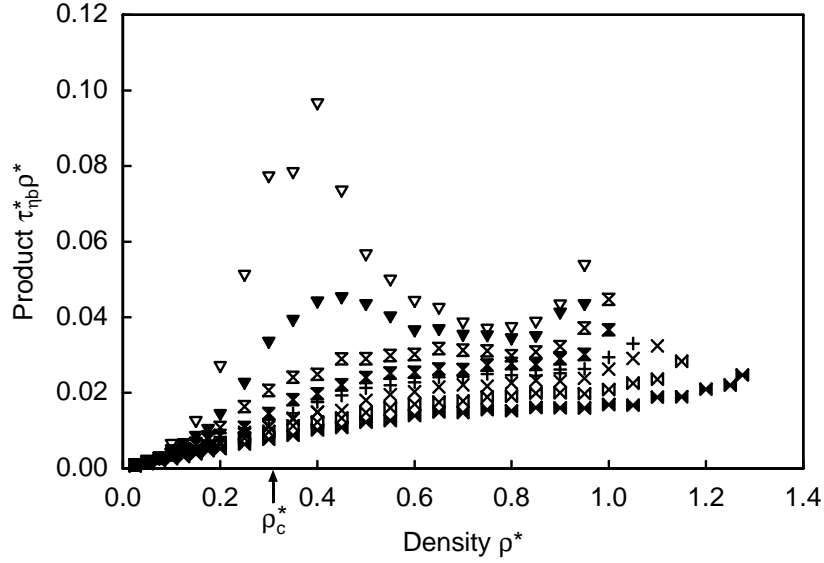
Figure 7.7. The product of bulk relaxation time and density $\tau_{\eta b}^* \rho^*$ as a function of density for all simulated supercritical isotherms. Symbols are the same as in the legend to Figure 7.1.

energy are expressed by the virial equation of state:

$$p_c = kT(B\rho^2 + C\rho^3 + \ldots) \tag{7.27}$$

$$u = -kT^2 \left(\frac{dB}{dT}\rho + \frac{dC}{dT}\rho^2 + \ldots \right) \quad . \tag{7.28}$$

Furthermore, the zero frequency speed of sound for an ideal monatomic gas,

$$w_0(\rho \to 0, T) = \sqrt{\frac{c_p}{c_V} \frac{kT}{m}} = \sqrt{\frac{5}{3} \frac{kT}{m}} \quad , \tag{7.29}$$

is required. When Eqs. (7.15), (7.16), (7.27) and (7.28) are used to express the infinite frequency bulk modulus, the zero density limit is evaluated as

$$\lim_{\rho \to 0} \frac{K_\infty - K_0}{\rho} = \lim_{\rho \to 0} \left[\frac{5}{3}kT + \frac{5p^c}{\rho} - 8u - mw_0^2 \right]$$

$$= \lim_{\rho \to 0} \left[\frac{5}{3}kT + 5kT(B\rho + C\rho^2 + \ldots) \right.$$

$$\left. +8kT^2 \left(\frac{dB}{dT}\rho + \frac{dC}{dT}\rho^2 + \ldots \right) \right] - \frac{5}{3}kT$$

$$= 0 \quad .$$

From the zero density limit, the isotherms increase almost linearly in the gas region, while the liquid parts of the isotherms have convex curvature and decrease

with density. The subcritical liquid isotherms intersect at approximately $\rho^* = 0.7$. Close to the critical temperature, the density dependence of the isotherms changes in the high density liquid region. At supercritical temperatures, they increase monotonically with density from the zero density limit to the freezing line.

In the gas region, $(K_\infty^* - K_0^*)/\rho^*$ decreases with temperature up to about $T^* = 1.0$, reaches a shallow minimum and then increases slightly at higher temperatures (not visible in Figures 7.4 and 7.5), while at high densities above the intersection point of the subcritical isotherms $(K_\infty^* - K_0^*)/\rho^*$ increases monotonically with temperature.

The product $\tau_{\eta_b}^* \rho$ closely resembles the behaviour of the bulk viscosity in Figures 6.3 and 6.5. It also shows the enhancement over a wide range of fluid states which is even on the highest isotherm $T^* = 6.0$ evident. This behaviour of $\tau_{\eta_b}^* \rho^*$ again proves that the enhancement of the bulk viscosity is caused by extremely slowly decaying pressure fluctuations.

As a last point in this section, it is shown that the second bulk viscosity virial coefficient $B_{\eta_b}^*$, i.e. the initial slope of the bulk viscosity isotherms, takes finite values that are in general non-zero. The slope of the isotherms is found by differentiating Eq. (7.23) with respect to density as

$$\frac{\partial \eta_b}{\partial \rho} = \frac{\partial}{\partial \rho}\left(\frac{K_\infty - K_0}{\rho}\right)(\tau_{\eta_b}\rho) + \frac{K_\infty - K_0}{\rho}\frac{\partial}{\partial \rho}(\tau_{\eta_b}\rho) \quad . \tag{7.30}$$

The second term vanishes in the zero density limit because $(K_\infty - K_0)/\rho$ is zero and the derivative of $\tau_{\eta_b}\rho$ with respect to density is finite. Thus, the initial slope of the bulk viscosity isotherms is given by

$$\lim_{\rho \to 0}\frac{\partial \eta_b}{\partial \rho} = \lim_{\rho \to 0}\frac{\partial}{\partial \rho}\left(\frac{K_\infty - K_0}{\rho}\right)(\tau_{\eta_b}\rho) \quad . \tag{7.31}$$

The derivative of $(K_\infty - K_0)/\rho$ with respect to density can be calculated as above using Eq. (7.15) and (7.16) by replacing the thermodynamic state variables by their expressions in terms of the virial equation of state. For the configurational pressure and internal energy, these expressions are given by Eqs. (7.27) and (7.28), while the relation for the square of the speed of sound for a monatomic gas reads [212]

$$w_0^2 = \frac{5}{3}\frac{kT}{m}(1 + \beta_a\rho + \gamma_a\rho^2 + \ldots) \quad , \tag{7.32}$$

where β_a and γ_a are the second and third acoustic virial coefficients. The second acoustic virial coefficient is related to the second thermal virial coefficient by [212]

$$\beta_a = 2B + \frac{4}{3}T\frac{dB}{dT} + \frac{4}{15}T^2\frac{d^2B}{dT^2} \quad . \tag{7.33}$$

With these expressions, the zero density limit of the derivative of $(K_\infty - K_0)/\rho$ with respect to density becomes

$$\lim_{\rho \to 0} \frac{\partial}{\partial \rho} \left(\frac{K_\infty - K_0}{\rho} \right) = \frac{5}{3} kTB + \frac{52}{9} kT^2 \frac{\mathrm{d}B}{\mathrm{d}T} - \frac{4}{9} kT^3 \frac{\mathrm{d}^2 B}{\mathrm{d}T^2} \neq 0 \quad , \tag{7.34}$$

which is finite and in general non-zero. Since τ_{η_b} has a first-order singularity at $\rho = 0$ due to the infinitely slow decay of pressure fluctuations, the product $\tau_{\eta_\mathrm{b}}\rho$ takes non-zero finite values. Therefore, the second bulk viscosity virial coefficient of the Lennard-Jones model fluid must in general be non-zero.

7.3 The Subdivision of Viscosity in the Relaxation Time Concept

According to Eq. (2.198), the viscosity can be written as a sum of three contributions, the translational-translational, translational-configurational and configurational-configurational contributions η_tt, η_tc and η_cc. In this section, an extension of the relaxation time concept is suggested which incorporates this subdivision of the viscosity. In analogy to the product $D\rho$, the viscosity and bulk viscosity, every viscosity contribution is represented by a product of a modulus and a relaxation time.

The translational shear modulus $G_{\mathrm{t},\infty}$ is related to the initial value of the translational-translational shear stress correlation function by

$$G_{\mathrm{t},\infty} = \frac{V}{kT} \langle [\tau_{\mathrm{xy,t}}(0)]^2 \rangle \tag{7.35}$$

and the configurational shear modulus $G_{\mathrm{c},\infty}$ to the initial value of the configurational-configurational shear stress correlation function by

$$G_{\mathrm{c},\infty} = \frac{V}{kT} \langle [\tau_{\mathrm{xy,c}}(0)]^2 \rangle \quad . \tag{7.36}$$

By introducing the shear relaxation times $\tau_{\eta,\mathrm{tt}}$ and $\tau_{\eta,\mathrm{cc}}$ for the integrals of the normalized contributions of the shear stress correlation functions, the translational-translational and configurational-configurational viscosity contributions are represented by

$$\eta_\mathrm{tt} = \frac{G_{\mathrm{t},\infty}}{\rho} (\tau_{\eta,\mathrm{tt}}\rho) \tag{7.37}$$

and

$$\eta_\mathrm{cc} = \frac{G_{\mathrm{c},\infty}}{\rho} (\tau_{\eta,\mathrm{cc}}\rho) \quad . \tag{7.38}$$

Since both relaxation times possess first order singularities in the zero density limit, it is again more convenient to discuss the products of the relaxation times and density.

The translational-configurational shear relaxation time corresponding to the viscosity contribution η_{tc} is defined as the integral of the normalized cross contribution of the shear stress correlation function. Since the translational and configurational shear stress contributions are not correlated instantaneously, the initial value of the cross correlation function is always zero. Therefore, the maximum of the cross correlation function is chosen as a normalization factor, which in practice turns out to be much smaller than the upper bound $2(G_{t,\infty}G_{c,\infty})^{1/2}$ imposed by the Schwartz inequality, Eq. (2.70). This choice is more convenient than $2(G_{t,\infty}G_{c,\infty})^{1/2}$ because it avoids the non-analyticity in density introduced by the square root function.

In analogy to Eqs. (7.37) and (7.38), η_{tc} is given by

$$\eta_{tc} = \frac{G_{tc,max}}{\rho}(\tau_{\eta,tc}\rho) \quad , \tag{7.39}$$

where $\tau_{\eta,tc}$ is the translational-configurational shear relaxation time and $G_{tc,max}$ is defined by

$$G_{tc,max} = \frac{V}{kT}\max(\langle \tau_c(0)\tau_t(t) + \tau_t(0)\tau_c(t)\rangle) \quad . \tag{7.40}$$

Contrary to $G_{t,\infty}$ and $G_{c,\infty}$, $G_{tc,max}$ is not an elastic modulus.

With the data for the viscosity contributions and the configurational shear modulus presented in Table D.3 and D.4, the translational-translational and configurational-configurational shear relaxation times can be calculated. The quotient $G_{t,\infty}^*/\rho^*$ is the reduced temperature T^*. The maxima of the translational-configurational shear stress correlation functions were obtained from the computed correlation functions for all state points of the first simulation series. The maximum of a correlation function was determined as the maximum of a second-order polynomial through the largest point and the two points next to the largest point. $G_{tc,max}^*$ was then calculated according to Eq. (7.40). The results for $G_{tc,max}^*$ are reported in Table D.3. Translational-configurational shear relaxation times were calculated by Eq. (7.39).

Figure 7.8 shows the results for the product $\tau_{\eta,tt}^*\rho^*$. The isotherms start with the value η_0^*/T^* at zero density. Since the product $\tau_{\eta,tt}^*\rho^*$ is η_{tt}^* divided by temperature, the isotherms have the same dependence on density as the η_{tt}^*-isotherms. However, the temperature dependence differs from that of η_{tt}^*. At high densities, it is reversed, while in the gas region $\tau_{\eta,tt}^*\rho^*$ follows the temperature dependence of η_0^*/T^*, which is similar to that of $\tau_D^*\rho^*$ in this state region.
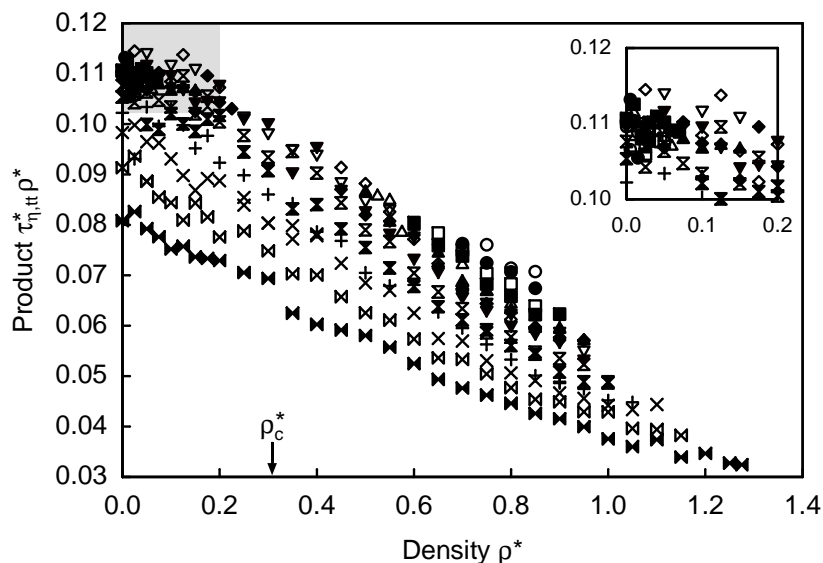
Figure 7.8. The product of the translational-translational shear relaxation time and density $\tau_{\eta,\mathrm{tt}}^*\rho^*$ as a function of density for all simulated isotherms. The shaded area is enlarged in the insert. Symbols are the same as in the legend to Figure 7.1.

The results for the quotient $G_{\mathrm{c},\infty}^*/\rho^*$ and the product $\tau_{\eta,\mathrm{cc}}^*\rho^*$ are depicted in Figures 7.9 and 7.10. In the zero density limit, $G_{\mathrm{c},\infty}^*/\rho^*$ vanishes, while $\tau_{\eta,\mathrm{cc}}^*\rho^*$ takes small finite non-zero values. The $G_{\mathrm{c},\infty}^*/\rho^*$-isotherms show the same dependence on density as G_{∞}^*/ρ^* since they differ from them only by the offset T^*. Both $G_{\mathrm{c},\infty}^*/\rho^*$ and $\tau_{\eta,\mathrm{cc}}^*\rho^*$ increase monotonically with density and, thus, yield similar contributions to the density dependence of η_{cc}^*. At high densities, the quotient $G_{\mathrm{c},\infty}^*/\rho^*$ decreases with temperature, whereas $\tau_{\eta,\mathrm{cc}}^*\rho^*$ increases. Thus, the temperature dependence of the viscosity contribution η_{cc}^* in the high density regime (see Figure 5.9) results from the product $\tau_{\eta,\mathrm{cc}}^*\rho^*$.

By using the same argumentation as applied in the last section to the second bulk viscosity virial coefficient, it can now be proved that the initial slope of the η_{cc}^*-isotherms is in general non-zero. The zero density limit of the derivative of $G_{\mathrm{c},\infty}^*/\rho^*$ with respect to density is given by

$$\lim_{\rho \to 0} \frac{\partial}{\partial \rho}\left(\frac{G_{\mathrm{c},\infty}}{\rho}\right) = 3kTB + \frac{24}{5}\,kT^2\,\frac{\mathrm{d}B}{\mathrm{d}T} \neq 0 \tag{7.41}$$

and is non-zero. As the product $\tau_{\eta,\mathrm{cc}}\rho$ generally takes finite non-zero values (see
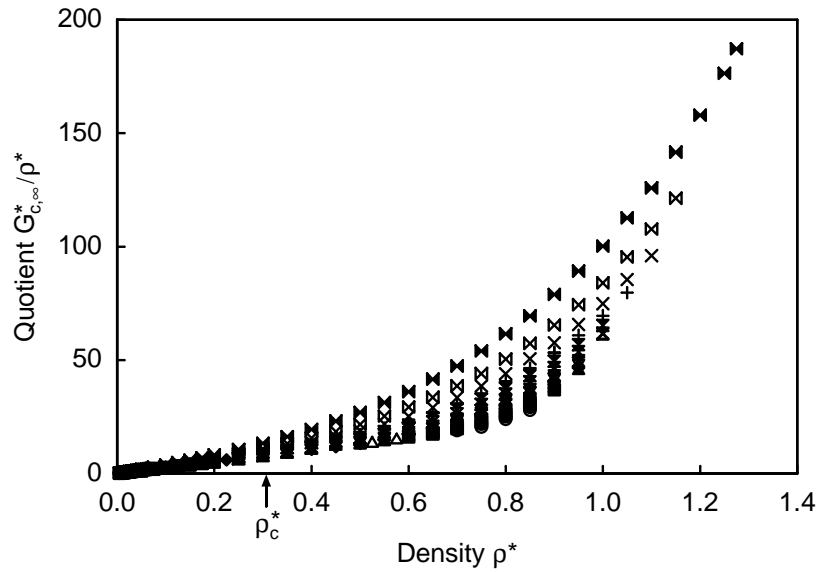
Figure 7.9. The quotient of the configurational shear modulus and density $G_{c,\infty}^*/\rho^*$ as a function of density for all simulated isotherms. Symbols are the same as in the legend to Figure 7.1.

Figure 7.10), the zero density limit of the derivative

$$\lim_{\rho\to 0}\frac{\partial\eta_{cc}}{\partial\rho} = \lim_{\rho\to 0}\frac{\partial}{\partial\rho}\left(\frac{G_{c,\infty}}{\rho}\right)(\tau_{\eta,cc}\rho) \tag{7.42}$$

must in general be non-zero.

Figures 7.11 and 7.12 show the quantities $G_{tc,max}^*/\rho^*$ and $\tau_{\eta,tc}^*\rho^*$ for the viscosity contribution η_{tc}^*. The isotherms of the quotient $G_{tc,max}^*/\rho^*$ increase almost linearly with density. Furthermore, this quantity increases monotonically with temperature from the low density gas to the compressed liquid.

The data for the product $\tau_{\eta,tc}^*\rho^*$ show quite large scatter as could be expected from the scatter of the data for the translational-configurational viscosity contribution. Since the data for $G_{tc,max}^*/\rho^*$ are very consistent, the scatter of the η_{tc}^* data is entirely contained in the $\tau_{\eta,tc}^*\rho^*$ data. Nevertheless, some trends become quite clear. Supercritical isotherms exhibit maxima, which occur at lower densities than the maxima of the η_{tc}^*-isotherms. In the liquid region, the isotherms intersect at approximately $\rho^* = 0.85$. Below this density, $\tau_{\eta,tc}^*\rho^*$ decreases with temperature, while at higher densities it increases. In the gas region, $\tau_{\eta,tc}^*\rho^*$ increases with temperature. The temperature dependence of η_{tc}^* is mainly due to the temperature dependence of $G_{tc,max}^*/\rho^*$, whereas the density dependence is caused by the product $\tau_{\eta,tc}^*\rho^*$.
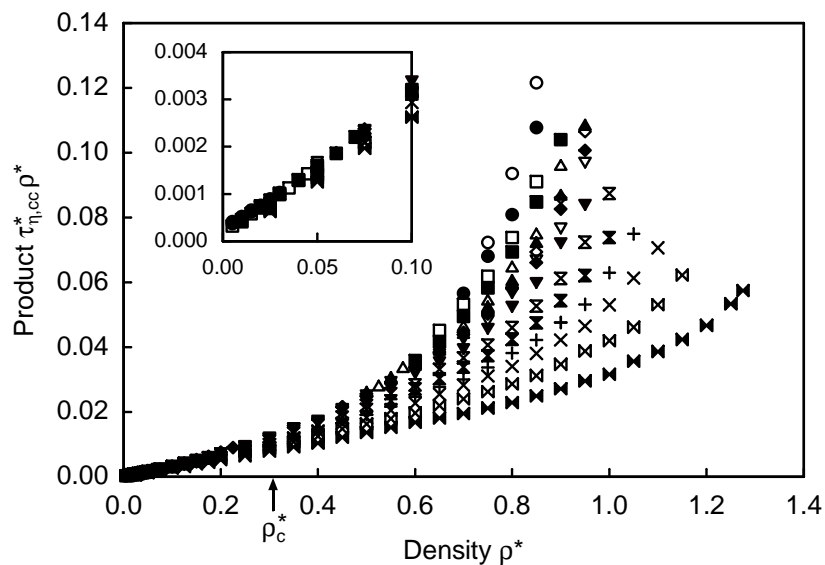
Figure 7.10. The product of the configurational-configurational shear relaxation time and density $\tau^*_{\eta,\mathrm{cc}}\rho^*$ as a function of density for all simulated isotherms. The low density regime is enlarged in the insert. Symbols are the same as in the legend to Figure 7.1.
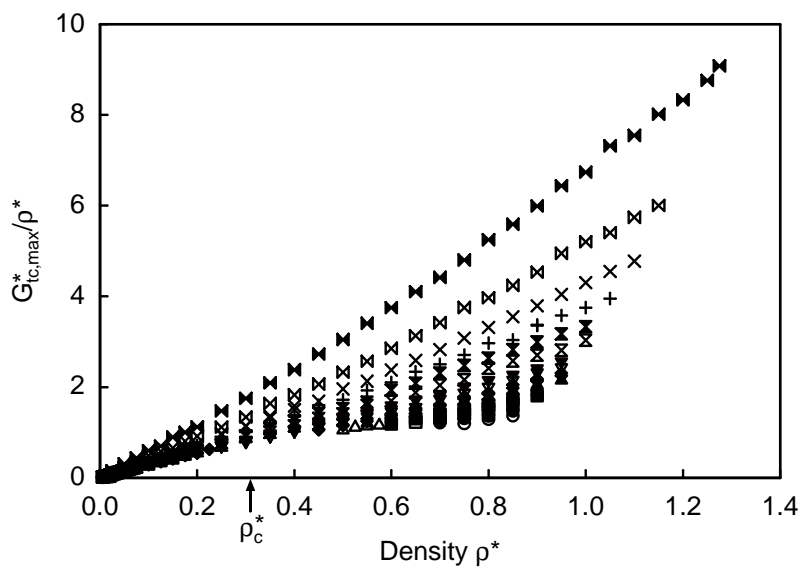
Figure 7.11. The quotient $G^*_{\mathrm{tc,max}}/\rho^*$ as a function of density for all simulated isotherms. Symbols are the same as in the legend to Figure 7.1.
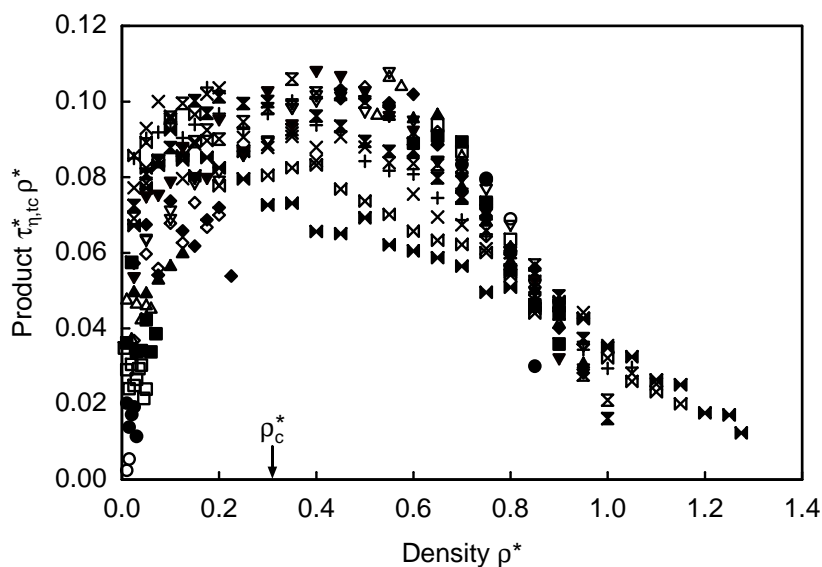
Figure 7.12. The product of translational-configurational shear relaxation time and density $\tau_{\eta,\mathrm{tc}}^* \rho^*$ as a function of density for all simulated isotherms. Symbols are the same as in the legend to Figure 7.1.

## 7.4 Evidence for the Critical Enhancement of Thermal Conductivity

The simulation results for the bulk viscosity in Chapter 6 showed that the behaviour of this transport coefficient in the fluid region is dominated by a critical enhancement, which extends far into the supercritical region. From experimental investigations of the thermal conductivity in the critical region, it is well known that the thermal conductivity exhibits a similar enhancement, see for example the works of Michels et al. on carbon dioxide [144] and Tiesinga et al. on the noble gas argon [208]. However, the effect is much weaker and restricted to the close vicinity of the critical point. In this section, it is examined if the enhancement of the thermal conductivity is also observed in molecular dynamics simulations of the Lennard-Jones model fluid with small systems of less than 1500 particles.

Only few authors reported simulation data for the thermal conductivity of the Lennard-Jones model fluid, examples are the works of Borgelt et al. [25], Heyes [80, 82, 84] and Hammonds and Heyes [66]. In particular, the behaviour of the thermal conductivity close to the critical point was examined by Searles et al. [192]. Their approach is based on the conventional subdivision of transport coefficients
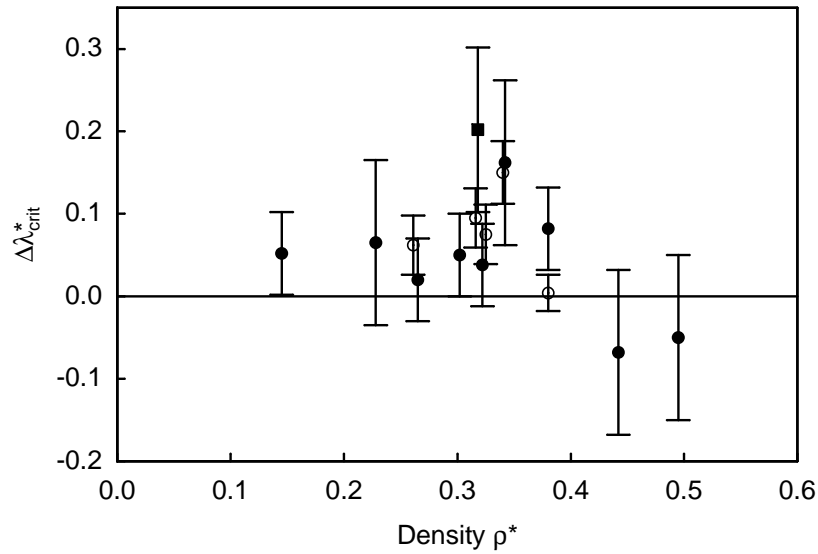
Figure 7.13. The literature data of Searles et al. [192] for the critical enhancement contribution to the thermal conductivity on the close-critical isotherm $T^* = 1.35$. Legend: (●) equilibrium molecular dynamics with 864 particles, (○) nonequilibrium molecular dynamics with 864 particles and (■) equilibrium molecular dynamics with 6912 particles. Error bars indicate the uncertainty of the data.

into the zero density contribution, the residual contribution and the contribution due to the critical enhancement as described in Section 2.5.5. They derived thermal conductivity data in the vicinity of the critical density on the supercritical isotherms $T^* = 1.35$ and $T^* = 2.5$ from equilibrium and nonequilibrium molecular dynamics simulations. Their simulations were mainly carried out with 864 particles, a cutoff radius of $r^*_{\mathrm{cut}} = 3.379$ and extended over at least 1000 reduced time units. Since the temperature $T^* = 1.35$ is very close to the critical temperature $T^*_{\mathrm{c}} = 1.328$ [142], this isotherm should show a clear critical enhancement. On the other hand, the temperature $T^* = 2.5$ is so far away from the critical temperature that this isotherm should not be influenced by the critical enhancement. Searles et al. assumed that the temperature dependence of the residual contribution is negligible and calculated the critical enhancement contribution on the isotherm $T^* = 1.35$ as the difference of isochoric thermal conductivity data on the two isotherms after subtraction of the zero density contributions. Their results for the critical enhancement contribution are depicted in Figure 7.13. A very small enhancement on the isotherm $T^* = 1.35$ was observed, but due to the uncertainty of the data the existence of the

critical enhancement could not be unambiguously proved. This method relies on the assumption that the residual thermal conductivity does not depend on temperature. However, this assumption is strictly not correct.

Therefore, a different approach is pursued here. First, the thermal conductivity λ^* is resolved into translational-translational, translational-configurational and configurational-configurational contributions λ_{tt}^*, λ_{tc}^* and λ_{cc}^* according to Eq. (2.199). Subsequently, the subdivision of the thermal conductivity is treated in the relaxation time concept, which was developed for the viscosity in the previous section. As in Section 7.2 for the bulk viscosity, the relaxation times should be sensitive indicators for the critical enhancement of the thermal conductivity.

A series of simulations was performed on the same close-critical isotherm $T^* = 1.35$ which was investigated by Searles et al. [192]. The reduced temperature of the isotherm $T^* = 1.35$ is about 1.0166 times larger than the reduced critical temperature $T_c^* = 1.328$ reported by Mecke et al. [142]. According to the experimental results of Michels et al. [144] for carbon dioxide and Tiesinga et al. [208] for argon, this isotherm should exhibit a clear enhancement in the vicinity of the critical density. The simulations were carried out as described in Section 3.5. At every simulated state point, the thermal conductivity λ^* as well as the contributions λ_{tt}^*, λ_{tc}^*, λ_{cc}^* and several other properties were calculated. The results for the thermal conductivity are summarized in Table D.8, while the results for thermodynamic state variables, the self-diffusion coefficient, the viscosity and viscosity contributions and the bulk viscosity are included in Tables D.1, D.2, D.3 and D.5, respectively.

Figure 7.14 shows the data for the thermal conductivity and the three contributions as well as literature data of Heyes [84] for the same isotherm $T^* = 1.35$. The thermal conductivity starts with the Chapman-Enskog value (see Appendix B) at zero density and increases slowly up to the density $\rho^* = 0.5$. At liquid densities, the increase becomes stronger. In the vicinity of the critical density, the expected enhancement is indeed observed. However, the effect is weaker than the enhancement found in experiments for real fluids. Moreover, in comparison with the enhancement of the bulk viscosity the enhancement of the thermal conductivity is much smaller and restricted to the close vicinity of the critical density on this isotherm.

The literature data of Heyes agree well with the present data at intermediate densities, but lie below the present data at densities above $\rho^* = 0.7$. From the investigation of the dependence of the viscosity on the number of particles close to the triple point in Section 3.4, it is known that viscosity data obtained from simulations of small systems with moderate particle numbers are too low. Therefore,
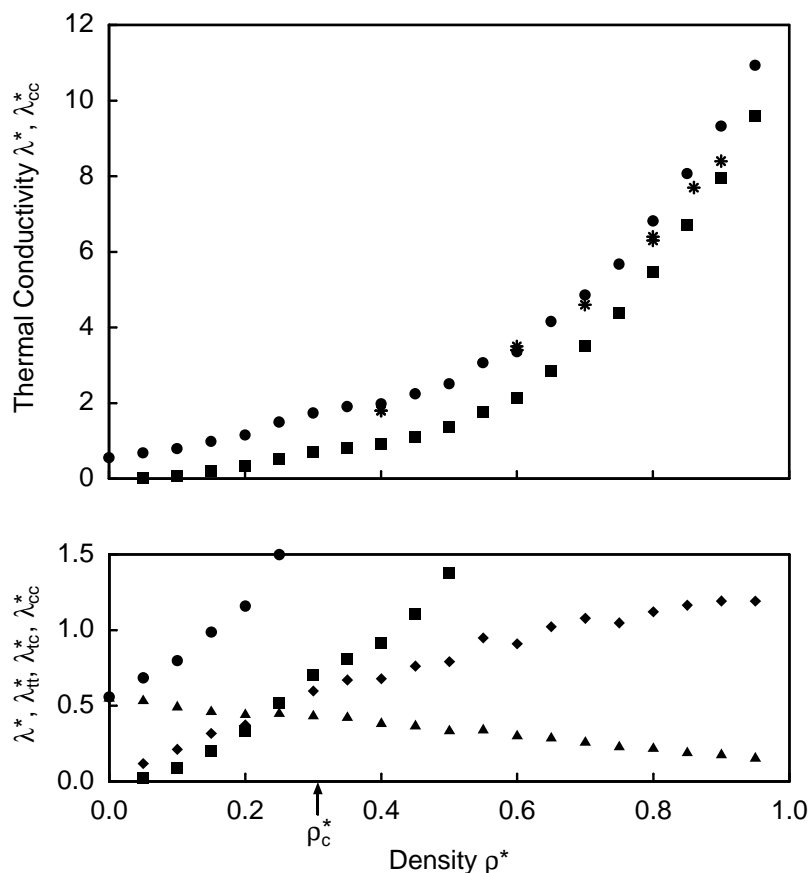
Figure 7.14. The thermal conductivity λ^* (●) and the thermal conductivity contributions λ^*_{tt} (▲), λ^*_{tc} (◆) and λ^*_{cc} (■) and literature data of Heyes [84] (✳) on the supercritical isotherm $T^* = 1.35$ as a function of density.

it is not unreasonable that the discrepancy between the two thermal conductivity data sets is also due to the use of different particle numbers. Heyes used 256 particles, whereas the present simulations were performed with 1372 particles.

As the viscosity contribution η^*_{tt}, the corresponding thermal conductivity contribution λ^*_{tt} decreases with density along the isotherm. The cross contribution λ^*_{tc} does not show the maximum found for η^*_{tc}, but increases monotonically from the low density gas to the compressed liquid close to the freezing line. The contribution λ^*_{cc} yields the largest contribution to the thermal conductivity at high density liquid states. Contrary to the viscosity contribution η^*_{cc}, λ^*_{cc} does not show the flat increase at low and intermediate densities. Instead, the enhancement determines the shape of the isotherm in the vicinity of the critical density. The enhancement is

only observed for λ_{cc}^*. It seems to exist for λ_{tt}^* and λ_{tc}^*, but the scatter of the data is too large to detect such a small effect unambiguously.

In Sections 6.3 and 7.2, the analysis of the pressure fluctuation autocorrelation functions and bulk relaxation times showed that the enhancement of the bulk viscosity is caused by the extremely slowly decay of the pressure fluctuation autocorrelation functions. In the remainder of this section, the enhancement of the thermal conductivity is analyzed from both view angles.

An extension of the theory of the high frequency elastic moduli of Zwanzig and Mountain [223] to thermal conductivity was suggested by Nossal [167]. In this work, in analogy to shear and bulk moduli G and K a thermal modulus Θ was introduced. Nossal [167] suggested that the initial value of the heat flux correlation function is related to the difference of the thermal modulus at infinite frequency and zero frequency

$$\Theta_\infty - \Theta_0 = \frac{V}{kT^2}\langle[\boldsymbol{J}^{\mathrm{q}}(0)]^2\rangle \quad . \tag{7.43}$$

As the zero frequency bulk modulus K_0, the zero frequency thermal modulus Θ_0 can be expressed by thermodynamic state variables as

$$\Theta_0 = \frac{\rho_{\mathrm{m}}}{T}\langle h_{\mathrm{m}}\rangle^2 \quad , \tag{7.44}$$

where h_{m} is the mass specific enthalpy. The difference $\Theta_\infty - \Theta_0$ can be separated into a translational and a configurational contribution that are related to the initial values of the translational-translational and configurational-configurational contribution of the heat flux correlation function by

$$(\Theta_{\mathrm{t},\infty} - \Theta_{\mathrm{t},0}) = \frac{V}{3kT^2}\langle[\boldsymbol{J}_{\mathrm{t}}^{\mathrm{q}}(0)]^2 \tag{7.45}$$

and

$$(\Theta_{\mathrm{c},\infty} - \Theta_{\mathrm{c},0}) = \frac{V}{3kT^2}\langle[\boldsymbol{J}_{\mathrm{c}}^{\mathrm{q}}(0)]^2\rangle \quad . \tag{7.46}$$

By a simple calculation in the canonical ensemble it can be shown that the translational contribution is given by

$$(\Theta_{\mathrm{t},\infty} - \Theta_{\mathrm{t},0}) = \frac{k}{m}\rho c_{\mathrm{p},0}T \quad , \tag{7.47}$$

in which $c_{\mathrm{p},0}$ is the isobaric heat capacity per particle of the ideal gas. The configurational contribution $(\Theta_{\mathrm{c},\infty} - \Theta_{\mathrm{c},0})$ cannot be expressed by thermodynamic state

variables. When the normalized integrals of the heat flux correlation functions are interpreted as thermal relaxation times, the total thermal conductivity and the three thermal conductivity contributions can be written as

$$\lambda \ = (\Theta_\infty - \Theta_0) \cdot \tau_\lambda \tag{7.48}$$

$$\lambda_{tt} = (\Theta_{t,\infty} - \Theta_{t,0}) \cdot \tau_{\lambda,tt} \tag{7.49}$$

$$\lambda_{tc} = \Theta_{tc,max} \cdot \tau_{\lambda,tc} \tag{7.50}$$

$$\lambda_{cc} = (\Theta_{c,\infty} - \Theta_{c,0}) \cdot \tau_{\lambda,cc} \quad . \tag{7.51}$$

As the shear and bulk relaxation times, the thermal relaxation times have first order singularities at zero density and it is more convenient to discuss the quotients of thermal moduli and density and products of thermal relaxation times and density. Hence, Eqs. (7.48) to (7.51) become

$$\lambda \ = \frac{\Theta_\infty - \Theta_0}{\rho} \cdot (\tau_\lambda \rho) \tag{7.52}$$

$$\lambda_{tt} = \frac{\Theta_{t,\infty} - \Theta_{t,0}}{\rho} \cdot (\tau_{\lambda,tt} \rho) \tag{7.53}$$

$$\lambda_{tc} = \frac{\Theta_{tc,max}}{\rho} \cdot (\tau_{\lambda,tc} \rho) \tag{7.54}$$

$$\lambda_{cc} = \frac{\Theta_{c,\infty} - \Theta_{c,0}}{\rho} \cdot (\tau_{\lambda,cc} \rho) \quad . \tag{7.55}$$

Figures 7.15 and 7.16 show these quantities for the close-critical isotherm $T^* = 1.35$. The translational contribution $(\Theta_{t,\infty}^* - \Theta_{t,0}^*)/\rho^*$ takes the constant value $c_{p,0}^* T^*$ = 3.375 predicted by theory along the isotherm. The configurational contribution starts from zero at zero density and increases slowly up to the density $\rho^* = 0.6$. From this point, the increase becomes stronger in the high density region. The total quotient is the sum of the translational and configurational contribution. Hence, the isotherm has the same shape as the configurational contribution isotherm, but is shifted upwards by $c_{p,0}^* T^* = 3.375$. The $\Theta_{tc,max}^*$-isotherm increases almost linearly with density. The thermal moduli do not show any sign of an enhancement close to the critical density.

The behaviour of the product $\tau_\lambda^* \rho^*$ is similar to that of the corresponding quantity for viscosity $\tau_\eta^* \rho^*$. However, at high densities close to the freezing line the increase is not as strong as for $\tau_\eta^* \rho^*$. Moreover, in the vicinity of the critical density the data show the expected enhancement. At zero density, $\tau_\lambda^* \rho^*$ and $\tau_{\lambda,tt}^* \rho^*$ take the value $\lambda_0^*/(c_{p,0}^* T^*)$.

The data for $\tau_{\lambda,tt}^* \rho^*$ and $\tau_{\lambda,tc}^* \rho^*$ at low and intermediate densities scatter so that it is difficult to resolve the details of the shape of the isotherms. An enhancement
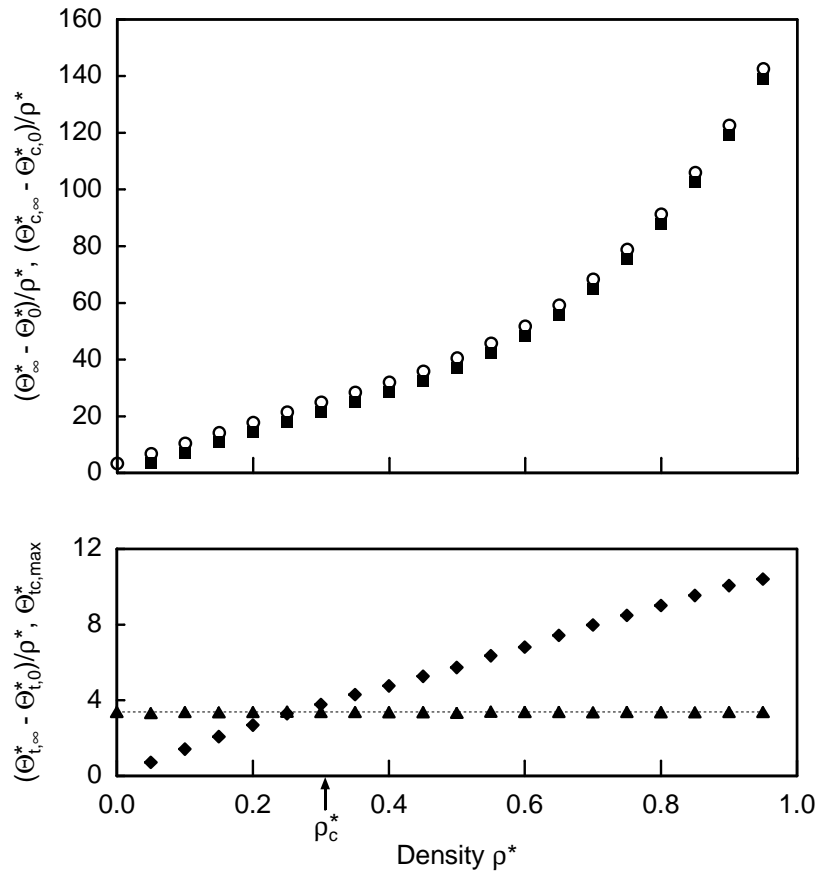
Figure 7.15. The quotients $(\Theta^*_\infty - \Theta^*_0)/\rho^*$ ($\bigcirc$), $(\Theta^*_{t,\infty} - \Theta^*_{t,0})/\rho^*$ ($\blacktriangledown$), $\Theta^*_{tc,max}/\rho^*$ ($\blacklozenge$) and $(\Theta^*_{c,\infty} - \Theta^*_{c,0})/\rho^*$ ($\blacksquare$) on the supercritical isotherm $T^* = 1.35$ as a function of density. The dashed line is the theoretical value $(\Theta^*_{t,\infty} - \Theta^*_{t,0})/\rho^* = c^*_{p,0}T^*$.

appears to exist for both quantities, but due to the scatter of the data this conclusion cannot be unambiguously drawn. At low and intermediate densities, the behaviour of $\tau^*_{\lambda,tt}\rho^*$ is similar to that found for the corresponding quantity for viscosity, but at high densities it is different. The product $\tau^*_{\lambda,tt}\rho^*$ continues to decrease strongly, whereas the $\tau^*_{\eta,tt}\rho^*$-isotherms become flatter close to the freezing line. $\tau^*_{\lambda,tc}\rho^*$ is non-zero at zero density and decreases with density along the isotherm.

The product $\tau^*_{\lambda,cc}\rho^*$ evidently shows the enhancement, which was already found for λ_{cc} in Figure 7.14 in the vicinity of the critical density. In this representation, the enhancement is even more clearly visible than in Figure 7.14 for the λ^*_{cc}-isotherm. At high densities, a stronger increase than that observed in Figure 7.16 from the behaviour of λ^*_{cc} and the results for the corresponding viscosity contribution is ex-
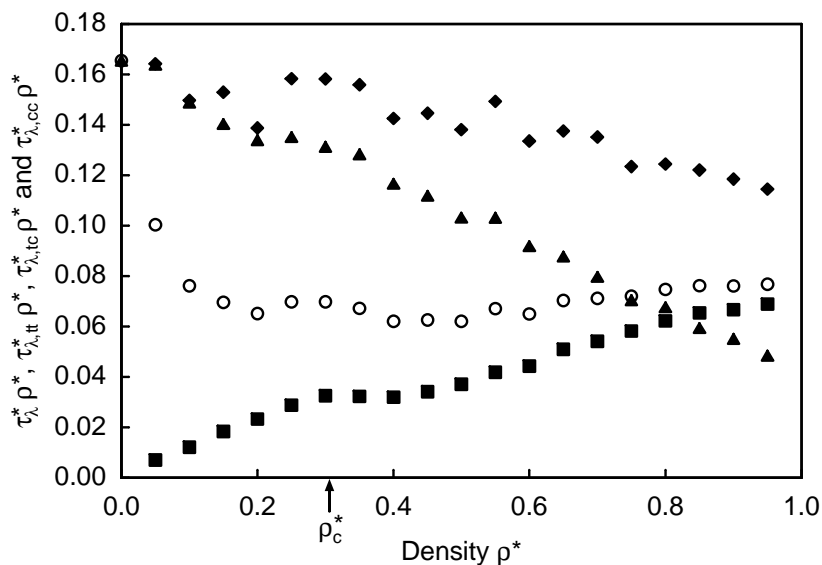
Figure 7.16. The products $\tau_\lambda^* \rho^*$ (○), $\tau_{\lambda,\mathrm{tt}}^* \rho^*$ (▲), $\tau_{\lambda,\mathrm{tc}}^* \rho^*$ (◆) and $\tau_{\lambda,\mathrm{cc}}^* \rho^*$ (■) on the supercritical isotherm $T^* = 1.35$ as a function of density.

pected. The discussion of λ_{cc}^* earlier in this section showed systematic differences between the present data and literature thermal conductivity data of Heyes obtained with 256 particles [84]. These differences were attributed to finite size effects. Since this effect is large at the highest densities on the isotherm, it is not unreasonable to assume that the present high density thermal conductivity data might be subject to finite-size effects and, therefore, might be too low although the simulations were carried out with large systems of 1372 particles. This effect would explain the shape of the $\tau_{\lambda,\mathrm{cc}}^* \rho^*$-isotherm close to the freezing line. Hence, simulations with more than 1372 particles are required to determine the macroscopic behaviour of the thermal conductivity in the high density region.

Figure 7.17 depicts the three contributions to the heat flux correlation function at selected state points on the isotherm $T^* = 1.35$. The translational-translational contribution shows the same behaviour as the corresponding contribution to the shear stress correlation function in Figure 5.15, while differences are observed for the translational-configurational and configurational-configurational heat flux correlation functions. At high densities, the translational-configurational heat flux correlation function does not show the negative region after the maximum that is observed for the corresponding contribution to the shear stress correlation function. This explains the different behaviour of the λ_{tc}^*- and η_{tc}^*-isotherms in this
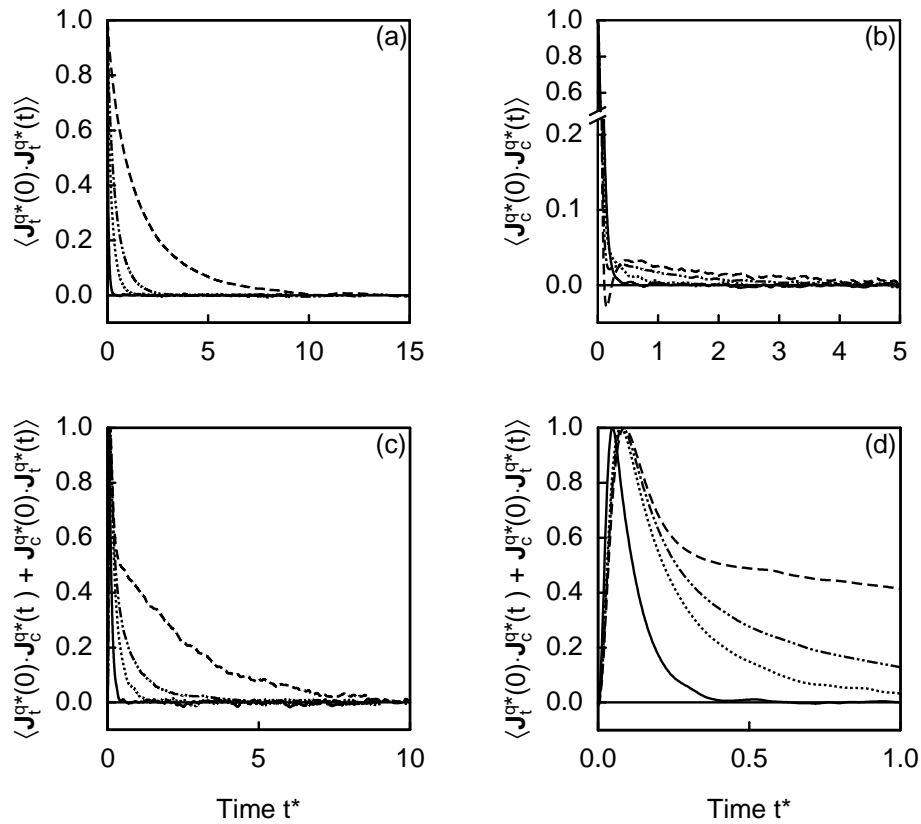
Figure 7.17. Normalized heat flux correlation function for selected densities on the isotherm $T^* = 1.35$. (a) translational-translational contribution; (b) configurational-configurational contribution; (c) long time behaviour of translational-configurational contribution and (d) short time behaviour of translational-configurational contribution. Note the different abscissa scale in the subfigures. Legend: $\rho^* = 0.1$ ($----$), $\rho^* = 0.3$ ($-\cdot-\cdot-$), $\rho^* = 0.5$ ($\cdots\cdots$) and $\rho^* = 0.95$ (———).

state region: the λ^*_{tc}-isotherm increases monotonically, whereas the η^*_{tc}-isotherm decreases at high densities due to the negative contribution to the integral of the translational-configurational shear stress correlation function. The configurational-configurational heat flux correlation function decays rapidly at high liquid densities and does not exhibit the pronounced slow decay at intermediate times observed for the configurational-configurational shear stress and pressure fluctuation correlation functions. At low densities, the configurational-configurational heat flux correlation function also shows a rapid decay to a minimum at short times followed by an increase with a maximum and a very slow approach to the time axis from above. As

expected, at the density $\rho^* = 0.3$ close to the critical density, the long time decay is slow, but at the lower gaseous density $\rho^* = 0.1$ it is even slower. This behaviour is different than the decay of the pressure fluctuation autocorrelation function at low densities on this isotherm (see Figure 6.8).

8 Conclusions

Thermophysical properties of model fluids are important references to develop an understanding of the behaviour of real fluids. The Lennard-Jones potential describes interactions between spherical non-polar molecules and is an important model in many applications of statistical thermodynamics.

In this work, extensive data for the self-diffusion coefficient, the viscosity and bulk viscosity of the Lennard-Jones model fluid were determined from equilibrium molecular dynamics simulations using the Einstein relation method. In this method, the transport coefficients are evaluated as the long time limit of the slope of generalized mean-squared displacement functions. Over 350 simulated state points cover the entire fluid region from the low density gas to the compressed liquid close to the freezing line in the reduced temperature range between $T^* = 0.7$ close to the triple point to $T^* = 6.0$ (about 4.5 times the critical temperature). By using more particles, larger cutoff radii and much longer simulation runs than considered before in conventional simulation work, the present simulation data for the transport coefficients are significantly more accurate than in previous studies. The uncertainties of the self-diffusion data are estimated to be ± 0.5 % in the gas region and ± 1 % in the liquid region, while the viscosity data have higher uncertainties of ± 3 % at liquid densities, increasing up to ± 10 % at low density gaseous states. The bulk viscosity data have uncertainties of 5 %, increasing up to 30 % at gaseous densities and in the vicinity of the critical point. The high accuracy of the present data is demonstrated by comparisons with literature data of other research groups. As a by-product of the long simulations, time-correlation functions of the thermodynamic fluxes and precise data for the thermodynamic state variables pressure, internal energy, isochoric heat capacity, thermal pressure coefficient and zero frequency speed of sound were obtained. The extensive simulations were enabled by well optimized simulation and analysis software and the availability of large computational resources on high performance parallel computers.

For the bulk viscosity, a large enhancement was found in the supercritical region, similar to that known for the thermal conductivity. However, the observed enhancement for the bulk viscosity extends over a much wider range of fluid states and is even observed at 4.5 times the critical temperature. This previously unexplored behaviour of the bulk viscosity can be interpreted in terms of pressure fluctuation

autocorrelation functions. It turns out that the enhancement is caused by extremely slowly decaying pressure fluctuations in this state region.

An additional series of simulations on the close-critical isotherm $T^* = 1.35$ characterizes the thermal conductivity in the vicinity of the critical point. An enhancement in the vicinity of the critical density is observed, but the effect is much weaker than the enhancement of the bulk viscosity.

With the accurate and comprehensive data, coherent insights into the nature of the transport coefficients from previously little explored view angles are possible. The translational-translational, translational-configurational and configurational-configurational viscosity contributions are resolved over the whole range of fluid states and their characteristic dependence on temperature and density is described. Moreover, the analysis of the correlation functions of the thermodynamic fluxes reveals aspects of the transport mechanisms on the molecular scale. For example, it is shown that the formation of bound states has an influence on the behaviour of the self-diffusion coefficient, the viscosity and the bulk viscosity at low temperature gaseous states.

Finally, the transport coefficients are discussed within the relaxation time concept based on the work of Zwanzig and Mountain on the elastic moduli of fluids. In this concept, the transport coefficients are expressed as products of moduli and relaxation times. Moduli are related to the initial values of the correlation functions of the thermodynamic fluxes, while relaxation times are the normalized integrals of the correlation functions. Based on the subdivision of the transport coefficients, an extension of the relaxation time concept is suggested by introducing separate relaxation times for every viscosity contribution. Data for the moduli and relaxation times are derived from the simulation results and their behaviour in the fluid region is characterized. It is shown how the density and temperature dependence of the transport coefficients arises in the relaxation time concept.

Appendix

A Reduced Quantities

In statistical thermodynamics, macroscopic properties are usually given in reduced from. Since the Lennard-Jones potential

$$u(r) = 4\varepsilon \left[\left(\frac{\sigma}{r} \right)^{12} - \left(\frac{\sigma}{r} \right)^{6} \right] \tag{A.1}$$

has the form

$$u(r) = \varepsilon f(\sigma/r) \quad , \tag{A.2}$$

a principle of corresponding states for thermodynamic state variables and transport coefficients applies. Any macroscopic property may be written in dimensionless form by using the two potential parameters ε and σ, the Boltzmann constant k and the particle mass m as reducing parameters. All quantities are scaled on the same order of magnitude ($\approx \mathcal{O}(1)$) in the reduced representation. Reduced quantities are denoted by the superscript '*'.

Definition of reduced quantities:

Length: $\qquad\qquad\qquad\qquad L^* = \dfrac{L}{\sigma}$

Time: $\qquad\qquad\qquad\qquad t^* = t\,\dfrac{\sqrt{\varepsilon/m}}{\sigma}$

Velocity: $\qquad\qquad\qquad\quad \boldsymbol{v}^* = \boldsymbol{v}\,\sqrt{\dfrac{m}{\varepsilon}}$

Temperature: $\qquad\qquad\quad T^* = \dfrac{kT}{\varepsilon}$

Volume: $\qquad\qquad\qquad\quad V^* = \dfrac{V}{\sigma^3}$

Particle density: $\qquad\qquad \rho^* = \rho\sigma^3$

Pressure: $\qquad\qquad\qquad\; p^* = \dfrac{p\sigma^3}{\varepsilon}$

Shear stress: $\qquad\qquad\quad\; \tau^* = \dfrac{\tau\sigma^3}{\varepsilon}$

Second virial coefficient: $\quad B^* = \dfrac{B}{\sigma^3}$

Energy: $\qquad$ $E^* = \dfrac{E}{\varepsilon}$

Isochoric heat capacity: $\qquad$ $C_{\mathrm{V}}^* = \dfrac{C_{\mathrm{V}}}{k}$

Heat flux: $\qquad$ $\boldsymbol{J}^{\mathrm{q}*} = \boldsymbol{J}^{\mathrm{q}} \, \dfrac{\sigma^3}{\varepsilon} \sqrt{\dfrac{m}{\varepsilon}}$

Energy flux: $\qquad$ $\boldsymbol{J}^{\mathrm{e}*} = \boldsymbol{J}^{\mathrm{e}} \, \dfrac{\sigma^3}{\varepsilon} \sqrt{\dfrac{m}{\varepsilon}}$

Isentropic compressibility: $\qquad$ $\beta_{\mathrm{S}}^* = \beta_{\mathrm{S}} \, \dfrac{\sigma^3}{\varepsilon}$

Thermal expansion coefficient: $\qquad$ $\alpha_{\mathrm{p}}^* = \alpha_{\mathrm{p}} \, \dfrac{k}{\epsilon}$

Speed of sound: $\qquad$ $w^* = w \, \sqrt{\dfrac{m}{\varepsilon}}$

Self-diffusion coefficient: $\qquad$ $D^* = D \, \dfrac{\sqrt{m/\varepsilon}}{\sigma}$

Viscosity: $\qquad$ $\eta^* = \eta \, \dfrac{\sigma^2}{\sqrt{m\epsilon}}$

Bulk viscosity: $\qquad$ $\eta_{\mathrm{b}}^* = \eta_{\mathrm{b}} \, \dfrac{\sigma^2}{\sqrt{m\epsilon}}$

Thermal conductivity: $\qquad$ $\lambda^* = \lambda \, \dfrac{\sigma^2}{k} \sqrt{\dfrac{m}{\varepsilon}}$

Thermal Modulus: $\qquad$ $\Theta^* = \Theta \, \dfrac{\sigma^3}{k} \dfrac{m}{\epsilon}$

B Dilute Gas Transport Coefficients

In the limit of zero density, the transport coefficients for spherical symmetric potential functions are given in terms of the Chapman-Enskog solution to the Boltzmann equation. Since this solution method is quite long and involved, only a brief outline and the results for the transport coefficients are presented in this appendix. A detailed treatment of this subject is for example given in the book of Hirschfelder et al. [88].

The Boltzmann equation is an integro-differential equation for the one particle nonequilibrium distribution function $f^{(1)}(\boldsymbol{r}, \boldsymbol{v}, t)$, which is the probability of finding a particle with the velocity $\boldsymbol{v}$ at time t at the position $\boldsymbol{r}$. This distribution function is required to calculate the zero density transport coefficients. The Chapman-Enskog method is based on a perturbation technique, in which the distribution function $f^{(1)}(\boldsymbol{r}, \boldsymbol{v}, t)$ is expanded around the equilibrium solution of the Boltzmann equation. When this series is truncated after the first correction term, the solution is conform with the macroscopic Navier-Stokes equations. The first order correction term is then related to the equilibrium solution by a perturbing function, which is determined only approximately. The transport coefficients are obtained as series expansions in terms of Sonine polynomials. These expansions usually converge rapidly so that only a few terms need to be considered to determine the transport coefficients accurately.

The expressions for the product of the self-diffusion coefficient and density, viscosity and thermal conductivity up to the second order terms read

$$(D\rho)_0(T) = \frac{3}{8}\sqrt{\frac{kT}{m\pi}}\frac{f_{\mathrm{D}\rho}}{\sigma^2 \Omega^{(1,1)*}} \quad , \tag{B.1}$$

where

$$f_{D\rho} = \frac{1}{1 - \Delta} \tag{B.2}$$

$$\Delta = \frac{(6C^* - 5)^2}{55 - 12B^* + 16A^*} \tag{B.3}$$

with the abbreviations

$$A^* = \frac{\Omega^{(2,2)*}}{\Omega^{(1,1)*}} \tag{B.4}$$

$$B^* = \frac{5\Omega^{(1,2)*} - 4\Omega^{(1,3)*}}{\Omega^{(1,1)*}} \tag{B.5}$$

$$C^* = \frac{\Omega^{(1,2)*}}{\Omega^{(1,1)*}} \quad , \tag{B.6}$$

$$\eta_0(T) = \frac{5}{16}\sqrt{\frac{mkT}{\pi}}\frac{f_\eta}{\sigma^2\Omega^{(2,2)*}} \quad , \tag{B.7}$$

where

$$f_\eta = 1 + \frac{b_{12}^2}{b_{11}b_{22} - b_{12}^2} \tag{B.8}$$

with

$$b_{11} = 4\Omega^{(2,2)*} \tag{B.9}$$

$$b_{12} = 7\Omega^{(2,2)*} - 8\Omega^{(2,3)*} \tag{B.10}$$

$$b_{22} = \frac{301}{12}\Omega^{(2,2)*} - 28\Omega^{(2,3)*} + 20\Omega^{(2,4)*} \tag{B.11}$$

and

$$\lambda_0(T) = \frac{25}{32}\sqrt{\frac{mkT}{\pi}}\frac{c_V}{m}\frac{f_\lambda}{\sigma^2\Omega^{(2,2)*}} \quad , \tag{B.12}$$

where

$$f_\lambda = 1 + \frac{a_{12}^2}{a_{11}a_{22} - a_{12}^2} \tag{B.13}$$

with

$$a_{11} = 4\Omega^{(2,2)*} = b_{11} \tag{B.14}$$

$$a_{12} = 7\Omega^{(2,2)*} - 8\Omega^{(2,3)*} = b_{12} \tag{B.15}$$

$$a_{22} = \frac{77}{4}\Omega^{(2,2)*} - 28\Omega^{(2,3)*} + 20\Omega^{(2,4)*} \quad . \tag{B.16}$$

The bulk viscosity vanishes in the zero density limit for spherical symmetric potential functions. This can be derived from the Green-Kubo integral formula for bulk viscosity [141]. In the molecular dynamics ensemble, the bulk viscosity is given by

$$\eta_b = \frac{V}{kT}\int_0^\infty \langle \delta p(t)\delta p(0)\rangle \quad . \tag{B.17}$$

In the zero density limit, the configurational contribution to the energy vanishes and the total energy is purely translational. In the molecular dynamics ensemble, the total energy is a constant of motion. Thus, the kinetic energy and also the temperature are constants of motion. Since the pressure is given by the ideal gas law $pV = NkT$, it is also a constant of motion and the pressure fluctuations δp vanish. Therefore, the bulk viscosity becomes zero.

The quantities $\Omega^{(i,j)*}$ depend on the intermolecular potential and are called reduced collision integrals since they describe the details of a collision between two molecules. In general, they are complicated integrals over the dynamics of binary collisions and must be calculated numerically. For the Lennard-Jones potential, several authors have computed the reduced collision integrals and published tabulated data, see for example [88, 107, 108, 133, 214]. Throughout this work, the correlations for $\Omega^{(1,1)*}$ and $\Omega^{(2,2)*}$ published by Fokin et al. [51] are used. Fokin et al. fitted their correlations to the tabulated data for the reduced collision integrals $\Omega^{(1,1)*}$, $\Omega^{(2,2)*}$, $\Omega^{(1,2)*}$, $\Omega^{(1,3)*}$ and $\Omega^{(2,3)*}$ published by Klein and Smith [107], Klein et al. [108] and Viehland et al. [214]. The original correlations are given for the general (m-6) Lennard-Jones potential

$$u(r) = \frac{\varepsilon\,m}{m-6} \left(\frac{m}{6}\right)^{6/(m-6)} \left[\left(\frac{\sigma}{r}\right)^m - \left(\frac{\sigma}{r}\right)^6\right] \tag{B.18}$$

as functions of the potential parameter m and reduced temperature T^*. Since only the Lennard-Jones (12-6) potential is used in this work, the m-dependent terms in the correlations can explicitly be evaluated. For the Lennard-Jones (12-6) potential, the correlations take the form

$$\ln \Omega^{(1,1)*} = -\frac{1}{6}\ln T^* + \sum_{i=1}^{6} a_i^{(1,1)*} \cdot (T^*)^{-(i-1)/2} \tag{B.19}$$

for $\Omega^{(1,1)*}$ and

$$\ln \Omega^{(2,2)*} = -\frac{1}{6}\ln T^* + \ln\frac{17}{18} + \sum_{i=1}^{6} a_i^{(2,2)*} \cdot (T^*)^{-(i-1)/2} \tag{B.20}$$

for $\Omega^{(2,2)*}$. The coefficients $a_i^{(1,1)*}$ and $a_i^{(2,2)*}$ are given in Table B.1. Figure B.1 shows the performance of the correlations for the five collisions integrals. The correlations represent the five collision integrals over the whole temperature range between $T^* = 0.7$ and 1000 within 0.5 %. Both integrals, $\Omega^{(1,1)*}$ and $\Omega^{(2,2)*}$, which appear in the first order terms, are represented within 0.3 % over the temperature range between $T^* = 0.7$ and 6.0 considered in this work.

Table B.1. Coefficients of the collision integral correlation of Fokin et al. [51] for the Lennard-Jones potential.

i	$a_{\mathrm{i}}^{(1,1)*}$	$a_{\mathrm{i}}^{(2,2)*}$
1	0.125431	0.310810
2	-0.167256	-0.171211
3	-0.265865	-0.715805
4	1.59760	2.48678
5	-1.19088	-1.78317
6	0.264833	0.394405

The collision integrals $\Omega^{(1,2)*}$, $\Omega^{(1,3)*}$, $\Omega^{(2,3)*}$ and $\Omega^{(2,4)*}$ occurring in the second-order terms for $D\rho$, η and λ are obtained from the recurrence relation [88]

$$\Omega^{(\mathrm{i,j+1})*} = \Omega^{(\mathrm{i,j})*} + \frac{1}{j+2}T^*\frac{\partial\Omega^{(\mathrm{i,j})*}}{\partial T^*} \quad . \tag{B.21}$$

The correction factors $f_{\mathrm{D}\rho}$, f_η and f_λ are shown as a function of temperature in Figure B.2. They are smaller than 0.1 % up to $T^* = 1.5$. Above this temperature, they increase, but never exceed 0.7 % for the product $D^*\rho^*$ and the viscosity and 1 % for the thermal conductivity in the whole temperature range between $T^* = 0.7$ and 6.0. Viehland et al. [215] showed that higher corrections up to fifth order add less than 0.02 % to the viscosity and 0.05 % to the thermal conductivity in this temperature range. Therefore, it is sufficient to include the second-order terms for the purposes of this work.
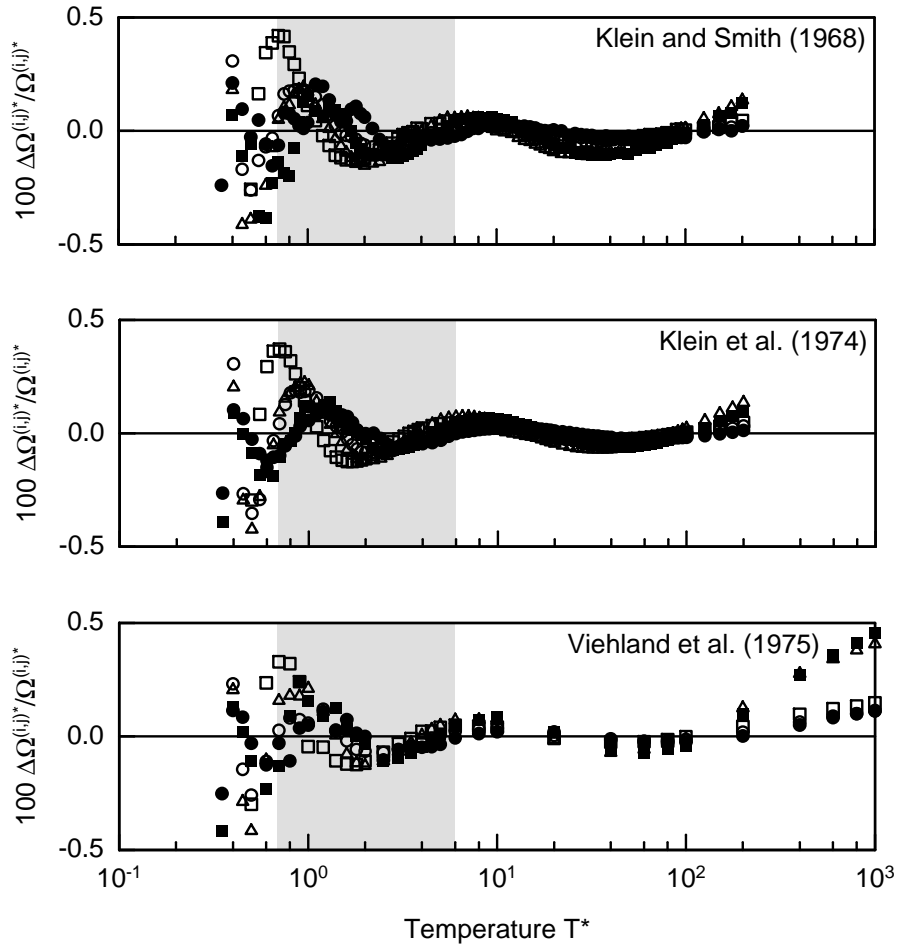
Figure B.1. Percentage deviations $100\,\Delta\Omega^{(i,j)*}/\Omega^{(i,j)*} = 100\,(\Omega^{(i,j)*} - \Omega^{(i,j)*}_{\mathrm{corr}})/\Omega^{(i,j)*}_{\mathrm{corr}}$ between tabulated data of the collision integrals $\Omega^{(1,1)*}$ ($\bullet$), $\Omega^{(2,2)*}$ ($\blacksquare$), $\Omega^{(1,2)*}$ ($\circ$), $\Omega^{(1,3)*}$ ($\square$) and $\Omega^{(2,3)*}$ ($\triangle$) published by Klein and Smith [107], Klein et al. [108] and Viehland et al. [214] and values calculated from the correlation of Fokin et al. [51] as a function of temperature.
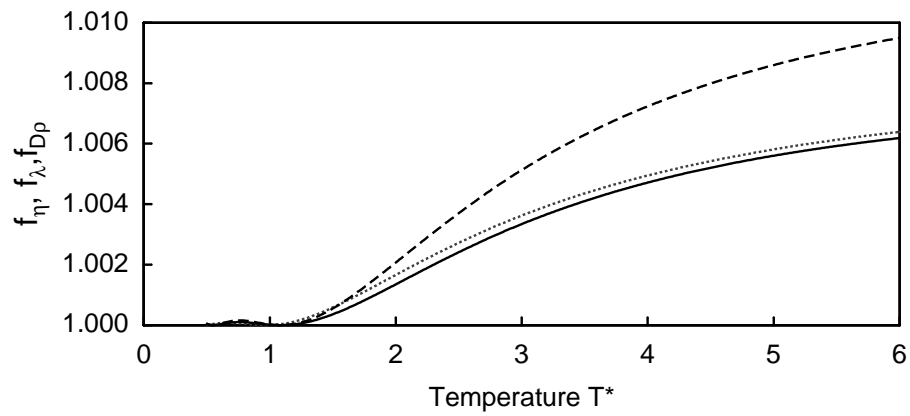
Figure B.2. The correction factors up to second-order $f_{\mathrm{D}\rho}$ (——), f_η (··········) and f_λ (----) as a function of temperature for the Lennard-Jones potential as calculated from the correlation of Fokin et al. [51].

C Statistical Thermodynamics in the Molecular Dynamics Ensemble

In Section 2.3, the molecular expressions for the thermodynamic state variables temperature T, internal energy E, pressure p, isochoric heat capacity C_{V}, isothermal pressure coefficient γ_{V} and zero frequency speed of sound w_0 in the $NVE\boldsymbol{MG}$-ensemble were presented in Table 2.1 without derivation. This appendix describes the derivation in detail since the mathematics is involved and the expressions for the pressure derivatives in the $NVE\boldsymbol{MG}$-ensemble have not yet been published. The essential step in the derivation, the Laplace-transform technique, was first outlined by Pearson et al. [171] for the microcanonical ensemble and later used by Cağin and Ray [28], Lustig [126, 127] and Ray and Zhang [184] to obtain expressions for thermodynamic state variables in the $NVE\boldsymbol{M}$- and $NVE\boldsymbol{MG}$-ensembles. This appendix follows these works without explicitly referring to them at the individual steps of the lengthy calculations.

Starting point for the derivation is the fundamental equation of state in the molecular dynamics ensemble $S = S(N, V, E, \boldsymbol{M}, \boldsymbol{G})$. The macroscopic entropy of the system is related to the phase space volume

$$
\Omega \;=\; \frac{1}{C_{\mathrm{N}}} \iint \Theta(E - H)\, \delta\!\left(\boldsymbol{M} - \sum_{i=1}^{N} \boldsymbol{p}_{\mathrm{i}}\right) \cdot
$$
$$
\cdot \delta\!\left(\boldsymbol{G} - t\sum_{i=1}^{N} \boldsymbol{p}_{\mathrm{i}} + \sum_{i=1}^{N} m\boldsymbol{r}_{\mathrm{i}}\right) \mathrm{d}\boldsymbol{r}_{\mathrm{N}}\mathrm{d}\boldsymbol{p}_{\mathrm{N}} \qquad (\text{C.1})
$$

by the entropy postulate

$$
S(N, V, E, \boldsymbol{M}, \boldsymbol{G}) = k \ln \Omega(N, V, E, \boldsymbol{M}, \boldsymbol{G}) \quad . \tag{C.2}
$$

The closely related phase space density is obtained from the phase space volume by differentiation with respect to energy

$$
\omega \;=\; \frac{\partial \Omega}{\partial E} \;=\; \frac{1}{C_{\mathrm{N}}} \iint \delta(E - H)\, \delta\!\left(\boldsymbol{M} - \sum_{i=1}^{N} \boldsymbol{p}_{\mathrm{i}}\right) \cdot
$$
$$
\cdot \delta\!\left(\boldsymbol{G} - t\sum_{i=1}^{N} \boldsymbol{p}_{\mathrm{i}} + \sum_{i=1}^{N} m\boldsymbol{r}_{\mathrm{i}}\right) \mathrm{d}\boldsymbol{r}_{\mathrm{N}}\mathrm{d}\boldsymbol{p}_{\mathrm{N}} \qquad (\text{C.3})
$$

and the ensemble average of an arbitrary phase variable is given by

$$\langle A \rangle = \frac{1}{\omega C_N} \iint A(\{\boldsymbol{r}_N\}, \{\boldsymbol{p}_N\}) \, \delta(E - H) \, \delta\left(\boldsymbol{M} - \sum_{i=1}^{N} \boldsymbol{p}_i\right) \cdot$$
$$\cdot \delta\left(\boldsymbol{G} - t \sum_{i=1}^{N} \boldsymbol{p}_i + \sum_{i=1}^{N} m\boldsymbol{r}_i\right) \mathrm{d}\boldsymbol{r}_N \mathrm{d}\boldsymbol{p}_N \quad . \quad \text{(C.4)}$$

In these integrals, the unit step function and δ-function ensure that only those phase points contribute to the value of the integral which are compatible with the mechanical constraints imposed on the system. The integration over the momenta extends from $-\infty$ to $+\infty$ and the integration over the coordinates covers the volume of the system.

A systematic representation of the thermodynamic state variables can be constructed by introducing the abbreviation

$$\Omega_{mn} = \frac{1}{\omega} \frac{\partial^{m+n}\Omega}{\partial E^m \partial V^n} \tag{C.5}$$

for derivatives of the phase space volume with respect to internal energy and volume. The quantities Ω_{mn} were termed phase space functions by Lustig. In a first step, the thermodynamic state variables are expressed in terms of phase space functions by standard relations between the thermodynamic state variables [29].

The relation for the thermodynamic temperature is established by using its definition,

$$\frac{1}{T} = \left(\frac{\partial S}{\partial E}\right)_V = \frac{\partial}{\partial E}(k \ln \Omega) = k \frac{1}{\Omega} \frac{\partial \Omega}{\partial E} = k \frac{\omega}{\Omega} \quad , \tag{C.6}$$

so that

$$kT = \frac{\Omega}{\omega} = \Omega_{00} \quad . \tag{C.7}$$

Similarly, the relation

$$\frac{p}{T} = \left(\frac{\partial S}{\partial V}\right)_E \tag{C.8}$$

yields

$$p = T \frac{\partial}{\partial V}(k \ln \Omega) = kT \frac{1}{\Omega} \frac{\partial \Omega}{\partial V} = kT \frac{\omega}{\Omega} \frac{1}{\omega} \frac{\partial \Omega}{\partial V} = \Omega_{01} \quad . \tag{C.9}$$

The expression for the isochoric heat capacity is obtained by

$$C_V^{-1} = \left(\frac{\partial T}{\partial E}\right)_V = \frac{1}{k} \frac{\partial}{\partial E}\left[\frac{\Omega}{\omega}\right] = \frac{1}{k}\left[\frac{1}{\omega} \frac{\partial \Omega}{\partial E} - \frac{\Omega}{\omega^2} \frac{\partial^2 \Omega}{\partial E^2}\right] = \frac{1}{k}(1 - \Omega_{00}\Omega_{20}) \,, \quad \text{(C.10)}$$

where it has been used that

$$\Omega_{10} = 1 \tag{C.11}$$

and

$$\frac{\partial^2 \Omega}{\partial E^2} = \frac{\partial \omega}{\partial E} \quad . \tag{C.12}$$

Before expressing the pressure derivatives by phase space functions, it is instructive to derive two general relations between phase space functions. A derivative with respect to energy can be written as

$$\frac{\partial \Omega_{mn}}{\partial E} = \frac{\partial}{\partial E} \left(\frac{1}{\omega} \frac{\partial^{m+n} \Omega}{\partial E^m \partial V^n} \right) = -\frac{1}{\omega^2} \frac{\partial \omega}{\partial E} \frac{\partial^{m+n} \Omega}{\partial E^m \partial V^n} + \frac{1}{\omega} \frac{\partial^{m+1+n} \Omega}{\partial E^{m+1} \partial V^n} \tag{C.13}$$

so that

$$\frac{\partial \Omega_{mn}}{\partial E} = \Omega_{m+1,n} - \Omega_{20} \Omega_{mn} \tag{C.14}$$

follows. A similar derivation for a volume derivative

$$\frac{\partial \Omega_{mn}}{\partial V} = \frac{\partial}{\partial V} \left(\frac{1}{\omega} \frac{\partial^{m+n} \Omega}{\partial E^m \partial V^n} \right) = -\frac{1}{\omega^2} \frac{\partial^2 \Omega}{\partial E \partial V} \frac{\partial^{m+n} \Omega}{\partial E^m \partial V^n} + \frac{1}{\omega} \frac{\partial^{m+n+1} \Omega}{\partial E^m \partial V^{n+1}} \tag{C.15}$$

leads to

$$\frac{\partial \Omega_{mn}}{\partial V} = \Omega_{m,n+1} - \Omega_{11} \Omega_{mn} \quad . \tag{C.16}$$

When Eq. (C.14) is applied to the energy derivative of the pressure, the expression of the thermal pressure coefficient can be established as

$$\gamma_V = \left(\frac{\partial p}{\partial T} \right)_V = \left(\frac{\partial p}{\partial E} \right)_V \left(\frac{\partial E}{\partial T} \right)_V = k \frac{\Omega_{11} - \Omega_{20} \Omega_{01}}{1 - \Omega_{00} \Omega_{20}} \quad . \tag{C.17}$$

Another state variable of interest is the zero frequency speed of sound since it is related to the zero frequency bulk modulus (see Chapter 7). The zero frequency speed of sound is the derivative of the pressure with respect to mass density at constant entropy

$$w_0 = \sqrt{\left(\frac{\partial p}{\partial \rho_m} \right)_S} = \sqrt{-\frac{V}{\rho_m} \left(\frac{\partial p}{\partial V} \right)_S} \tag{C.18}$$

and

$$\beta_S^{-1} = -V \left(\frac{\partial p}{\partial V} \right)_S \tag{C.19}$$

is the inverse of the isentropic compressibility β_S. The derivative at constant entropy must be expressed by derivatives at constant energy and constant volume. Using the general relation for partial derivatives [29, p. 475]

$$\left(\frac{\partial f}{\partial y}\right)_x = \left(\frac{\partial f}{\partial y}\right)_z + \left(\frac{\partial f}{\partial z}\right)_y \left(\frac{\partial z}{\partial y}\right)_x \quad , \tag{C.20}$$

it is found that

$$\left(\frac{\partial p}{\partial V}\right)_E = \left(\frac{\partial p}{\partial V}\right)_S + \left(\frac{\partial p}{\partial S}\right)_V \left(\frac{\partial S}{\partial V}\right)_E \quad . \tag{C.21}$$

Inserting Eq. (C.8) and rearranging the pressure derivative with respect to energy leads to

$$\left(\frac{\partial p}{\partial V}\right)_S = \left(\frac{\partial p}{\partial V}\right)_E - \frac{p}{T}\left(\frac{\partial p}{\partial E}\right)_V \left(\frac{\partial E}{\partial S}\right)_V = \left(\frac{\partial p}{\partial V}\right)_E - p\left(\frac{\partial p}{\partial E}\right)_V \quad . \tag{C.22}$$

Applying Eqs. (C.9), (C.14) and (C.16) to express the pressure and the pressure derivatives by phase space functions the result

$$\beta_S^{-1} = -V\left(\frac{\partial p}{\partial V}\right)_S = V[\Omega_{01}(2\Omega_{11} - \Omega_{01}\Omega_{20}) - \Omega_{02}] \tag{C.23}$$

is found for the isentropic compressibility. With these quantities, other thermodynamic state variables of practical interest can be calculated by thermodynamic relations. The expressions for them are stated here for completeness and without derivation. These are the isothermal compressibility

$$\beta_T^{-1} = \beta_S^{-1} - \frac{TV\gamma_V^2}{C_V} \quad , \tag{C.24}$$

the isobaric heat capacity

$$C_p = \frac{C_V\beta_T}{\beta_S} \tag{C.25}$$

and the Joule-Thompson coefficient

$$\mu_{JT} = V\frac{T\gamma_V\beta_T - 1}{C_p} \quad . \tag{C.26}$$

This completes the expressions for thermodynamic state variables in terms of phase space functions.

In the second step, the phase space functions are related to ensemble averages of instantaneous phase variables. In order to simplify the expression for the phase

space volume, the integrals over the constants of motion, the total momentum of the system and the centre of mass, are evaluated and the integration over the remaining momenta is carried out. For the performance of the integrals over the total momentum of the system and the centre of mass, the six respective coordinates must explicitly appear as independent variables. This is achieved by a transformation from Cartesian coordinates and momenta to Jacobi coordinates and momenta. For N spherical particles the Jacobi coordinates and momenta are related to the corresponding Cartesian quantities by

$$\boldsymbol{R}_\alpha = \frac{\sum\limits_{i=1}^{\alpha} m_i \boldsymbol{r}_i}{\sum\limits_{i=1}^{\alpha} m_i} - \boldsymbol{r}_{\alpha+1} \quad \text{with} \quad 1 \leq \alpha \leq N \quad \text{and} \quad \boldsymbol{r}_{N+1} = \boldsymbol{0} \tag{C.27}$$

$$\boldsymbol{P}_\alpha = \frac{m_{\alpha+1}}{M_1^{\alpha+1}} \sum\limits_{i=1}^{\alpha} \boldsymbol{p}_i - \frac{M_1^\alpha}{M_1^{\alpha+1}} \boldsymbol{p}_{\alpha+1} \quad \text{with} \quad 1 \leq \alpha \leq N-1 \quad, \tag{C.28}$$

and

$$\boldsymbol{P}_N = \sum\limits_{i=1}^{N} \boldsymbol{p}_i \tag{C.29}$$

is the total momentum of the system. M_i^j is defined by

$$M_i^j = \sum\limits_{k=i}^{j} m_k \quad \text{with} \quad i \leq j \quad \text{and} \quad 1 \leq i,j,k \leq N \quad . \tag{C.30}$$

Jacobi coordinates are a generalization of the usual coordinates of the centre of mass and relative coordinates of a two particle system. The the centre of mass and total momentum of the system appear as the Nth Jacobi position vector $\boldsymbol{R}_N$ and N^{th} Jacobi momentum vector $\boldsymbol{P}_N$. In Jacobi coordinates, the kinetic energy of the system becomes

$$K = \sum\limits_{i=1}^{N} \frac{\boldsymbol{p}_i^2}{2m_i} = \sum\limits_{\alpha=1}^{N-1} \frac{\boldsymbol{P}_\alpha^2}{2\mu_\alpha} + \frac{\boldsymbol{P}_N^2}{2\mu_N} \quad, \tag{C.31}$$

in which the reduced masses μ_i are defined by

$$\mu_\alpha = \frac{m_{\alpha+1} M_1^\alpha}{M_1^{\alpha+1}} \quad \text{for} \quad 1 \leq \alpha \leq N-1 \quad \text{and} \quad \mu_N = M_1^N = Nm \quad . \tag{C.32}$$

The reduced masses satisfy the relation

$$\prod\limits_{\alpha=1}^{N-1} \mu_\alpha = \frac{\prod\limits_{\alpha=1}^{N-1} (m_{\alpha+1} M_1^\alpha)}{\prod\limits_{\alpha=1}^{N-1} M_1^{\alpha+1}} = \frac{M_1^1 \prod\limits_{\alpha=1}^{N-1} m_{\alpha+1}}{M_1^N} = \frac{M_1^1 \prod\limits_{\alpha=2}^{N} m_\alpha}{\mu_N} = \frac{\prod\limits_{\alpha=1}^{N} m_\alpha}{\mu_N} \quad . \tag{C.33}$$

When the Jacobi coordinates and momenta are substituted into Eq. (C.1), the expression for the phase space volume reads

$$\Omega = \frac{1}{C_N} \iint \Theta\left(E - \sum_{\alpha=1}^{N-1} \frac{\boldsymbol{P}_\alpha^2}{2\mu_\alpha} - \frac{\boldsymbol{P}_N^2}{2\mu_N} - U\right) \delta(\boldsymbol{M} - \boldsymbol{P}_N) \cdot$$

$$\cdot \delta(\boldsymbol{G} - \boldsymbol{P}_N t + Nm\boldsymbol{R}_N)\, \mathrm{d}\boldsymbol{R}_N \mathrm{d}\boldsymbol{P}_N \quad . \tag{C.34}$$

First, the integration over the total momentum of the system $\boldsymbol{P}_N$ is carried out by using the property of δ-functions,

$$f(t_0) = \int_{-\infty}^{\infty} \delta(t - t_0) f(t) \mathrm{d}t \quad , \tag{C.35}$$

so that

$$\Omega = \frac{1}{C_N} \iint \Theta\left(E - \frac{\boldsymbol{M}^2}{2Nm} - \sum_{\alpha=1}^{N-1} \frac{\boldsymbol{P}_\alpha^2}{2\mu_\alpha} - U\right) \cdot$$

$$\cdot \delta(\boldsymbol{G} - \boldsymbol{M}t + Nm\boldsymbol{R}_N)\, \mathrm{d}\boldsymbol{R}_N \mathrm{d}\boldsymbol{P}_{N-1} \tag{C.36}$$

is obtained. Integration over the centre of mass coordinate $\boldsymbol{R}_N$ yields

$$\Omega = \frac{1}{C_N} \iint \Theta\left(E - \frac{\boldsymbol{M}^2}{2Nm} - \sum_{\alpha=1}^{N-1} \frac{\boldsymbol{P}_\alpha^2}{2\mu_\alpha} - U\right) \mathrm{d}\boldsymbol{R}_{N-1} \mathrm{d}\boldsymbol{P}_{N-1} \tag{C.37}$$

For the evaluation of the integrals over the remaining Jacobi momenta, the phase space volume is Laplace transformed with respect to energy. Using the correspondence

$$\mathcal{L}_E\{\Theta(E)\} = \frac{1}{s} \tag{C.38}$$

and the translation property of Laplace-transforms [1, p. 1021]

$$\mathcal{L}_E\{\Omega\} = \frac{1}{C_N} \iint \frac{1}{s} \exp\left\{-s\left(U + \frac{\boldsymbol{M}^2}{2Nm} + \sum_{\alpha=1}^{N-1} \frac{\boldsymbol{P}_\alpha^2}{2\mu_\alpha}\right)\right\} \mathrm{d}\boldsymbol{P}_{N-1}\, \mathrm{d}\boldsymbol{R}_{N-1} \tag{C.39}$$

is obtained, where the integrals over the remaining $N - 1$ Jacobi momenta are integrals over Gaussian exponential functions. When these integrals are evaluated, the result for the phase space volume in reciprocal Laplace space is

$$\mathcal{L}_E\{\Omega\} = \frac{1}{C_0} \iint \left(\frac{1}{s}\right)^{(3N-3)/2+1} \exp\left\{-s\left(U + \frac{\boldsymbol{M}^2}{2Nm}\right)\right\} \mathrm{d}\boldsymbol{R}_{N-1} \quad , \tag{C.40}$$

with

$$C_0 = C_N N m / \left[(2\pi)^{(3N-3)/2} m^{3N/2} \right] \quad . \tag{C.41}$$

Application of the inverse Laplace transform by using the correspondence [1, p. 1022]

$$\mathcal{L}_{\mathrm{E}} \left\{ \frac{E^{x-1}}{\Gamma(x)} \right\} = \left(\frac{1}{s} \right)^x \tag{C.42}$$

yields

$$\Omega = \frac{1}{C_0} \frac{1}{\Gamma([3N-3]/2 + 1)} \int \left(E - \frac{\boldsymbol{M}^2}{2Nm} - U \right)^{(3N-3)/2}$$
$$\Theta \left(E - \frac{\boldsymbol{M}^2}{2Nm} - U \right) \mathrm{d}\boldsymbol{R}_{\mathrm{N-1}} \quad . \tag{C.43}$$

Since molecular dynamics simulations are carried out at $\boldsymbol{M} = \boldsymbol{0}$, i.e. the system is at rest, the phase space volume becomes

$$\Omega = \frac{1}{C_0} \frac{1}{\Gamma([3N-3]/2 + 1)} \int (E - U)^{(3N-3)/2} \, \Theta(E - U) \, \mathrm{d}\boldsymbol{R}_{\mathrm{N-1}} \quad . \tag{C.44}$$

For every real system, the kinetic energy $K = E - U$ is positive, so that the unit step function is always equal to one. Thus, the simplified expression for the phase space density is found by differentiation with respect to energy

$$\omega = \frac{\partial \Omega}{\partial E} = \frac{1}{C_0} \frac{1}{\Gamma([3N-3]/2)} \int (E - U)^{(3N-3)/2-1} \, \Theta(E - U) \, \mathrm{d}\boldsymbol{R}_{\mathrm{N-1}} \quad . \tag{C.45}$$

If a phase variable A depends only on the N spatial coordinates $\{\boldsymbol{r}_{\mathrm{N}}\}$, Eq. (C.4) can be simplified in the same way as the phase space volume and density. In fact, it will be found later in this appendix that any phase variable required to calculate thermodynamic state variables depends only on powers of the kinetic energy of the system and on the configurational energy or volume derivatives of it. The latter two quantities depend only on the coordinates $\{\boldsymbol{r}_{\mathrm{N}}\}$ *per definitionem*. Since the total energy of the system is the sum of the kinetic and configurational energy and is constant in the $NVE\boldsymbol{M}\boldsymbol{G}$-ensemble, it follows that the kinetic energy also depends only on the coordinates

$$K = E - U(\{\boldsymbol{r}_N\}) = K(\{\boldsymbol{r}_N\}) \quad . \tag{C.46}$$

Therefore, it is always guaranteed that the phase variable A depends only on the coordinates $\{\boldsymbol{r}_{\mathrm{N}}\}$. After the transformation of the integral in Eq. (C.4) to Jacobi

momenta and coordinates, the integrations over the Jacobi momenta $\{\boldsymbol{P}_N\}$ and the centre of mass coordinate $\boldsymbol{R}_N$ in Eq. (C.4) can be carried out. The resulting expression for the ensemble average,

$$\langle A \rangle = \frac{1}{\omega C_N} \frac{1}{\Gamma([3N-3]/2)} \int A \, (E-U)^{(3N-3)/2-1} \, \Theta(E-U) \, \mathrm{d}\boldsymbol{R}_{N-1} \quad , \quad \text{(C.47)}$$

has the same structure as Eq. (C.45).

With these preparations, expressions for the phase space functions in terms of simple ensemble averages can be found by a simple procedure. Starting from Eq. (C.44), the derivatives of the phase space volume with respect to the independent variables E and V are calculated. By comparing the results of the differentiation with the general formula for an arbitrary ensemble average, Eq. (C.47), the expressions for the corresponding phase space functions Ω_{mn} are found. Ω_{mn} corresponds to $\langle A \rangle$ and A is to be identified by the comparison. For this comparison, the recurrence formula for the Γ-function [1, p. 256]

$$\Gamma(x+1) = x\Gamma(x) \tag{C.48}$$

is required.

Ω_{00} is found by comparing the equation for the phase space volume with the expression for the ensemble average:

$$\Omega_{00} = \frac{\Omega}{\omega} = \frac{2}{3N-3}(E - \langle U \rangle) = \frac{2}{3N-3}\langle K \rangle \quad . \tag{C.49}$$

The first derivative of the phase space volume with respect to energy is the phase space density (C.3) so that the simple result

$$\Omega_{10} = 1 \tag{C.50}$$

follows. The comparison of the second derivative of the phase space volume with respect to energy,

$$\frac{\partial^2 \Omega}{\partial E^2} = \frac{1}{C_0} \frac{1}{\Gamma([3N-3]/2-1)} \int (E-U)^{(3N-3)/2-2} \Theta(E-U) \, \mathrm{d}\boldsymbol{R}_{N-1} \quad , \quad \text{(C.51)}$$

with Eq. (C.47) yields

$$\Omega_{20} = \left(\frac{3N-3}{2} - 1 \right) \langle K^{-1} \rangle \quad . \tag{C.52}$$

Before calculating volume derivatives, the coordinate transformation

$$\boldsymbol{R}_i = V^{1/3} \boldsymbol{R}_i' \tag{C.53}$$

is introduced in the expressions for the phase space volume

$$\Omega = \frac{1}{C_0} \frac{1}{\Gamma([3N-3]/2+1)} \int (E-U)^{(3N-3)/2} \, \Theta(E-U) \, V^{N-1} \mathrm{d}\boldsymbol{R}'_{\mathrm{N}-1} \qquad \text{(C.54)}$$

and the arbitrary ensemble average

$$\langle A \rangle = \frac{1}{\omega C_0} \frac{1}{\Gamma([3N-3]/2)} \int A \, (E-U)^{(3N-3)/2-1} \, \Theta(E-U) \, V^{N-1} \mathrm{d}\boldsymbol{R}'_{\mathrm{N}-1} \quad . \tag{C.55}$$

This transformation ensures that the integration limits do not depend on the volume of the system.

To find the expression for Ω_{01}, Ω_{02} and Ω_{11}, the first and second volume derivatives of the phase space volume

$$\frac{\partial \Omega}{\partial V} = \frac{1}{C_0} \frac{1}{\Gamma[(3N-3)/2+1]} \int \left[\frac{N-1}{V} (E-U)^{(3N-3)/2} \right.$$

$$\left. - \frac{3N-3}{2} (E-U)^{(3N-3)/2-1} \left(\frac{\partial U}{\partial V} \right) \right] V^{N-1} \, \Theta(E-U) \, \mathrm{d}\boldsymbol{R}'_{\mathrm{N}-1} \tag{C.56}$$

and

$$\frac{\partial^2 \Omega}{\partial V^2} = \frac{1}{C_0} \frac{1}{\Gamma[(3N-3)/2+1]} \int \left[-2 \frac{N-1}{V} \frac{3N-3}{2} (E-U)^{(3N-3)/2-1} \left(\frac{\partial U}{\partial V} \right) \right.$$

$$\left. - \frac{3N-3}{2} (E-U)^{(3N-3)/2-1} \left(\frac{\partial^2 U}{\partial V^2} \right) + \frac{N-1}{V} \frac{N-2}{V} (E-U)^{(3N-3)/2} \right.$$

$$\left. + \frac{3N-3}{2} \left[\frac{3N-3}{2} - 1 \right] (E-U)^{(3N-3)/2-2} \left(\frac{\partial U}{\partial V} \right)^2 \right] V^{N-1} \, \Theta(E-U) \, \mathrm{d}\boldsymbol{R}'_{\mathrm{N}-1} \tag{C.57}$$

as well as the mixed derivative

$$\frac{\partial^2 \Omega}{\partial E \partial V} = \frac{1}{C_0} \frac{1}{\Gamma[(3N-3)/2]} \int \left[\frac{N-1}{V} (E-U)^{(3N-3)/2-1} \right.$$

$$\left. - \left[\frac{3N-3}{2} - 1 \right] (E-U)^{(3N-3)/2-2} \left(\frac{\partial U}{\partial V} \right) \right] V^{N-1} \, \Theta(E-U) \, \mathrm{d}\boldsymbol{R}'_{\mathrm{N}-1} \tag{C.58}$$

are evaluated. When compared with Eq. (C.55), the results for the three phase space functions follow as

$$\Omega_{01} = \frac{N-1}{V} \frac{2}{3N-3} \langle K \rangle - \left\langle \frac{\partial U}{\partial V} \right\rangle \quad , \tag{C.59}$$

$$
\Omega_{02} \;=\; \frac{N-1}{V}\frac{N-2}{V}\frac{2}{3N-3}\langle K\rangle - \left\langle\frac{\partial^2 U}{\partial V^2}\right\rangle - 2\left\langle\frac{\partial U}{\partial V}\right\rangle\frac{N-1}{V}
$$

$$
+ \left(\frac{3N-3}{2}-1\right)\left\langle K^{-1}\left(\frac{\partial U}{\partial V}\right)^2\right\rangle \tag{C.60}
$$

and

$$
\Omega_{11} = \frac{N-1}{V} + \left(\frac{3N-3}{2}-1\right)\left\langle K^{-1}\frac{\partial U}{\partial V}\right\rangle \quad . \tag{C.61}
$$

The evaluation of the volume derivatives of the instantaneous configurational internal energy that appear in the expressions for the phase space functions was described in detail by Lustig [126, 127] and is therefore not repeated here. The results of this appendix are summarized in Table 2.1.

D Simulation Data for Thermodynamic State Variables and Transport Coefficients

Table D.1. Simulation data for thermodynamic state variables of the Lennard-Jones model fluid. The simulations extended over 2 million time steps if not denoted otherwise († 10 million time steps).

ρ^*	T^*	p^*	u^*	c_V^*	γ_V^*	w_0^*	$w_0'^*$
			$T^* = 0.7$				
0.85	0.699715	0.10929	-6.14344	2.6645	6.6152	5.6854	5.6344
0.8	0.699845	-0.52742	-5.81590	2.4924	5.4624	4.9184	4.7772
0.75	0.698757	-0.88032	-5.46771	2.3912	4.4282	4.0763	3.8381
0.015	0.701012	0.0089092	-0.194108	1.8678	0.017276	1.0397	0.98646
0.01	0.700092	0.0062938	-0.125982	1.7003	0.010903	1.0555	1.0213
0.005	0.700063	0.0033242	-0.0615707	1.5879	0.0052041	1.0677	1.0511
			$T^* = 0.8$				
0.85	0.800689	0.75578	-6.02904	2.5946	6.1965	5.9027	5.9096
0.8	0.801086	0.016217	-5.71692	2.4664	5.3032	5.1351	5.0573
0.75	0.801714	-0.43048	-5.37933	2.3380	4.3305	4.3787	4.2173
0.7	0.799703	-0.65740	-5.03496	2.3082	3.3716	3.4951	3.2337
0.03	0.806426	0.018395	-0.353324	2.0641	0.037251	1.0975	1.0047
0.025	0.803405	0.016074	-0.289370	2.0152	0.030441	1.1060	1.0302
0.02	0.801202	0.013474	-0.226853	1.7993	0.022770	1.1159	1.0568
0.015	0.800258	0.010575	-0.167169	1.6937	0.016390	1.1284	1.0852
0.01	0.800211	0.0073686	-0.110036	1.6270	0.010641	1.1350	1.1067
0.005	0.800415	0.0038423	-0.0545818	1.5597	0.0051502	1.1457	1.1318
			$T^* = 0.9$				
0.85	0.900526	1.3665	-5.92050	2.5642	5.9866	6.0839	6.1410
0.8	0.900832	0.52748	-5.62378	2.4167	5.0320	5.3448	5.3212
0.75	0.901804	-0.0069023	-5.29820	2.2915	4.1635	4.6239	4.5230
0.7	0.900372	-0.31756	-4.95892	2.2093	3.3518	3.8560	3.6743
0.65	0.902284	-0.44396	-4.62155	2.2807	2.4843	7.5197	2.6418
0.05	0.908833	0.031003	-0.534993	2.3804	0.069448	1.1526	1.0182
0.045	0.907587	0.029105	-0.479012	2.2714	0.060146	1.1525	1.0318
0.04	0.902939	0.026901	-0.418473	2.0898	0.050856	1.1677	1.0635
						Continued on next page.	

Continued from previous page.

ρ^*	T^*	p^*	u^*	c_V^*	γ_V^*	w_0^*	$w_0'^*$
0.035	0.901869	0.024505	-0.363268	1.8902	0.041841	1.1729	1.0828
0.03	0.900482	0.021839	-0.307930	1.8399	0.035288	1.1843	1.1085
0.025	0.900045	0.018903	-0.255048	1.7522	0.028310	1.1906	1.1281
0.02	0.899670	0.015689	-0.202075	1.6773	0.021953	1.1953	1.1459
0.015	0.900407	0.012205	-0.151193	1.6315	0.016110	1.2047	1.1681
0.01	0.900501	0.084244	-0.100232	1.5778	0.010473	1.2108	1.1866
0.005	0.900929	0.043562	-0.0504647	1.5382	0.0032261	1.2196	1.2075
			$T^* = 1.0$				
0.9	0.999972	3.2745	-6.05535	2.6766	6.7108	7.0198	7.2046
0.85	1.00042	1.9513	-5.81627	2.5147	5.6960	6.2595	6.3614
0.8	1.00046	1.0198	-5.53418	2.3781	4.8305	5.5182	5.5422
0.75	1.00124	0.40195	-5.22067	2.2681	4.0612	4.8098	4.7602
0.7	1.00028	0.016282	-4.88988	2.1752	3.3140	4.1124	3.9903
0.65	1.00149	-0.18528	-4.55205	2.1423	2.6353	3.4135	3.2171
0.6	1.00382	-0.25524	-4.22797	2.3379	1.9205	2.5116	2.2019
0.07	1.00952	0.045246	-0.685340	2.4044	0.098274	1.2190	1.0580
0.065	1.00829	0.043528	-0.634741	2.2719	0.088509	1.2208	1.0718
0.06	1.00535	0.041532	-0.581554	2.0982	0.078376	1.2365	1.1016
0.055	1.00314	0.039359	-0.530064	2.0531	0.070771	1.2312	1.1072
0.05	1.00120	0.036986	-0.478385	1.9561	0.062582	1.2294	1.1171
0.045	1.00130	0.034418	-0.429815	1.8581	0.054380	1.2489	1.1496
0.04	1.00049	0.031606	-0.380282	1.8005	0.047020	1.2444	1.1563
0.035	0.999804	0.028547	-0.330740	1.7781	0.040626	1.2494	1.1728
0.03	0.999532	0.025241	-0.281977	1.7125	0.033813	1.2609	1.1963
0.025	0.999915	0.021690	-0.235024	1.6697	0.027737	1.2664	1.2129
0.02	1.00014	0.017876	-0.187427	1.6323	0.021669	1.2741	1.2315
0.015	1.00044	0.013808	-0.140201	1.5943	0.015958	1.2777	1.2460
0.01	1.00025	0.0094674	-0.0926889	1.5571	0.010395	1.2811	1.2602
0.005	1.00071	0.0048671	-0.0466587	1.5280	0.0050964	1.2860	1.2755
			$T^* = 1.1$				
0.9	1.10011	3.9348	-5.93939	-	-	-	7.3946
0.85	1.10034	2.5161	-5.71528	-	-	-	6.5443
0.8	1.10021	1.4964	-5.44721	-	-	-	5.7320
0.75	1.10050	0.79932	-5.14565	-	-	-	4.9905
0.7	1.09969	0.34281	-4.8239	2.1475	3.2460	4.3241	4.2517
0.65	1.10136	0.078644	-4.4911	2.0836	2.6149	3.6821	3.5449
0.6	1.10156	-0.056635	-4.1613	2.1053	2.0583	2.9887	2.7787

Continued from previous page.

ρ^*	T^*	p^*	u^*	c_V^*	γ_V^*	w_0^*	$w_0^{'*}$
0.575	1.10251	-0.088051	-4.00085	-	-	-	2.4367
0.55	1.10416	-0.098723	-3.84665	-	-	-	1.9456
0.525	1.10962	-0.090234	-3.70302	-	-	-	1.4983
0.07	1.10287	0.053927	-0.627962	1.9688	0.089482	1.3170	1.1829
0.065	1.10137	0.051459	-0.580898	1.9250	0.082411	1.3168	1.1926
0.06	1.10049	0.048811	-0.534681	1.8599	0.073942	1.3135	1.1984
0.055	1.09955	0.045943	-0.488955	1.8227	0.066772	1.3129	1.2074
0.05	1.09923	0.042942	-0.443473	1.7732	0.059106	1.3152	1.2198
0.045	1.09978	0.039705	-0.399286	1.7478	0.052498	1.3198	1.2342
0.04	1.09976	0.036225	-0.354548	1.7138	0.046035	1.3281	1.2525
0.035	1.09985	0.032537	-0.309700	1.6796	0.039377	1.3303	1.2644
0.03	1.10018	0.028601	-0.265257	1.6535	0.033325	1.3363	1.2800
0.025	1.09972	0.024432	-0.220321	1.6204	0.027192	1.3297	1.2828
0.02	1.10043	0.020035	-0.176621	1.5968	0.021465	1.3392	1.3018
0.015	1.10069	0.015394	-0.132354	1.5701	0.015795	1.3448	1.3169
0.01	1.10053	0.010507	-0.0877628	1.5429	0.010335	1.3465	1.3280
0.005	1.10039	0.0053759	-0.0435272	1.5200	0.0050820	1.3498	1.3406
			$T^* = 1.2$				
0.95	1.20061	6.5983	-5.97662	-	-	-	8.4566
0.9	1.20016	4.5736	-5.82688	-	-	-	7.5639
0.85	1.20041	3.0620	-5.61772	-	-	-	6.7209
0.8	1.20015	1.9592	-5.36262	-	-	-	5.9358
0.75	1.20041	1.18600	-5.07290	-	-	-	5.1703
0.7	1.20054	0.66610	-4.75986	-	-	-	4.4569
0.65	1.20087	0.33904	-4.43376	-	-	-	3.7758
0.6	1.20141	0.15018	-4.10508	-	-	-	3.1207
0.55	1.20135	0.056558	-3.78237	-	-	-	2.4880
0.5	1.20376	0.026777	-1.67111	-	-	-	1.8586
0.125	1.20330	0.085591	-1.05131	-	-	-	1.1450
0.1	1.20179	0.077591	-0.839530	-	-	-	1.2019
0.075	1.20003	0.065457	-0.630510	-	-	-	1.2617
0.05	1.19929	0.048806	-0.419640	-	-	-	1.3100
0.025	1.20012	0.027148	-0.209622	-	-	-	1.3603
0.05	1.19363	0.048485	-0.420487	-	-	-	1.3001
0.025	1.20001	0.027154	-0.209475	-	-	-	1.3621
			$T^* = 1.25$				
0.95	1.25091	6.9612	-5.91371	2.7259	7.0952	8.1836	8.5462

Continued from previous page.

ρ^*	T^*	p^*	u^*	c_V^*	γ_V^*	w_0^*	$w_0'^*$
0.9	1.25033	4.8849	-5.77205	2.5802	6.1492	7.3801	7.6572
0.85	1.25076	3.3289	-5.56977	2.4435	5.2788	6.6188	6.8166
0.8	1.25016	2.1861	-5.32110	2.3200	4.4846	5.9028	6.0261
0.75	1.25031	1.3765	-5.03682	2.2050	3.7584	5.2248	5.2796
0.7	1.24914	0.82014	-4.72934	2.1143	3.1403	4.5772	4.5675
0.65	1.25096	0.46722	-4.40635	2.0472	2.5833	3.9562	3.8869
0.6	1.25154	0.25465	-4.07892	2.0078	2.0890	3.3750	3.2482
0.55	1.25100	0.13766	-3.75556	2.0149	1.6494	2.8544	2.6707
0.5	1.25282	0.089235	-3.44338	2.1141	1.2744	2.3426	2.0969
0.45	1.25550	0.077904	-3.14491	2.3239	0.9891	1.9649	1.6612
0.2	1.26932	0.11067	-1.59715	2.8287	0.32616	1.4029	1.1146
0.175	1.26182	0.10683	-1.40632	2.4824	0.27453	1.4036	1.1452
0.15	1.25743	0.10198	-1.21437	2.3276	0.22391	1.3952	1.1680
0.125	1.25407	0.094599	-1.01851	2.0804	0.17609	1.4170	1.2276
0.1	1.25085	0.084169	-0.816757	1.9328	0.13221	1.4247	1.2716
0.075	1.24973	0.070037	-0.614940	1.7944	0.092730	1.4167	1.2996
0.05	1.24923	0.051717	-0.409872	1.6836	0.057761	1.4290	1.3514
0.025	1.24991	0.028498	-0.205007	1.5862	0.026940	1.4331	1.3942

$$T^* = 1.3$$

ρ^*	T^*	p^*	u^*	c_V^*	γ_V^*	w_0^*	$w_0'^*$
0.95	1.30059	7.3114	-5.85307	2.7198	7.0466	8.2429	8.6215
0.9	1.30075	5.1912	-5.71815	2.5721	6.0976	-	-
0.9	1.30059	5.1912	-5.71814	2.5776	6.1196	-	-
0.85	1.30055	3.5922	-5.52255	2.4314	5.2024	6.6885	6.9029
0.8	1.30054	2.4099	-5.28010	2.3089	4.4305	5.9666	6.1077
0.75	1.30027	1.5645	-5.00159	2.2123	3.7859	5.2721	5.3452
0.7	1.30025	0.97982	-4.69796	2.1129	3.1237	4.6398	4.6492
0.65	1.30067	0.59607	-4.37905	2.0373	2.5589	4.0558	4.0066
0.6	1.30118	0.35769	-4.05390	1.9896	2.0532	3.5124	3.4087
0.55	1.30134	0.22134	-3.73052	1.9891	1.6681	2.9785	2.8215
0.5	1.30134	0.15203	-3.41505	2.0283	1.3010	2.5233	2.3142
0.45	1.30279	0.12490	-3.10971	2.1254	1.0251	2.1453	1.8875
0.225	1.31023	0.12634	-1.72247	2.4160	0.36013	1.5047	1.2275
0.2	1.30869	0.12368	-1.54748	2.3432	0.31372	1.4833	1.2263
0.175	1.30689	0.11893	-1.36748	2.2439	0.26585	1.4650	1.2302
0.15	1.30296	0.11200	-1.18214	2.1079	0.21585	1.4636	1.2573
0.125	1.30141	0.10282	-0.991698	1.9768	0.17160	1.4582	1.2820
0.1	1.29987	0.090600	-0.796924	1.8661	0.13040	1.4537	1.3101
0.075	1.29901	0.074648	-0.600042	1.7525	0.091513	1.4586	1.3499

Continued from previous page.

ρ^*	T^*	p^*	u^*	c_V^*	γ_V^*	w_0^*	$w_0^{'*}$
0.05	1.29950	0.054612	-0.400984	1.6609	0.057403	1.4638	1.3909
0.025	1.30030	0.029844	-0.201143	1.5748	0.026769	1.4613	1.4243
			$T^* = 1.35$				
0.95	1.35091	7.6638	-5.79187	2.6998	6.9347	8.3080	8.7022
0.9	1.35062	5.4942	-5.66468	2.5471	5.9518	7.5164	7.8256
0.85	1.35098	3.8527	-5.47582	2.4207	5.1381	6.7521	6.9829
0.8	1.35036	2.6310	-5.23976	2.3079	4.4121	6.0233	6.1812
0.75	1.35039	1.7507	-4.96663	2.1955	3.7047	5.3507	5.4410
0.7	1.34897	1.1308	-4.66841	2.1064	3.1088	4.6895	4.7166
0.65	1.35060	0.72272	-4.35244	2.0205	2.5177	4.1248	4.0944
0.6	1.35071	0.46032	-4.02965	1.9762	2.0572	3.5831	3.4989
0.55	1.35108	0.30386	-3.70678	1.9653	1.6663	3.0522	2.9160
0.5	1.35118	0.21738	-3.38907	1.9848	1.3317	2.5856	2.3991
0.45	1.35217	0.17649	-3.08086	2.0470	1.0392	2.2368	2.0076
0.4	1.35457	0.16038	-2.77972	2.1746	0.82265	1.9348	1.6666
0.35	1.35615	0.15393	-2.47878	2.2311	0.66058	1.7847	1.5029
0.3	1.35835	0.15151	-2.17171	2.2954	0.52193	1.6837	1.4041
0.3	1.34596	0.14477	-2.18444	2.3492	0.52389	1.6171	1.3192
0.25	1.35875	0.14705	-1.85185	2.3121	0.41042	1.5813	1.3121
0.2	1.35619	0.13817	-1.51426	2.1955	0.30979	1.5424	1.3064
0.15	1.35204	0.12253	-1.15547	1.9854	0.21295	1.5075	1.3164
0.1	1.35011	0.097051	-0.781130	1.8131	0.12900	1.4862	1.3514
0.05	1.34991	0.057472	-0.394382	1.6388	0.056898	1.4923	1.4233
$0.35^\dagger$	1.34619	0.14765	-2.48760	2.3362	0.64850	1.7148	1.4154
$0.3^\dagger$	1.34576	0.14484	-2.18414	2.3836	0.52007	1.6085	1.3088
$0.45^\dagger$	1.34991	0.17418	-3.08180	2.0538	1.0467	2.2417	2.0122
$0.4^\dagger$	1.34943	0.15609	-2.78223	2.1670	0.82208	1.9292	1.6583
$0.35^\dagger$	1.35066	0.15047	-2.48388	2.2891	0.65179	1.7305	1.4356
$0.3^\dagger$	1.35145	0.14778	-2.17979	2.3783	0.52611	1.6290	1.3356
$0.25^\dagger$	1.35057	0.14380	-1.85916	2.3427	0.41063	1.5634	1.2885
$0.2^\dagger$	1.35006	0.13626	-1.51899	2.1851	0.30884	1.5242	1.2837
$0.15^\dagger$	1.35043	0.12214	-1.15713	2.0059	0.21411	1.5105	1.3194
$0.1^\dagger$	1.34962	0.097000	-0.780396	1.8141	0.12841	1.5009	1.3676
$0.05^\dagger$	1.34942	0.057455	-0.393656	1.6431	0.057147	1.4910	1.4220
			$T^* = 1.5$				
0.95	1.50111	8.68084	-5.61554	2.6548	6.6652	8.4918	8.9296
0.9	1.50096	6.37790	-5.50872	2.5056	5.7090	7.7043	8.0579

Continued from previous page.

ρ^*	T^*	p^*	u^*	c_V^*	γ_V^*	w_0^*	$w_0'^*$
0.85	1.50146	4.61207	-5.33937	2.3970	4.9903	6.9294	7.2064
0.8	1.50082	3.27666	-5.12126	2.2750	4.2330	6.2191	6.4234
0.75	1.50051	2.29638	-4.86388	2.1710	3.5812	5.5352	5.6735
0.7	1.49888	1.58729	-4.57945	2.0796	2.9926	4.9237	5.0001
0.65	1.50037	1.09970	-4.27467	2.0060	2.4785	4.3356	4.3562
0.6	1.50055	0.767538	-3.95989	1.9555	2.0505	3.7901	3.7592
0.55	1.50127	0.552941	-3.64121	1.9185	1.6598	3.2956	3.2174
0.5	1.50183	0.417798	-3.32340	1.9030	1.3282	2.8905	2.7705
0.45	1.50213	0.334403	-3.00998	1.9156	1.0621	2.5283	2.3713
0.4	1.50285	0.284289	-2.70087	1.9446	0.84982	2.2527	2.0668
0.35	1.50334	0.251835	-2.39405	1.9675	0.66385	2.0373	1.8321
0.3	1.50385	0.227893	-2.08351	1.9914	0.52650	1.8760	1.6634
0.25	1.50334	0.206124	-1.76570	1.9638	0.40365	1.7533	1.5454
0.2	1.50219	0.182477	-1.43843	1.9029	0.29728	1.6855	1.4984
0.175	1.50129	0.169102	-1.26910	1.8617	0.25286	1.6612	1.4899
0.15	1.50038	0.153682	-1.09631	1.8289	0.20719	1.6643	1.5134
0.125	1.49959	0.136137	-0.920365	1.7711	0.16477	1.6163	1.4828
0.1	1.50014	0.116079	-0.742011	1.7225	0.12565	1.6081	1.4981
0.075	1.49941	0.0927829	-0.559608	1.6608	0.089521	1.5841	1.4986
0.05	1.49974	0.0659945	-0.374880	1.6049	0.056354	1.5832	1.5252
0.025	1.50032	0.0351848	-0.188369	1.5511	0.026564	1.5809	1.5514
			$T^* = 1.8$				
1.0	1.80118	13.825	-5.27369	2.6918	7.0228	9.6748	10.277
1.0	1.80184	13.822	-5.27449	2.6741	-	-	10.279
0.95	1.80124	10.608	-5.28112	2.5828	6.2482	8.8184	9.3336
0.9	1.80133	8.0533	-5.21256	2.4505	5.3890	8.0264	8.4591
0.85	1.80200	6.0566	-5.07934	2.3343	4.6393	7.2760	7.6324
0.8	1.80192	4.5129	-4.89436	2.2267	3.9610	6.5695	6.8547
0.75	1.80127	3.3416	-4.66750	2.1351	3.3874	5.8845	6.1047
0.7	1.80075	2.4686	-4.40862	2.0524	2.8617	5.2580	5.4185
0.65	1.80046	1.8289	-4.12678	1.9782	2.3828	4.6900	4.7958
0.6	1.80043	1.3694	-3.82964	1.9192	1.9789	4.1456	4.2018
0.55	1.80133	1.0437	-3.52390	1.8711	1.6184	3.6760	3.6878
0.5	1.80206	0.81512	-3.21365	1.8388	1.3200	3.2645	3.2364
0.45	1.80314	0.65430	-2.90321	1.8136	1.0577	2.9289	2.8668
0.4	1.80369	0.53930	-2.59349	1.8014	0.84900	2.6045	2.5138
0.35	1.80332	0.45275	-2.28514	1.7886	0.67170	2.3881	2.2773
0.3	1.80323	0.38500	-1.97623	1.7690	0.52387	2.2137	2.0914

Continued from previous page.

ρ^*	T^*	p^*	u^*	c_V^*	γ_V^*	w_0^*	$w_0'^*$
0.25	1.80321	0.32653	-1.66432	1.7578	0.40041	2.0576	1.9317
0.2	1.80199	0.27131	-1.34749	1.7336	0.29257	1.9508	1.8320
0.175	1.80178	0.24357	-1.18668	1.7128	0.24538	1.9070	1.7953
0.15	1.79827	0.21433	-1.02469	1.6827	0.20079	1.8649	1.7622
0.125	1.80093	0.18503	-0.858345	1.6573	0.16006	1.8269	1.7363
0.1	1.80076	0.15339	-0.691015	1.6308	0.12258	1.8000	1.7239
0.075	1.80035	0.11939	-0.521074	1.6019	0.087767	1.7775	1.7176
0.05	1.80084	0.082819	-0.349706	1.5667	0.055639	1.7577	1.7161
0.025	1.80078	0.043140	-0.175658	1.5328	0.026376	1.7414	1.7199

$$T^* = 2.1$$

ρ^*	T^*	p^*	u^*	c_V^*	γ_V^*	w_0^*	$w_0'^*$
1.0	2.09999	15.894	-4.92127	2.6435	6.7346	9.9582	10.628
0.95	2.10129	12.419	-4.96692	2.5198	5.8925	9.1153	9.6979
0.9	2.10164	9.6292	-4.93400	2.4023	5.1143	8.3194	8.8204
0.85	2.10234	7.4179	-4.83387	2.2895	4.3926	7.5737	7.9984
0.8	2.10193	5.6788	-4.67972	2.1967	3.7966	6.8511	7.2058
0.75	2.10155	4.3367	-4.48010	2.1021	3.2109	6.2021	6.4912
0.7	2.09985	3.3035	-4.24715	2.0279	2.7364	5.5707	5.8001
0.65	2.10086	2.5299	-3.98629	1.9554	2.2916	4.9945	5.1697
0.6	2.10137	1.9516	-3.70748	1.8979	1.9120	4.4734	4.5992
0.55	2.10092	1.5213	-3.41576	1.8447	1.5714	4.0110	4.0916
0.5	2.10272	1.2058	-3.11727	1.8053	1.2890	3.5892	3.6306
0.45	2.10323	0.96997	-2.81521	1.7757	1.0479	3.2168	3.2237
0.4	2.10572	0.79370	-2.51161	1.7520	0.84649	2.9062	2.8840
0.35	2.10334	0.65304	-2.20878	1.7280	0.66412	2.6521	2.6057
0.3	2.10307	0.54095	-1.90415	1.7130	0.52058	2.4486	2.3852
0.25	2.10362	0.44569	-1.59825	1.6887	0.39648	2.2816	2.2091
0.2	2.10281	0.35868	-1.28984	1.6626	0.28877	2.1547	2.0809
0.175	2.10274	0.31694	-1.13403	1.6512	0.24243	2.0927	2.0211
0.15	2.10233	0.27513	-0.976489	1.6319	0.19917	2.0440	1.9766
0.125	2.10173	0.23299	-0.817570	1.6153	0.15843	2.0049	1.9442
0.1	2.10187	0.19000	-0.657379	1.5927	0.12116	1.9648	1.9125
0.075	2.10129	0.14563	-0.495697	1.5714	0.086742	1.9360	1.8942
0.05	2.10160	0.099445	-0.332641	1.5479	0.055115	1.9131	1.8835
0.025	2.10122	0.051041	-0.166948	1.5244	0.026273	1.8888	1.8732

$$T^* = 2.5$$

ρ^*	T^*	p^*	u^*	c_V^*	γ_V^*	w_0^*	$w_0'^*$
1.05	2.50019	23.143	-4.28998	2.6774	7.1063	11.208	12.048
1.0	2.49980	18.487	-4.48064	2.5687	6.3090	10.314	11.061

Continued from previous page.

ρ^*	T^*	p^*	u^*	c_V^*	γ_V^*	w_0^*	$w_0^{'*}$
0.95	2.50130	14.694	-4.57263	2.4535	5.5206	9.4722	10.133
0.9	2.50171	11.611	-4.58357	2.3553	4.8448	8.6643	9.2443
0.9	2.50171	11.611	-4.58356	2.3474	4.8047	8.6769	9.2561
0.85	2.50252	9.1342	-4.52435	2.2489	4.1659	7.9179	8.4215
0.8	2.50221	7.1557	-4.40788	2.1556	3.5766	7.2104	7.6434
0.75	2.50223	5.5968	-4.24303	2.0796	3.0841	6.5347	6.9028
0.7	2.50041	4.3725	-4.04077	2.0044	2.6225	5.9051	6.2133
0.65	2.50131	3.4299	-3.80732	1.9359	2.2024	5.3441	5.5969
0.6	2.50087	2.7010	-3.55242	1.8783	1.8455	4.8159	5.0185
0.55	2.50129	2.1416	-3.28144	1.8281	1.5326	4.3296	4.4864
0.5	2.50195	1.7147	-2.99915	1.7849	1.2609	3.9151	4.0306
0.45	2.50272	1.3827	-2.71099	1.7491	1.0251	3.5534	3.6316
0.4	2.50315	1.1240	-2.41864	1.7181	0.82692	3.2251	3.2711
0.35	2.50297	0.91687	-2.12473	1.6934	0.65573	2.9498	2.9683
0.3	2.50324	0.74712	-1.82886	1.6680	0.51044	2.7388	2.7354
0.25	2.50309	0.60242	-1.53144	1.6457	0.38899	2.5425	2.5232
0.2	2.50295	0.47355	-1.23312	1.6236	0.28558	2.3890	2.3599
0.175	2.50261	0.41296	-1.08201	1.6120	0.23913	2.3260	2.2946
0.15	2.50290	0.35406	-0.931144	1.5977	0.19651	2.2747	2.2428
0.125	2.50278	0.29600	-0.779172	1.5840	0.15637	2.2167	2.1857
0.1	2.50283	0.23822	-0.625694	1.5688	0.11986	2.1704	2.1423
0.075	2.50197	0.18020	-0.471049	1.5531	0.085975	2.1302	2.1068
0.05	2.50177	0.12146	-0.315208	1.5355	0.054759	2.1002	2.0830
0.025	2.50156	0.061539	-0.158235	1.5172	0.026171	2.0683	2.0589
			$T^* = 3.0$				
1.1	3.00181	32.676	-3.35701	2.7132	7.5024	12.540	13.563
1.05	3.00002	26.582	-3.71907	2.6026	6.6744	11.601	12.525
1.0	2.99953	21.529	-3.96500	2.5032	5.9370	10.703	11.536
0.95	3.00122	17.363	-4.11075	2.3964	5.1995	9.8598	10.606
0.9	3.00162	13.941	-4.17206	2.2935	4.5147	9.0657	9.7294
0.85	3.00273	11.155	-4.16025	2.2059	3.9306	8.3063	8.8939
0.8	3.00188	8.9033	-4.08611	2.1261	3.4092	7.5877	8.1048
0.75	3.00226	7.0943	-3.96122	2.0461	2.9158	6.9222	7.3732
0.7	3.00078	5.6476	-3.79523	1.9749	2.4779	6.3085	6.6970
0.65	3.00198	4.5067	-3.59444	1.9165	2.1116	5.7209	6.0539
0.6	3.00141	3.6029	-3.36814	1.8566	1.7646	5.2038	5.4837
0.55	3.00147	2.8920	-3.12194	1.8113	1.4796	4.7141	4.9465
0.5	3.00216	2.3327	-2.86167	1.7676	1.2219	4.2764	4.4657

Continued from previous page.

ρ^*	T^*	p^*	u^*	c_V^*	γ_V^*	w_0^*	$w_0'^*$
0.45	3.00225	1.8870	-2.59145	1.7316	1.0015	3.8981	4.0471
0.4	3.00254	1.5307	-2.31511	1.6994	0.80992	3.5589	3.6719
0.4	3.00225	1.5316	-2.31468	1.6990	0.80826	3.5699	3.6829
0.35	3.00189	1.2409	-2.03425	1.6707	0.64390	3.2798	3.3607
0.35	3.00173	1.2408	-2.03401	1.6713	0.64580	3.2765	3.3576
0.3	3.00221	1.0005	-1.75046	1.6468	0.50503	3.0384	3.0920
0.3	3.00246	1.0007	-1.75082	1.6463	0.50440	3.0366	3.0902
0.25	3.00263	0.79547	-1.46493	1.6241	0.38591	2.8087	2.8399
0.25	3.00240	0.79532	-1.46458	1.6225	0.38389	2.8371	2.8678
0.2	3.00210	0.61531	-1.17683	1.6014	0.28258	2.6590	2.6724
0.175	3.00250	0.53182	-1.03242	1.5882	0.23636	2.5802	2.5869
0.175	3.00246	0.53170	-1.03235	1.5886	0.23611	2.5893	2.5958
0.15	3.00292	0.45156	-0.887586	1.5775	0.19402	2.5151	2.5163
0.125	3.00226	0.37370	-0.740970	1.5651	0.15491	2.4489	2.4461
0.1	3.00262	0.29787	-0.594497	1.5532	0.11881	2.4005	2.3955
0.075	3.00237	0.22301	-0.447732	1.5406	0.085386	2.3521	2.3460
0.05	3.00155	0.14876	-0.299108	1.5269	0.054512	2.3055	2.3000
0.025	3.00191	0.074613	-0.150068	1.5134	0.026110	2.2692	2.2657
			$T^* = 4.0$				
1.15	4.00066	47.886	-1.61121	2.6806	7.5260	14.216	15.482
1.1	4.00094	39.777	-2.20880	2.5875	6.7715	13.227	14.391
1.05	4.00009	32.903	-2.67476	2.4901	6.0327	12.284	13.350
1.0	3.99971	27.122	-3.02114	2.3981	5.3508	11.388	12.361
0.95	4.00129	22.284	-3.26277	2.3084	4.7145	10.536	11.421
0.9	4.00121	18.250	-3.41370	2.2258	4.1436	9.7220	10.525
0.85	4.00206	14.908	-3.48548	2.1489	3.6240	8.9526	9.6785
0.8	4.00175	12.152	-3.48965	2.0787	3.1576	8.2248	8.8780
0.75	4.00223	9.8925	-3.43594	2.0038	2.6977	7.5711	8.1545
0.7	4.00109	8.0420	-3.33531	1.9419	2.3123	6.9444	7.4633
0.65	4.00220	6.5432	-3.19330	1.8863	1.9740	6.3553	6.8150
0.6	4.00182	5.3203	-3.02049	1.8373	1.6778	5.7984	6.2031
0.55	4.00180	4.3288	-2.82196	1.7873	1.3952	5.3389	5.6889
0.5	4.00216	3.5224	-2.60378	1.7472	1.1624	4.8838	5.1851
0.45	4.00176	2.8643	-2.37064	1.7103	0.95521	4.4956	4.7505
0.4	4.00119	2.3229	-2.12628	1.6791	0.77920	4.1340	4.3461
0.35	4.00024	1.8741	-1.87395	1.6516	0.62724	3.8056	3.9789
0.3	4.00051	1.4969	-1.61557	1.6252	0.49125	3.5469	3.6831
0.25	4.00107	1.1745	-1.35314	1.6021	0.37656	3.3098	3.4129

Continued from previous page.

ρ^*	T^*	p^*	u^*	c_V^*	γ_V^*	w_0^*	$w_0^{'*}$
0.2	4.00120	0.89407	-1.08732	1.5807	0.27731	3.1019	3.1763
0.175	4.00170	0.76559	-0.953386	1.5704	0.23244	3.0171	3.0781
0.15	4.00213	0.64403	-0.818867	1.5603	0.19117	2.9416	2.9907
0.125	4.00238	0.52762	-0.683955	1.5501	0.15312	2.8616	2.8995
0.1	4.00292	0.41595	-0.548308	1.5398	0.11751	2.7949	2.8228
0.075	4.00248	0.30804	-0.412073	1.5294	0.084596	2.7348	2.7541
0.05	4.00278	0.20315	-0.275573	1.5197	0.054191	2.6781	2.6896
0.05	4.00269	0.20318	-0.275440	1.5197	0.054190	2.6763	2.6880
0.025	4.00259	0.10069	-0.138006	1.5094	0.026019	2.6278	2.6330
			$T^* = 6.0$				
1.275	5.99620	92.955	3.26001	2.7402	8.4712	17.992	19.763
1.25	5.99469	85.810	2.63132	2.6972	8.0847	17.432	19.144
1.2	5.99437	72.962	1.51608	2.6086	7.3162	16.350	17.947
1.15	5.99613	61.866	0.577432	2.5177	6.5727	15.316	16.803
1.1	5.99953	52.308	-0.203397	2.4268	5.8591	14.334	15.716
1.05	5.99957	44.083	-0.846135	2.3600	5.3010	13.364	14.648
1.0	5.99992	37.042	-1.36306	2.2727	4.6709	12.470	13.657
0.95	6.00049	31.054	-1.76441	2.2069	4.1690	11.594	12.692
0.9	6.00037	25.962	-2.06738	2.1310	3.6490	10.787	11.798
0.85	6.00076	21.660	-2.28068	2.0655	3.2001	10.012	10.941
0.8	6.00087	18.032	-2.41750	2.0046	2.7933	9.2819	10.133
0.75	6.00187	14.986	-2.48656	1.9510	2.4378	8.5804	9.3586
0.7	6.00107	12.431	-2.49873	1.8976	2.1030	7.9395	8.6473
0.65	6.00300	10.296	-2.46101	1.8463	1.7961	7.3513	7.9916
0.6	6.00286	8.5103	-2.38286	1.8042	1.5377	6.7835	7.3611
0.55	6.00303	7.0177	-2.27046	1.7628	1.2987	6.2771	6.7931
0.5	6.00290	5.7706	-2.12948	1.7262	1.0906	5.8003	6.2586
0.45	6.00198	4.7235	-1.96609	1.6921	0.90342	5.3825	5.7842
0.4	6.00099	3.8414	-1.78453	1.6631	0.74335	4.9813	5.3301
0.35	5.99962	3.0959	-1.58817	1.6366	0.60126	4.6342	4.9311
0.3	5.99964	2.4610	-1.38001	1.6111	0.47519	4.3300	4.5770
0.25	6.00016	1.9153	-1.16312	1.5887	0.36556	4.0624	4.2618
0.2	6.00060	1.4403	-0.939190	1.5680	0.27024	3.8306	3.9842
0.175	6.00115	1.2253	-0.824792	1.5585	0.22775	3.7175	3.8497
0.15	6.00192	1.0226	-0.709550	1.5494	0.18792	3.6190	3.7301
0.125	6.00260	0.83092	-0.593568	1.5405	0.12505	2.9855	3.6200
0.1	6.00342	0.64944	-0.476240	1.5318	0.11609	3.4418	3.5126
0.075	6.00351	0.47645	-0.358472	1.5233	0.083825	3.3634	3.4153

Continued on next page.

Continued from previous page.

ρ^*	T^*	p^*	u^*	c_V^*	γ_V^*	w_0^*	$w_0'^*$
0.05	6.00378	0.31117	-0.239504	1.5151	0.053847	3.2894	3.3230
0.025	6.00400	0.15265	-0.120180	1.5069	0.025934	3.2231	3.2395

Table D.2. Simulation data for the self-diffusion coefficient D^* and the product $D^*\rho^*$ of the Lennard-Jones model fluid. Simulation details are reported in Section 4.1.

ρ^*	T^*	D^*	$D^*\rho^*$	ρ^*	T^*	D^*	$D^*\rho^*$
			$T^* = 0.7$				
0.85	0.699715	0.029682	0.025230	0.015	0.701476	6.5571	0.098356
0.8	0.699845	0.042860	0.034288	0.01	0.699888	9.9717	0.099717
0.75	0.698757	0.058016	0.043512	0.005	0.700236	20.208	0.101038
			$T^* = 0.8$				
0.85	0.800689	0.036833	0.031308	0.025	0.803405	4.4568	0.11142
0.8	0.801086	0.051408	0.041126	0.02	0.801202	5.6418	0.11284
0.75	0.801714	0.068895	0.051671	0.015	0.800258	7.5835	0.11375
0.7	0.799703	0.088129	0.061690	0.01	0.800211	11.447	0.11447
0.03	0.806426	3.7064	0.11119	0.005	0.800415	23.314	0.11657
			$T^* = 0.9$				
0.85	0.900526	0.043797	0.037227	0.035	0.901869	3.6224	0.12678
0.8	0.900832	0.059760	0.047808	0.03	0.900482	4.1962	0.12589
0.75	0.901804	0.078152	0.058614	0.025	0.900045	5.1070	0.12768
0.7	0.900372	0.10009	0.070064	0.02	0.899670	6.4022	0.12805
0.65	0.902284	0.12464	0.081013	0.015	0.900407	8.6122	0.12918
0.05	0.908833	2.4989	0.12494	0.01	0.900501	12.982	0.12982
0.045	0.907587	2.7759	0.12492	0.005	0.900599	26.241	0.13121
0.04	0.902939	3.1392	0.12557				
			$T^* = 1.0$				
0.9	0.999972	0.036656	0.032990	0.05	1.00120	2.8108	0.14054
0.85	1.00042	0.050949	0.043307	0.045	1.00130	3.1287	0.14079
0.8	1.00046	0.068246	0.054597	0.04	1.00049	3.5264	0.14106
0.75	1.00124	0.089433	0.067075	0.035	0.999804	4.0371	0.14130
0.7	1.00028	0.11111	0.077777	0.03	0.999532	4.7664	0.14299
0.65	1.00149	0.13842	0.089970	0.025	0.999915	5.7058	0.14265
0.6	1.00382	0.16677	0.10006	0.02	1.00014	7.1973	0.14395
0.07	1.00952	2.0123	0.14086	0.015	1.00044	9.5876	0.14381
0.065	1.00829	2.1678	0.14091	0.01	1.00025	14.536	0.14536
0.06	1.00535	2.3463	0.14078	0.005	1.00071	29.406	0.14703
0.055	1.00314	2.5425	0.13984				
			$T^* = 1.1$				
0.9	1.10011	0.042409	0.038168	0.06	1.10049	2.5913	0.15548

Continued from previous page.

ρ^*	T^*	D^*	$D^*\rho^*$	ρ^*	T^*	D^*	$D^*\rho^*$
0.85	1.10034	0.058082	0.049370	0.055	1.09955	2.8212	0.15516
0.8	1.10021	0.076815	0.061452	0.05	1.09923	3.0961	0.15481
0.75	1.10050	0.098123	0.073592	0.045	1.09978	3.4659	0.15597
0.7	1.10083	0.12345	0.086414	0.04	1.09976	3.8936	0.15575
0.65	1.10136	0.15026	0.097668	0.035	1.09985	4.4517	0.15581
0.6	1.10183	0.18155	0.10893	0.03	1.10018	5.2528	0.15758
0.575	1.10251	0.19982	0.11489	0.025	1.09972	6.2878	0.15720
0.55	1.10416	0.21759	0.11967	0.02	1.10043	7.9368	0.15874
0.525	1.10962	0.23668	0.12426	0.015	1.10069	10.623	0.15934
0.07	1.10287	2.2010	0.15407	0.01	1.10053	15.922	0.15922
0.065	1.10137	2.3785	0.15460	0.005	1.10039	31.785	0.15893

$T^* = 1.2$

ρ^*	T^*	D^*	$D^*\rho^*$	ρ^*	T^*	D^*	$D^*\rho^*$
0.95	1.20091	0.034640	0.032908	0.55	1.20135	0.23432	0.12888
0.9	1.20016	0.048709	0.043838	0.5	1.20376	0.27749	0.13875
0.85	1.20041	0.065210	0.055429	0.125	1.20330	1.3603	0.17003
0.8	1.20015	0.085382	0.068306	0.1	1.20179	1.6958	0.16962
0.75	1.20041	0.10845	0.081339	0.075	1.20003	2.2583	0.16929
0.7	1.20054	0.13492	0.094441	0.05	1.19929	3.3936	0.16968
0.65	1.20087	0.16355	0.10631	0.025	1.20012	6.8893	0.17221
0.6	1.20141	0.19752	0.11851				

$T^* = 1.25$

ρ^*	T^*	D^*	$D^*\rho^*$	ρ^*	T^*	D^*	$D^*\rho^*$
0.95	1.25091	0.037104	0.035249	0.45	1.25550	0.34114	0.15351
0.9	1.25033	0.051618	0.046456	0.2	1.26932	0.89784	0.17957
0.85	1.25076	0.068628	0.058334	0.175	1.26182	1.02257	0.17895
0.8	1.25016	0.089132	0.071306	0.15	1.25743	1.1862	0.17793
0.75	1.25031	0.11287	0.084653	0.125	1.25407	1.4233	0.17791
0.7	1.24914	0.13893	0.097252	0.1	1.25085	1.7618	0.17618
0.65	1.25096	0.17050	0.11082	0.075	1.24973	2.3539	0.17654
0.6	1.25154	0.20419	0.12251	0.05	1.24923	3.5414	0.17707
0.55	1.25100	0.24502	0.13476	0.025	1.24991	7.1406	0.17852
0.5	1.25282	0.28863	0.14432				

$T^* = 1.3$

ρ^*	T^*	D^*	$D^*\rho^*$	ρ^*	T^*	D^*	$D^*\rho^*$
0.95	1.30059	0.039732	0.037745	0.45	1.30279	0.35244	0.15860
0.9	1.30059	0.054693	0.049224	0.225	1.31023	0.81632	0.18367
0.9	1.30075	0.054900	0.049410	0.2	1.30869	0.92317	0.18464
0.85	1.30055	0.072545	0.061663	0.175	1.30689	1.0579	0.18514
0.8	1.30054	0.093435	0.074748	0.15	1.30296	1.2281	0.18421

Continued on next page.

Continued from previous page.

ρ^*	T^*	D^*	$D^*\rho^*$	ρ^*	T^*	D^*	$D^*\rho^*$
0.75	1.30027	0.11734	0.088002	0.125	1.30141	1.4670	0.18337
0.7	1.30025	0.14514	0.10160	0.1	1.29987	1.8415	0.18415
0.65	1.30067	0.17754	0.11540	0.075	1.29901	2.4469	0.18352
0.6	1.30118	0.21226	0.12735	0.05	1.29950	3.6809	0.18405
0.55	1.30134	0.25384	0.13961	0.025	1.30030	7.4568	0.18642
0.5	1.30134	0.29884	0.14942				

<div align="center">

$T^* = 1.35$

</div>

ρ^*	T^*	D^*	$D^*\rho^*$	ρ^*	T^*	D^*	$D^*\rho^*$
0.95	1.35091	0.042394	0.040274	0.45	1.35217	0.36515	0.16432
0.9	1.35062	0.057711	0.051940	0.4	1.35457	0.43195	0.17278
0.85	1.35098	0.076286	0.064843	0.35	1.35615	0.51573	0.18051
0.8	1.35036	0.097246	0.077797	0.3	1.35835	0.61297	0.18389
0.75	1.35039	0.12224	0.091678	0.3	1.34596	0.61172	0.18352
0.7	1.34897	0.15020	0.10514	0.25	1.35875	0.75822	0.18955
0.65	1.35060	0.18261	0.11870	0.2	1.35619	0.95151	0.19030
0.6	1.35071	0.21970	0.13182	0.15	1.35204	1.2750	0.19124
0.55	1.35108	0.26035	0.14319	0.1	1.35011	1.9065	0.19065
0.5	1.35118	0.30770	0.15385	0.05	1.34991	3.8094	0.19047

<div align="center">

$T^* = 1.5$

</div>

ρ^*	T^*	D^*	$D^*\rho^*$	ρ^*	T^*	D^*	$D^*\rho^*$
0.95	1.50111	0.049922	0.047426	0.35	1.50334	0.56116	0.19641
0.9	1.50096	0.067278	0.060550	0.3	1.50385	0.67106	0.20132
0.85	1.50146	0.086944	0.073902	0.25	1.50334	0.82151	0.20538
0.8	1.50082	0.10971	0.087767	0.2	1.50219	1.0462	0.20924
0.75	1.50051	0.13709	0.10282	0.175	1.50129	1.1974	0.20955
0.7	1.49888	0.16675	0.11672	0.15	1.50038	1.4019	0.21029
0.65	1.50037	0.20147	0.13095	0.125	1.49959	1.6777	0.20971
0.6	1.50055	0.24102	0.14461	0.1	1.50014	2.0996	0.20996
0.55	1.50127	0.28559	0.15708	0.075	1.49941	2.8041	0.21031
0.5	1.50183	0.33675	0.16838	0.05	1.49974	4.2093	0.21046
0.45	1.50213	0.39797	0.17909	0.025	1.50032	8.5057	0.21264
0.4	1.50285	0.47045	0.18818				

<div align="center">

$T^* = 1.8$

</div>

ρ^*	T^*	D^*	$D^*\rho^*$	ρ^*	T^*	D^*	$D^*\rho^*$
1.0	1.80118	0.049399	0.049399	0.4	1.80369	0.53922	0.21569
0.95	1.80124	0.065991	0.062691	0.35	1.80332	0.64040	0.22414
0.9	1.80133	0.085661	0.077095	0.3	1.80323	0.77443	0.23233
0.85	1.80200	0.10814	0.091916	0.25	1.80321	0.95533	0.23883
0.8	1.80192	0.13486	0.10789	0.2	1.80199	1.2157	0.24314
0.75	1.80127	0.16411	0.12309	0.175	1.80178	1.3946	0.24405

Continued from previous page.

ρ^*	T^*	D^*	$D^*\rho^*$	ρ^*	T^*	D^*	$D^*\rho^*$
0.7	1.80075	0.19796	0.13857	0.15	1.79827	1.6346	0.24518
0.65	1.80046	0.23608	0.15346	0.125	1.80093	1.9682	0.24603
0.6	1.80043	0.28061	0.16836	0.1	1.80076	2.4679	0.24679
0.55	1.80133	0.33098	0.18204	0.075	1.80035	3.2976	0.24732
0.5	1.80206	0.38976	0.19488	0.05	1.80084	4.9682	0.24841
0.45	1.80314	0.45657	0.20546	0.025	1.80078	10.048	0.25119
			$T^* = 2.1$				
1.0	2.09999	0.063812	0.063812	0.4	2.10572	0.60464	0.24185
0.95	2.10129	0.082384	0.078265	0.35	2.10334	0.71901	0.25165
0.9	2.10164	0.10390	0.093509	0.3	2.10307	0.87031	0.26109
0.85	2.10234	0.12934	0.10994	0.25	2.10362	1.0663	0.26657
0.8	2.10193	0.15761	0.12609	0.2	2.10281	1.3648	0.27296
0.75	2.10155	0.19136	0.14352	0.175	2.10274	1.5778	0.27611
0.7	2.09985	0.22795	0.15957	0.15	2.10233	1.8459	0.27688
0.65	2.10086	0.27048	0.17581	0.125	2.10173	2.2311	0.27889
0.6	2.10137	0.31720	0.19032	0.1	2.10187	2.7968	0.27968
0.55	2.10092	0.37276	0.20502	0.075	2.10129	3.7530	0.28147
0.5	2.10272	0.43727	0.21864	0.05	2.10160	5.6533	0.28266
0.45	2.10323	0.51393	0.23127	0.025	2.10122	11.471	0.28678
			$T^* = 2.5$				
1.05	2.50019	0.063464	0.066637	0.4	2.50315	0.68639	0.27456
1.0	2.49980	0.082244	0.082244	0.35	2.50297	0.81375	0.28481
0.95	2.50130	0.10382	0.098625	0.3	2.50324	0.98133	0.29440
0.9	2.50171	0.12864	0.11578	0.25	2.50309	1.2160	0.30400
0.85	2.50252	0.15695	0.13341	0.2	2.50295	1.5538	0.31077
0.8	2.50221	0.18876	0.15101	0.175	2.50261	1.7905	0.31333
0.75	2.50223	0.22622	0.16966	0.15	2.50290	2.1089	0.31634
0.7	2.50041	0.26727	0.18709	0.125	2.50278	2.5542	0.31927
0.65	2.50131	0.31474	0.20458	0.1	2.50283	3.2168	0.32168
0.6	2.50087	0.36724	0.22034	0.075	2.50197	4.3128	0.32346
0.55	2.50129	0.42934	0.23614	0.05	2.50151	6.5248	0.32624
0.5	2.50195	0.49958	0.24979	0.025	2.50157	13.214	0.33036
0.45	2.50272	0.58216	0.26197				
			$T^* = 3.0$				
1.1	3.00181	0.065456	0.072006	0.4	3.00254	0.78164	0.31266
1.05	3.00002	0.084094	0.088295	0.35	3.00173	0.92464	0.32362

Continued from previous page.

ρ^*	T^*	D^*	$D^*\rho^*$	ρ^*	T^*	D^*	$D^*\rho^*$
1.0	2.99953	0.10556	0.10556	0.35	3.00189	0.92673	0.32436
0.95	3.00122	0.13051	0.12399	0.3	3.00246	1.1126	0.33378
0.9	3.00162	0.15885	0.14297	0.3	3.00221	1.1151	0.33452
0.85	3.00273	0.19113	0.16246	0.25	3.00240	1.3770	0.34424
0.8	3.00188	0.22710	0.18168	0.25	3.00263	1.3743	0.34357
0.75	3.00226	0.26766	0.20075	0.2	3.00210	1.7651	0.35303
0.7	3.00078	0.31428	0.22000	0.175	3.00246	2.0419	0.35733
0.65	3.00198	0.36824	0.23936	0.15	3.00292	2.4158	0.36237
0.6	3.00141	0.42606	0.25564	0.125	3.00226	2.9287	0.36608
0.55	3.00147	0.49243	0.27084	0.1	3.00262	3.6958	0.36958
0.5	3.00216	0.57658	0.28829	0.075	3.00237	4.9757	0.37318
0.45	3.00225	0.67131	0.30209	0.05	3.00155	7.5464	0.37732
0.4	3.00225	0.78110	0.31244	0.025	3.00191	15.250	0.38126

<div align="center">

$T^* = 4.0$

</div>

ρ^*	T^*	D^*	$D^*\rho^*$	ρ^*	T^*	D^*	$D^*\rho^*$
1.15	4.00066	0.081336	0.093536	0.45	4.00176	0.82381	0.37071
1.1	4.00094	0.10240	0.11264	0.4	4.00119	0.95886	0.38354
1.05	4.00009	0.12544	0.13172	0.35	4.00024	1.1319	0.39618
1.0	3.99971	0.15274	0.15274	0.3	4.00051	1.3617	0.40851
0.95	4.00129	0.18267	0.17353	0.25	4.00107	1.6833	0.42083
0.9	4.00121	0.21711	0.19540	0.2	4.00120	2.1587	0.43174
0.85	4.00206	0.25593	0.21755	0.175	4.00170	2.4996	0.43743
0.8	4.00175	0.30020	0.24016	0.15	4.00213	2.9513	0.44270
0.75	4.00223	0.34791	0.26093	0.125	4.00238	3.5900	0.44875
0.7	4.00109	0.40227	0.28159	0.1	4.00292	4.5538	0.45538
0.65	4.00220	0.46328	0.30113	0.075	4.00248	6.1439	0.46079
0.6	4.00182	0.53563	0.32138	0.05	4.00269	9.3077	0.46825
0.55	4.00180	0.61433	0.33788	0.025	4.00259	18.897	0.47242
0.5	4.00216	0.70909	0.35455				

<div align="center">

$T^* = 6.0$

</div>

ρ^*	T^*	D^*	$D^*\rho^*$	ρ^*	T^*	D^*	$D^*\rho^*$
1.275	5.99620	0.089259	0.11381	0.55	6.00303	0.83122	0.45717
1.25	5.99469	0.099247	0.12406	0.5	6.00290	0.95236	0.47618
1.2	5.99437	0.12157	0.14588	0.45	6.00198	1.0903	0.49065
1.15	5.99613	0.14642	0.16838	0.4	6.00099	1.2663	0.50654
1.1	5.99953	0.17528	0.19281	0.35	5.99962	1.4911	0.52188
1.05	5.99957	0.20739	0.21776	0.3	5.99964	1.7920	0.53760
1.0	5.99992	0.24378	0.24378	0.25	6.00016	2.2168	0.55419
0.95	6.00049	0.28414	0.26993	0.2	6.00060	2.8482	0.56964

Continued from previous page.

ρ^*	T^*	D^*	$D^*\rho^*$	ρ^*	T^*	D^*	$D^*\rho^*$
0.9	6.00037	0.32851	0.29566	0.175	6.00115	3.3062	0.57858
0.85	6.00076	0.37825	0.32151	0.15	6.00192	3.8972	0.58458
0.8	6.00087	0.43283	0.34626	0.125	6.00260	4.7458	0.59322
0.75	6.00187	0.49425	0.37069	0.1	6.00342	6.0117	0.60117
0.7	6.00107	0.56377	0.39464	0.075	6.00351	8.1748	0.61311
0.65	6.00300	0.63878	0.41520	0.05	6.00378	12.478	0.62391
0.6	6.00286	0.72844	0.43706	0.025	6.00400	25.329	0.63321

Table D.3. Simulation data for the viscosity η^*, the viscosity contributions η_{tt}^*, η_{tc}^* and η_{cc}^*, configurational shear modulus $G_{c,\infty}^*$ and normalization factor for the translational-configurational shear stress correlation function $G_{tc,max}^*$ of the Lennard-Jones model fluid. The simulations extended over 2 million time steps if not denoted otherwise († 10 million time steps).

ρ^*	T^*	η^*	η_{tt}^*	η_{tc}^*	η_{cc}^*	$G_{c,\infty}^*$	$G_{tc,max}^*$
				$T^* = 0.7$			
0.85	0.699715	3.515	0.04943	0.07240	3.393	23.72	1.165
0.8	0.699845	2.380	0.05011	0.08920	2.240	19.16	1.034
0.75	0.698757	1.628	0.05284	0.09552	1.479	15.34	0.8984
0.015	0.701012	0.07550	0.07537	-0.0003230	0.0004506	0.009207	0.0007681
0.01	0.700092	0.07543	0.07443	0.0007653	0.0002361	0.003951	0.0003693
0.005	0.700063	0.04947	0.04955	-0.0001621	0.00008449	0.0009612	0.00007549
				$T^* = 0.8$			
0.85	0.800689	3.246	0.05396	0.04427	3.148	24.83	1.252
0.8	0.801086	2.164	0.05652	0.08240	2.026	20.03	1.092
0.75	0.801714	1.646	0.05792	0.1038	1.484	16.35	0.9814
0.7	0.799703	1.233	0.06094	0.1016	1.071	13.24	0.8534
0.03	0.803295	0.08567	0.08068	0.003792	0.001195	0.03371	0.003249
0.025	0.802965	0.09540	0.09274	0.001845	0.0008153	0.02268	0.002042
0.02	0.800700	0.08465	0.08379	0.0003490	0.0005153	0.01416	0.001234
0.015	0.800480	0.07473	0.07363	0.0007653	0.0003412	0.007792	0.0007698
0.01	0.800439	0.07673	0.07623	0.0003453	0.0001560	0.003412	0.0003508
				$T^* = 0.9$			
0.85	0.900526	2.918	0.05741	0.07468	2.786	26.01	1.382
0.8	0.900832	2.095	0.06133	0.09610	1.938	20.99	1.210
0.75	0.901804	1.573	0.06316	0.1026	1.407	17.07	1.054
0.7	0.900372	1.237	0.06753	0.1169	1.053	13.84	0.9423
0.65	0.902284	0.9708	0.07075	0.1152	0.7848	11.30	0.7972
0.05	0.909642	0.1090	0.1025	0.003866	0.002702	0.08625	0.008365
0.045	0.907209	0.1077	0.1005	0.005064	0.002168	0.06831	0.006716
0.04	0.902970	0.1044	0.09945	0.003220	0.001701	0.05292	0.005131
0.035	0.900743	0.09796	0.09321	0.003301	0.001446	0.04012	0.003924
0.03	0.898053	0.1001	0.09698	0.002174	0.0009924	0.02919	0.002810
0.025	0.900334	0.09601	0.09308	0.002201	0.0007209	0.01997	0.001981
0.02	0.900045	0.1012	0.09878	0.001931	0.0004882	0.01255	0.001265
0.015	0.900353	0.1035	0.1008	0.002417	0.0002688	0.007028	0.0006630

Continued on next page.

Continued from previous page.

ρ^*	T^*	η^*	η_{tt}^*	η_{tc}^*	η_{cc}^*	$G_{c,\infty}^*$	$G_{tc,max}^*$
0.01	0.900418	0.09682	0.09542	0.001254	0.0001523	0.003077	0.0003148
0.005	0.900599	0.08578	0.08531	0.0004216	0.00004864	0.0007712	0.00007599
			$T^* = 1.0$				
0.9	0.999972	3.969	0.06203	0.06496	3.842	33.24	1.629
0.85	1.00042	2.833	0.06194	0.08009	2.691	26.97	1.472
0.8	1.00046	2.053	0.06578	0.08919	1.898	21.88	1.286
0.75	1.00124	1.558	0.06823	0.1097	1.380	17.75	1.122
0.7	1.00028	1.222	0.07380	0.1253	1.023	14.46	0.9820
0.65	1.00149	0.9427	0.07580	0.1185	0.7484	11.66	0.8470
0.6	1.00382	0.7631	0.08029	0.1059	0.5769	9.658	0.7140
0.07	1.00987	0.1193	0.1058	0.008282	0.005290	0.1536	0.01522
0.065	1.00651	0.1203	0.1089	0.007098	0.004305	0.1323	0.01327
0.06	1.00467	0.1215	0.1096	0.008219	0.003606	0.1111	0.01130
0.055	1.00220	0.1164	0.1072	0.006218	0.002956	0.09279	0.009496
0.05	1.00158	0.1045	0.09799	0.004208	0.002271	0.07618	0.007690
0.045	1.00093	0.1084	0.1024	0.004193	0.001798	0.06085	0.005986
0.04	0.999160	0.1280	0.1200	0.006480	0.001598	0.04773	0.005030
0.035	0.998963	0.09249	0.08812	0.003192	0.001173	0.03647	0.003694
0.03	0.995815	0.1212	0.1160	0.004396	0.0008600	0.02655	0.002895
0.025	1.00029	0.1230	0.1212	0.001134	0.0006469	0.01832	0.001882
0.02	1.00030	0.1102	0.1076	0.002193	0.0004025	0.01168	0.0007642
0.015	1.00014	0.1222	0.1199	0.002070	0.0002269	0.006518	0.0004678
0.01	1.00062	0.1134	0.1121	0.001187	0.0001339	0.002865	0.0003019
0.005	1.00035	0.07796	0.07743	0.0004895	0.00004073	0.0007174	0.00007710
			$T^* = 1.1$				
0.9	1.10011	3.814	0.06578	0.08006	3.668	34.32	1.736
0.85	1.10034	2.623	0.06827	0.08755	2.468	27.95	1.558
0.8	1.10021	2.019	0.07094	0.09742	1.851	22.83	1.346
0.75	1.10050	1.525	0.07344	0.1120	1.340	18.39	1.198
0.7	1.10083	1.201	0.07977	0.1254	0.9955	14.96	1.023
0.65	1.10136	0.9780	0.08287	0.1223	0.7729	12.12	0.8841
0.575	1.10251	0.7334	0.08683	0.1244	0.5222	8.877	0.6852
0.55	1.10416	0.6692	0.09397	0.1257	0.4495	8.031	0.6476
0.525	1.10962	0.5993	0.09563	0.1111	0.3925	7.326	0.6026
0.07	1.10130	0.1267	0.1133	0.009220	0.004258	0.1407	-
0.065	1.10099	0.1370	0.1235	0.009572	0.003927	0.1205	0.01287
0.06	1.10102	0.1373	0.1252	0.008819	0.003319	0.1024	0.01076

Continued from previous page.

ρ^*	T^*	η^*	η^*_{tt}	η^*_{tc}	η^*_{cc}	$G^*_{c,\infty}$	$G^*_{tc,max}$
0.055	1.09980	0.1311	0.1204	0.007973	0.002768	0.08593	0.009263
0.05	1.09965	0.1205	0.1138	0.004532	0.002240	0.07094	0.007072
0.045	1.09994	0.1331	0.1251	0.006278	0.001671	0.05714	0.006182
0.035	1.09894	0.1307	0.1248	0.004879	0.001055	0.03416	0.003499
0.03	1.09905	0.1230	0.1193	0.002867	0.0008039	0.02508	0.002624
0.025	1.09982	0.1186	0.1154	0.002603	0.0005934	0.01737	0.001890
0.02	1.10032	0.1082	0.1052	0.002603	0.0003842	0.01105	0.001296
0.015	1.10012	0.1185	0.1153	0.002896	0.0002362	0.006242	0.0006971
0.01	1.10066	0.1194	0.1184	0.0008053	0.0001152	0.002743	0.0002975
0.005	1.10066	0.09852	0.09796	0.0005379	0.00003044	0.0006835	0.00007678

<div align="center">$T^* = 1.2$</div>

ρ^*	T^*	η^*	η^*_{tt}	η^*_{tc}	η^*_{cc}	$G^*_{c,\infty}$	$G^*_{tc,max}$
0.95	1.20061	5.130	0.06870	0.06764	4.993	43.68	2.077
0.9	1.20016	3.627	0.07154	0.09075	3.465	35.84	1.870
0.85	1.20041	2.658	0.07198	0.09866	2.487	29.18	1.661
0.8	1.20015	1.967	0.07620	0.1121	1.779	23.45	1.454
0.75	1.20041	1.534	0.08032	0.1181	1.336	19.08	1.293
0.7	1.20054	1.190	0.08304	0.1231	0.9839	15.53	1.110
0.65	1.20087	0.9842	0.08967	0.1396	0.7549	12.51	0.9377
0.6	1.20141	0.8070	0.09644	0.1289	0.5817	10.13	0.8070
0.55	1.20135	0.6651	0.09691	0.1195	0.4487	8.167	0.6812
0.5	1.20376	0.5748	0.1045	0.1236	0.3467	6.619	0.5612
0.125	1.20330	0.1806	0.1377	0.02849	0.01439	0.4366	0.04601
0.1	1.20179	0.1558	0.1284	0.01882	0.008540	0.2750	0.02899
0.075	1.20003	0.1559	0.1360	0.01463	0.005256	0.1536	0.01730
0.05	1.19363	0.1377	0.1278	0.007824	0.002077	0.06730	0.007455
0.025	1.20001	0.1243	0.1204	0.003424	0.0005349	0.01670	0.001836

<div align="center">$T^* = 1.25$</div>

ρ^*	T^*	η^*	η^*_{tt}	η^*_{tc}	η^*_{cc}	$G^*_{c,\infty}$	$G^*_{tc,max}$
0.95	1.25091	5.113	0.07162	0.08047	4.961	44.24	2.138
0.9	1.25033	3.640	0.07225	0.09591	3.472	36.29	1.934
0.85	1.25076	2.593	0.07380	0.09680	2.423	29.67	1.684
0.8	1.25016	1.947	0.07596	0.1109	1.760	24.09	1.479
0.75	1.25031	1.493	0.08059	0.1122	1.300	19.41	1.308
0.7	1.24914	1.219	0.08483	0.1295	1.005	15.76	1.114
0.65	1.25096	0.9856	0.09056	0.1376	0.7573	12.78	0.9716
0.6	1.25154	0.7977	0.09675	0.1236	0.5773	10.25	0.8220
0.55	1.25100	0.6649	0.1033	0.1232	0.4384	8.277	0.6872
0.5	1.25282	0.5699	0.1098	0.1195	0.3406	6.664	0.5751

Continued from previous page.

ρ^*	T^*	η^*	η^*_{tt}	η^*_{tc}	η^*_{cc}	$G^*_{c,\infty}$	$G^*_{tc,max}$
0.45	1.25550	0.4801	0.1149	0.1079	0.2573	5.350	0.4819
0.2	1.26932	0.2136	0.1363	0.03813	0.03918	1.102	0.1089
0.175	1.26182	0.1922	0.1289	0.03330	0.03000	0.8399	0.08730
0.15	1.25743	0.1867	0.1339	0.03200	0.02077	0.6190	0.06549
0.125	1.25407	0.1776	0.1410	0.02268	0.01399	0.4241	0.04523
0.1	1.25085	0.1627	0.1338	0.02023	0.008703	0.2687	0.02982
0.075	1.24973	0.1537	0.1362	0.01297	0.004534	0.1502	0.01740
0.05	1.24923	0.1490	0.1380	0.009073	0.001988	0.06619	0.007600
0.025	1.24991	0.1438	0.1406	0.002612	0.0005078	0.01648	0.001773
				$T^* = 1.3$			
0.95	1.30059	4.897	0.07413	0.06525	4.757	44.86	2.194
0.9	1.30059	3.539	0.07468	0.08750	3.377	36.79	1.918
0.85	1.30055	2.529	0.07738	0.1145	2.337	30.06	1.741
0.8	1.30054	1.971	0.08098	0.1151	1.775	24.45	1.501
0.75	1.30027	1.540	0.08362	0.1237	1.333	19.76	1.340
0.7	1.30025	1.223	0.08729	0.1298	1.006	16.07	1.131
0.65	1.30067	0.9876	0.09300	0.1356	0.7590	12.93	0.9954
0.6	1.30118	0.8282	0.1010	0.1438	0.5835	10.39	0.8462
0.55	1.30134	0.6749	0.1049	0.1297	0.4403	8.326	0.7156
0.5	1.30134	0.5545	0.1059	0.1179	0.3306	6.641	0.5847
0.45	1.30279	0.4780	0.1128	0.1094	0.2558	5.349	0.4770
0.225	1.31023	0.2387	0.1343	0.05027	0.05416	1.354	0.1410
0.2	1.30869	0.2157	0.1360	0.03963	0.04001	1.072	0.1101
0.175	1.30689	0.2055	0.1425	0.03377	0.02923	0.8198	0.08597
0.15	1.30296	0.1804	0.1329	0.02588	0.02164	0.6037	0.06281
0.125	1.30141	0.1760	0.1390	0.02349	0.01348	0.4154	0.04463
0.1	1.29987	0.1686	0.1388	0.02118	0.008601	0.2645	0.02873
0.075	1.29901	0.1581	0.1409	0.01212	0.005012	0.1476	0.01680
0.05	1.29950	0.1499	0.1380	0.009876	0.002077	0.06512	0.007319
0.025	1.30030	0.1464	0.1418	0.004209	0.0004754	0.01613	0.001838
				$T^* = 1.35$			
0.95	1.35091	4.808	0.07435	0.08444	4.649	45.55	2.278
0.9	1.35062	3.371	0.07955	0.1038	3.187	37.43	2.056
0.85	1.35098	2.588	0.07868	0.1049	2.404	30.58	1.800
0.8	1.35036	1.971	0.08400	0.1323	1.755	24.75	1.576
0.75	1.35039	1.517	0.08689	0.1410	1.289	20.07	1.379
0.7	1.34897	1.213	0.08924	0.1355	0.9880	16.25	1.190

Continued from previous page.

ρ^*	T^*	η^*	η_{tt}^*	η_{tc}^*	η_{cc}^*	$G_{c,\infty}^*$	$G_{tc,max}^*$
0.65	1.35060	0.9908	0.1011	0.1281	0.7616	13.08	0.9899
0.6	1.35071	0.8114	0.1047	0.1353	0.5713	10.60	0.8568
0.55	1.35108	0.7154	0.1119	0.1414	0.4621	8.517	0.7229
0.5	1.35118	0.5716	0.1145	0.1167	0.3404	6.799	0.6007
0.45	1.35217	0.4950	0.1208	0.1130	0.2613	5.371	0.4966
0.4	1.35457	0.4052	0.1212	0.1018	0.1821	4.196	0.4044
0.35	1.35615	0.3344	0.1230	0.08308	0.1283	3.204	0.3133
0.3	1.35835	0.2960	0.1330	0.07115	0.09187	2.369	0.2378
0.3	1.34596	0.2912	0.1303	0.07362	0.08731	2.370	0.2289
0.25	1.35875	0.2666	0.1413	0.06167	0.06372	1.645	0.1680
0.2	1.35619	0.2084	0.1323	0.03896	0.03713	1.050	0.1074
0.15	1.35204	0.1952	0.1419	0.03259	0.02072	0.5952	0.06384
0.1	1.35011	0.1748	0.1457	0.02061	0.008548	0.2610	0.03023
0.05	1.34991	0.1493	0.1403	0.007021	0.002026	0.06441	0.007475
0.35†	1.34619	0.3531	0.1293	0.08899	0.1347	3.213	0.3135
0.3†	1.34576	0.2961	0.1321	0.06918	0.09483	2.375	0.2326
0.45†	1.34991	0.4809	0.1193	0.1116	0.2500	5.366	0.4925
0.4†	1.34943	0.4046	0.1264	0.1011	0.1771	4.187	0.3986
0.35†	1.35066	0.3541	0.1279	0.08787	0.1383	3.213	0.3138
0.3†	1.35145	0.2938	0.1324	0.07092	0.09047	2.369	0.2378
0.25†	1.35057	0.2544	0.1366	0.05751	0.06037	1.653	0.1678
0.2†	1.35006	0.2223	0.1407	0.04367	0.03795	1.059	0.1107
0.15†	1.35043	0.2036	0.1495	0.03386	0.02026	0.5920	0.06499
0.1†	1.34962	0.1791	0.1499	0.02076	0.008433	0.2613	0.02926
0.05†	1.34942	0.1657	0.1540	0.009488	0.002169	0.06469	0.007512
$T^* = 1.5$							
0.95	1.50111	4.354	0.07983	0.07377	4.201	47.57	2.400
0.9	1.50096	3.287	0.08503	0.07551	3.126	39.03	2.134
0.85	1.50146	2.439	0.08805	0.1169	2.234	31.73	1.899
0.8	1.50082	1.912	0.08934	0.1237	1.699	25.90	1.691
0.75	1.50051	1.515	0.09403	0.1389	1.282	21.05	1.480
0.7	1.49888	1.189	0.09764	0.1353	0.9559	16.98	1.251
0.65	1.50037	0.9946	0.1056	0.1419	0.7471	13.72	1.097
0.6	1.50055	0.8419	0.1099	0.1431	0.5888	11.05	0.9326
0.55	1.50127	0.6902	0.1172	0.1349	0.4381	8.801	0.7728
0.5	1.50183	0.5818	0.1235	0.1304	0.3278	6.998	0.6363
0.45	1.50213	0.5049	0.1301	0.1225	0.2523	5.483	0.5173
0.4	1.50285	0.4386	0.1430	0.1109	0.1846	4.250	0.4113

Continued from previous page.

ρ^*	T^*	η^*	η_{tt}^*	η_{tc}^*	η_{cc}^*	$G_{c,\infty}^*$	$G_{tc,max}^*$
0.35	1.50334	0.3606	0.1349	0.08801	0.1376	3.217	0.3286
0.3	1.50385	0.3275	0.1513	0.08191	0.09422	2.328	0.2397
0.25	1.50334	0.2707	0.1511	0.05859	0.06105	1.604	0.1692
0.2	1.50219	0.2529	0.1624	0.05425	0.03626	1.030	0.1141
0.175	1.50129	0.2238	0.1582	0.03859	0.02695	0.7859	0.8486
0.15	1.50038	0.2115	0.1562	0.03518	0.02007	0.5759	0.06612
0.125	1.49959	0.2033	0.1592	0.03124	0.01288	0.3981	0.04448
0.1	1.50014	0.1989	0.1659	0.02427	0.008702	0.2556	0.03088
0.075	1.49941	0.1849	0.1628	0.01755	0.004496	0.1429	0.01752
0.05	1.49974	0.1839	0.1698	0.01208	0.001978	0.06328	0.008087
0.025	1.50032	0.1658	0.1610	0.004208	0.0005731	0.01578	0.001972
				$T^* = 1.8$			
1.0	1.80118	5.526	0.08759	0.06383	5.374	61.50	3.035
0.95	1.80124	4.058	0.09453	0.07777	3.885	50.98	2.671
0.9	1.80133	3.078	0.09611	0.1244	2.858	42.03	2.432
0.85	1.80200	2.374	0.09874	0.1465	2.129	34.37	2.191
0.8	1.80192	1.855	0.1037	0.1403	1.611	28.01	1.933
0.75	1.80127	1.485	0.1047	0.1424	1.238	22.84	1.623
0.7	1.80075	1.233	0.1145	0.1528	0.9658	18.42	1.429
0.65	1.80046	1.031	0.1196	0.1568	0.7542	14.78	1.223
0.6	1.80029	0.8321	0.1265	0.1421	0.5634	11.93	1.019
0.55	1.80133	0.7358	0.1377	0.1559	0.4422	9.480	0.8789
0.5	1.80206	0.6139	0.1428	0.1408	0.3302	7.488	0.7051
0.45	1.80314	0.5403	0.1519	0.1335	0.2549	5.809	0.5896
0.4	1.80369	0.4625	0.1620	0.1173	0.1832	4.460	0.4584
0.35	1.80332	0.4122	0.1720	0.1069	0.1333	3.303	0.3530
0.3	1.80323	0.3501	0.1684	0.08953	0.09215	2.385	0.2736
0.25	1.80321	0.3032	0.1752	0.06836	0.05957	1.628	0.1806
0.2	1.80199	0.2683	0.1782	0.05401	0.03608	1.028	0.1199
0.175	1.80178	0.2678	0.1932	0.04834	0.02631	0.7810	0.09149
0.15	1.79827	0.2394	0.1808	0.03936	0.01923	0.5736	0.06604
0.125	1.80093	0.2482	0.1962	0.03824	0.01380	0.3949	0.04803
0.1	1.80076	0.2246	0.1860	0.03026	0.008380	0.2527	0.03157
0.075	1.80035	0.2141	0.1898	0.01980	0.004458	0.1411	0.01765
0.05	1.80084	0.2070	0.1927	0.01230	0.002014	0.06239	0.007847
0.025	1.80078	0.1919	0.1862	0.005164	0.0005030	0.01555	0.001868

Continued from previous page.

ρ^*	T^*	η^*	η_{tt}^*	η_{tc}^*	η_{cc}^*	$G_{c,\infty}^*$	$G_{tc,max}^*$
				$T^* = 2.1$			
1.0	2.09999	4.972	0.1022	0.05382	4.816	65.24	3.332
0.95	2.10129	3.747	0.1029	0.1186	3.525	53.94	3.016
0.9	2.10164	2.942	0.1069	0.1455	2.689	44.54	2.694
0.85	2.10234	2.315	0.1137	0.1532	2.048	36.67	2.401
0.8	2.10193	1.863	0.1180	0.1585	1.587	29.94	2.111
0.75	2.10155	1.525	0.1247	0.1763	1.224	24.57	1.858
0.7	2.09985	1.261	0.1284	0.1718	0.9607	19.88	1.615
0.65	2.10086	1.046	0.1347	0.1665	0.7445	15.99	1.356
0.6	2.10137	0.8874	0.1418	0.1685	0.5772	12.77	1.160
0.55	2.10092	0.7253	0.1488	0.1449	0.4316	10.14	0.9182
0.5	2.10272	0.6251	0.1587	0.1368	0.3296	7.914	0.7643
0.45	2.10323	0.5520	0.1677	0.1330	0.2513	6.149	0.6402
0.4	2.10572	0.4921	0.1771	0.1209	0.1941	4.696	0.5026
0.35	2.10334	0.4062	0.1737	0.1009	0.1317	3.461	0.3813
0.3	2.10307	0.3783	0.1921	0.09266	0.09354	2.482	0.2780
0.25	2.10362	0.3352	0.1976	0.07753	0.06000	1.674	0.1948
0.2	2.10281	0.3202	0.2155	0.06666	0.03807	1.051	0.1316
0.175	2.10274	0.2930	0.2127	0.05309	0.02728	0.7960	0.09586
0.15	2.10233	0.2732	0.2055	0.04788	0.01988	0.5805	0.07166
0.125	2.10173	0.2572	0.2084	0.03576	0.01313	0.4027	0.05131
0.1	2.10187	0.2567	0.2185	0.02960	0.008628	0.2560	0.03368
0.075	2.10129	0.2374	0.2118	0.02071	0.004852	0.1433	0.01839
0.05	2.10160	0.2269	0.2111	0.01379	0.002024	0.06302	0.008522
0.025	2.10122	0.2250	0.2184	0.006130	0.0004929	0.01568	0.002114
				$T^* = 2.5$			
1.05	2.50019	6.204	0.1119	0.1172	5.975	83.73	4.149
1.0	2.49980	4.601	0.1127	0.1105	4.378	69.54	3.752
0.95	2.50130	3.480	0.1182	0.1231	3.239	57.85	3.402
0.9	2.50171	2.819	0.1213	0.1518	2.546	48.08	3.034
0.9	2.50171	2.805	0.1228	0.1530	2.529	47.86	3.020
0.85	2.50252	2.236	0.1253	0.1508	1.960	39.48	2.585
0.8	2.50221	1.865	0.1328	0.1798	1.552	32.53	2.376
0.75	2.50223	1.504	0.1408	0.1758	1.187	26.41	2.032
0.7	2.50041	1.238	0.1486	0.1719	0.9180	21.42	1.751
0.65	2.50131	1.072	0.1576	0.1741	0.7399	17.33	1.519
0.6	2.50087	0.9096	0.1709	0.1698	0.5689	13.82	1.261

Continued from previous page.

ρ^*	T^*	η^*	η_{tt}^*	η_{tc}^*	η_{cc}^*	$G_{c,\infty}^*$	$G_{tc,max}^*$
0.55	2.50129	0.7742	0.1698	0.1573	0.4471	10.96	1.059
0.5	2.50195	0.6483	0.1746	0.1448	0.3289	8.577	0.8597
0.45	2.50272	0.5987	0.1912	0.1476	0.2599	6.635	0.7211
0.4	2.50315	0.5102	0.1953	0.1266	0.1883	5.040	0.5399
0.35	2.50297	0.4715	0.2109	0.1203	0.1403	3.700	0.4202
0.3	2.50324	0.4095	0.2158	0.1005	0.09315	2.614	0.3114
0.25	2.50309	0.3649	0.2251	0.08047	0.05935	1.761	0.2169
0.2	2.50295	0.3366	0.2305	0.06896	0.03714	1.104	0.1425
0.175	2.50261	0.3380	0.2447	0.06432	0.02900	0.8357	0.1085
0.15	2.50290	0.3045	0.2385	0.04684	0.01917	0.6054	0.07478
0.125	2.50278	0.3018	0.2480	0.04061	0.01323	0.4189	0.05613
0.1	2.50283	0.2934	0.2506	0.03353	0.009301	0.2655	0.03557
0.075	2.50197	0.2789	0.2496	0.02462	0.004585	0.1479	0.02009
0.05	2.50177	0.2794	0.2602	0.01686	0.002133	0.06477	0.009333
0.025	2.50156	0.2387	0.2301	0.008071	0.0005051	0.01618	0.002375
				$T^* = 3.0$			
1.1	3.00181	7.037	0.1328	0.1209	6.784	105.6	5.253
1.05	3.00002	5.500	0.1304	0.1281	5.242	89.75	4.778
1.0	2.99953	4.253	0.1324	0.1526	3.968	74.82	4.302
0.95	3.00122	3.369	0.1366	0.1789	3.054	62.39	3.842
0.9	3.00162	2.751	0.1400	0.1786	2.432	51.86	3.411
0.85	3.00273	2.258	0.1476	0.1862	1.924	42.96	3.017
0.8	3.00188	1.832	0.1520	0.1825	1.498	35.17	2.651
0.75	3.00226	1.546	0.1589	0.1882	1.199	28.91	2.310
0.7	3.00078	1.307	0.1705	0.1906	0.9460	23.43	1.978
0.65	3.00198	1.092	0.1718	0.1797	0.7405	18.89	1.682
0.6	3.00141	0.9401	0.1885	0.1796	0.5720	15.11	1.427
0.55	3.00147	0.8249	0.1996	0.1785	0.4469	11.98	1.171
0.5	3.00216	0.7203	0.2049	0.1724	0.3429	9.367	0.9797
0.45	3.00225	0.6359	0.2170	0.1531	0.2657	7.244	0.7599
0.4	3.00254	0.5561	0.2342	0.1319	0.1900	5.429	0.6001
0.4	3.00225	0.5623	0.2350	0.1336	0.1937	5.479	0.6334
0.35	3.00189	0.4911	0.2308	0.1236	0.1366	4.012	0.4765
0.35	3.00173	0.4965	0.2399	0.1212	0.1353	3.997	0.4625
0.3	3.00221	0.4323	0.2387	0.1006	0.09293	2.824	0.3406
0.3	3.00246	0.4348	0.2410	0.1005	0.09325	2.827	0.3432
0.25	3.00263	0.3994	0.2504	0.08597	0.06305	1.897	0.2372
0.25	3.00240	0.4047	0.2566	0.08446	0.06372	1.901	0.2426

Continued from previous page.

ρ^*	T^*	η^*	η^*_{tt}	η^*_{tc}	η^*_{cc}	$G^*_{c,\infty}$	$G^*_{tc,max}$
0.2	3.00210	0.3839	0.2651	0.07707	0.04174	1.177	0.1487
0.175	3.00246	0.3636	0.2691	0.06610	0.02835	0.8891	0.1134
0.15	3.00292	0.3297	0.2596	0.04992	0.02013	0.6426	0.08435
0.125	3.00226	0.3222	0.2708	0.03855	0.01290	0.4403	0.06050
0.1	3.00262	0.3243	0.2785	0.03717	0.008618	0.2778	0.03865
0.075	3.00237	0.3195	0.2866	0.02829	0.004546	0.1557	0.02121
0.05	3.00155	0.3152	0.2950	0.01813	0.002072	0.06831	0.009754
0.025	3.00191	0.3063	0.2988	0.007073	0.0004903	0.01684	0.002290
			$T^* = 4.0$				
1.15	4.00066	7.819	0.1528	0.1203	7.546	139.5	6.902
1.1	4.00094	6.008	0.1580	0.1332	5.717	118.5	6.315
1.05	4.00009	4.699	0.1578	0.1404	4.401	100.2	5.673
1.0	3.99971	3.866	0.1715	0.1674	3.527	84.02	5.203
0.95	4.00129	3.266	0.1713	0.2113	2.883	70.64	4.700
0.9	4.00121	2.659	0.1798	0.2120	2.268	58.83	4.078
0.85	4.00206	2.156	0.1809	0.1868	1.789	48.71	3.604
0.8	4.00175	1.849	0.1904	0.2148	1.444	40.33	3.174
0.75	4.00223	1.583	0.2014	0.2254	1.156	33.02	2.814
0.7	4.00109	1.353	0.2120	0.2127	0.9283	27.03	2.393
0.65	4.00220	1.150	0.2150	0.1981	0.7370	21.82	2.035
0.6	4.00182	0.9928	0.2290	0.1874	0.5763	17.55	1.711
0.55	4.00180	0.8777	0.2445	0.1802	0.4529	13.91	1.413
0.5	4.00216	0.7735	0.2501	0.1713	0.3521	10.81	1.163
0.45	4.00176	0.6939	0.2625	0.1586	0.2728	8.283	0.9288
0.4	4.00119	0.6271	0.2786	0.1522	0.1962	6.265	0.7317
0.35	4.00024	0.5572	0.2806	0.1351	0.1415	4.595	0.5734
0.3	4.00051	0.5014	0.2983	0.1077	0.09543	3.232	0.4014
0.25	4.00107	0.4745	0.3106	0.09678	0.06717	2.149	0.2787
0.2	4.00120	0.4187	0.3084	0.07141	0.03888	1.326	0.1837
0.175	4.00170	0.4259	0.3249	0.07235	0.02863	1.000	0.1412
0.15	4.00213	0.4222	0.3367	0.06373	0.02173	0.7217	0.09896
0.125	4.00238	0.3878	0.3236	0.04955	0.01464	0.4935	0.07235
0.1	4.00292	0.4037	0.3475	0.04626	0.009930	0.3115	0.04849
0.075	4.00248	0.3757	0.3413	0.02957	0.004834	0.1731	0.02631
0.05	4.00278	0.3792	0.3567	0.02043	0.002129	0.07580	0.01145
0.05	4.00269	0.3756	0.3542	0.01935	0.002045	0.07600	0.01174
0.025	4.00259	0.3870	0.3763	0.01020	0.0005208	0.01870	0.002975

Continued from previous page.

ρ^*	T^*	η^*	η^*_{tt}	η^*_{tc}	η^*_{cc}	$G^*_{\mathrm{c},\infty}$	$G^*_{\mathrm{tc,max}}$
				$T^* = 6.0$			
1.275	5.99620	11.06	0.1946	0.1123	10.75	238.7	11.58
1.25	5.99469	9.756	0.1959	0.1499	9.410	220.45	10.95
1.2	5.99437	7.730	0.2066	0.1471	7.376	189.54	9.998
1.15	5.99613	6.402	0.2030	0.2011	5.998	162.86	9.215
1.1	5.99953	5.285	0.2245	0.1991	4.862	138.46	8.301
1.05	5.99957	4.470	0.2157	0.2377	4.016	118.31	7.682
1.0	5.99992	3.626	0.2255	0.2352	3.165	100.16	6.737
0.95	6.00049	3.151	0.2399	0.2741	2.636	84.74	6.116
0.9	6.00037	2.654	0.2490	0.2624	2.143	71.00	5.391
0.85	6.00076	2.239	0.2544	0.2528	1.732	59.02	4.749
0.8	6.00087	1.940	0.2659	0.2669	1.407	49.24	4.198
0.75	6.00187	1.658	0.2759	0.2377	1.144	40.50	3.600
0.7	6.00107	1.458	0.2862	0.2493	0.9223	33.14	3.092
0.65	6.00300	1.289	0.2959	0.2409	0.7518	27.00	2.666
0.6	6.00286	1.146	0.3148	0.2269	0.6042	21.61	2.250
0.55	6.00303	1.021	0.3329	0.2115	0.4763	17.20	1.873
0.5	6.00290	0.9272	0.3486	0.2111	0.3675	13.46	1.523
0.45	6.00198	0.8132	0.3551	0.1774	0.2807	10.39	1.227
0.4	6.00099	0.7161	0.3582	0.1563	0.2016	7.763	0.9526
0.35	5.99962	0.6741	0.3717	0.1530	0.1494	5.662	0.7322
0.3	5.99964	0.6465	0.4144	0.1272	0.1049	3.980	0.5252
0.25	6.00016	0.6076	0.4219	0.1173	0.06841	2.651	0.3685
0.2	6.00060	0.5707	0.4353	0.09260	0.04272	1.631	0.2246
0.175	6.00115	0.5556	0.4394	0.08537	0.03074	1.218	0.1753
0.15	6.00192	0.5321	0.4369	0.07202	0.02311	0.8814	0.1344
0.125	6.00260	0.5307	0.4566	0.05885	0.01521	0.6016	0.08700
0.1	6.00342	0.5108	0.4457	0.05513	0.009904	0.3772	0.05959
0.075	6.00351	0.4965	0.4547	0.03634	0.005469	0.2085	0.03278
0.05	6.00378	0.5052	0.4789	0.02364	0.002603	0.09151	0.01533
0.025	6.00400	0.5024	0.4911	0.01065	0.0005801	0.02239	0.003960

Table D.4. Simulation data for the viscosity η^*, the viscosity contributions η_{tt}^*, η_{tc}^* and η_{cc}^* and configurational shear modulus $G_{c,\infty}^*$ of the Lennard-Jones model fluid at low temperature gaseous states. The simulations extended over 50 million time steps.

ρ^*	T^*	η^*	η_{tt}^*	η_{tc}^*	η_{cc}^*	$G_{c,\infty}^*$
$T^* = 0.7$
0.015	0.701737	0.07687	0.07619	0.0002798	0.0004057	0.009262
0.01	0.700261	0.07720	0.07690	0.00009168	0.0002074	0.003952
0.005	0.700042	0.07383	0.07379	-0.00003588	0.00008097	0.0009571
$T^* = 0.8$
0.03	0.805997	0.08943	0.08704	0.001244	0.001148	0.03345
0.025	0.802795	0.09009	0.08770	0.001575	0.0008120	0.02265
0.02	0.801016	0.08830	0.08669	0.001063	0.0005395	0.01416
0.015	0.800502	0.08527	0.08423	0.0007139	0.0003221	0.007804
0.01	0.800297	0.08895	0.08808	0.0007105	0.0001665	0.003407
0.005	0.800417	0.09158	0.09109	0.0004282	0.00006229	0.0008391
$T^* = 0.9$
0.05	0.911084	0.1051	0.09829	0.004010	0.002764	0.08592
0.045	0.906600	0.1029	0.09749	0.003209	0.002162	0.06818
0.04	0.903904	0.1030	0.09743	0.003891	0.001725	0.05301
0.035	0.902210	0.1034	0.09881	0.003291	0.001288	0.04002
0.03	0.901239	0.1014	0.09798	0.002490	0.0009784	0.02902
0.025	0.900315	0.09764	0.09498	0.001975	0.0006890	0.01991
0.02	0.900276	0.09945	0.09705	0.001928	0.0004720	0.01261
0.015	0.900297	0.1002	0.09887	0.001064	0.0002733	0.007015
0.01	0.900497	0.09835	0.09730	0.0009155	0.0001409	0.003092
0.005	0.900443	0.09924	0.09866	0.0005293	0.00004899	0.0007652
$T^* = 1.0$
0.07	1.01026	0.1236	0.1104	0.008395	0.004884	0.1547
0.06	1.00481	0.1191	0.1093	0.006371	0.003441	0.1112
0.05	1.00170	0.1191	0.1103	0.006501	0.002390	0.07596
0.04	1.00028	0.1168	0.1110	0.004292	0.001539	0.04791
0.03	1.00007	0.1145	0.1104	0.003268	0.0008723	0.02656
0.02	0.999982	0.1114	0.1088	0.002196	0.0004195	0.01166
0.01	1.00058	0.1147	0.1135	0.001092	0.0001195	0.002884
$T^* = 1.1$
0.07	1.10155	0.1331	0.1193	0.009362	0.004394	0.1409
						Continued on next page.

Continued from previous page.

ρ^*	T^*	η^*	η^*_{tt}	η^*_{tc}	η^*_{cc}	$G^*_{c,\infty}$
0.06	1.10063	0.1294	0.1180	0.008153	0.003229	0.1025
0.05	1.09959	0.1276	0.1188	0.006557	0.002216	0.07063
0.04	1.09951	0.1269	0.1201	0.005323	0.001439	0.04491
0.03	1.09992	0.1254	0.1205	0.004093	0.0008243	0.02506
0.02	1.10010	0.1229	0.1201	0.002424	0.0003804	0.01105
0.01	1.10065	0.1242	0.1227	0.001425	0.0001134	0.002750
			$T^* = 1.2$			
0.15	1.21424	0.1796	0.1305	0.02797	0.02116	0.6353
0.125	1.20713	0.1661	0.1293	0.02213	0.01468	0.4364
0.1	1.20249	0.1535	0.1282	0.01646	0.008827	0.2762
0.075	1.19962	0.1467	0.1295	0.01226	0.004875	0.1536
0.05	1.19919	0.1418	0.1323	0.007390	0.002100	0.06748
0.025	1.19994	0.1366	0.1324	0.003657	0.0005558	0.01667

Table D.5. Simulation data for the bulk viscosity and difference between the infinite frequency and zero frequency bulk modulus $K_\infty^* - K_0^*$ of the Lennard-Jones model fluid. The simulations extended over 2 million time steps if not denoted otherwise († 10 million time steps).

ρ^*	T^*	η_b^*	$K_\infty^* - K_0^*$	ρ^*	T^*	η_b^*	$K_\infty^* - K_0^*$
			$T^* = 0.7$				
0.85	0.699715	1.281	12.57	0.015	0.701012	0.004582	0.01506
0.8	0.699845	1.327	12.43	0.01	0.700092	0.001414	0.006415
0.75	0.698757	1.968	12.58	0.005	0.700063	0.0003879	0.0008930
			$T^* = 0.8$				
0.85	0.800689	1.091	12.98	0.025	0.802965	0.007636	0.03711
0.8	0.801086	1.152	12.73	0.02	0.800700	0.003504	0.02288
0.75	0.801714	1.324	12.84	0.015	0.800480	0.002346	0.01175
0.7	0.799703	3.094	13.24	0.01	0.800439	0.0009345	0.004985
0.03	0.803295	0.01568	0.05470	0.005	0.800436	-	0.001423
			$T^* = 0.9$				
0.85	0.900526	1.022	13.77	0.035	0.900743	0.008161	0.1048
0.8	0.900832	0.9964	13.15	0.03	0.898053	0.003934	0.08318
0.75	0.901804	1.030	12.86	0.025	0.900334	0.002543	0.06362
0.7	0.900372	1.445	12.78	0.02	0.900045	0.001614	0.04623
0.65	0.902284	5.175	13.21	0.015	0.900353	0.001217	0.03075
0.05	0.909642	0.02548	0.1900	0.01	0.900418	0.0005779	0.01915
0.045	0.907209	0.02954	0.1582	0.005	0.900599	0.0002048	0.008740
0.04	0.902970	0.01761	0.1298				
			$T^* = 1.0$				
0.9	0.999972	1.062	14.92	0.05	1.00158	0.009849	0.1208
0.85	1.00042	0.8897	14.16	0.045	1.00093	0.007800	0.09566
0.8	1.00046	0.8775	13.66	0.04	0.999160	0.006747	0.07512
0.75	1.00124	0.9321	13.14	0.035	0.998963	-	0.05707
0.7	1.00028	1.233	12.76	0.03	0.995815	0.002676	0.04152
0.65	1.00149	1.899	12.12	0.025	1.00029	0.002858	0.02807
0.6	1.00382	6.048	12.47	0.02	1.00030	0.001265	0.01722
0.07	1.00987	0.05535	0.2432	0.015	1.00014	0.0008958	0.009779
0.065	1.00651	0.03425	0.2118	0.01	1.00062	0.0004715	0.005172
0.06	1.00467	0.01733	0.1780	0.005	1.00035	0.00009544	0.0005691
0.055	1.00220	0.02053	0.1477				

Continued on next page.

Continued from previous page.

ρ^*	T^*	η_b^*	$K_\infty^* - K_0^*$	ρ^*	T^*	η_b^*	$K_\infty^* - K_0^*$
			$T^* = 1.1$				
0.9	1.10011	0.8023	15.53	0.06	1.10102	0.01269	0.1628
0.85	1.10034	0.9360	14.89	0.055	1.09980	0.009393	0.1346
0.8	1.10021	0.9154	14.47	0.05	1.09965	0.006691	0.1335
0.75	1.10050	0.7918	13.29	0.045	1.09994	0.006435	0.08990
0.7	1.09969	1.032	12.61	0.04	1.09907	-	0.07179
0.65	1.10136	1.185	12.01	0.035	1.09894	0.002999	0.05251
0.6	1.10156	1.883	11.43	0.03	1.09905	0.002596	0.03851
0.575	1.10251	2.971	10.99	0.025	1.09982	0.001724	0.02570
0.55	1.10416	3.965	10.66	0.02	1.10032	0.001005	0.01625
0.525	1.10962	6.330	10.90	0.015	1.10012	0.0007041	0.009202
0.07	1.10130	0.02245	0.2200	0.01	1.10066	0.0004487	0.004275
0.065	1.10099	0.01527	0.1902	0.005	1.10066	0.0001063	0.0008754
			$T^* = 1.2$				
0.95	1.20061	1.323	17.68	0.55	1.20135	1.608	10.10
0.9	1.20016	1.011	17.03	0.5	1.20376	2.468	9.157
0.85	1.20041	0.8159	16.03	0.125	1.20330	0.08662	0.6860
0.8	1.20015	0.7784	14.49	0.1	1.20179	0.03068	0.4280
0.75	1.20041	0.8022	13.81	0.075	1.20003	0.01561	0.2381
0.7	1.20054	0.8804	13.04	0.05	1.19929	0.006178	0.1032
0.65	1.20087	0.9988	12.00	0.025	1.20012	0.001251	0.02367
0.6	1.20141	1.172	11.10	0.025	1.20001	0.001192	0.02454
			$T^* = 1.25$				
0.95	1.25091	1.178	17.87	0.45	1.25550	2.653	7.643
0.9	1.25033	1.024	17.12	0.2	1.26932	0.5455	1.725
0.85	1.25076	0.8068	16.25	0.175	1.26182	0.2112	1.310
0.8	1.25016	0.7728	15.12	0.15	1.25743	0.1397	0.9685
0.75	1.25031	0.7826	13.89	0.125	1.25407	0.05727	0.6524
0.7	1.24914	0.7830	13.02	0.1	1.25085	0.02976	0.4101
0.65	1.25096	0.8701	12.15	0.075	1.24973	0.01226	0.2308
0.6	1.25154	0.9699	11.01	0.05	1.24923	0.005111	0.1020
0.55	1.25100	1.221	9.918	0.025	1.24991	0.001122	0.02455
0.5	1.25282	1.717	8.871				
			$T^* = 1.3$				
0.95	1.30059	0.9738	18.36	0.45	1.30279	1.439	7.360
0.9	1.30075	0.8751	-	0.225	1.31023	0.4204	2.069

Continued from previous page.

ρ^*	T^*	η_{b}^*	$K_\infty^* - K_0^*$	ρ^*	T^*	η_{b}^*	$K_\infty^* - K_0^*$
0.9	1.30059	0.8914	-	0.2	1.30869	0.2638	1.645
0.85	1.30055	0.7758	16.40	0.175	1.30689	0.1314	1.261
0.8	1.30054	0.7474	15.37	0.15	1.30296	0.1146	0.9263
0.75	1.30027	0.7417	14.32	0.125	1.30141	0.04935	0.6373
0.7	1.30025	0.7597	13.31	0.1	1.29987	0.02527	0.4059
0.65	1.30067	0.7877	12.02	0.075	1.29901	0.01355	0.2242
0.6	1.30118	0.8561	10.80	0.05	1.29950	0.005099	0.09873
0.55	1.30134	1.025	9.699	0.025	1.30030	0.001385	0.02452
0.5	1.30134	1.285	8.470				
			$T^* = 1.35$				
0.95	1.35091	1.065	18.88	0.45	1.35217	1.173	7.289
0.9	1.35062	0.8568	17.86	0.4	1.35457	1.143	6.015
0.85	1.35098	0.7648	16.85	0.35	1.35615	0.9498	4.697
0.8	1.35036	0.7240	15.59	0.3	1.35835	0.8344	3.524
0.75	1.35039	0.7051	14.40	0.3	1.34596	1.107	3.581
0.7	1.34897	0.7382	13.46	0.25	1.35875	0.4268	2.492
0.65	1.35060	0.7831	12.04	0.2	1.35619	0.2448	1.587
0.6	1.35071	0.8059	10.97	0.15	1.35204	0.06452	0.9053
0.55	1.35108	0.8931	9.877	0.1	1.35011	0.02732	0.4037
0.5	1.35118	0.9775	8.665	0.05	1.34991	0.003945	0.09802
$0.35^\dagger$	1.34619	1.400	4.792	$0.3^\dagger$	1.34576	1.056	3.596
$0.45^\dagger$	1.34991	1.183	7.269	$0.2^\dagger$	1.35006	0.2169	1.617
$0.4^\dagger$	1.34943	1.447	6.010	$0.15^\dagger$	1.35043	0.07402	0.9021
$0.35^\dagger$	1.35066	1.066	4.776	$0.1^\dagger$	1.34962	0.02468	0.3963
$0.3^\dagger$	1.35145	0.9176	3.573	$0.05^\dagger$	1.34942	0.004068	0.09937
$0.25^\dagger$	1.35057	0.5125	2.514				
			$T^* = 1.5$				
0.95	1.50111	0.9300	20.42	0.35	1.50334	0.5034	4.511
0.9	1.50096	0.8617	18.93	0.3	1.50385	0.3725	3.360
0.85	1.50146	0.7182	17.54	0.25	1.50334	0.2119	2.361
0.8	1.50082	0.6964	16.31	0.2	1.50219	0.1088	1.534
0.75	1.50051	0.7071	15.16	0.175	1.50129	0.06861	1.176
0.7	1.49888	0.6829	13.62	0.15	1.50038	0.04744	0.8488
0.65	1.50037	0.6993	12.41	0.125	1.49959	0.03081	0.5966
0.6	1.50055	0.6756	11.17	0.1	1.50014	0.01869	0.3862
0.55	1.50127	0.7133	9.807	0.075	1.49941	0.008362	0.2161
0.5	1.50183	0.7273	8.407	0.05	1.49974	0.003875	0.09804

Continued from previous page.

ρ^*	T^*	η_b^*	$K_\infty^* - K_0^*$	ρ^*	T^*	η_b^*	$K_\infty^* - K_0^*$
0.45	1.50213	0.7054	7.049	0.025	1.50032	0.001010	0.02397
0.4	1.50285	0.6306	5.742				

$$T^* = 1.8$$

ρ^*	T^*	η_b^*	$K_\infty^* - K_0^*$	ρ^*	T^*	η_b^*	$K_\infty^* - K_0^*$
1.0	1.80118	1.070	23.92	0.4	1.80369	0.3573	5.738
0.95	1.80124	0.8942	22.87	0.35	1.80332	0.3030	4.395
0.9	1.80133	0.7596	21.20	0.3	1.80323	0.2238	3.253
0.85	1.80200	0.7021	19.37	0.25	1.80321	0.1492	2.279
0.8	1.80192	0.6576	17.63	0.2	1.80199	0.07876	1.456
0.75	1.80127	0.6778	16.33	0.175	1.80178	0.05334	1.128
0.7	1.80075	0.6553	14.66	0.15	1.79827	0.03605	0.8224
0.65	1.80046	0.6316	12.94	0.125	1.80093	0.02394	0.5742
0.6	1.80043	0.5861	11.66	0.1	1.80076	0.01398	0.3705
0.55	1.80133	0.5469	10.07	0.075	1.80035	0.007618	0.2091
0.5	1.80206	0.4979	8.577	0.05	1.80084	0.003195	0.09324
0.45	1.80314	0.4523	7.020	0.025	1.80078	0.0008315	0.02264

$$T^* = 2.1$$

ρ^*	T^*	η_b^*	$K_\infty^* - K_0^*$	ρ^*	T^*	η_b^*	$K_\infty^* - K_0^*$
1.0	2.09999	0.9858	26.87	0.4	2.10572	0.2866	5.808
0.95	2.10129	0.7856	24.74	0.35	2.10334	0.2312	4.444
0.9	2.10164	0.7368	22.84	0.3	2.10307	0.1601	3.309
0.85	2.10234	0.6788	20.97	0.25	2.10362	0.09890	2.281
0.8	2.10193	0.6649	19.16	0.2	2.10281	0.06424	1.468
0.75	2.10155	0.6383	17.51	0.175	2.10274	0.04950	1.124
0.7	2.09985	0.5868	15.70	0.15	2.10233	0.03420	0.8223
0.65	2.10086	0.5616	13.90	0.125	2.10173	0.02337	0.5731
0.6	2.10137	0.5119	12.07	0.1	2.10187	0.01352	0.3772
0.55	2.10092	0.4735	10.33	0.075	2.10129	0.007581	0.2134
0.5	2.10272	0.4166	8.661	0.05	2.10160	0.003323	0.09248
0.45	2.10323	0.3540	7.207	0.025	2.10122	0.0007742	0.02051

$$T^* = 2.5$$

ρ^*	T^*	η_b^*	$K_\infty^* - K_0^*$	ρ^*	T^*	η_b^*	$K_\infty^* - K_0^*$
1.05	2.50019	1.024	32.55	0.45	2.50272	0.3217	7.504
1.0	2.49980	0.8723	29.68	0.4	2.50315	0.2644	6.021
0.95	2.50130	0.7613	27.46	0.35	2.50297	0.1928	4.624
0.9	2.50171	0.7191	25.68	0.3	2.50324	0.1446	3.359
0.9	2.50171	0.7322	25.15	0.25	2.50309	0.09988	2.341
0.85	2.50252	0.6660	23.08	0.2	2.50295	0.06256	1.504
0.8	2.50221	0.6515	21.11	0.175	2.50261	0.04339	1.152
0.75	2.50223	0.6279	18.85	0.15	2.50290	0.02995	0.8380

Continued from previous page.

ρ^*	T^*	η_{b}^*	$K_\infty^* - K_0^*$	ρ^*	T^*	η_{b}^*	$K_\infty^* - K_0^*$
0.7	2.50041	0.5835	16.83	0.125	2.50278	0.02132	0.5851
0.65	2.50131	0.5514	14.86	0.1	2.50283	0.01314	0.3650
0.6	2.50087	0.4881	12.84	0.075	2.50197	0.006954	0.2121
0.55	2.50129	0.4402	11.01	0.05	2.50177	0.003096	0.09350
0.5	2.50195	0.3899	9.164	0.025	2.50156	0.0008006	0.02201

<div align="center">

$T^* = 3.0$

</div>

ρ^*	T^*	η_{b}^*	$K_\infty^* - K_0^*$	ρ^*	T^*	η_{b}^*	$K_\infty^* - K_0^*$
1.1	3.00181	1.118	37.91	0.35	3.00189	0.1807	4.858
1.05	3.00002	1.025	36.99	0.35	3.00173	0.1845	4.850
1.0	2.99953	0.8848	33.68	0.3	3.00221	0.1330	3.524
0.95	3.00122	0.7754	30.90	0.3	3.00246	0.1298	3.547
0.9	3.00162	0.7248	28.22	0.25	3.00263	0.09460	2.478
0.85	3.00273	0.7070	25.83	0.25	3.00240	0.08879	2.453
0.8	3.00188	0.6523	23.08	0.2	3.00210	0.05369	1.559
0.75	3.00226	0.6046	20.84	0.175	3.00250	0.04100	1.202
0.7	3.00078	0.5760	18.24	0.175	3.00246	0.04168	1.195
0.65	3.00198	0.5313	16.02	0.15	3.00292	0.03031	0.8708
0.6	3.00141	0.4651	13.76	0.125	3.00226	0.02149	0.6110
0.55	3.00147	0.4165	11.72	0.1	3.00262	0.01282	0.3831
0.5	3.00216	0.3537	9.797	0.075	3.00237	0.007040	0.2147
0.45	3.00225	0.2740	8.024	0.05	3.00155	0.003170	0.1016
0.4	3.00254	0.2357	6.320	0.025	3.00191	0.0007461	0.02362
0.4	3.00225	0.2371	6.372				

<div align="center">

$T^* = 4.0$

</div>

ρ^*	T^*	η_{b}^*	$K_\infty^* - K_0^*$	ρ^*	T^*	η_{b}^*	$K_\infty^* - K_0^*$
1.15	4.00066	1.258	51.07	0.45	4.00176	0.2598	8.771
1.1	4.00094	1.024	47.76	0.4	4.00119	0.2139	6.983
1.05	4.00009	0.9481	44.19	0.35	4.00024	0.1734	5.394
1.0	3.99971	0.8371	40.14	0.3	4.00051	0.1269	3.904
0.95	4.00129	0.7712	37.10	0.25	4.00107	0.08565	2.661
0.9	4.00121	0.7484	33.66	0.2	4.00120	0.05400	1.705
0.85	4.00206	0.7074	30.23	0.175	4.00170	0.04094	1.301
0.8	4.00175	0.6526	27.39	0.15	4.00213	0.02740	0.9469
0.75	4.00223	0.6022	23.93	0.125	4.00238	0.01992	0.6593
0.7	4.00109	0.5400	21.19	0.1	4.00292	0.01306	0.4398
0.65	4.00220	0.4961	18.40	0.075	4.00248	0.006879	0.2344
0.6	4.00182	0.4538	16.00	0.05	4.00278	0.003013	0.1060
0.55	4.00180	0.3882	13.31	0.025	4.00259	0.0007250	0.02660
0.5	4.00216	0.3237	10.94				

Continued from previous page.

ρ^*	T^*	η_{b}^*	$K_\infty^* - K_0^*$	ρ^*	T^*	η_{b}^*	$K_\infty^* - K_0^*$
			$T^* = 6.0$				
1.275	5.99620	1.609	83.16	0.55	6.00303	0.3730	16.20
1.25	5.99469	1.382	78.43	0.5	6.00290	0.3279	13.38
1.2	5.99437	1.272	72.84	0.45	6.00198	0.2602	10.80
1.15	5.99613	1.123	68.14	0.4	6.00099	0.2144	8.420
1.1	5.99953	1.054	61.50	0.35	5.99962	0.1599	6.389
1.05	5.99957	0.9227	57.95	0.3	5.99964	0.1196	4.658
1.0	5.99992	0.8865	52.52	0.25	6.00016	0.08199	3.201
0.95	6.00049	0.8131	48.40	0.2	6.00060	0.05274	2.015
0.9	6.00037	0.7688	43.18	0.175	6.00115	0.04125	1.534
0.85	6.00076	0.7240	38.20	0.15	6.00192	0.02843	1.110
0.8	6.00087	0.6540	34.34	0.125	6.00260	0.01936	0.7819
0.75	6.00187	0.6268	30.25	0.1	6.00342	0.01212	0.4810
0.7	6.00107	0.5563	26.36	0.075	6.00351	0.006963	0.2572
0.65	6.00300	0.5210	22.78	0.05	6.00378	0.003060	0.1262
0.6	6.00286	0.4498	19.33	0.025	6.00400	0.0007442	0.02780

Table D.6. Simulation data for the bulk viscosity η_b^* of the Lennard-Jones model fluid at low temperature gaseous states. The simulations extended over 50 million time steps ([†] 256 particles).

ρ^*	T^*	η_b^*	ρ^*	T^*	η_b^*
		$T^* = 0.7$			
0.015	0.701737	0.007179	0.005	0.700042	0.0008032
0.01	0.700261	0.002559			
		$T^* = 0.8$			
0.03	0.805997	0.02408	0.015	0.800502	0.002586
0.025	0.802795	0.009713	0.01	0.800297	0.001189
0.02	0.801016	0.004642	0.005	0.800417	0.0004664
		$T^* = 0.9$			
0.05	0.911084	0.1049	0.02	0.900276	0.002293
0.045	0.906600	0.03144	0.015	0.900297	0.001378
0.04	0.903904	0.01579	0.01	0.900497	0.0006703
0.035	0.902210	0.008236	0.005	0.900443	0.0002981
0.03	0.901239	0.005161	0.005	0.903340	0.0002419[†]
0.025	0.900315	0.003026			
		$T^* = 1.0$			
0.07	1.01026	0.09162	0.03	1.00007	0.003432
0.06	1.00481	0.02718	0.02	0.999982	0.001386
0.05	1.00170	0.01214	0.01	1.00058	0.0004646
0.04	1.00028	0.006525			
		$T^* = 1.1$			
0.07	1.10155	0.02022	0.03	1.09992	0.002361
0.06	1.10063	0.01196	0.02	1.10010	0.001161
0.05	1.09959	0.006883	0.01	1.10065	0.0003296
0.04	1.09951	0.004499			
		$T^* = 1.2$			
0.15	1.21424	0.2652	0.075	1.19962	0.01542
0.125	1.20713	0.1079	0.05	1.19919	0.005599
0.1	1.20249	0.04212	0.025	1.19994	0.001288

Table D.7. Simulation data for thermodynamic state variables and transport coefficients at the state point ($T^* = 0.722$, $\rho^* = 0.8442$) close to the triple point of the Lennard-Jones model fluid. The simulations extended over 10 million time steps († 25 million time steps)

N	r^*_{cut}	T^*	u^*	p^*_c	C^*_V	$D^*\rho^*$	$G^*_{t,\infty}$	$G^*_{c,\infty}$	η^*_{tt}	η^*_{tc}	η^*_{cc}	η^*	η^*_{b}
108	2.5	0.731262	-6.09389	-0.52928	2.6193	-	0.6073	22.67	0.04786	0.05222	2.884	2.984	1.290
256	3.25	0.733052	-6.07404	-0.40931	2.6191	-	0.6161	23.32	0.04999	0.06119	2.994	3.105	1.185
500	4.0	0.722001	-6.08159	-0.44847	2.6290	-	0.6075	23.30	0.04937	0.06132	3.077	3.188	1.102
864	5.0	0.721355	-6.08250	-0.45235	2.6269	-	0.6084	23.33	0.04959	0.05621	3.208	3.314	1.139
2048	5.5	0.721444	-6.08250	-0.45044	2.6288	-	0.6097	23.32	0.05149	0.05840	3.114	3.224	1.217
4000	5.5	0.722109	-6.08182	-0.44672	2.6314	-	0.6098	23.37	0.05097	0.06146	3.163	3.275	1.194
4000	5.5†	0.722096	-6.08180	-0.44653	2.6248	-	0.6099	23.31	0.05060	0.06330	3.132	3.246	1.145
1372	2.5	0.723441	-6.08996	-0.46290	2.6352	0.027441	0.6086	23.40	0.04885	0.07249	3.156	3.277	1.186
1372	2.75	0.732155	-6.06498	-0.38897	2.6204	0.027975	0.6181	23.46	0.05165	0.06307	3.156	3.271	1.092
1372	3.0	0.712572	-6.09053	-0.49576	2.6280	0.026920	0.6006	23.14	0.04990	0.06345	3.182	3.295	1.123
1372	3.25	0.730478	-6.07433	-0.40435	2.6192	0.027910	0.6168	23.45	0.05041	0.06661	3.107	3.224	1.196
1372	3.5	0.717710	-6.08725	-0.47427	2.6218	0.027069	0.6051	23.30	0.05000	0.06614	3.153	3.269	1.163
1372	3.75	0.719279	-6.08423	-0.46284	2.6338	0.027347	0.6078	23.32	0.05030	0.05918	3.128	3.237	1.147
1372	4.0	0.721561	-6.08231	-0.45028	2.6217	0.027577	0.6085	23.24	0.05112	0.05442	3.140	3.245	1.163
1372	4.25	0.718948	-6.08563	-0.46545	2.6306	0.027298	0.6053	23.25	0.04929	0.05898	3.091	3.199	1.137
1372	4.5	0.721795	-6.08211	-0.44977	2.6238	0.027447	0.6086	23.28	0.05023	0.07637	3.123	3.249	1.159
1372	4.75	0.721195	-6.08266	-0.45269	2.6248	0.027523	0.6065	23.33	0.05073	0.05840	3.082	3.191	1.153
1372	5.0	0.721228	-6.08280	-0.45261	2.6262	0.027517	0.6095	23.31	0.05085	0.05804	3.113	3.222	1.140
1372	5.25	0.722564	-6.08127	-0.44504	2.6296	0.027630	0.6099	23.27	0.05039	0.05581	3.055	3.161	1.148
1372	5.5	0.722266	-6.08154	-0.44678	2.6305	0.027687	0.6096	23.30	0.05067	0.06013	3.174	3.284	1.133

Table D.8. Simulation data for the thermal conductivity λ^*, thermal conductivity contributions λ_{tt}^*, λ_{tc}^* and λ_{cc}^*, configurational thermal modulus $\Theta_{c,\infty}^* - \Theta_{c,0}^*$ and normalization factor for the translational-configurational heat flux correlation function $\Theta_{tc,max}^*$ on the close-critical isotherm $T^* = 1.35$. The simulations extended over 2 million time steps if not denoted otherwise († 10 million time steps).

ρ^*	T^*	λ^*	λ_{tt}^*	λ_{tc}^*	λ_{cc}^*	$\Theta_{c,\infty}^* - \Theta_{c,0}^*$	$\Theta_{tc,max}$
0.95	1.35091	10.94	0.1629	1.191	9.584	132.2	9.886
0.9	1.35062	9.328	0.1854	1.192	7.950	107.3	9.059
0.85	1.35098	8.072	0.1990	1.165	6.708	87.24	8.112
0.8	1.35036	6.820	0.2273	1.122	5.471	70.36	7.210
0.75	1.35039	5.676	0.2373	1.048	4.391	56.59	6.365
0.7	1.34897	4.863	0.2673	1.078	3.517	45.50	5.586
0.65	1.35060	4.162	0.2957	1.023	2.843	36.28	4.832
0.6	1.35071	3.360	0.3098	0.9099	2.141	29.02	4.087
0.55	1.35108	3.069	0.3493	0.9488	1.771	23.30	3.495
0.5	1.35118	2.513	0.3430	0.7916	1.378	18.60	2.866
0.45	1.35217	2.307	0.3968	0.7909	1.119	14.69	2.361
0.4	1.35457	2.001	0.3972	0.6869	0.9166	11.46	1.911
0.35	1.35615	1.783	0.4080	0.6142	0.7608	8.735	1.498
0.3	1.35835	1.551	0.4293	0.5311	0.5902	6.465	1.131
0.3	1.34596	1.644	0.4148	0.5588	0.6704	6.449	1.125
0.25	1.35875	1.401	0.4466	0.4950	0.4598	4.503	0.8190
0.2	1.35619	1.180	0.4508	0.3949	0.3346	2.889	0.5303
0.15	1.35204	0.9876	0.4992	0.3105	0.1779	1.611	0.3167
0.1	1.35011	0.8410	0.5419	0.2138	0.08534	0.7141	0.1408
0.05	1.34991	0.6848	0.5427	0.1174	0.02468	0.1762	0.03730
$0.35^\dagger$	1.34619	1.792	0.4250	0.6238	0.7428	8.778	1.495
$0.3^\dagger$	1.34576	1.646	0.4138	0.5770	0.6553	6.462	1.129
$0.45^\dagger$	1.34991	2.247	0.3758	0.7618	1.109	14.64	2.371
$0.4^\dagger$	1.34943	1.984	0.3919	0.6784	0.9139	11.45	1.904
$0.35^\dagger$	1.35066	1.911	0.4319	0.6705	0.8084	8.778	1.505
$0.3^\dagger$	1.35145	1.742	0.4421	0.5975	0.7020	6.476	1.133
$0.25^\dagger$	1.35057	1.500	0.4581	0.5211	0.5205	4.526	0.8231
$0.2^\dagger$	1.35006	1.159	0.4508	0.3726	0.3359	2.887	0.5370
$0.15^\dagger$	1.35043	0.9869	0.4708	0.3173	0.1988	1.625	0.3112
$0.1^\dagger$	1.34962	0.7988	0.5011	0.2115	0.08618	0.7125	0.1413
$0.05^\dagger$	1.34942	0.6336	0.5110	0.1002	0.02244	0.1756	0.03575

Bibliography

[1] **Abramowitz, M.; Stegun, I.A. (Eds.)**: *Handbook of Mathematical Functions*, Applied Mathematics Series No. 55, National Bureau of Standards, Washington, 1964.

[2] **Agrawal, R.; Kofke, D.A.**: Thermodynamic and structural properties of model systems at solid-fluid coexistence. II. Melting and sublimation of the Lennard-Jones system, Molec. Phys., **85** (1) 43-59, 1995.

[3] **Alavi, S.; Snider, R.F.**: Complete binary collision approximation for the gas transport coefficients via the time correlation formulation, J. Chem. Phys., **109** (9) 3452-3460, 1998.

[4] **Alavi, S.; Snider, R.F.**: Moderately dense gas transport coefficients via time correlation functions. II. Shear viscosity and thermal conductivity, J. Chem. Phys., **111** (15) 6922-6931, 1999.

[5] **Alder, B.J.; Wainwright, T.E.**: Molecular dynamics by electronic computers, in: *Proc. of the Int. Symp. on Statistical Mechanical Theory of Transport Processes (Brussels, 1956)*, pp. 97-131, edited by I. Prigogine (John Wiley & Sons, New York, 1958).

[6] **Alder, B.J.; Wainwright, T.E.**: Velocity autocorrelations for hard spheres, Phys. Rev. Lett., **18** (23) 988-990, 1967.

[7] **Alder, B.J.; Gass, D.M.; Wainwright, T.E.**: Studies in molecular dynamics. VIII. The transport coefficients for a hard-sphere fluid, J. Chem. Phys., **53** (10) 3813-3826, 1970.

[8] **Alder, B.J.; Wainwright, T.E.**: Decay of the velocity autocorrelation function, Phys. Rev. A, **1** (1) 18-21, 1970.

[9] **Alder, B.J.; Alley, W.E.**: Generalized hydrodynamics, Phys. Today, **37** (1) 56-63, 1984.

[10] **Allen, M.P.; Tildesley, D.J.**: *Computer Simulation of Liquids* (Clarendon Press, Oxford, 1987).

[11] **Arends, B.; Prins, K.O.; Trappeniers, N.J.**: Self-diffusion in gaseous and liquid ethylene, Physica A, **107**, 307-318, 1981.

[12] **Arya, G.; Maginn, E.J.; Chang, H.-C.**: Efficient viscosity estimation from molecular dynamics simulation via momentum impulse relaxation, J.

Chem. Phys., **113** (6) 2079-2087, 2000.

[13] **Ashurst, W.T.; Hoover, W.G.**: Dense-fluid shear viscosity via nonequilibrium molecular dynamics, Phys. Rev. A, **11** (2) 658-678, 1975.

[14] **Assael, M.J.; Trusler, J.P.M.; Tsolakis, T.F.**: *Thermophysical Properties of Fluids - An Introduction to their Prediction* (Imperial College Press, London, 1996).

[15] **Avoird, A. van der; Wormer, P.E.S.; Jansen, A.P.J.**: An improved intermolecular potential for nitrogen, J. Chem. Phys., **84** (3) 1629-1635, 1986.

[16] **Aziz, R.A.**: A highly accurate interatomic potential for argon, J. Chem. Phys., **99** (6) 4518-4525, 1993.

[17] **Baehr, H.D.; Stephan, K.**: *Heat and Mass Transfer* (Springer-Verlag, Berlin, 1998).

[18] **Becker, R.**: *Theorie der Wärme (in German)* (Springer-Verlag, Berlin, 1955).

[19] **Bennett, D.E.; Curtiss, C.F.**: Density effects on the transport coefficients of gaseous mixtures, J. Chem. Phys., **51** (7) 2811-2825, 1969.

[20] **Bich, E.; Vogel, E.**: Initial Density Dependence, pp. 72-82 in: *Transport properties of fluids: their correlation, prediction and estimation*, edited by J. Millat; J.H. Dymond and C.A. Nieto de Castro (Cambridge University Press, Cambridge, 1996).

[21] **Bishop, M.; Michels, J.P.J.**: The influence of the attractive part of the Lennard-Jones potential on the viscosity, Chem. Phys. Lett., **94** (2) 209-212, 1983.

[22] **Bock, S.; Bich, E.; Vogel, E.**: A new intermolecular potential energy surface for carbon dioxide from ab initio calculations, Chem. Phys., **257**, 147-156, 2000.

[23] **Bock, S.**: *Rechnungen zur Potentialhyperfläche und ausgewählten thermophysikalischen Eigenschaften von Kohlendioxid* (Dr. rer. nat.-Thesis, Mathematisch-Naturwissenschaftliche Fakultät, Universität Rostock, 2002).

[24] **Boon, J.P.; Yip, S.**: *Molecular Hydrodynamics* (McGraw-Hill, New York, 1980).

[25] **Borgelt, P.; Hoheisel, C.; Stell, G.**: Exact molecular dynamics and kinetic theory results for thermal transport coefficients of the Lennard-Jones argon fluid in a wide region of states, Phys. Rev. A, **42** (2) 789-794, 1990.

[26] **Brandt, S.**: *Datenanalyse (in German)*, 4th edition (Spektrum Akademischer Verlag, Heidelberg, 1999).

[27] **Brunson, R.R.; Byers, C.H.**: Viscosities of alcohol-hydrocarbon systems in the critical region: a dynamic laser light scattering approach. J. Chem. Eng. Data, 34 (1) 46-52, 1989.

[28] **Caǧin, T.; Ray, J.R.**: Fundamental treatment of molecular-dynamics ensembles, Phys. Rev. A, **37** (1) 247-251, 1988.

[29] **Callen, H.B.**: *Thermodynamics and an Introduction to Thermostatistics*, 2nd edition (John Wiley & Sons, New York, 1985).

[30] **Canales, M.; Padró, J.A.**: Dynamic properties of Lennard-Jones fluids and liquid metals, Phys. Rev. E, **60** (1) 551-558, 1999.

[31] **Castillo, R.; Villaverde, A.; Orozco, J.**: Prediction of transport properties for Lennard-Jones fluids and their binary mixtures using effective-diameter hard-sphere kinetic theory, Molec. Phys., **74** (6) 1315-1334, 1991.

[32] **Chen, S.-H.; Rahman, A.**: Molecular dynamics simulation of dense gases. I. Test particle motion, Molec. Phys., **34** (5) 1247-1262, 1977.

[33] **Cowan, J.A.; Ball, R.N.**: Temperature dependence of bulk viscosity in liquid argon, J. Can. Phys., **50**, 1881-1886, 1972.

[34] **Curtiss, C.F.; McElroy, M.B.; Hoffman, D.K.**: The transport properties of a moderately dense Lennard-Jones gas, Int. J. Eng. Sci., **3**, 269-283, 1965.

[35] **Dufty, J.W.; Gubbins, K.E.**: The self-diffusion coefficient for a square well fluid, Chem. Phys. Lett., **64** (1) 142-145, 1979.

[36] **Dymond, J.H.; Patterson, P.M.; Harris, K.R.; Woolf, L.A.**: Diffusion in molecular fluids, High Temp.-High Pres., **23**, 97-105, 1991.

[37] **Einstein, A.**: Über die von der molekularkinetischen Theorie der Wärme geforderte Bewegung von in ruhenden Flüssigkeiten suspendierten Teilchen (in German), Ann. Phys., **17**, 549-560, 1905.

[38] **Einstein, A.**: *Investigations on the Theory of the Brownian Movement*, edited by R. Fürth (Dover Publications, New York, 1956).

[39] **Ermakova, E.; Solca, J.; Huber, H.; Welker, M.**: Argon in condensed phase: Quantitative calculations of structural, thermodynamic, and transport properties from pure theory, J. Chem. Phys., **102** (12) 4942-4951, 1995.

[40] **Ernst, M.H.; Hauge, E.H.; van Leeuwen, J.M.J.**: Asymptotic time behaviour of correlation functions. I. Kinetic terms, Phys. Rev. A, **4** (5) 2955-2065, 1971.

[41] **Ernst, M.H.; Hauge, E.H.; van Leeuwen, J.M.J.**: Asymptotic time behaviour of correlation functions. II. Kinetic and potential terms, J. Stat. Phys., **15** (1) 7-22, 1976.

[42] **Ernst, M.H.; Hauge, E.H.; van Leeuwen, J.M.J.**: Asymptotic time behaviour of correlation functions. III. Local equilibrium and mode-coupling theory, J. Stat. Phys., **15** (1) 23-58, 1976.

[43] **Erpenbeck, J.J.; Wood, W.W.**: Molecular dynamics calculations of shear viscosity time-correlation functions for hard spheres, J. Stat. Phys., **24** (3) 455-468, 1981.

[44] **Erpenbeck, J.J.**: Comparison of Green-Kubo and nonequlibrium calculations of the self-diffusion constant of a Lennard-Jones fluid, Phys. Rev. A, **35** (1) 218-232, 1987.

[45] **Erpenbeck, J.J.**: Shear viscosity of the Lennard-Jones fluid near the triple point: Green-Kubo results, Phys. Rev. A, **38** (12) 6255-6266, 1988.

[46] **Erpenbeck, J.J.**: Einstein-Kubo-Helfand and McQuarrie relations for transport coefficients, Phys. Rev. E, **51** (5) 4296-4308, 1995.

[47] **Evans, D.J.**: Rheological properties of simple fluids by computer simulation, Phys. Rev. A, **23** (4) 1988-1997, 1981.

[48] **Evans, D.J.; Morriss, G.P.; Hood, L.M.**: On the number dependence of viscosity in three dimensional fluids, Molec. Phys., **68** (3) 637-646, 1989.

[49] **Evans, D.J.; Morriss, G.P.**: *Statistical Mechanics of Nonequilibrium Liquids* (Academic Press, London, 1990).

[50] **Ferrario, M.; Cicotti, G.; Holian, B.L.; Ryckaert, J.P.**: Shear-rate dependence of the viscosity of the Lennard-Jones liquid at the triple point, Phys. Rev. A, **44** (10) 6936-6939, 1991.

[51] **Fokin, L.R.; Popov, V.N.; Kalashnikov, A.N.**: Analytical representation of collision integrals for the (*m*-6) Lennard-Jones potentials in the EPIDIF database, High Temp., **37** (1) 45-51, 1999.

[52] **Frenkel, D.; Smit, B.**: *Understanding Molecular Simulation - From Algorithms to Applications* (Academic Press, San Diego, 1996).

[53] **Friedberg, R.; Cameron, J.E.**: Test of the Monte Carlo method: Fast simulation of a small Ising lattice, J. Chem. Phys., **52** (12) 6049-6058, 1970.

[54] **Friend, D.G.; Rainwater, J.C.**: Transport properties of a moderately dense gas. Chem. Phys. Lett., **107** (6) 590-594, 1984.

[55] **Gardner, P.J.; Heyes, D.M.; Preston, S.R.**: Molecular dynamics computer simulations of binary Lennard-Jones fluid mixtures: Thermodynamics of mixing and transport coefficients, Molec. Phys., **73** (1) 141-173, 1991.

[56] **Gracki, J.A.; Flynn, G.P.; Ross, J.**: Viscosity of nitrogen, helium, hydrogen, and argon from -100 to 25 °C up to 150-250 atm, J. Chem. Phys., **51** (9) 3856-3863, 1969.

[57] **Graves, R.E.; Argrow, B.M.**: Bulk viscosity: Past to present, J. Thermophys. Heat Transfer, **13** (3) 337-342, 1999.

[58] **Green, M.S.**: Markoff random processes and the statistical mechanics of time-dependent phenomena, J. Chem. Phys., **20** (8) 1281-1295, 1952.

[59] **Green, M.S.**: Markoff random processes and the statistical mechanics of time-dependent phenomena. II. Irreversible processes in fluids, J. Chem. Phys., **22** (3) 398-413, 1954.

[60] **Green, M.S.**: Comment on a paper of Mori on time-correlation expressions for transport properties, Phys. Rev., **119** (3) 829-830, 1960.

[61] **Groot, S.R. de; Mazur, P.**: *Non-equilibrium Thermodynamics* (North-Holland Publishing Company, Amsterdam, 1962).

[62] **Gulik, P.S. van der; Trappeniers, N.J.**: The viscosity of argon at high densities, Physica A, **135**, 1-20, 1986.

[63] **Gulik, P.S. van der**: Contribution of the van der Waals laboratory to the knowledge of transport properties of fluids, Int. J. Thermophys., **22** (2) 377-393, 2001.

[64] **Gulik, P.S. van der; Seldam, C.A. ten**: Density dependence of the viscosity of some noble gases, Int. J. Thermophys., **23** (1) 15-26, 2002.

[65] **Haile, J.M.**: *Molecular Dynamics Simulation - Elementary Methods* (John Wiley & Sons, New York, 1992).

[66] **Hammonds, K.D.; Heyes, D.M.**: Transport coefficients of model simple liquids, J. Chem. Soc., Faraday Trans. 2, **84** (6) 705-725, 1988.

[67] **Hanley, H.J.M. (Ed.)**: *Transport Phenomena in Fluids* (Marcel Dekker, New York, 1969).

[68] **Hanley, H.J.M.; Cohen, E.G.D.**: Analysis of the transport coefficients for simple dense fluids: The diffusion and bulk viscosity coefficients, Physica A, **83**, 215-232, 1976.

[69] **Hansen, J.P.; McDonald, I.R.**: *Theory of Simple Liquids*, 2nd edition (Academic Press, London, 1986).

[70] **Harris, K.R.**: The density dependence of the self-diffusion coefficient of methane at -50 °, 25 ° and 50 °C. Physica A, **94**, 448-464, 1978.

[71] **Harris, K.R.; Trappeniers, N.J.**: The density dependence of the self-diffusion coefficient of liquid methane. Physica A, **104**, 262-280, 1980.

[72] **Harris, K.R.**: Correlation of dense-fluid self-diffusion and shear viscosity coefficients. High Temp.-High Pres., **25**, 359-366, 1993.

[73] **Haynes, W.M.**: Viscosity of gaseous and liquid argon, Physica, **67**, 440-470, 1973.

[74] **Heck, E.L.; Dickinson, A.S.**: Transport and relaxation properties of N_2, Molec. Phys., **81** (6) 1325-1352, 1994.

[75] **Heck, E.L.; Dickinson, A.S.; Vesovic, V.**: Second-order corrections for transport properties of pure diatomic gases, Molec. Phys., **83** (5) 907-932, 1994.

[76] **Heck, E.L.**: Traditional transport properties of CO, Physica A, **217**, 107-123, 1995.

[77] **Helfand, E.**: Transport coefficients from dissipation in a canonical ensemble, Phys. Rev., **119** (1) 1-9, 1960.

[78] **Heyes, D.M.; Kim, J.J.; Montrose, C.J.; Litovitz, T.A.**: Time dependent nonlinear shear stress effects in simple liquids: A molecular dynamics study, J. Chem. Phys., **73** (8) 3987-3996, 1980.

[79] **Heyes, D.M.**: Self-diffusion and shear viscosity of simple fluids, J. Chem. Soc., Faraday Trans. 2, **79**, 1741-1758, 1983.

[80] **Heyes, D.M.**: Thermal conductivity and bulk viscosity of simple fluids. A molecular-dynamics study, J. Chem. Soc., Faraday Trans. 2, **80**, 1363-1394, 1984.

[81] **Heyes, D.M.**: Some physical consequences of large shear rates on simple liquids, J. Chem. Phys., **85** (2) 997-1008, 1986.

[82] **Heyes, D.M.**: Transport coefficients of the Lennard-Jones fluid by molecular dynamics, Can. J. Phys., **64**, 773-781, 1986.

[83] **Heyes, D.M.**: Viscosity and self-diffusion of simple liquids. Hard-sphere treatment of molecular dynamics data, J. Chem. Soc., Faraday Trans. 2, **83** (11) 1985-2009, 1987.

[84] **Heyes, D.M.**: Transport coefficients of Lennard-Jones fluids: A molecular dynamics and effective-hard-sphere treatment, Phys. Rev. B, **37** (10) 5677-5696, 1988.

[85] **Heyes, D.M.; Powles, J.G.**: Information theory applied to the transport coefficients of Lennard-Jones fluids, Molec. Phys., **71** (4) 781-800, 1990.

[86] **Heyes, D.M.; Powles, J.G.; J.C. Gil Montero**: Information theory applied to the transport coefficients of Lennard-Jones fluids II, Molec. Phys., **78** (1) 229-234, 1993.

[87] **Hilbers, P.A.J.; Esselink, K.**: Parallel Computing and Molecular Dynamics Simulation, in: *Computer Simulation in Chemical Physics*, NATO ASI Series C, Vol. 397, pp. 473-496, edited by M.P. Allen and D.J. Tildesley (Kluwer Academic Publishers, Dordrecht, 1993).

[88] **Hirschfelder, J.O.; Curtiss, C.F.; Bird, R.B.**: *Molecular Theory of Gases and Liquids* (John Wiley & Sons, New York, 1954).

[89] **Hoffman, D.K.; Curtiss, C.F.**: Kinetic theory of dense gases. III. The generalized Enskog equation, Phys. Fluids, **7** (12) 1887-1897, 1964.

[90] **Hoffman, D.K.; Curtiss, C.F.**: Kinetic theory of dense gases. IV. Transport virial coefficients, Phys. Fluids, **8** (4) 667-682, 1965.

[91] **Hoffman, D.K.; Curtiss, C.F.**: Kinetic theory of dense gases. V. Evaluation of the second transport virial coefficients, Phys. Fluids, **8** (5) 890-895, 1965.

[92] **Hoheisel, C.**: Transport coefficients of dense fluids composed of globular molecules. Equilibrium molecular dynamics investigations using more-center Lennard-Jones potentials, J. Chem. Phys., **89** (5) 3195-3202, 1988.

[93] **Hoheisel, C.; Würflinger, A.**: Thermodynamic and transport properties of cyclohexane computed by molecular dynamics with use of a six-center Lennard-Jones potential, J. Chem. Phys., **91** (1) 473-476, 1989.

[94] **Hoheisel, C.**: Transport properties of molecular liquids, Phys. Rep., **245**, 111-157, 1994.

[95] **Holian, B.L.; Evans, D.J.**: Shear viscosities away from the melting line: A comparison of equilibrium and nonequilibrium molecular dynamics, J. Chem. Phys., **78** (8) 5147-5150, 1983.

[96] **Hoover, W.G.; Evans, D.J.; Hickman, R.B.; Ladd, A.J.C.; Ashurst, W.T.; Moran, B.**: Lennard-Jones triple-point bulk and shear viscosities. Green-Kubo theory, Hamiltonian mechanics, and nonequilibrium molecular dynamics, Phys. Rev. A, **22** (4) 1690-1697, 1980.

[97] **Hoover, W.G.**: *Computational Statistical Mechanics* (Elsevier, Amsterdam, 1991).

[98] **Huber, H.; Dyson, A.J.; Kirchner, B.**: Calculation of bulk properties of liquids and supercritical fluids from pure theory, Chem. Soc. Rev., **28**, 121-133, 1999.

[99] **Hurly, J.J.; Moldover, M.R.**: Ab initio values of the thermophysical properties of helium as standards, J. Res. Natl. Inst. Stand. Technol., **105** (5) 667-688, 2000.

[100] **Irving, J.H.; Kirkwood, J.G.**: The statistical mechanical theory of transport processes. IV. The equations of hydrodynamics, J. Chem. Phys., **18** (6) 817-829, 1950.

[101] **Jackson, J.L.; Mazur, P.**: On the statistical mechanical derivation of the correlation formula for the viscosity, Physica, **30**, 2295-2304, 1964.

[102] **Johnson, J.K.; Zollweg, J.A.; Gubbins, K.E.**: The Lennard-Jones equation of state revisited, Molec. Phys., **78** (3) 591-618, 1993.

[103] **Jones, J.E.**: On the determination of molecular fields. - II. From the equation of state of a gas, Proc. Roy. Soc. London A, **106**, 463-477, 1924.

[104] **Kadanoff, L.P.; Martin, P.C.**: Hydrodynamic equations and correlation functions, Ann. Phys., **24**, 419-469, 1963.

[105] **Kawasaki, K.; Oppenheim, I.**: Logarithmic term in the density expansion of transport coefficients, Phys. Rev., **139**, 6A, A1763-A1768, 1965.

[106] **Kincaid, J.M.; Tuo, R.-F.; de Haro, M.L.**: A test of the modified Enskog theory for self-diffusion, Molec. Phys., **81** (4) 837-840, 1994.

[107] **Klein, M.; Smith, F.J.**: Tables of collision integrals for the $(m,6)$ potential function for 10 values of m, J. Res. Natl. Bur. Stand., **72A** (4) 359-423, 1968.

[108] **Klein, M.; Hanley, H.J.M.; Smith, F.J.; Holland, P.**: *Tables of Collision Integrals and Second Virial Coefficients for the (m,6,8) Intermolecular Potential Function*, National Standard Reference Data Series No. 47, National Bureau of Standards, Washington, 1974.

[109] **Kolafa, J.; Vörtler, H.L.; Aim, K.; Nezbeda, I.**: The Lennard-Jones fluid revisited: Computer simulation results, Molec. Simul., **11** (5) 305-319, 1993.

[110] **Kolafa, J.; Nezbeda, I.**: The Lennard-Jones fluid: An accurate analytic and theoretically-based equation of state, Fluid Phase Equilib., **100**, 1-34, 1994.

[111] **Kubo, R.**: Statistical-mechanical theory of irreversibel processes. I. General theory and simple applications to magnetic and conduction problems, J. Phys. Soc. Japan, **12** (6) 570-586, 1957.

[112] **Kubo, R.; Yokota, M.; Nakajima, S.**: Statistical-mechanical theory of irreversible processes. II. Response to thermal disturbance, J. Phys. Soc. Japan, **12** (11) 1203-1211, 1957.

[113] **Kushick, J.; Berne, B.J.**: Role of attractive forces in self-diffusion in dense Lennard-Jones fluids, J. Chem. Phys., **59** (7) 3732-3736, 1973.

[114] **Lebowitz, J.L.; Percus, J.K.; Verlet, L.**: Ensemble dependence of fluctuations with application to machine computations, Phys. Rev., **153** (1) 250-254, 1967.

[115] **Lee, S.H.; Cummings, P.T.**: Shear viscosity of model mixtures by nonequilibrium molecular dynamics. II. Effect of dipolar interactions, J. Chem. Phys., **105** (5) 2044-2055, 1996.

[116] **Leegwater, J.A.**: Velocity autocorrelation function of Lennard-Jones fluids, J. Chem. Phys., **94** (11) 7402-7410, 1991.

[117] **Leipertz, A.**: Transport properties of transparent liquids by photon-correlation spectroscopy, Int. J. Thermophys., **9** (6) 897-909, 1988.

[118] **Levesque, D.; Verlet, L.; Kürkijarvi, J.**: Computer "experiments" on classical fluids. IV. Transport properties and time-correlation functions of the Lennard-Jones liquid near its triple point, Phys. Rev. A, **7** (5) 1690-1700, 1973.

[119] **Levesque, D.; Verlet, L.**: Molecular dynamics calculations of transport coefficients, Molec. Phys., **61** (1) 143-159, 1987.

[120] **Liem, S.Y.; Brown, D.; Clarke, J.H.R.**: Investigation of the homogeneous-shear nonequilibrium-molecular-dynamics method, Phys. Rev. A, **45** (6) 3706-3713, 1992.

[121] **Liu, H.; Silva, C.M.; Macedo, E.A.**: Unified approach to the self-diffusion coefficients of dense fluids over wide ranges of temperature and pressure - hard-sphere, square-well, Lennard-Jones and real substances, Chem. Eng. Sci., **53** (13) 2403-2422, 1998.

[122] **Lotfi, A.; Vrabec, J.; Fischer, J.**: Vapour liquid equilibria of the Lennard-Jones fluid from the NpT plus test particle method, Molec. Phys., **76** (6) 1319-1333, 1992.

[123] **Lucas, K.; Moser, B.**: A memory function model for the velocity autocorrelation function and the self-diffusion coefficient in simple dense fluids, Molec. Phys., **37** (6) 1849-1857, 1979.

[124] **Luckas, M.**: *Die Berechnung von Transporteigenschaften fluider Stoffe aus Memory-Funktionen (in German)* (Dr.-Ing.-Thesis, Fachgebiet Thermodynamik, Universität Duisburg, 1984).

[125] **Luo, H.**: *Computation of Thermal Transport Properties of Molecular Liquids* (Dr. rer. nat.-Thesis, Department of Chemistry, Ruhr-University Bochum, 1993).

[126] **Lustig, R.**: *Thermodynamik molekularer Fluide aus Computersimulationen (in German)* (Habilitationsschrift, Fachbereich Chemie, RWTH Aachen, 1994).

[127] **Lustig, R.**: Statistical thermodynamics in the classical molecular dynamics ensemble. I. Fundamentals, J. Chem. Phys., **100** (4) 3048-3059, 1994.

[128] **Lustig, R.**: Statistical thermodynamics in the classical molecular dynamics ensemble. II. Application to computer simulation, J. Chem. Phys., **100** (4) 3060-3067, 1994.

[129] **Lustig, R.**: Statistical thermodynamics in the classical molecular dynamics ensemble. III. Numerical results, J. Chem. Phys., **100** (4) 3068-3078, 1994.

[130] **Lustig, R.**: Microcanonical Monte Carlo simulations of thermodynamic properties, J. Chem. Phys., **109** (20) 8816-8828, 1998.

[131] **Luttinger, J.M.**: Theory of thermal transport coefficients, Phys. Rev., **135** (6A) A1505-A1514, 1964.

[132] **Madigosky, W.M.**: Density dependence of the bulk viscosity in argon, J. Chem. Phys., **46** (11) 4441-4444, 1967.

[133] **Maitland, G.C.; Rigby, M.; Smith, E.B.; Wakeham, W.A.**: *Intermolecular Forces - Their Origin and Determination* (Clarendon Press, Oxford, 1987).

[134] **Marchetti, M.C.; Dufty, J.W.**: Memory function for the velocity autocorrelation function at moderate densities, Chem. Phys. Lett., **70** (3) 539-543, 1980.

[135] **Marchetti, M.C.; Dufty, J.W.**: Bound-state and finite-collision-time effects in the binary-collision approximation, Phys. Rev. A, **24** (4) 2116-2134, 1981.

[136] **McDonough, A.; Russo, S.P.; Snook, I.K.**: Long-time behavior of the velocity autocorrelation function for moderately dense, soft-repulsive, and Lennard-Jones fluids, Phys. Rev. E, **63** (2) 6109, 2001.

[137] **McLennan, J.A.**: Statistical mechanics of transport in fluids, Phys. Fluids, **3** (4) 493-502, 1960.

[138] **McLennan, J.A.**: The formal statistical theory of transport processes, Adv. Chem. Phys., **5**, 261-317, 1963.

[139] **McLennan, J.A.; Swenson, R.J.**: Theory of transport coefficients in low-density gases, J. Math. Phys., **4** (12) 1527-1536, 1963.

[140] **McLennan, J.A.**: Comment on the theory of transport coefficients, Prog. Theor. Phys., **30**, 408-409, 1963.

[141] **McQuarrie, D.A.**: *Statistical Mechanics* (Harper & Row, New York, 1976).

[142] **Mecke, M.; Müller, A.; Winkelmann, J.; Vrabec, J.; Fischer, J.; Span, R.; Wagner, W.**: An accurate van der Waals-type equation of state for the Lennard-Jones fluid, Int. J. Thermophys., **17** (2) 391-404, 1996.

[143] **Michels, A.; Botzen, A.; Schuurmann, W.**: The viscosity of argon at pressures up to 2000 atmospheres, Physica, **20**, 1141-1148, 1954.

[144] **Michels, A.; Sengers, J.V.; Gulik, P.S. van der**: The thermal conductivity of carbon dioxide in the critical region. II. Measurements and conclusions, Physica, **28**, 1216-1237, 1962.

[145] **Michels, J.P.J.; Trappeniers, N.J.**: Molecular-dynamical calculations of the self-diffusion coefficient below the critical density, Chem. Phys. Lett., **33**, 195-200, 1975.

[146] **Michels, J.P.J.; Trappeniers, N.J.**: The self-diffusion coefficient in the gas phase at moderate densities, obtained by computer simulations, Physica A, **90**, 179-195, 1978.

[147] **Michels, J.P.J.; Trappeniers, N.J.**: Molecular dynamical calculations on the viscosity of a square-well fluid, Chem. Phys. Lett., **66** (1) 20-23, 1979.

[148] **Michels, J.P.J.; Trappeniers, N.J.**: Molecular dynamical calculations of the transport properties of a square-well fluid. I. The viscosity below critical density, Physica A, **101**, 156-166, 1980.

[149] **Michels, J.P.J.; Trappeniers, N.J.**: Molecular dynamical calculations on the transport properties of a square-well fluid. II. The viscosity above the critical density, Physica A, **104**, 243-254, 1980.

[150] **Michels, J.P.J.; Trappeniers, N.J.**: Molecular dynamical calculations on the transport properties of a square-well fluid. III. The thermal conductivity, Physica A, **107**, 158-165, 1981.

[151] **Michels, J.P.J.; Trappeniers, N.J.**: Molecular dynamical calculations on the transport properties of a square-well fluid. IV. The influence of the well-width on the viscosity and the thermal conductivity, Physica A, **107**, 299-306, 1981.

[152] **Michels, J.P.J.; Trappeniers, N.J.**: Molecular dynamical calculations of the transport properties of a square-well fluid. V. The coefficient of self-diffusion, Physica A, **116**, 516-525, 1982.

[153] **Michels, J.P.J.; Trappeniers, N.J.**: Molecular dynamical calculations of the viscosity of Lennard-Jones systems, Physica A, **133**, 281-290, 1985.

[154] **Mohr, P.J.; Taylor, B.N.**: CODATA recommended values of the fundamental physical constants: 1998, J. Phys. Chem. Ref. Data, **28** (6) 1713-1852, 1999.

[155] **Mori, H.**: Statistical-mechanical theory of transport in fluids, Phys. Rev., **112** (6) 1829-1842, 1958.

[156] **Mori, H.**: Transport, collective motion, and Brownian motion, Prog. Theor. Phys., **33** (3) 423-455, 1965.

[157] **Mori, H.**: A continued-fraction representation of the time-correlation functions, Prog. Theor. Phys., **34** (3) 399-416, 1965.

[158] **Mountain, R.D.; Zwanzig, R.**: Shear relaxation times of simple fluids, J. Chem. Phys., **44** (7) 2777-2779, 1966.

[159] **Mountain, R.D.**: Spectral distribution of scattered light in a simple fluid, Rev. Mod. Phys., **38** (1) 205-214, 1966.

[160] **Müller-Plathe, F.**: A simple nonequilibrium molecular dynamics method for calculating the thermal conductivity, J. Chem. Phys., **106** (14) 6082-6085, 1997.

[161] **Müller-Plathe, F.**: Reversing the perturbation in nonequilibrium molecular dynamics: An easy way to calculate the shear viscosity of fluids, Phys. Rev. E, **59** (5) 4894-4898, 1999.

[162] **Münster, A.**: *Statistische Thermodynamik (in German)* (Springer-Verlag, Berlin, 1956).

[163] **Murad, S.; Singh, D.P.; Hanley, H.J.M.; Evans, D.J.**: Thermal conductivity of a model diatomic fluid, Molec. Phys., **72** (2) 487-490, 1991.

[164] **Najafi, B.; Ghayeb, Y.; Rainwater, J.C.; Alavi, S.; Snider, R.F.**: Improved initial density dependence of the viscosity and a corresponding states function for high pressures, Physica A, **260** 31-48, 1998.

[165] **Naugle, D.G.**: Excess ultrasonic attenuation and instrinsic-volume viscosity in liquid argon, J. Chem. Phys., **44** (2) 741-744, 1966.

[166] **Naugle, D.G.; Lunsford, J.H.; Singer, J.R.**: Volume viscosity in liquid argon at high pressures, J. Chem. Phys., **45** (12) 4669-4676, 1966.

[167] **Nossal, R.**: Collective motion in simple classical fluids, Phys. Rev., **166** (1) 81-88, 1968.

[168] **Onsager, L.**: Reciprocal relations in irreversible processes. I., Phys. Rev., **37**, 405-426, 1931.

[169] **Onsager, L.**: Reciprocal relations in irreversible processes. II., Phys. Rev., **38**, 2265-2279, 1931.

[170] **Oosting, P.H.; Trappeniers, N.J.**: Proton-spin-lattice relaxation and self-diffusion in methanes. IV. Self-diffusion in methane. Physica, **51**, 418-431, 1971.

[171] **Pearson, E.M.; Halicioglu, T.; Tiller, W.A.**: Laplace-transform technique for deriving thermodynamic equations from the classical microcanonical ensemble, Phys. Rev. A, **32** (5) 3030-3039, 1985.

[172] **Peereboom, P.W.E.; Luigjes H.; Prins, K.O.; Trappeniers, N.J.**: NMR spin-echo study of self-diffusion in xenon and ethene. Physica B, **139 & 140**, 134-136, 1986.

[173] **Peereboom, P.W.E.; Luigjes H.; Prins, K.O.**: An NMR spin-echo study of self-diffusion in xenon. Physica A, **156**, 260-276, 1989.

[174] **Petravic, J.; Evans, D.J.**: Approach to the non-equilibrium time-periodic state in a 'steady' shear flow model, Molec. Phys., **95** (2) 219-231, 1998.

[175] **Pinches, M.R.S.; Tildesley, D.J.; Smith, W.**: Large Scale Molecular Dynamics on Parallel Computers Using the Link-Cell Algorithm, in: *Molecular Simulation and Industrial Applications - Methods, Examples and Prospects*, pp. 225-264, edited by K.E. Gubbins and N. Quirke (Gordon and Breach Science Publishers, Amsterdam, 1996).

[176] **Pol, A. van der; Avoird, A. van der; Wormer, P.E.S.**: An *ab initio* intermolecular potential for the carbon monoxide dimer $(CO)_2$, J. Chem. Phys., **92** (12) 7498-7504, 1990.

[177] **Pollock, E.L.**: Simulation data reported by Hoover et al. in Ref. [96].

[178] **Pomeau, Y.; Résibois, P.**: Time dependent correlation functions and mode-mode coupling theories, Phys. Rep., **19** (2) 63-139, 1975.

[179] **Prausnitz, J.M.; R.N. Lichtenthaler; Azevedo, E.G. de**: *Molecular Thermodynamics of Fluid-Phase Equilibria*, 2nd edition (Prentice-Hall, Englewood Cliffs, New Jersey, 1986).

[180] **Rainwater, J.C.**: On the phase space subdivision of the second virial coefficient and its consequences for kinetic theory. J. Chem. Phys., **81** (1) 495-510, 1984.

[181] **Rainwater, J.C.; Friend, D.G.**: Second viscosity and thermal-conductivity virial coefficients of gases: Extension to low reduced temperature. Phys. Rev. A, **36** (8) 4062-4066, 1987.

[182] **Rapaport, D.C.**: *The Art of Molecular Dynamics Simulation* (Cambridge University Press, Cambridge, 1995).

[183] **Ratanapisit, J.**: *Studies of Thermal Transport Properties Using Molecular Dynamics Simulation Techniques* (Ph.D.-Thesis, Chemical Engineering Department, Colorado School of Mines, Golden, 1999).

[184] **Ray, J.R.; Zhang, H.**: Correct microcanonical ensemble in molecular dynamics, Phys. Rev. E, **59** (5) 4781-4785, 1999.

[185] **Rowley, R.L.; Painter, M.M.**: Diffusion and viscosity equations of state for a Lennard-Jones fluid obtained from molecular dynamics simulations, Int. J. Thermophys., **18** (5) 1109-1121, 1997.

[186] **Ruckenstein, E.; Liu, H.**: Self-diffusion in gases and liquids, Ind. Eng. Chem. Res., **36**, 3927-3936, 1997.

[187] **Saager, B.; Fischer, J.**: Predictive power of effective intermolecular potentials: MD simulation results for methane up to 1000 MPa, Fluid Phase Equilib., **57**, 35-46, 1990.

[188] **Sadus, R.J.**: *Molecular simulation of fluids: theory, algorithms and object-orientation* (Elsevier, Amsterdam, 1999).

[189] **Schoen, M.; Hoheisel, C.**: The shear viscosity of a Lennard-Jones fluid calculated by equilibrium molecular dynamics, Molec. Phys., **56** (3) 653-672, 1985.

[190] **Schoen, M.**: *Berechnung zeitabhängiger kollektiver Eigenschaften von Lennard-Jones Fluiden unter besonderer Berücksichtigung der Scherviskosität (in German)* (Dr. rer. nat.-Thesis, Abteilung für Chemie, Ruhr-Universität Bochum, 1986).

[191] **Schofield, P.**: Computer simulation studies of the liquid state, Comput. Phys. Commun., **5**, 17-23, 1973.

[192] **Searles, D.J.; Evans, D.J.; Hanley, H.J.M.; Murad, S.**: Simulations of the thermal conductivity in the vicinity of the critical point, Molec. Simul., **20**, 385-395, 1998.

[193] **Shanmugan, K.S.; Breipohl, A.M.**: *Random Signals: Detection, Estimation and Data Analysis* (John Wiley & Sons, New York, 1988).

[194] **Sharma, S.; Woodcock, L.V.**: Interfacial viscosities *via* stress autocorrelation functions, J. Chem. Soc. Faraday Trans., **87** (13) 2023-2030, 1991.

[195] **Sharma, S.**: *Computer Simulation of Liquid Transport Coefficients at Solid Surfaces* (Ph.D.-Thesis, Chemical Engineering Department, University of Bradford, 1994).

[196] **Silva, C.M.; Liu, H.; Macedo, E.A.**: Models for self-diffusion coefficients of dense fluids, including hydrogen-bonding substances, Chem. Eng. Sci., **53** (13) 2423-2429, 1998.

[197] **Singer, K.; Singer, J.V.L.; Fincham, D.**: Determination of the shear viscosity of atomic liquids by non-equilibrium molecular dynamics, Molec. Phys., **40** (2) 515-519, 1980.

[198] **Snider, R.F.; Curtiss, C.F.**: Kinetic theory of moderately dense gases, Phys. Fluids, **1** (2) 122-138, 1958.

[199] **Snider, R.F.; Alavi, S.**: Moderately dense gas transport coefficients via time correlation functions. I. General formalism, J. Chem. Phys., **111** (15) 6909-6921, 1999.

[200] **Speedy, R.J.; Prielmeier, F.X.; Vardag, T.; Lang, E.W.; Lüdemann, H.-D.**: Diffusion in simple liquids, Molec. Phys., **66** (3) 577-590, 1989.

[201] **Stassen, H.; Steele, W.A.**: Simulation Studies of shear viscosity time correlation functions, J. Chem. Phys., **102** (2) 932-938, 1995.

[202] **Stassen, H.; Steele, W.A.**: Many-body correlations and the cancellation effect in the Green-Kubo time correlation functions for the shear viscosity, J. Chem. Phys., **102** (21) 8533-8540, 1995.

[203] **Steele, W.A.**: Time-correlation Functions, pp. 209-312 in: *Transport Phenomena in Fluids*, edited by H.J.M Hanley (Marcel Dekker, New York, 1969).

[204] **Stogryn, D.E.; Hirschfelder, J.O.**: Contribution of bound, metastable, and free molecules to the second virial coeffcient and some properties of double molecules, J. Chem. Phys., **31** (6) 1531-1545, 1959.

[205] **Straub, J.E.**: Analysis of the role of attractive forces in self-diffusion of a simple fluid, Molec. Phys., **76** (2) 373-385, 1992.

[206] **Swope, W.C.; Andersen, H.C.; Berens, P.H.; Wilson, K.R.**: A computer simulation method for the calculation of equilibrium constants for the formation of physical clusters of molecules: Application to small water clusters, J. Chem. Phys., **76** (1) 637-649, 1982.

[207] **Swyt, D.S.; Havlice, J.F.; Carome, E.F.**: Ultrasonic attenuation in liquid argon, J. Chem. Phys., **47**, 1199-1200, 1967.

[208] **Tiesinga, B.W.; Sakonidou, E.P.; Berg, H.R. van den; Luettmer-Strathmann, J.; Sengers, J.V.**: The thermal conductivity of argon in the critical region, J. Chem. Phys., **101** (8) 6944-6963, 1994.

[209] **Trappeniers, N.J.; Gulik, P.S. van der; Hooff, H. van den**: The viscosity of argon at very high pressure, up to the melting line, Chem. Phys. Lett., **70** (3) 438-443, 1980.

[210] **Travis, K.P.; Searles, D.J.; Evans, D.J.**: Strain rate dependent properties of a simple fluid, Molec. Phys., **95** (2) 195-202, 1998.

[211] **Trozzi, C.; Cicotti, G.**: Sationary nonequilibrium states by molecular dynamics. II. Newton's law, Phys. Rev. A, **29** (2) 916-925, 1984.

[212] **Trusler, J.P.M.**: Physical Acoustics and Metrology of Fluids (Adam Hilger, Bristol, 1991).

[213] **Tuckerman, M.; Berne, B.J.; Martyna, G.J.**: Reversible multiple time scale molecular dynamics, J. Chem. Phys., **97** (3) 1990-2001, 1992.

[214] **Viehland, L.A.; Mason, E.A.; Morrison, W.F.; Flannery, M.R.**: Tables of transport collision integrals for $(n,6,4)$ ion-neutral potentials, Atomic Data and Nuclear Data Tables, **16**, 495-514, 1975.

[215] **Viehland, L.A.; Janzen A.R.; Aziz, R.A.**: High approximations to the transport properties of pure atomic gases, J. Chem. Phys., **102** (13) 5444-5450, 1995.

[216] **Vogel, E.; Küchenmeister, C.; Bich, E.; Laesecke, A.**: Reference correlation of the viscosity of propane. J. Phys. Chem. Ref. Data, **27** (5) 947-970, 1998.

[217] **Zabaloy, M.S.; Machado, J.M.V.; Macedo, E.A.**: A study of Lennard-Jones equivalent analytical relationships for modeling viscosities, Int. J. Thermophys., **2** (3) 829-858, 2001.

[218] **Zwanzig, R.**: Statistical Mechanics of Irreversibility, in: *Lectures in Theoretical Physics*, edited by W.E. Brittin, B.W. Browns and J. Downs, Vol. **III**, 106-141 (Interscience Publishers, New York, 1961).

[219] **Zwanzig, R.**: Memory effects in irreversible thermodynamics, Phys. Rev., **124** (4) 983-992, 1961.

[220] **Zwanzig, R.**: Method for finding the density expansion of transport coefficients of gases, Phys. Rev., **129** (1) 486-494, 1963.

[221] **Zwanzig, R.**: Elementary derivation of time-correlation function formulas for transport coefficients, J. Chem. Phys., **40** (9) 2527-2533, 1964.

[222] **Zwanzig, R.**: Time-correlation functions and transport coefficients in statistical mechanics, Ann. Rev. Phys. Chem., **16**, 67-102, 1965.

[223] **Zwanzig, R.; Mountain, R.D.**: High-frequency elastic moduli of simple fluids, J. Chem. Phys., **43** (12) 4464-4471, 1965.

Curriculum Vitae

Name:	Karsten Meier
Date of birth:	6th August 1970
Place of birth:	Rehren
Marital Status:	Single
Nationality:	German

Education:

1976-81	Elementary school in Rehren
1981-83	Orientierungsstufe (junior high school) in Obernkirchen
1983-90	Gymnasium Ernestinum (high school) in Rinteln
05.90	Abitur (high school diploma)

Studies:

10.90-03.96	Mechanical engineering at the University of Hannover, major fields: energy technology and chemical engineering, degree: Dipl.-Ing. (diploma)
04.94-12.94	Guest researcher at the National Institute of Standards and Technology in Boulder, Colorado, U.S.A.

Employments:

04.96-08.96	Student assistant at the University of Hannover, Institute for Thermodynamics
10.96-09.97	Visiting research fellow at Murdoch University in Perth, Western Australia
10.97-04.01	Research assistant at the University of Hannover, Institute for Thermodynamics Supervisor: Univ.-Prof. Dr.-Ing. habil. Stephan Kabelac
07.99-08.99	Guest researcher at the National Institute of Standards and Technology in Boulder, Colorado, U.S.A.
since 05.01	Research assistant at the University of the Federal Armed Forces Hamburg, Institute for Thermodynamics Supervisor: Univ.-Prof. Dr.-Ing. habil. Stephan Kabelac